Markus Krammer

Charge Transport in Organic Semiconductor Devices

DOCTORAL THESIS

to achieve the university degree of

Doktor der technischen Wissenschaften

submitted to

Graz University of Technology

Supervisor:

Ao.Univ.-Prof. Dipl.-Ing. Dr.techn. Egbert Zojer

Co-Supervisor:

Dipl.-Phys. Dr.rer.nat. Karin Zojer

Institute of Solid State Physics

Graz, October 2019

AFFIDAVIT

I declare that I have authored this thesis independently, that I have not used other than the declared sources/resources, and that I have explicitly indicated all material which has been quoted either literally or by content from the sources used. The text document uploaded to TUGRAZonline is identical to the present doctoral thesis.

EIDESSTATTLICHE ERKLÄRUNG

Ich erkläre an Eides statt, dass ich die vorliegende Arbeit selbstständig verfasst, andere als die angegebenen Quellen/Hilfsmittel nicht benutzt, und die den benutzten Quellen wörtlich und inhaltlich entnommenen Stellen als solche kenntlich gemacht habe. Das in TUGRAZonline hochgeladene Textdokument ist mit der vorliegenden Doktorarbeit identisch.

Date/Datum

Signature/Unterschrift

Danksagung/Acknowledgement

Leider läßt sich eine wahrhafte Dankbarkeit mit Worten nicht ausdrücken.

(Johann Wolfgang von Goethe)

Dennoch sind es nur die Worte, die mir an dieser Stelle zur Verfügung stehen, um Dankbarkeit zu vermitteln. Ein expliziter Dank scheint mir unpassend, da es eine derart umfangreiche Vielfalt an Momenten in Zusammenhang mit Menschen gab, für die ich dankbar bin. Ob wissentlich oder unwissentlich, direkt oder indirekt, durch zeitraubende Diskussionen oder dem richtigen Wort zur richtigen Zeit, durch Motivation oder Ablenkung, irgendwie hattet ihr alle an der Entstehung dieser Doktorarbeit Anteil und nahmt einen vielleicht kleinen, vielleicht aber auch großen Einfluss darauf. Ganz egal wie klein der Einfluss war, dankbar bin ich jedem Einzelnen von ganzem Herzen.

My thankfulness is not just limited to German-speaking people. As already written in German, I am grateful for all influences of all people enabling the progression of this thesis, regardless of kind and amount of the influence. Every part of the jigsaw puzzle counts and there were quite a number of people involved. I thank you all.

Abstract

Although organic electronics are a multi-billion dollar market, from the viewpoint of basic research there are still numerous unsolved fundamental questions associated to, e.g., operation and fabrication. The unsolved questions we will raise and shine light on in this thesis are related to charge transport in organic electronic devices. Considering a device, it is useful to distinguish two distinctly different forms of charge transport. On the one hand, charge transport appears in the bulk of the organic semiconductor. On the other hand, charge transport through a metal-organic semiconductor interface is required to get charge carriers into and out of the device.

Well suited devices to investigate both aspects, i.e., charge transport in organic semiconductors and through metal-organic semiconductor interfaces, are organic thin-film transistors. In organic thin-film transistors suitable for this purpose, charge transport is limited to one type of charge carriers (holes or electrons) within only one organic semiconducting material. The theoretical description of those organic thin-film transistors relies on a correct description of the charge transport mechanisms, because other mechanisms like recombination processes or exciton creation and dissociation, that are predominant in organic light-emitting diodes or organic solar cells, are of negligible importance. Furthermore, two of the most important quantities influencing charge transport through a certain material, the charge-carrier density and the electric field, can be nearly independently tuned in organic thin-film transistors. By means of measured data of organic thin-film transistors from two different teams, we developed a method to test the validity of state-of-the-art transistor models. These tests attested the failure of the investigated transistor models. This failure originates either from a wrong description of charge transport within the organic thin-film transistor or from an inappropriate consideration of the influence of charge accumulations within the device on the charge transport through the interface between organic semiconductor and contacts. Those origins of the failure of the transistor models serve as a motivation for the remaining topics covered in this thesis.

The central part of this thesis is the development of a new simulation technique for hopping transport, which is an important theoretical concept to describe charge transport in disordered materials like organic semiconductors. Our new technique is combining the benefits of the two currently established simulation techniques, which are kinetic Monte Carlo and the Master equation approach. The basic idea is to map the hopping rates onto energies in a Master equation-like approach. We name them correction energies, because they correct the local charge-carrier density. This correction is required to consider field-induced charge rearrangements. Within this framework, which we call correction energy concept, correlations and interactions can be included more straight forwardly compared to the Master equation approach. At the same time, the computational effort of a simulation is significantly decreased compared to kinetic Monte Carlo simulations.

This correction energy concept is not just a useful numerical simulation technique. As a further benefit, the correction energies themselves provide valuable insight into the theoretical background governing charge transport. We demonstrate the applicability of the correction energy concept to improve the theoretical understanding of charge transport in the context of the field and charge-carrier-density dependence of the bulk mobility in an organic semiconductor. We explain the reason for the evolution of the charge-carrier mobility with respect to the electric field and the charge-carrier density. An estimate for a transition field, separating different charge transport regimes, provides a first step towards improved analytical charge transport models.

In the last part of this thesis, we look into charge transport through a metal-organic semiconductor interface. The conceptual ideas, that were developed during the derivation of the correction energy concept, are used to improve the description of the injection and extraction rates for charge carriers hopping from the metal contact to the organic semiconductor and vice versa. Commonly, the injection and extraction rates are determined by an energy level of the metal contact from where injection and to where extraction happens. Our improved description of the rates additionally enables to consider a certain value for the Fermi level of the metal contact, which sets the occupation probability of the energy level of the metal contact. Those novel injection and extraction rates are fed into a kinetic Monte Carlo simulation of a metal-organic semiconductor interface to investigate the transition from a bulk-limited regime to a contact-limited regime. From the simulations, we propose a rough estimate for the transition work function at which the bulk-limited regime turns into the contact-limited regime. We show that this simple estimate is in line with experimental data.

Kurzfassung

Die organische Halbleiterindustrie ist mittlerweile ein Multimilliarden-Dollar-Markt. Dennoch sind zahlreiche grundlegende Fragestellungen, bespielsweise bezüglich Arbeitsweise und Herstellung, ungelöst. Daher befassen wir uns in der vorliegenden Doktorarbeit mit ungelösten Fragestellungen aus dem Bereich des Ladungstransports in organischen Halbleiterbauelementen. In einem Bauelement unterscheidet man zwei Arten von Ladungstransport. Einerseits tritt Ladungstransport innerhalb des organischen Halbleiters auf und andererseits ist Ladungstransport durch eine Grenzfläche zwischen einem Metall und dem organischem Halbleiter nötig, um Ladungen in das Bauelement hinein und wieder heraus zu bekommen.

Um Ladungstransport in organischen Halbleitermaterialien und durch die Grenzfläche zwischen einem Metall und einem organischem Halbleiter zu untersuchen, bieten sich organische Dünnschichttransistoren an. Geeignete Transistoren beschränken sich auf eine Art von Ladungsträgern (Elektronen oder Löcher) und beinhalten nur ein organisches Halbleitermaterial. Um einen organischen Dünnschichttransistor theoretisch zu beschreiben, ist damit lediglich das passende Verständnis für die Vorgänge nötig, die den Ladungstransport bestimmen. Weitere Vorgänge, die in organischen Leuchtdioden oder Solarzellen beobachtet werden, wie Rekombinationsprozesse oder Exzitonenerzeugung und -aufspaltung, spielen im Transistor eine sehr untergeordnete Rolle. Außerdem lassen sich in einem Dünnschichttransistor die Ladungsträgerdichte und die elektrische Feldstärke, zwei der wichtigsten Einflussgrößen auf die Mobilität eines gegebenen Materials, nahezu unabhängig voneinander variieren. Anhand gemessener Dünnschichttransistordaten von zwei verschiedenen Arbeitsgruppen haben wir ein Hilfsmittel entwickelt, um etablierte Modelle zur Beschreibung der Arbeitsweise organischer Transistoren zu testen. Diese Tests zeigten ein klares Scheitern aller getesteten Transistormodelle. Grund dafür ist entweder eine falsche Beschreibung des Ladungstransports im Bauelement oder eine fehlende Berücksichtigung des Einflusses von Ladungsanhäufungen im Bauelement auf den Ladungstransport durch den Kontakt. Die Gründe für das Scheitern der theoretischen Beschreibung des organischen Dünnschichttransistors dienen als Motivation für die weiteren Themen dieser Doktorarbeit.

Die wesentlichste Neuerung dieser Doktorarbeit befasst sich mit der Entwicklung einer neuen Simulationsmethode für das sogenannte Konzept des Hopping Transport, welcher Ladungstransport in ungeordneten Materialien wie organischen Halbleitern theoretisch beschreibt. Dabei kombiniert unsere neue Simulationsmethode die Vorteile der beiden etablierten Methoden: kinetische Monte Carlo Simulationen und die Lösung der Mastergleichung. Grundgedanke der Methode ist, dass wir die Hüpfraten mittels eines Ansatzes ähnlich der Mastergleichung in Energien umwandeln. Diese Energien nennen wir Korrekturenergien, da sie lokal die Ladungsträgerdichte korregieren. Diese Korrektur ist notwendig um die Ladungsumverteilung aufgrund eines elektrischen Feldes richtig zu erfassen. Diese neue Methode ermöglicht es, zum einen, Korrelationen und Wechselwirkungen einfacher zu berücksichtigen als mittels Mastergleichungsverfahren und, zum anderen, Simulationen mit wesentlich geringerem numerischen Aufwand als bei kinetischen Monte Carlo Simulationen durchzuführen.

Das Konzept der Korrekturenergien liefert, zusätzlich zur Simulationsmethode, auch einen wichtigen Einblick in die theoretischen Hintergründe, welche dem Ladungstransport in organischen Halbleitern zugrunde liegen. Wir zeigen die Nützlichkeit der Korrekturenergien, indem wir das Zustandekommen der Abhängigkeit der Mobilität im Inneren des organischen Halbleiters von der Ladungsträgerdichte und vom elektrischen Feld beleuchten. Die Hintergründe für diese Abhängigkeit werden geklärt und wir

erhalten zusätzlich eine Abschätzung für eine Übergangsfeldstärke, die unterschiedliche Transportregime separiert. Diese Übergangsfeldstärke ist ein erster Schritt in Richtung eines verbesserten Modells für Ladungstransport.

Zuletzt befassen wir uns mit dem Ladungstransport durch eine Grenzfläche zwischen einem Metallkontakt und einem organischen Halbleiter. Die Ableitungen im Zusammenhang mit den Korrekturenergien stellen sich auch hier als nützlich heraus, da durch ähnliche Ableitungen eine verbesserte Beschreibung der Raten für den Hüpfprozess von Ladungsträgern aus dem Metall in den organischen Halbleiter - und umgekehrt - erhalten wird. Üblicher Weise wird ein Metallkontakt durch ein diskretes Energieniveau beschrieben, von welchem Ladungsträger in den Halbleiter hüpfen und zu welchem sie zurück in den Metallkontakt hüpfen. Wir erweitern diese Beschreibung indem wir die Wahl eines konkreten Wertes für das Fermi-Niveau des Metallkontaktes ermöglichen. Damit wird die Besetzungswahrscheinlichkeit des diskreten Energieniveaus des Metallkontakts festgelegt. Mit der neuen Kontaktbeschreibung führen wir kinetische Monte Carlo Simulationen der Region nahe der Grenzfläche zwischen einem Metallkontakt und einem organischen Halbleiter durch, um den Übergang von raumladungslimitiertem zu injektionslimitiertem Strom zu verstehen. Dank der Simulationen gelingt uns eine grobe analytische Abschätzung der Austrittsarbeit, bei der der Übergang zwischen den Regimen stattfindet. Diese Abschätzung können wir mit experimentellen Ergebnissen in Einklang bringen.

Preface: Structure of this Work

This thesis starts with a short introduction to the topic of charge transport in organic semiconductor devices in Chapter 1 and ends with a summary of all discussed topics and an outlook of the challenges arising from the thesis in Chapter 6. The main text of this thesis is split in three parts: (i), the development of an approach to test theoretical models for organic thin-film transistors via measurements, (ii), the introduction of a novel theoretical concept to simulate and understand charge transport in organic semiconductors, and, (iii), an explanation for the transition from the contact-limited to the bulk-limited regime observed for charge transport through a metal-organic semiconductor interface.

The first part, covered in Chapter 2, is dealing with the development of a model testing algorithm to examine the validity of a suggested transistor model for organic thin-film transistors. After an introduction to organic thin-film transistors, state-of-the-art transistor models are introduced and their rationale is discussed in Chapter 2.1. In Chapter 2.2, our approach to fit the measured data and extract the parameters of the tested transistor model is described. With the ability to reliably extract parameters for tested transistor models from measured data, we introduce our model testing approach in Chapter 2.3. From the model testing approach, we obtain insight into the necessary improvement of transistor models, which will be discussed in Chapter 2.4. This evaluation of the tested transistor models in Chapter 2.4 serves as a motivation of the remaining two parts of this thesis.

The second part spans two chapters, namely Chapter 3 and Chapter 4. In Chapter 3, we introduce a new simulation technique for hopping transport providing a competitive alternative to kinetic Monte Carlo and Master equation approaches. We demonstrate this new simulation technique, which we call correction energy concept, for the example of charge transport in the bulk of an organic semiconductor. In Chapter 3.1, we explain, how to translate the hopping rates for charge carriers, that hop through the bulk of an organic semiconductor, to the so-called correction energies, which enter the site-occupation probabilities of the charge carriers. To quantify the modification of the site occupation probabilities by the correction energies, the next step is to consider the correct occupation statistics for this system, which is discussed in Chapter 3.2. The numerical implementation of this correction energy concept is described in detail in Chapter 3.3 and in Chapter 3.4, the simulation results of the correction energy concept are compared to very accurate results from kinetic Monte Carlo simulations. The second half of this part, discussed in Chapter 4, makes use of the insight gained from the correction energies to improve the understanding of charge transport in the bulk of an organic semiconductor. It starts by elucidating the nature of the correction energies in Chapter 4.1, that opens a novel view on charge transport in the bulk, at least to our knowledge. This view suggests to think of charge transport in terms of basins and barriers through which charge carriers are flowing and is discussed in Chapter 4.2. With this view, the evolution of the bulk mobility with respect to the applied electric field and the charge-carrier density is discussed in Chapter 4.3.

The third part of this thesis, found in Chapter 5, investigates charge transport through a metal-organic semiconductor interface by means of kinetic Monte Carlo simulations. In Chapter 5.1, the model system we use to describe charge transport through the interface is introduced, followed by a discussion of the simulation results in Chapter 5.2, suggesting a bulk-limited and a contact-limited regime. With those regimes, we derive a rough estimate of the current density through the interface and the transition barrier between the bulk-limited and contact-limited regimes in chapter 5.3. Chapter 5.4 contains a critical discussion about the applicability of our model system of the interface and Chapter 5.5 provides

a plausibility test of our model system by means of experimental data.

Parts of Chapter 2 already have been published. In

A. Petritz, M. Krammer, E. Sauter, M. Gärtner, G. Nascimbeni, B. Schrode, A. Fian, H. Gold, A. Cojocaru, E. KarnerPetritz, R. Resel, A. Terfort, E. Zojer, M. Zharnikov, K. Zojer, and B. Stadlober, "Embedded Dipole Self-Assembled Monolayers for Contact Resistance Tuning in p-Type and n-Type Organic Thin Film Transistors and Flexible Electronic Circuits," *Advanced Functional Materials*, vol. 28, p. 1804462, Nov. 2018,

I performed the fitting to extract the ohmic and non-ohmic contact resistances as well as the equivalence mobility, which is partly covered in Chapter 2.2. I was supervised by Karin Zojer. The transistors were fabricated, measured and characterised by Andreas Petritz, Alexander Fian, Herbert Gold, Andreea Cojocaru, Esther KarnerPetritz, and Barbara Stadlober. The self-assembled monolayers were characterised by Eric Sauter, Alexander Fian, and Michael Zharnikov and simulated by Giulia Nascimbeni, and Egbert Zojer. The molecules for the self-assembled monolayers were synthesised by Michael Gärtner, and Andreas Terfort. The structure of the organic semiconductor was characterised by Benedikt Schrode, and Roland Resel.

The bottom line of Chapter 2 was published in

M. Krammer, J. W. Borchert, A. Petritz, E. Karner-Petritz, G. Schider, B. Stadlober, H. Klauk, and K. Zojer, "Critical Evaluation of Organic Thin-Film Transistor Models," *Crystals*, vol. 9, p. 85, Feb. 2019,

in which I developed the method, did all the data analysis and wrote the manuscript. Karin Zojer supervised me. James W. Borchert, and Hagen Klauk provided the measurements for the DNTT transistors and Andreas Petritz, Esther Karner-Petritz, Gerburg Schider, and Barbara Stadlober provided the measurements for the remaining transistors.

Further publications related to this thesis are

M. Krammer and K. Zojer, "Modelling Organic Devices - Foundation, Implementation, and Merit of the Kinetic Monte Carlo Method," in *World Scientific Reference of Hybrid Materials*, World Scientific Series in Nanoscience and Nanotechnology, pp. 135–185, World Scientific, Mar. 2019. ISBN: 9789813270534,

in which my supervisor, Karin Zojer, and me described the kinetic Monte Carlo simulation approach that we are using, and

M. L. Tietze, J. Benduhn, P. Pahner, B. Nell, M. Schwarze, H. Kleemann, M. Krammer, K. Zojer, K. Vandewal, and K. Leo, "Elementary steps in electrical doping of organic semiconductors," *Nature Communications*, vol. 9, p. 1182, Mar. 2018,

in which Karin Zojer and I assisted Bernhard Nell to do the kinetic Monte Carlo simulations and the discussion related to the simulations. Most of this work was accomplished by Max L. Tietze, who performed the UPS measurements, developed the doping model and wrote the manuscript. The absorption/transmission measurements were done by Max L. Tietze, and Johannes Benduhn. Impedance spectroscopy and Mott-Schottky analysis were done by Max L. Tietze, Paul Pahner, and Hans Kleemann. Some temperature-dependent UPS measurements were performed by Martin Schwarze. Koen Vandewal, and Karl Leo functioned as supervisors and contributed with fruitful discussions.

Contents

1 Introduction

Organic semiconductors (OSCs) have evolved into an important class of materials for industry. The organic electronics industry is nowadays a multi-billion dollar market with the potential to further grow. [5] This growth is particularly promoted by the splendid match of key properties of OSCs and our modern lifestyle. The lightweight and flexible nature of OSCs enables a broad range of future applications, especially in the financially strong branch of consumer electronics. The biocompatibility of many OSCs might also trigger medical applications, the easy tunability of properties by changing the chemical composition makes OSCs ideal candidates for sensing applications and the rather simple and cheap production, compared to inorganic semiconductors, could open up new perspectives in energy harvesting.

This big potential of OSCs comes along with big challenges. The research on OSCs lags some decades behind their inorganic counterpart, resulting in problems that have already been solved for inorganic semiconductors. Especially in terms of mobility and switching speed, OSCs will, most likely, never be able to compete with inorganic semiconductors. However, being competitive with respect to mobility and switching speed is commonly not required because the fields of application of organic and inorganic semiconductors is mostly complementary. Nevertheless, many future applications require at least an improvement of the properties of OSCs and their implementation in OSC devices.

Improving properties of OSCs and their implementation in devices is a very demanding task due to the numerous possibilities provided by the world of organic molecules. In fact, one of the most important strengths, namely that the properties of the OSCs can be deliberately tuned by designing molecules or substituting parts of molecules, poses, at the same time, one of the biggest challenges. This challenge, to find the most suitable material for a certain purpose out of millions and billions of possibilities, can be facilitated by a solid understanding of the ongoing processes in the OSC device. If we know, how particular properties of the OSC change the device performance, a specific design of materials becomes possible.

The topic for which we want to improve the understanding in this thesis is charge transport in OSC devices. From an experimental point of view, the organic thin-film transistor (OTFT) is a well suited device to develop a basic understanding of charge transport. The OTFT my still be viewed as a rather academic device, especially compared to the organic light-emitting diode (OLED), which holds the largest share of industrial applications. Future applications of OTFTs as display drivers, in sensors or in integrated circuits that exclusively consist of OSC devices might raise the importance of OTFTs for industry.

Our interest in OTFTs within this thesis is purely academic. In Chapter 2, we developed a method to test theoretical transistor models, including state-of-the-art charge-transport models, via measured data. This means we can verify or falsify theoretical assumptions of charge transport with the help of experimentally measured transistor data and, hence, utilise the OTFT to look into charge transport. Measured data sets from different types of OTFTs performed by the group of Hagen Klauk in Stuttgart[1] and Barbara Stadlober in Weiz[2] reveal that there is an inconsistency in our current view on charge transport in OTFTs. The method further provides insight into possible problems associated to our current view on charge transport. The two problems obtained by our method are associated to, (i), the particular dependence of the charge-carrier mobility in the OTFT on the charge-carrier density and the electric field or,

[1]Max Planck Institute for Solid State Research, Heisenbergstraße 1, 70569 Stuttgart, Germany; H.Klauk@fkf.mpg.de

[2]Joanneum Research Materials, Institute for Surface Technologies and Photonics, Franz-Pichler-Straße 30, 8160 Weiz, Austria; barbara.stadlober@joanneum.at

(ii), the influence of charge accumulations within the device on the region close to the interface between metal contact and organic semiconductor. This insight, and the two problems associated to it, serve as motivation for the remaining thesis.

The first problem is associated to a lack of understanding of charge transport within the OSC. To improve this understanding, we develop a novel simulation technique for hopping transport in Chapter 3, which is a formal link between the two established simulation techniques, kinetic Monte Carlo (KMC) and master equation (ME). This novel simulation technique, which we call correction energy concept (CEC), combines the benefits of the two methods with reduced computational cost compared to KMC and reduced methodological error compared to ME. The correction energy concept is not only a simulation technique, it further provides physical insight into charge transport mechanisms by casting the effect of an externally applied electric field to so-called correction energies that modify the energy landscape through which the charge carriers are travelling in a characteristic way. In Chapter 4, we demonstrate the usage of the such gained physical insight to understand the evolution of the bulk mobility with respect to the applied electric field strength and the charge-carrier density.

The second problem, detected during our investigation of measurements of OTFTs, comes from the long-ranging nature of the Coulomb potential causing a non-negligible effect of charge accumulations in the device on the contact region. In Chapter 5, the contact region of a metal-OSC interface is simulated with kinetic Monte Carlo. We develop a new description of the hopping rates associated with the contact to properly account for its occupation. The simulations are performed to identify the reason behind the transition from a contact-limited regime to a bulk-limited regime related to the current from the metal contact to the OSC. From the simulation results, a strongly simplifying model is suggested to receive the current density through the interface. This model describes the qualitative behaviour of the interface quite well and, furthermore, agrees semi-quantitatively with experimental data measured by the group of Dieter Neher in Potsdam[3].

A major outcome of this thesis are newly developed methods. We developed, (i), a method to test theoretical transistor models with the help of experimentally measured data from OTFTs, (ii), a novel technique to simulate hopping transport, derived on the example of charge transport in the bulk of OSCs, and, (iii), a refinement of the description of a metal contact exchanging charge carriers with an OSC. All three new methods are described in detail to enable the interested reader to implement, advance and further refine the methods.

We hope that this thesis is appealing for a broad audience, be them methodologically inclined (method reader) or, rather, interested in the insights generated by the methods (outcome reader). For each type of reader, some parts are more relevant than others and some parts might be skipped entirely. Below, we provide a recommendation regarding the conduciveness of certain chapters for both, the method reader and the outcome reader, .

In Chapter 2 'Organic Thin-Film Transistor', the method reader is well advised to have a close look at Chapter 2.1.2 'Derivation of the Transistor Models', Chapter 2.1.3 'Numerical Implementation' and Chapter 2.2 'Fitting Procedure'. The method reader might also go through the remaining chapters to be able to analyse and interpret the outcomes of their own investigation of OTFT data with our method, in particular Chapter 2.1.4 'Influence of Parameters on Output Characteristics' in combination with Chapter 2.4 'Model Evaluation'. In contrast, the outcome reader can mainly focus on Chapter 2.3 'Model

[3]University of Potsdam, Soft Matter Physics, Karl-Liebknecht-Straße 24-25, 14476 Potsdam-Golm, Germany; neher@uni-potsdam.de

Testing' and Chapter 2.4 'Model Evaluation'. Additionally, the outcome reader is recommended to take a look at Chapter 2.1.4 'Influence of Parameters on Output Characteristics' to fully appreciate the interpretations in Chapter 2.4 'Model Evaluation'.

The whole Chapter 3 'Correction Energy Concept' is rather dedicated to the method reader, whereas Chapter 4 'Charge Transport in Bulk' is mainly of interest for the outcome reader. To develop a better understanding for the correction energy concept, a look at Chapter 4 'Charge Transport in Bulk' might also be beneficial for the method reader.

In Chapter 5 'Metal-Organic Semiconductor Interface', the method reader can mainly focus on Chapter 5.1 'Model System for the Interface'. Chapter 5.2 'Bulk- and Contact-Limited Regime', Chapter 5.3 'Estimation of the Current Density' and Chapter 5.4 'Interpretability of the Model System' might be of interest for both, the method and the outcome reader. Chapter 5.5 'Comparison with Experiment' is devoted to the outcome reader.

2 Organic Thin-Film Transistor

In comparison to organic light-emitting diodes (OLEDs) and organic solar cells, which are devices that already arrived at the industry with a broad range of commercial applications, the focus of the organic thin-film transistor (OTFT) still lies in academic research. This might change in the next couple of years due to advances enabling commercial applications. [6]

One of the most important academic applications of OTFTs is for testing material parameters with respect to charge transport. [7] Due to the ability to nearly independently tune the charge-carrier density and the electric field within the semiconducting layers of the OTFT, the dependence of the mobility on those two quantities can be investigated for the material of interest. Especially in organic semiconductors (OSCs), the mobility shows a pronounced dependence on the charge-carrier density and the electric field. The existence of this dependence is commonly known, from an experimental as well as from a theoretical point of view. Nevertheless, the precise appearance of this dependence is still debated. [8–17]

A crucial factor to be able to investigate charge transport properties of materials properly is, that the working principle of the OTFT is well understood. This includes, (i), that non-idealities at the interfaces of the OSC and the dielectric, as well as at the interface of the OSC and the contacts, have to be kept to a minimum experimentally and, (ii), that the theoretical description of the device has to be as accurate as possible. Bad devices and/or wrong transistor models lead to untrustworthy results. [18–20]

The significant improvement of the manufacturing process of OTFTs providing a nicely defined dielectric and nearly ideal contacts, [1, 20–24] enables a decent test of theoretical charge transport models. A possible procedure to perform such charge transport model tests is given in this chapter. We start with introducing commonly used transistor models in Chapter 2.1. In Chapter 2.2, we describe how to properly fit those transistor models to measured transistor data. This fitting procedure is the first step of our model testing approach. The second step of this model testing approach and its application to measured transistor data is found in Chapter 2.3. Our model testing approach can provide hints to find out what is wrong with a transistor model, which is discussed in Chapter 2.4.

2.1 Transistor Models

An adequate transistor model is the key to, (i), properly extract material parameters, like the mobility, from measured data, (ii), understand the behaviour of an OTFT correctly and, moreover, (iii), gain insight into charge transport mechanisms in OSCs. If the transistor model is wrong, we might learn nothing or imply even wrong conclusions from the measured data used to extract the material parameters. With our new approach to test transistor models, we can easily distinguish correct from false transistor models. To be able to explain the failure of a transistor model, we have to know the behaviour of this transistor model very well. Hence, we will introduce the basics of thin-film transistors in Chapter 2.1.1 before deriving the utilised transistor models in Chapter 2.1.2 and describe their numerical implementation in Chapter 2.1.3 followed by a visualisation of the impact of parameters on the behaviour of the transistor in Chapter 2.1.4.

2.1.1 Basics of Thin-Film Transistors

Our explanation of the working principle of a thin-film transistor (also called field-effect transistor) is inspired by the subtle explanation in a review by Zaumseil and Sirringhaus. [25] A transistor is a device

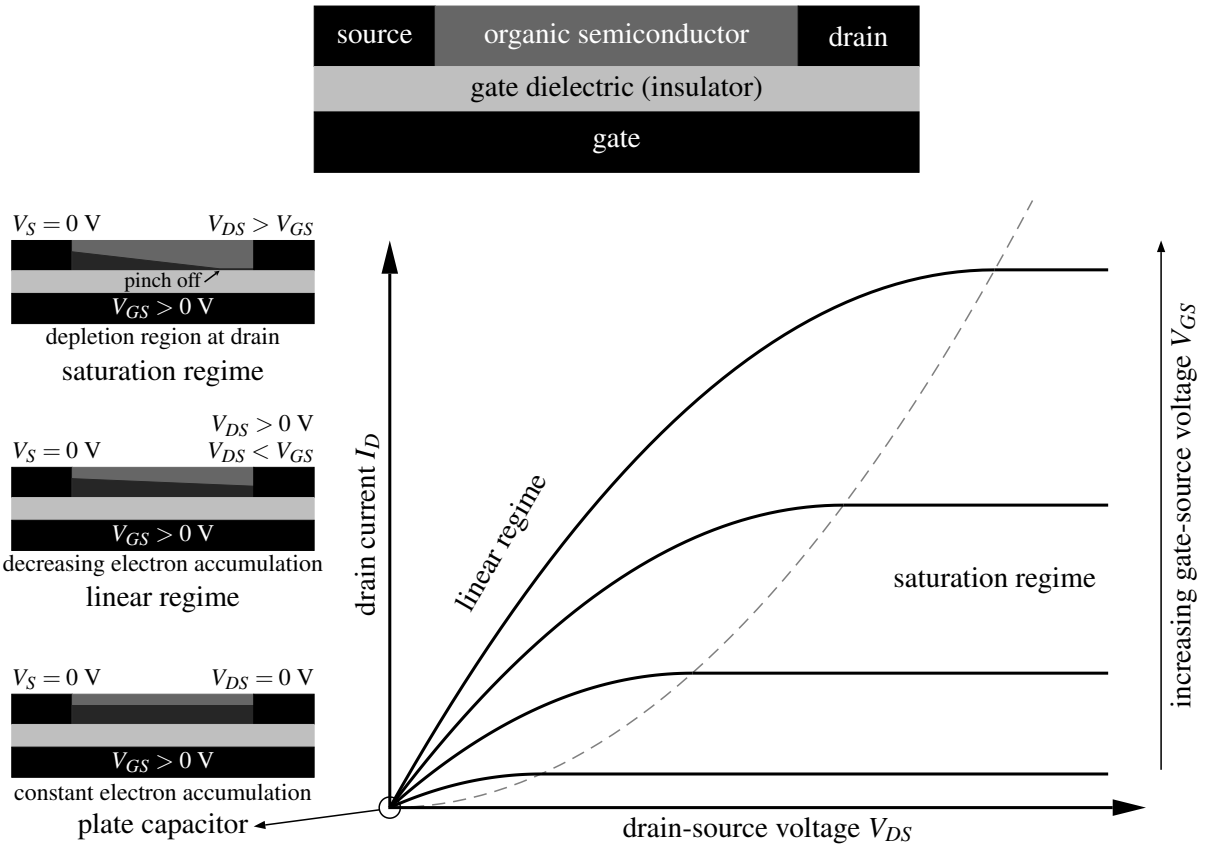

Figure 2.1: The upper part shows a schematic drawing of an organic thin-film transistor with the three contacts gate, drain and source. Between drain and source, the organic semiconductor (OSC) is found. The gate is separated from the remaining device by an insulating dielectric. The lower part illustrates the working principle of an electron conducting (n-type) organic thin-film transistor with exemplary electron distributions for different regimes indicated in dark grey at the left side and a typical output characteristics (drain current I_D as a function of the applied drain-source voltage V_{DS} for different values of the gate-source voltage V_{GS}) of an ideal OTFT with constant mobility at the right side. When no drain-source voltage is applied $V_{DS} = 0$ V, the device acts as a plate capacitor. If we apply a gate-source voltage $V_{GS} > 0$ V, electrons are accumulated in the OSC at the interface to the dielectric. This electron accumulation region is called the channel. Applying a low drain-source voltage $V_{DS} \ll V_{GS}$, the accumulated electrons in the channel start to move and the drain current I_D increases linear with V_{DS}. In this so-called linear regime, the electron density decreases from source to drain. If the drain-source voltage is large than the gate-source voltage $V_{DS} > V_{GS}$, the gate voltage is not strong enough to accumulate electrons close to the drain contact. As a consequence, a depletion region forms from the drain contact to a certain position in the channel which is called pinch off. Due to the formation of this depletion region, the drain current saturates to a constant value entering the saturation regime. The dashed grey line marks the equality of drain-source voltage and gate-source voltage $V_{DS} = V_{GS}$, separating linear and saturation regime.

with three contacts: a gate, a drain and a source, shown in the upper part of Figure 2.1. Between the drain and source contact, the OSC is placed and the gate contact is separated from the OSC by an insulating dielectric.

The lower part of Figure 2.1 demonstrates the working principle of an OTFT on the example of an n-type OTFT. The term n-type specifies that the majority charge carriers in the device are electrons, whereas p-type would refer to holes. When applying a voltage between gate an source, V_{GS}, the device

acts like a plate capacitor and electrons accumulate in the OSC at the interface to the dielectric. This region where the electrons are accumulated is called the channel. When applying an additional voltage between drain and source, V_{DS}, the accumulated electrons feel a force and start to move, creating a current between drain and source. This so-called drain current I_D depends on the electron density in the channel, mostly determined by the gate-source voltage V_{GS}, and the electric field between drain and source, mostly determined by the drain-source voltage V_{DS}.

In the lower part of Figure 2.1, a typical output characteristics of an ideal thin-film transistor with constant mobility is shown on the right side and the electron distribution in the channel for different operation regimes is indicated in dark grey on the left side. The term output characteristics refers to the plot of the drain current I_D as a function of the applied drain-source voltage V_{DS} for different values of the gate-source voltage V_{GS}.

In the so-called linear regime, the drain-source voltage is lower than the gate-source voltage $V_{DS} < V_{GS}$. If $V_{DS} \ll V_{GS}$, the drain current I_D increases linear with the applied drain-source voltage V_{DS}. In this linear regime, the electron density is decreasing when going from source to drain. As soon as we reach a drain-source voltage that exceeds the gate-source voltage $V_{DS} > V_{GS}$, the gate voltage is no longer sufficient to accumulate electrons at the drain contact (only electrons can be accumulated in an n-type OTFT, discussed in Chapter 2.1.2). Hence, a depletion region forms at the drain contact that reaches into the channel up to a certain position called pinch off. This depletion causes the drain current I_D to saturate, entering the saturation regime. The separation of the linear regime and the saturation regime at $V_{DS} = V_{GS}$ is indicated as a grey dashed line in the output characteristics shown in Figure 2.1.

2.1.2 Derivation of the Transistor Models

The lumped element model for the most complex transistor model that we tested is shown in Figure 2.2. All transistor models, that we tested, are based on this lumped element model, sometimes omitting certain aspects. We derive this established transistor model in the following to realise the associated assumptions and approximations.

The experimentally accessible contacts are labelled G for gate, D for drain and S for source in Figure 2.2. The experimentally applied voltages are the gate-source voltage V_{GS} between gate and source and the drain-source voltage V_{DS} between drain and source. The reaction of the transistor to those applied voltages is the drain current I_D flowing from drain to source. In this transistor model, we assume a perfectly insulating gate dielectric, resulting in a vanishing gate current $I_G = 0$ A. The core of the transistor model is the ideal thin-film transistor in the gradual channel approximation [26, 27], with a charge-carrier-density- and field-dependent mobility, situated between the ideal gate G', drain D' and source S' contacts. Ideal means that all contact effects, i.e., at the interface between dielectric and OSC as well as contacts and OSC, are not included. Those contact effects are considered in the lumped element model by introducing external elements in Figure 2.2. The threshold voltage V_T between G and G' accounts for non-idealities at the dielectric-OSC interface like a dipole layer, doping or traps causing a shift of the gate potential. [28–31] A mismatch of the Fermi level of the contacts and the charge transport level in the OSC might shift the gate potential as well. The contact resistances R_D at the drain side and R_S at the source side account for ohmic losses at the contacts, but can also include non-ohmic contributions. The source is defined as the contact at which the charge carriers are injected. During injection, a mismatch of the energy levels in the contact and the OSC can cause an additional non-ohmic contribution to the contact losses, which is not present at the drain side. This asymmetry regarding the contacts is

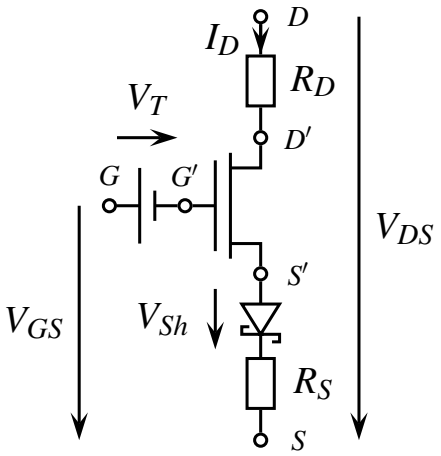

Figure 2.2: Lumped element model of the most complex transistor model that we tested. The experimentally accessible contacts are labelled G for gate, D for drain and S for source with the corresponding experimentally adjusted voltages V_{GS} for the gate-source voltage and V_{DS} for the drain-source voltage. The measurable outcome of applying V_{GS} and V_{DS} is the drain current I_D. Between the contacts G', D' and S', we place an ideal thin-film transistor in the gradual channel approximation [26,27] with a charge-carrier-density- and field-dependent mobility. Between ideal and accessible gate contact G' and G, the threshold voltage V_T accounts for dipoles or traps at the dielectric-OSC interface and other non-idealities shifting the gate potential. The contact resistances R_D at the drain side and R_S at the source side can contain non-ohmic contributions and the Schottky-diode at the source side, causing a voltage drop V_{Sh}, accounts for injection barriers at the source side as the contact at which charge injection occurs.

captured by a Schottky-diode at the source side creating a voltage loss V_{Sh}.

OTFTs can be divided in p-type and n-type transistors. Unlike inorganic transistors, this division is not related with doping. Due to the typically large band gap in OSCs, the position of the Fermi level of the contacts with respect to the highest occupied molecular orbital (HOMO) and the lowest unoccupied molecular orbital (LUMO) of the OSC decides, whether holes or electrons are injected more efficiently and act, hence, as the majority charge carriers, resulting in p-type or n-type devices, respectively. If the Fermi level is close to the HOMO, hole transport is predominant creating a p-type transistor and if the Fermi level is close to the LUMO, electron transport is predominant creating an n-type transistor. A decent match of the energy levels for one type of charge carriers implies a substantial mismatch for the other type of charge carriers caused by the typically large band gap of OSCs. This match and mismatch results in the fact, that usually only one type of charge carriers can be accumulated in the channel, because injection can hardly be achieved for the minority charge carriers associated to the mismatch of the energy levels. For both types of transistors with respect to the majority charge carriers, the source is always defined as the injecting contact, injecting holes for p-type transistors and electrons for n-type transistors. As a consequence, the sign of the applied voltages V_{GS} and V_{DS} as well as the measured drain current I_D is negative for p-type transistors and positive for n-type transistors. The transistor model is valid for both transistor types with only the sign being changed. To describe both transistor types at once, we define a variable q that holds the charge sign with $q = 1\ \mathrm{V}^{-1}$ for hole transport (p-type) and $q = -1\ \mathrm{V}^{-1}$ for electron transport (n-type). The unit of q is required to be able to define reduced voltages $\upsilon = qV$. Those reduced voltages υ possess no unit, which will be important when inserting reduced voltages consistently in exponential functions. With those definitions, the reduced voltages $\upsilon_{GS} = qV_{GS}$, $\upsilon_{DS} = qV_{DS}$ and the reduced drain current qI_D are negative under normal operation conditions (negative

voltages and current for p-type transistor and negative q for n-type transistor).

The mobility μ in the OSC at a position x in the channel is assumed to be charge-carrier-density and field dependent in the form

$$\mu(x) = \mu_0 \exp\left(\kappa\sqrt{\frac{L_0}{L}\upsilon_{S'D'}}\right)\Theta\left(\upsilon_{S'D'}\right)\left(\upsilon_{Ch}(x)-\upsilon_{G'}\right)^{\gamma}\Theta\left(\upsilon_{Ch}(x)-\upsilon_{G'}\right) \tag{2.1}$$

with the mobility prefactor μ_0, the exponent of the field sensitivity κ, the constant length scale $L_0 = 1\ \mu$m enabling a reduced length in the exponent, the channel length L, the reduced channel potential $\upsilon_{Ch}(x)$ at the requested position x in the channel, the exponent of the sensitivity with respect to the charge-carrier density γ and the Heaviside-step-function $\Theta(\upsilon) = 1$ for $\upsilon \geq 0$ and $\Theta(\upsilon) = 0$ for $\upsilon < 0$. When the mobility is not depending on the charge-carrier density and the electric field, the two exponents are zero ($\kappa = 0$ and $\gamma = 0$) and the mobility prefactor μ_0 gives the mobility value $\mu = \mu_0$.

The second term in Equation (2.1) is a strongly simplified form of a Poole-Frenkel field dependence of the mobility. [32, 33] The reduced electric field $f \approx \frac{\upsilon_{S'D'}}{L}L_0$ is approximated via dividing the reduced source-drain voltage $\upsilon_{S'D'} = qV_{S'D'}$ by the channel length L and multiplying it with a constant length scale $L_0 = 1\ \mu$m to receive a dimensionless reduced field f. With this reduced field, the exponential square root behaviour of the Poole-Frenkel field dependence $\exp(\kappa\sqrt{f})$ is approximated. The Heaviside-step-function $\Theta(\upsilon_{S'D'})$ corresponds to the definition of source as the injecting contact, requiring a positive reduced voltage $\upsilon_{S'D'}$. Furthermore, it prevents the appearance of complex numbers.

The third term in Equation (2.1) represents an approximation for the charge-carrier-density dependence of the mobility. The reduced voltage $\upsilon_{Ch}(x) - \upsilon_{G'}$ between the ideal gate contact and the channel at a position x is approximately proportional to the accumulated charge in the channel via the gate capacity of the dielectric C_G (gate capacitance per unit area) due to its plate-capacitor behaviour. An exponential behaviour of the mobility with respect to the charge-carrier density is suggested by, (i), variable-range hopping in combination with percolation theory [34] and, (ii), multiple trapping and release [35]. The Heaviside-step-function takes into account, that only one type of charge carriers can be accumulated in the channel and prevents the appearance of complex numbers.

With this mobility model, Equation (2.1), we can derive an implicit system of equations to determine the drain current I_D for given values of the drain-source voltage V_{DS} and the gate-source voltage V_{GS}. This derivation makes use of the gradual channel approximation [26, 27]. This approximation relies on the assumption that the electric field along the channel (from drain to source) varies much less than the field across the channel (from gate to the OSC). Typically, this assumption is valid if the channel length L is much larger than the thickness of the gate dielectric. Within the gradual channel approximation, the charge per unit area $e\rho_{Ch}(x)$ at a position x in the channel is determined by the gate capacitance per unit area C_G and the reduced voltage $\upsilon_{Ch}(x) - \upsilon_{G'}$ on both sides of the dielectric via the charge-voltage relation of a plate capacitor.

$$e\rho_{Ch}(x) = \frac{C_G}{|q|}\left(\upsilon_{Ch}(x)-\upsilon_{G'}\right)\Theta\left(\upsilon_{Ch}(x)-\upsilon_{G'}\right) \tag{2.2}$$

The Heaviside-step-function accounts for the fact that only one type of charge carriers can be accumulated in the channel and e stands for the elemental charge. The charge per unit area $e\rho_{Ch}(x)$ and the charge carriers per unit area $\rho_{Ch}(x)$ are positive for holes and electrons. The factor $\frac{1}{|q|}$ ensures the correct unit of the charge per unit area.

The current density j_{Ch} in the channel is given by the electric field $F = -\frac{\partial V_{Ch}(x)}{\partial x}$, the mobility μ and the charge per unit area $e\rho_{Ch}(x)$

$$j_{Ch} = e\frac{\rho_{Ch}(x)}{h}\mu F = -e\frac{\rho_{Ch}(x)}{h}\mu\frac{\partial V_{Ch}(x)}{\partial x} \tag{2.3}$$

with the channel height h perpendicular to the interface between the dielectric and the OSC and the charge carriers per unit volume $\frac{\rho_{Ch}(x)}{h}$. Assuming a homogeneous current density along the cross section of the channel with its height h and its width W, the reduced drain current is given by

$$qI_D = qj_{Ch}hW = -e\rho_{Ch}(x)W\mu\frac{\partial \upsilon_{Ch}(x)}{\partial x}. \tag{2.4}$$

In steady state, the charge per unit area $e\rho_{Ch}(x)$ does not change over time, resulting in a constant drain current I_D all along the channel due to the continuity equation. Both sides of Equation (2.4) are integrated over the channel, considering the mobility μ of Equation (2.1) and the charge per unit area of Equation (2.2).

$$\begin{aligned} qI_D L &= \int_0^L -e\rho_{Ch}(x)W\mu\frac{\partial \upsilon_{Ch}(x)}{\partial x}dx = \\ &= -\frac{W\mu_0 C_G}{|q|}\int_{\upsilon_{D'}}^{\upsilon_{S'}} \exp\left(\kappa\sqrt{\frac{L_0}{L}\upsilon_{S'D'}}\right)\Theta(\upsilon_{S'D'})\,(\upsilon_{Ch}-\upsilon_{G'})^{\gamma+1}\,\Theta(\upsilon_{Ch}-\upsilon_{G'})\,d\upsilon_{Ch} \end{aligned} \tag{2.5}$$

The integration is performed from drain to source, i.e., a possible reduction of the channel length L due to pinch off in the saturation regime is neglected. This integration of Equation (2.4) results in a factor L on the left-hand side of Equation (2.5) due to the constant drain current I_D. On the right-hand side, we can transform the integral to integrate over the reduced channel υ_{Ch}. Evaluating this integral provides the relation

$$qI_D = -\frac{W\mu_0 C_G}{|q|L(\gamma+2)}\exp\left(\kappa\sqrt{\frac{L_0}{L}\upsilon_{S'D'}}\right)\Theta(\upsilon_{S'D'})\left(\upsilon_{S'G'}^{\gamma+2}\Theta(\upsilon_{S'G'}) - \upsilon_{D'G'}^{\gamma+2}\Theta(\upsilon_{D'G'})\right) \tag{2.6}$$

This Equation (2.6) represents the ideal OTFT. To introduce non-idealities from the contacts in Equation (2.6), we have to switch over from the ideal contacts gate G', drain D' and source S' to the external contacts gate G, drain D and source S as suggested by our lumped element model, shown in Figure 2.2. At the gate, the threshold voltage V_T is considered $\upsilon_G = \upsilon_{G'} + qV_T$. The drain resistance R_D leads to $\upsilon_D = \upsilon_{D'} + qI_D R_D$ and the source resistance R_S and Schottky-diode voltage loss V_{Sh} provides $\upsilon_S = \upsilon_{S'} - qI_D R_S - qV_{Sh}$.

For the drain and source resistance R_D and R_S, we assume

$$R_D = \frac{r_{D,o}}{W} + \frac{\alpha_D}{W\upsilon_{D'G'}^{\gamma+1}}\Theta(\upsilon_{D'G'}) \quad \text{and} \quad R_S = \frac{r_{S,o}}{W} + \frac{\alpha_S}{W\upsilon_{S'G'}^{\gamma+1}}\Theta(\upsilon_{S'G'}) \tag{2.7}$$

with ohmic channel-width-reduced drain and source resistances $r_{D,o}$ and $r_{S,o}$ and a non-ohmic contribution weighted by α_D and α_S. The non-ohmic contribution approximates a space-charge-limited current close to the contacts. [36]

The voltage loss V_{Sh} across the Schottky-diode for a given drain current I_D is received by assuming

gate-voltage-dependent thermionic emission. [1, 37, 38]

$$V_{Sh} = -\frac{|q|k_B T_{Sh}}{qe} \ln\left[1 + \frac{I_D}{W j_0} \exp\left(\eta \frac{qeV_{GS}}{|q|k_B T_{Sh}}\right)\right] \tag{2.8}$$

The parameters determining the Schottky-diode behaviour are the Schottky temperature T_{Sh}, the channel-width-reduced Schottky current j_0 and gate-source voltage sensitivity η. Additionally, the Boltzmann constant k_B and the elemental charge e are required. At $T_{Sh} = 0$ K, we define

$$V_{Sh} = \begin{cases} V_0 & \text{if } qI_D < 0 \ \frac{\mathrm{A}}{\mathrm{V}} \\ 0 & \text{if } qI_D = 0 \ \frac{\mathrm{A}}{\mathrm{V}} \end{cases} \tag{2.9}$$

which means that if a current is flowing, the voltage V_0 drops at the Schottky diode, while no voltage loss is present when no current is flowing. Positive reduced drain currents $qI_D > 0 \ \frac{\mathrm{A}}{\mathrm{V}}$ are not consistent with our definition of source as injecting contact and, hence, are not required to be considered.

In total, the implicit system of equations

$$\begin{aligned}
qV_{Sh} &= \begin{cases} -\frac{|q|k_B T_{Sh}}{e} \ln\left[1 + \frac{I_D}{W j_0} \exp\left(\eta \frac{qeV_{GS}}{|q|k_B T_{Sh}}\right)\right] & \text{if } T_{Sh} > 0 \text{ K} \\ \begin{cases} qV_0 & \text{if } qI_D < 0 \ \frac{\mathrm{A}}{\mathrm{V}} \\ 0 & \text{if } qI_D = 0 \ \frac{\mathrm{A}}{\mathrm{V}} \end{cases} & \text{if } T_{Sh} = 0 \text{ K} \end{cases} \\
\upsilon_{D'G'} &= q\left(V_T - V_{GS} + V_{DS} - I_D \frac{r_{D,o}}{W} - I_D \frac{\alpha_D}{W \upsilon_{D'G'}^{\gamma+1}} \Theta(\upsilon_{D'G'})\right) \\
\upsilon_{S'G'} &= q\left(V_T - V_{GS} + V_{Sh} + I_D \frac{r_{S,o}}{W} + I_D \frac{\alpha_S}{W \upsilon_{S'G'}^{\gamma+1}} \Theta(\upsilon_{S'G'})\right) \\
\upsilon_{S'D'} &= \upsilon_{S'G'} - \upsilon_{D'G'} \\
qI_D &= -\frac{W\mu_0 C_G}{|q|L(\gamma+2)} \exp\left(\kappa\sqrt{\frac{L_0}{L}\upsilon_{S'D'}}\right) \Theta(\upsilon_{S'D'}) \left(\upsilon_{S'G'}^{\gamma+2} \Theta(\upsilon_{S'G'}) - \upsilon_{D'G'}^{\gamma+2} \Theta(\upsilon_{D'G'})\right)
\end{aligned} \tag{2.10}$$

determines the drain current I_D for a given applied drain-source voltages V_{DS} and a given applied gate-source voltage V_{GS}. In Chapter 2.1.3, we explore how to numerically solve this implicit system of equations efficiently to be able to calculate transistor characteristics.

2.1.3 Numerical Implementation

When fitting a large data set of measured output and transfer characteristics of an OTFT, the drain current I_D has to be calculated many times. Hence, an efficient algorithm to calculate the drain current I_D from the implicit system of linear equations, Equation (2.10), is crucial for a proper data evaluation. In the following, we distinguish between three different options to numerically solve the implicit system of equations, Equation (2.10), with respect to the choice of the non-ohmic components α_D and α_S. The first option assumes no contribution from the non-ohmic components $\alpha_D = \alpha_S = 0$ kΩcm. As a consequence, the second and the third line in Equation (2.10) explicitly determine $\upsilon_{D'G'}$ and $\upsilon_{S'G'}$. So we only need to iteratively calculate the implicitly given drain current I_D. In contrast, for the second and third option when non-ohmic components $\alpha_D > 0$ kΩcm and/or $\alpha_S > 0$ kΩcm are present, the reduced voltages $\upsilon_{D'G'}$ and/or $\upsilon_{S'G'}$ are implicitly determined by the second and third line in Equation (2.10). Hence, inside each

iterative loop related to the evaluation of the implicitly determined drain current I_D, the reduced voltages $\upsilon_{D'G'}$ and/or $\upsilon_{S'G'}$ have to be calculated iteratively. The second option assumes a non-ohmic component only at the drain side $\alpha_D > 0$ kΩcm and $\alpha_S = 0$ kΩcm, whereas the third option focuses on the solution when $\alpha_S > 0$ kΩcm with an arbitrary choice of $\alpha_D \geq 0$ kΩcm.

Below, we will discuss the algorithms to iteratively solve each of the implicit equations. We will start with the first option involving explicitly accessible $\upsilon_{D'G'}$ and $\upsilon_{S'G'}$ before discussing the second and third option with non-ohmic components $\alpha_D > 0$ kΩcm and/or $\alpha_S > 0$ kΩcm. The approach to receive a solution is, in principle, the same for all implicit equations. Each implicit equation has the form $u = f(u)$, which can be seen as searching for the intercept of the straight line u and a function $f(u)$. From considerations regarding the monotonicity of the function $f(u)$, an initial interval $[u_{min}, u_{max}]$ containing only one solution is determined. With this interval $[u_{min}, u_{max}]$, one step of the iteration starts with calculating the midpoint $u_1 = \frac{u_{min}+u_{max}}{2}$ and the corresponding function value $u_2 = f(u_1)$. Those values u_1 and u_2 deliver a refined search interval, which is at least reduced to half the size of the old interval. By continuing this iteration, the solution is found swift and efficient.

Solving Equation (2.10) **for explicitly accessible $\upsilon_{D'G'}$ and $\upsilon_{S'G'}$ ($\alpha_D = \alpha_S = 0$ kΩcm)**

Without non-ohmic components $\alpha_D = \alpha_S = 0$ kΩcm, only the last line in Equation (2.10) has an implicit form $qI_D = f(qI_D)$. To find the initial interval $[qI_{D,min}, qI_{D,max}]$ the monotonicity of $f(qI_D)$ is determined from its derivative with respect to qI_D from Equation (2.10):

$$\begin{aligned}\frac{\partial f(qI_D)}{\partial qI_D} = -\frac{W\mu_0 C_G}{|q|L}\exp\left(\kappa\sqrt{\frac{L_0}{L}\upsilon_{S'D'}}\right)\Theta(\upsilon_{S'D'})\Bigg\{&\left[\frac{r_{S,o}}{W} - \frac{|q|k_B T_{Sh}}{qe\left[I_D + Wj_0\exp\left(-\eta\frac{qeV_{GS}}{|q|k_B T_{Sh}}\right)\right]}\right]\\ &\times\left[\upsilon_{S'G'}^{\gamma+1}\Theta(\upsilon_{S'G'}) + \kappa\sqrt{\frac{L_0}{L}}\frac{\upsilon_{S'G'}^{\gamma+2}\Theta(\upsilon_{S'G'}) - \upsilon_{D'G'}^{\gamma+2}\Theta(\upsilon_{D'G'})}{2(\gamma+2)\sqrt{\upsilon_{S'D'}}}\right]\\ &+\frac{r_{D,o}}{W}\left[\upsilon_{D'G'}^{\gamma+1}\Theta(\upsilon_{D'G'}) + \kappa\sqrt{\frac{L_0}{L}}\frac{\upsilon_{S'G'}^{\gamma+2}\Theta(\upsilon_{S'G'}) - \upsilon_{D'G'}^{\gamma+2}\Theta(\upsilon_{D'G'})}{2(\gamma+2)\sqrt{\upsilon_{S'D'}}}\right]\Bigg\}\end{aligned} \tag{2.11}$$

The constants L_0, k_B, e, geometry factors L, W, C_G[4], parameters μ_0, κ, $\gamma+1$, $r_{S,o}$, $r_{D,o}$, T_{Sh} and the reduced voltages $\upsilon_{S'D'}\Theta(\upsilon_{S'D'})$, $\upsilon_{S'G'}\Theta(\upsilon_{S'G'}) \geq \upsilon_{D'G'}\Theta(\upsilon_{D'G'})$ are positive while the reduced currents qI_D, qWj_0 are negative. As a consequence, every single term in equation (2.11) results in a positive value. Due to the leading minus sign, we get in total $\frac{\partial f(qI_D)}{\partial qI_D} \leq 0$.

This negative slope of $f(qI_D)$ guarantees, that the straight line qI_D has exactly one intercept with $f(qI_D)$. Furthermore, the intercept is between any pair of values $qI_{D,1}$ and $qI_{D,2} = f(qI_{D,1})$, because between the points $(qI_{D,1}, f(qI_{D,1}))$ on the curve $f(qI_D)$ and $(qI_{D,2}, qI_{D,2})$ on the straight line with the same second coordinate $qI_{D,2} = f(qI_{D,1})$, the curves must intercept. As discussed in Chapter 2.1.2, the reduced drain current must be negative $qI_D \leq 0\ \frac{\mathrm{A}}{\mathrm{V}}$. Hence, the interval $[qI_{D,min}, 0)$, with an initial guess for a minimum reduced drain current $qI_{D,min} = f(qI_D = 0^-)$, contains a unique solution for qI_D.

Knowing that $\frac{df(qI_D)}{dqI_D} \leq 0$ and that the unique solution is located in the interval $[qI_{D,min}, qI_{D,max}]$, we can find the solution for the equation $qI_D = f(qI_D)$ by combining a bisection method with a fixed

[4]The gate capacitance per unit area is considered as a geometry factor because it is usually estimated from the thickness and permittivity of the dielectric.

point iteration of a recursive sequence. Starting from the search interval $[qI_{D,min}, qI_{D,max}]$, the midpoint $qI_{D,1} = \frac{qI_{D,min}+qI_{D,max}}{2}$ and the corresponding function value $qI_{D,2} = f(qI_{D,1})$ are calculated. With those values for $qI_{D,1}$ and $qI_{D,2}$, three cases can be distinguished:

- If $qI_{D,2} = qI_{D,1}$, the solution is found and the search algorithm is finished.
- If $qI_{D,2} > qI_{D,1}$, the solution has to be greater than $qI_{D,1}$, which makes $qI_{D,1}$ the new lower bound of the search interval and $qI_{D,2}$ a potential new upper bound. The old search interval $[qI_{D,min}, qI_{D,max}]$ turns into the new search interval $[qI_{D,1}, \min(qI_{D,max}, qI_{D,2})]$.
- If $qI_{D,2} < qI_{D,1}$, the solution has to be lower than $qI_{D,1}$, which makes $qI_{D,1}$ the new upper bound of the search interval and $qI_{D,2}$ a potential new lower bound. The old search interval $[qI_{D,min}, qI_{D,max}]$ turns into the new search interval $[\max(qI_{D,min}, qI_{D,2}), qI_{D,1}]$.

With the new search interval, the new midpoint is calculated in the next step of the iteration and so on. Due to using $\min(qI_{D,max}, qI_{D,2})$ as new upper bound or $\max(qI_{D,min}, qI_{D,2})$ as new lower bound, the search interval is at least cut in half. However, the convergence can be much faster, if the fixed point iteration provides much better new upper or lower bounds.

Solving Equation (2.10) **for implicitly determined $\upsilon_{D'G'}$ and explicitly accessible $\upsilon_{S'G'}$ ($\alpha_D > 0$ kΩcm, $\alpha_S = 0$ kΩcm)**

Considering a non-ohmic component $\alpha_D > 0$ kΩcm in the implicit system of equations, Equation (2.10), the second line in Equation (2.10) for $\upsilon_{D'G'}$ becomes implicit. So we need to perform an iteration to determine $\upsilon_{D'G'}$ for a given value of qI_D in each step of the iteration for qI_D.

Iteration for $\upsilon_{D'G'}$: The equation for $\upsilon_{D'G'}$ in the second line in Equation (2.10) has the form

$$u = A + \frac{B}{u^C} \tag{2.12}$$

with constants $A \in \mathbb{R}$ and $B, C \in \mathbb{R}^+$. Comparing the second line in Equations (2.10) and (2.12), the constants are given by $A = q\left(V_T - V_{GS} + V_{DS} - I_D \frac{r_{D,o}}{W}\right)$, $B = -\frac{qI_D\alpha_D}{W} > 0$ and $C = \gamma + 1 > 0$. The right-hand side of this equation $f(u) = A + \frac{B}{u^C}$ represents a continuous function in $\upsilon_{D'G'} = u > 0$ with $\frac{\partial f(u)}{\partial u} = -\frac{BC}{u^{C+1}} < 0$, $\lim_{u\to\infty} f(u) = A$ and $\lim_{u\to 0^+} f(u) = \infty$. Hence, exactly one solution for $u = \upsilon_{D'G'}$ is found for $\upsilon_{D'G'} > 0$.

To find this solution of Equation (2.12) for $u = \upsilon_{D'G'} > 0$, a proper guess for the initial interval is beneficial. To receive this guess, we distinguish between three cases depending on the value of A: If (i) $A = 0$, then $u = \upsilon_{D'G'}$ can be calculated explicitly $u = B^{\frac{1}{C+1}}$. If (ii) $A < 0$, then the solution is close to zero and we can assume $u_{min} = 0$. An upper bound is given by either setting the left-hand side of Equation (2.12) to zero or setting A to zero, resulting in $u_{max} = \min((-\frac{B}{A})^{\frac{1}{C}}, B^{\frac{1}{C+1}})$. If (iii) $A > 0$, then the minimum can be set to $u_{min} = A$ and the maximum to $u_{max} = A + \frac{B}{A^C}$, which represents the first step of the iteration to find $u = \upsilon_{D'G'}$. With the minimum u_{min} and maximum u_{max} and the knowledge that the $f(u) = A + \frac{B}{u^C}$ is monotonically decreasing $\frac{\partial f(u)}{\partial u} < 0$, the iterative approach described above for qI_D is utilised.

Iteration for qI_D: The iteration scheme determining qI_D is exactly the same as described above for $\alpha_D = 0$ kΩcm. The only prerequisite, which has to be checked to ensure the success of the same iteration scheme, is that the derivative $\frac{\partial f(qI_D)}{\partial qI_D} \leq 0$ is still negative. The derivative

$$\frac{\partial \upsilon_{D'G'}}{\partial qI_D} = \frac{-\frac{r_{D,o}}{W} - \frac{\alpha_D}{W\upsilon_{D'G'}^{\gamma+1}}\Theta(\upsilon_{D'G'})}{1 - \frac{qI_D\alpha_D(\gamma+1)}{W\upsilon_{D'G'}^{\gamma+2}}\Theta(\upsilon_{D'G'})} \tag{2.13}$$

is negative for $\alpha_D > 0$ kΩcm and for $\alpha_D = 0$ kΩcm. Hence, including $\alpha_D > 0$ kΩcm does not change the sign of the derivative $\frac{\partial f(qI_D)}{\partial qI_D}$, which means it is still negative.

Solving Equation (2.10) **for implicitly determined $\upsilon_{S'G'}$ ($\alpha_S > 0$ kΩcm, $\alpha_D \geq 0$ kΩcm)**

Due to the non-ohmic component $\alpha_S > 0$ kΩcm, $\upsilon_{S'G'}$ has to be calculated iteratively for a given reduced drain current qI_D in each step of the iteration for qI_D to solve the implicit system of equations, Equation (2.10). The reduced voltage $\upsilon_{D'G'}$ is calculated explicitly when $\alpha_D = 0$ kΩcm or implicitly as described above when $\alpha_D > 0$ kΩcm. Whether $\upsilon_{D'G'}$ is determined explicitly or implicitly does not affect the iteration scheme to evaluate $\upsilon_{S'G'}$ and qI_D for $\alpha_S > 0$ kΩcm.

Iteration for $\upsilon_{S'G'}$: For the evaluation of $\upsilon_{S'G'}$ via the third line in Equation (2.10), we have to solve an implicit equation of the form

$$u = A - \frac{B}{u^C} \tag{2.14}$$

with constants $A \in \mathbb{R}$ and $B, C \in \mathbb{R}^+$. Comparing the third line in Equations (2.10) and (2.14), the constants are given by $A = q\left(V_T - V_{G'} + V_{Sh} + I_D\frac{r_{S,o}}{W}\right)$, $B = -\frac{qI_D\alpha_S}{W} > 0$ and $C = \gamma + 1 > 0$. For small positive or negative values of A, no positive value for u can satisfy this equation. If A is positive and B is large, no solution can be found as well. Continuously reducing B leads to the point at which the function $A - \frac{B}{u^C}$ touches the straight line u and exactly one solution is received. Further reducing B leads to two solutions.

To numerically calculate $\upsilon_{S'G'}$, the number of positive solutions for $u = \upsilon_{S'G'}$ has to be evaluated first. If it has exactly one solution, the two curves (left- and right-hand side of Equation (2.14)) have to touch each other. Touching implies that the slopes have to be equal at the touching point, which means that the right-hand side of Equation (2.14) has to have a slope of 1. This slope of 1 is obtained at $u_{sl1} = (BC)^{\frac{1}{C+1}}$. The value $f(u_{sl1}) = A - B/(u_{sl1})^C$ decides how many solutions are present. If, (i), $u_{sl1} = f(u_{sl1})$, the curves are touching each other and u_{sl1} is the only positive solution. If, (ii), $u_{sl1} > f(u_{sl1})$, the right-hand side of Equation (2.14) will always be lower than the left-hand side, which means that no positive solution exists. If, (iii), $u_{sl1} < f(u_{sl1})$, two positive solutions $u_1 > u_{sl1}$ and $u_2 < u_{sl1}$ can be found.

To find the first solution u_1, the limits $u_{min} = u_{sl1}$ and $u_{max} = A$ are appropriate. The slope of the right-hand side of the equation is between zero and one, motivating the following iteration scheme: Calculate the midpoint $u_{1,1} = \frac{u_{min}+u_{max}}{2}$ and the right-hand side function value $u_{1,2} = A - B/(u_{1,1})^C$. If $u_{1,1} = u_{1,2}$, then the solution u_1 is found. If $u_{1,1} > u_{1,2}$, then the solution u_1 is below $u_{1,1}$ and $u_{1,2}$ resulting in $[u_{min}, u_{max}] \rightarrow [u_{min}, u_{1,2}]$. If $u_{1,1} < u_{1,2}$, then the solution u_1 is above $u_{1,1}$ and $u_{1,2}$ resulting in $[u_{min}, u_{max}] \rightarrow [u_{1,2}, u_{max}]$. Iteratively reducing this interval $[u_{min}, u_{max}]$ delivers u_1.

To find the second solution u_2, the limits $u_{min} = 0$ and $u_{max} = u_{sl1}$ are used. As the slope of the

right-hand side of Equation (2.14) is larger than one, the function value of the right-hand side is not pointing towards the solution like for u_1, but pointing away from the solution leading to the following iteration scheme: Calculate the midpoint $u_{2,1} = \frac{u_{min}+u_{max}}{2}$ and the right-hand side function value $u_{2,2} = A - B/(u_{2,1})^C$. If $u_{2,1} = u_{2,2}$, then the solution u_2 is found. If $u_{2,1} > u_{2,2}$, then the solution u_2 is above $u_{2,1}$ and $u_{2,2}$ resulting in $[u_{min}, u_{max}] \rightarrow [u_{2,1}, u_{max}]$. If $u_{2,1} < u_{2,2}$, the solution u_2 is below $u_{2,1}$ and $u_{2,2}$ resulting in $[u_{min}, u_{max}] \rightarrow [u_{min}, u_{2,1}]$. Iteratively reducing this interval $[u_{min}, u_{max}]$ delivers u_2.

Iteration for qI_D: With the iteration scheme to receive a solution for $\upsilon_{D'G'}$ and two solutions for $\upsilon^1_{S'G'}$ and $\upsilon^2_{S'G'}$, we can move on to develop an iteration scheme to calculate qI_D from the implicit system of equations, Equation (2.10). According to the two solutions for $\upsilon^1_{S'G'}$ and $\upsilon^2_{S'G'}$, the right-hand side $f(qI_D)$ of the last line in the implicit system of equations, Equation (2.10), provides two corresponding values, as illustrated in the upper panel in Figure 2.3. When the drain current is approaching zero $qI_D \rightarrow 0^-$ ($B \rightarrow 0^+$), one of the two solutions for $\upsilon_{S'G'}$ results in $\upsilon^1_{S'G'} = q(V_T - V_{GS} + V_{Sh}(qI_D \rightarrow 0^-))$, which is the solution belonging to $\alpha_S = 0$ kΩcm, and the second solution is $\upsilon^2_{S'G'} \rightarrow 0^+$. If $\upsilon^1_{S'G'} \leq 0$, the reduced drain current is zero $qI_D = 0 \frac{\mathrm{A}}{\mathrm{V}}$. Else, the function $f(qI_D)$ has a negative value corresponding to $\upsilon^1_{S'G'}$ and a vanishing value $f(qI_D \rightarrow 0^-) = 0^-$ corresponding to $\upsilon^2_{S'G'}$. For negative values of the reduced drain current qI_D, the function value $f(qI_D)$ for $\upsilon^1_{S'G'}$ becomes less negative and for $\upsilon^2_{S'G'}$ more negative until they meet in a single point corresponding to only one solution for $\upsilon_{S'G'}$. Reduced drain currents below this value with only one solution for $\upsilon_{S'G'}$ cannot provide a function value $f(qI_D)$, resulting in a minimum reduced drain current $qI_{D,min}$.

The upper half-bow of $-f(qI_D)$ for $\upsilon^1_{S'G'}$ and the lower half-bow of $-f(qI_D)$ for $\upsilon^2_{S'G'}$ are nicely visualised in the upper panel in Figure 2.3, in which the function value $-f(qI_D)$ is shown as a function of the absolute reduced drain current $-qI_D$ for different applied drain-source voltages V_{DS} and a gate-source voltage of $V_{GS} = -5$ V. The simulated device is a p-type OTFT with constant mobility $\mu_0 = 1 \frac{\mathrm{Vs}}{\mathrm{cm}^2}$, ohmic drain resistance $r_{D,o} = 0.1$ kΩcm, ohmic source resistance $r_{S,o} = 0.1$ kΩcm, non-ohmic contributions $\alpha_D = 0.1$ kΩcm and $\alpha_S = 10$ kΩcm. The black line in the upper panel in Figure 2.3 corresponds to the straight line $-qI_D$ and the intercept with a bow of $-f(qI_D)$ determines the solution for qI_D for the chosen drain-source voltage V_{DS}.

The iterative approach to find this intercept and the associated solution $qI_D = f(qI_D)$ for the implicit system of equations, Equation (2.10), starts on the upper half-bow of $-f(qI_D)$ for $\upsilon^1_{S'G'}$. The upper half-bow is chosen, because in most of the relevant cases, the solution for qI_D is found on this upper half-bow.

Finding a solution on the upper half-bow is achieved in the same way as for the case of explicit $\upsilon_{D'G'}$ and $\upsilon_{S'G'}$. Starting with $qI_{D,max} = 0 \frac{\mathrm{A}}{\mathrm{V}}$, $\upsilon_{D'G'}$ and $\upsilon^1_{S'G'}$ are calculated to receive $f(qI_{D,max}) = qI_{D,min}$. This precalculation provides proper values as long as our prerequisites $qV_{GS} \leq 0$ and $qV_{DS} \leq 0$ are fulfilled. If those prerequisites are not fulfilled, the drain current is zero anyway. With the interval $[qI_{D,min}, qI_{D,max}]$, each step of the iteration starts by calculating the midpoint $qI_{D,1} = \frac{qI_{D,min}+qI_{D,max}}{2}$ and the function value $qI_{D,2} = f(qI_{D,1})$ on the upper half-bow representing $\upsilon^1_{S'G'}$. If $f(qI_{D,1})$ has no solution, $qI_{D,1}$ is too low and the search interval is changed from $[qI_{D,min}, qI_{D,max}]$ to $[qI_{D,1}, qI_{D,max}]$. If $qI_{D,1} = qI_{D,2}$, the solution is found. If $qI_{D,2} > qI_{D,1}$, the search interval is changed from $[qI_{D,min}, qI_{D,max}]$ to $[qI_{D,1}, \min(qI_{D,max}, qI_{D,2})]$. If $qI_{D,2} < qI_{D,1}$, the search interval is changed from $[qI_{D,min}, qI_{D,max}]$ to $[\max(qI_{D,min}, qI_{D,2}), qI_{D,1}]$.

The result from the iteration for the upper half-bow is an interval $[qI_{D,min}, qI_{D,max}]$. If $f(qI_{D,min})$ provides a solution, the value from the iteration for the upper half-bow is the correct solution for qI_D.

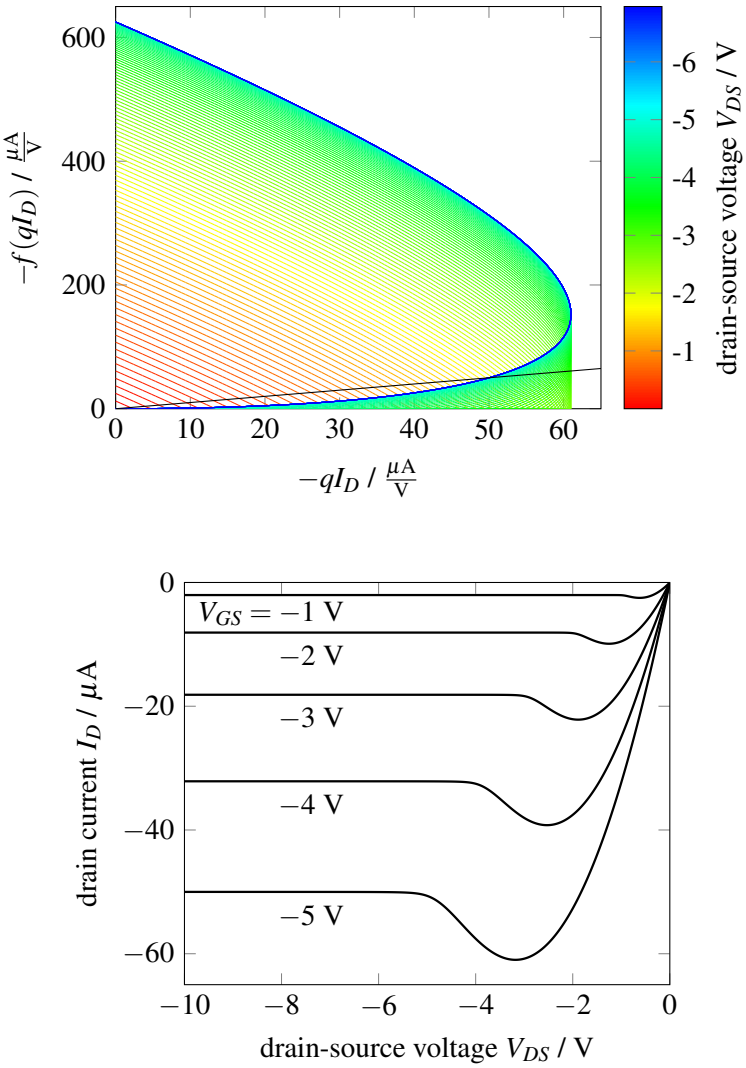

Figure 2.3: The upper panel shows the right-hand side $-f(qI_D)$ of the last equation of the implicit system of equations given in Equation (2.10) as a function of the assumed drain current $-qI_D$ for different applied drain-source voltages V_{DS} (colour coded) and a gate-source voltage of $V_{GS} = -5$ V. The simulated p-type OTFT has a constant mobility $\mu_0 = 1\ \frac{\mathrm{Vs}}{\mathrm{cm}^2}$, ohmic drain resistance $r_{D,o} = 0.1$ kΩcm, ohmic source resistance $r_{S,o} = 0.1$ kΩcm, non-ohmic contributions $\alpha_D = 0.1$ kΩcm and $\alpha_S = 10$ kΩcm. All remaining parameters of the transistor model are zero. The solution for $-qI_D$ is determined by the intercept of $-f(qI_D)$ and the straight line $-qI_D$ indicated as a black line. The lower panel shows the output characteristics of this device. The initial increase of the absolute drain current $-I_D$ with respect to the absolute drain-source voltage $-V_{DS}$ reaches a maximum. When the solution for $qI_D = f(qI_D)$ swaps from the upper half-bow of $-f(qI_D)$ to the lower half-bow of $-f(qI_D)$, the absolute drain current $-I_D$ starts to decrease. This behaviour is clearly non-physical indicating a violation of the model assumptions in this operation region of the transistor. As we are only interested in model assumptions describing the transistor as a whole, the non-ohmic contributions to the contact resistances $\alpha_D = \alpha_S = 0$ kΩcm are omitted from now on.

If not, we only found the minimum drain current qI_D, below which no solution exists, i.e., we have to search for the solution on the lower half-bow corresponding to the solution $\upsilon^2_{S'G'}$. For this search, the initial search interval can be set to $[qI_{D,min}, 0)$ with the minimum $qI_{D,min}$ of the iteration for the upper half-bow. One step of the iteration with an initial interval $[qI_{D,min}, qI_{D,max}]$, again, starts with the midpoint $qI_{D,1} = \frac{qI_{D,min}+qI_{D,max}}{2}$ and the function value $qI_{D,2} = f(qI_{D,1})$ on the lower half-bow representing

$\upsilon^2_{S'D'}$. Equivalent to the upper half-bow, when no solution for $f(qI_{D,1})$ exists, $qI_{D,1}$ is a lower bound changing the search interval from $[qI_{D,min}, qI_{D,max}]$ to $[qI_{D,1}, qI_{D,max}]$. If $qI_{D,1} = qI_{D,2}$, the solution is found. In contrast to the upper half-bow, the search interval in case of $qI_{D,2} > qI_{D,1}$ changes from $[qI_{D,min}, qI_{D,max}]$ to $[qI_{D,min}, qI_{D,1}]$ and in case of $qI_{D,2} < qI_{D,1}$ from $[qI_{D,min}, qI_{D,max}]$ to $[qI_{D,1}, qI_{D,max}]$. With this search on the lower half-bow, the solution qI_D is found. In the unlikely event that qI_D is precisely at the meeting point of the upper and the lower half-bow and has only one solution, the search interval after the iteration for the lower half-bow will result in a lower bound $qI_{D,min}$ for which, again, no solution $f(qI_{D,min})$ exists. Nevertheless, even in this case the found solution qI_D is the correct solution, within its numerical uncertainty.

Output characteristics for large α_S: The lower panel in Figure 2.3 shows the output characteristics of the p-type OTFT described above. The observed decrease of the absolute drain current $-I_D$ with increasing absolute drain-source voltage $-V_{DS}$ (e.g. seen at $V_{GS} = -5$ V and $V_{DS} \approx -4$ V in the lower panel in Figure 2.3) is non-physical and inherent to the transistor model. In the following, we will discuss the numerical reason for this behaviour before drawing our conclusions from this behaviour.

The peculiar form of the characteristics is a consequence of the two solutions for $\upsilon_{S'G'}$ associated to the upper and lower half-bow of $-f(qI_D)$ plotted in the upper panel in Figure 2.3. To understand the peculiar shape of the output characteristics in the lower panel in Figure 2.3, we will pursue the origin of the formation of the curve for $V_{GS} = -5$ V with the help of the upper panel in Figure 2.3. The bow of $-f(qI_D)$ is best spotted from the blue lines for $-V_{DS} \gtrsim 5.5$ V in the upper panel in Figure 2.3. Decreasing the absolute drain-source voltage $-V_{DS}$ results mainly in a rigid shift of this bow towards lower values for $-f(qI_D)$. For low absolute drain-source voltage $-V_{DS} \lesssim 2$ V (red to yellow curves in the upper panel in Figure 2.3), the intercept of the black line for $-qI_D$ and the bow of $-f(qI_D)$ lies on the upper half-bow. With increasing absolute drain-source voltage $-V_{DS}$, the absolute drain current $-I_D$ increases as the bow of $-f(qI_D)$ shifts upwards. Around $-V_{DS} = 3$ V, the absolute drain current $-I_D$ saturates and reaches a maximum (see lower panel in Figure 2.3). This maximum corresponds precisely to the condition when the black line $-qI_D$ in the upper panel in Figure 2.3 intercepts with the bow of $-f(qI_D)$ at its meeting point of the upper and lower half-bow. Increasing the absolute drain-source voltage $-V_{DS}$ beyond this maximum shifts the bow of $-f(qI_D)$ further up. The solution for $-qI_D$ is now found on the lower half-bow of $-f(qI_D)$ resulting in a decrease in the absolute drain current $-I_D$. Beyond an absolute drain-source voltage $-V_{DS} \gtrsim 5.5$ V, the bow of $-f(qI_D)$ does not change anymore and the drain current saturates.

The decrease of the absolute drain current $-I_D$ with increasing absolute drain-source voltage $-V_{DS}$, observed in the output characteristics in the lower panel in Figure 2.3, is clearly non-physical. The reason for this non-physical behaviour is the assumed dependence of the non-ohmic contact resistance on the charge-carrier density involving the exponent of the sensitivity with respect to the charge-carrier density of the mobility γ. The consequence of this non-physical behaviour is, that the transistor model is not able to describe the transistor for all operation conditions (V_{DS} and V_{GS}) in a physically reasonable way. Although the transistor model leads to physical behaviour for many instances of the choice of the parameters α_D and α_S, we are exclusively interested in a transistor model describing transistors as a whole with all possible operation conditions and parameters. Thus, all non-ohmic contributions to the contact resistance, that are associated with the parameters α_D and α_S, will be omitted from now on by setting $\alpha_D = \alpha_S = 0$ kΩcm.

Omitting the non-ohmic components $\alpha_D = \alpha_S = 0$ kΩcm, the implicit system of linear equations considered from now on is given by:

$$
\begin{aligned}
qV_{Sh} &= \begin{cases} -\frac{|q|k_B T_{Sh}}{e} \ln\left[1 + \frac{I_D}{Wj_0} \exp\left(\eta \frac{qeV_{GS}}{|q|k_B T_{Sh}}\right)\right] & \text{if } T_{Sh} > 0 \text{ K} \\ \begin{cases} qV_0 & \text{if } qI_D < 0 \ \frac{\text{A}}{\text{V}} \\ 0 & \text{if } qI_D = 0 \ \frac{\text{A}}{\text{V}} \end{cases} & \text{if } T_{Sh} = 0 \text{ K} \end{cases} \\
\upsilon_{D'G'} &= q\left(V_T - V_{GS} + V_{DS} - I_D \frac{r_{D,o}}{W}\right) \\
\upsilon_{S'G'} &= q\left(V_T - V_{GS} + V_{Sh} + I_D \frac{r_{S,o}}{W}\right) \\
\upsilon_{S'D'} &= \upsilon_{S'G'} - \upsilon_{D'G'} \\
qI_D &= -\frac{W\mu_0 C_G}{|q|L(\gamma+2)} \exp\left(\kappa\sqrt{\frac{L_0}{L}\upsilon_{S'D'}}\right) \Theta(\upsilon_{S'D'}) \left(\upsilon_{S'G'}^{\gamma+2}\Theta(\upsilon_{S'G'}) - \upsilon_{D'G'}^{\gamma+2}\Theta(\upsilon_{D'G'})\right)
\end{aligned}
\tag{2.15}
$$

with four constants, k_B, e, q, L_0, three geometry factors, L, W, C_G, ten parameters, V_T, μ_0, $r_{S,o}$, $r_{D,o}$, γ, κ, j_0, T_{Sh}, η, V_0, two input quantities, V_{DS}, V_{GS}, and one output quantity I_D.

2.1.4 Influence of Parameters on Output Characteristics

To be able to interpret deviations of measured and calculated characteristics, it is essential to know the influence of a change in the parameters of the applied transistor model, Equation (2.15), on the characteristics. This knowledge enables an interpretation of the reasons for the deviations between measurement and calculations, which is the prerequisite for a precise statement about how to improve the transistor model. Due to the large amount of up to 9 simultaneously active parameters, the knowledge of their influence on the characteristics is of particular importance.

Figure 2.4 and Figure 2.5 visualise the deformation of the output characteristics of a p-type OTFT (channel length $L = 10$ µm, channel width $W = 1$ mm and gate capacitance per unit area $C_G = 500 \ \frac{\text{nF}}{\text{cm}^2}$) when changing one parameter after the other. Note that these Figures do not address the threshold voltage V_T and the Schottky-diode voltage loss V_0 at Schottky temperature $T_{Sh} = 0$ K. Those two parameters only change the gate voltage $V_G \to V_G - V_T$ and the drain-source voltage $V_{DS} \to V_{DS} - V_0$ resulting in a rigid shift of the characteristics, but no change in their shape.

The upper left panel in Figure 2.4 shows the output characteristics for the most basic transistor model with a constant mobility, no contact resistances and no Schottky diode. All parameters are set to zero, only the mobility prefactor receives a certain value $\mu_0 = 1 \ \frac{\text{Vs}}{\text{cm}^2}$. For a certain gate-source voltage V_{GS}, the absolute drain current $-I_D$ increases parabolic with the absolute drain-source voltage $-V_{DS}$ up to the apex of the parabola at $V_{DS} = V_{GS}$. At this voltage, the saturation regime is entered and the absolute drain current $-I_D$ stays constant. The increase of the absolute drain current $-I_D$ in the saturation regime with respect to the absolute gate-source voltage $-V_{GS}$ is quadratic for the ideal OTFT. Hence, the spacing between the saturation curves increases with increasing absolute gate-source voltage.

In the upper panels in Figure 2.4, from the left to the right, the channel-width-reduced ohmic source resistance $r_{S,o} = 0.1$ kΩcm is changed. The output characteristics prior to the change is indicated with grey dashed lines in the upper right panel in Figure 2.4 and the black lines show the output characteristics after the change. The source resistance has an impact on the linear and the saturation regime and scales down the drain current I_D in approximately equal fashion for all drain-source voltages V_{DS}. This scaling

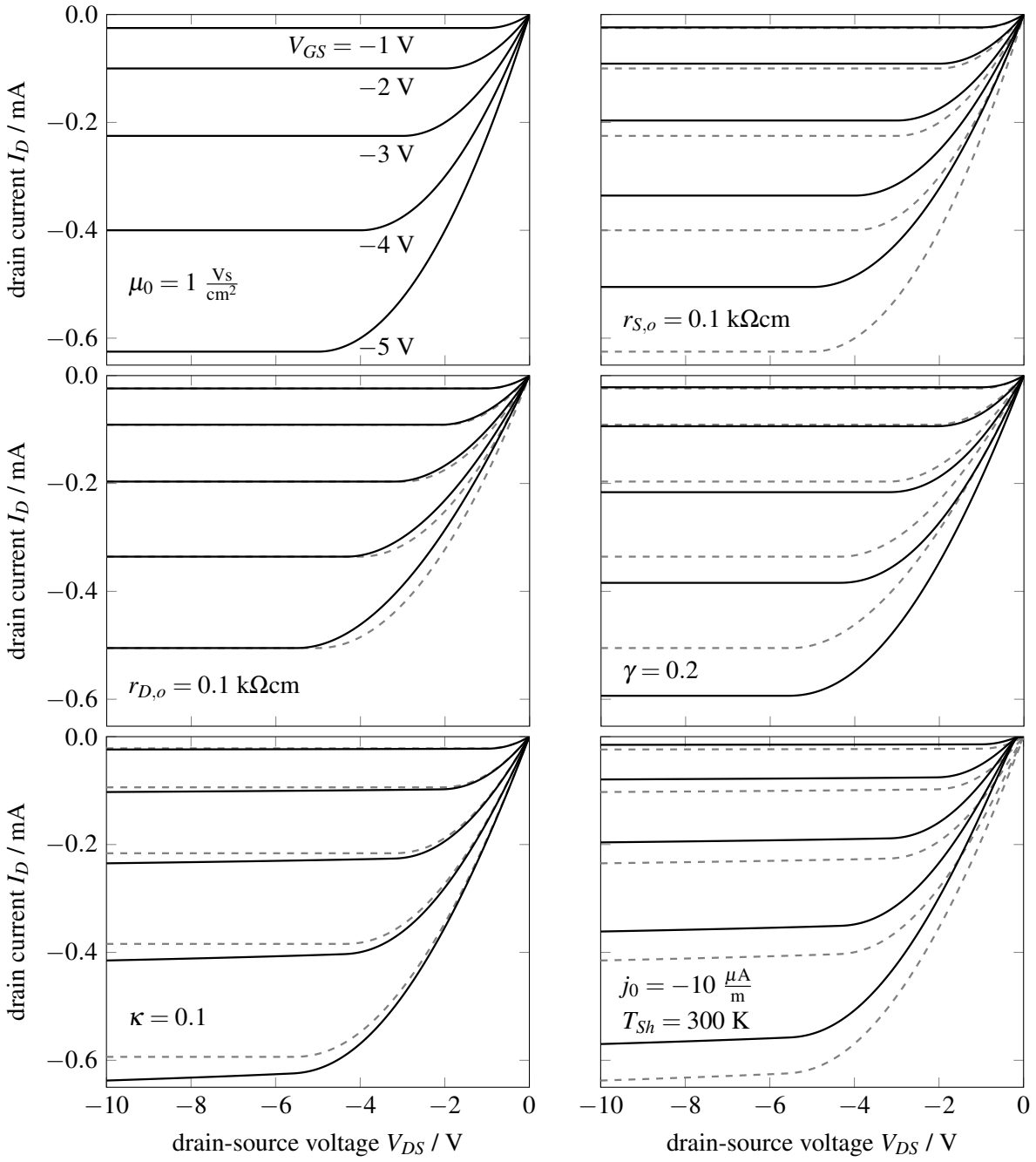

Figure 2.4: Influence of the parameters on the shape of the output characteristics for a p-type OTFT. In the upper left panel, all parameters of the transistor model are set to zero, except the mobility prefactor $\mu_0 = 1\ \frac{\mathrm{Vs}}{\mathrm{cm}^2}$. For the remaining panels, one after the other parameter is set to the specified values. The dashed grey lines indicate the output characteristics prior to the inclusion of the new parameter. From upper left to upper right, the ohmic source resistance $r_{S,o} = 0.1$ kΩcm is included; upper right to middle left: ohmic drain resistance $r_{D,o} = 0.1$ kΩcm; middle left to middle right: exponent of the sensitivity with respect to the charge-carrier density $\gamma = 0.2$; middle right to lower left: the exponent of the field sensitivity κ; lower left to lower right: Schottky temperature $T_{Sh} = 300$ K and Schottky current $j_0 = -10\ \frac{\mu\mathrm{A}}{\mathrm{m}}$. The influence of the Schottky-diode parameters T_{Sh}, j_0 and η on the output characteristics are illustrated in Figure 2.5.

is more pronounced for larger absolute gate-source voltages $-V_{GS}$ resulting in a more equal spacing between the saturation curves and, hence, a more linear rather than quadratic increase of the absolute

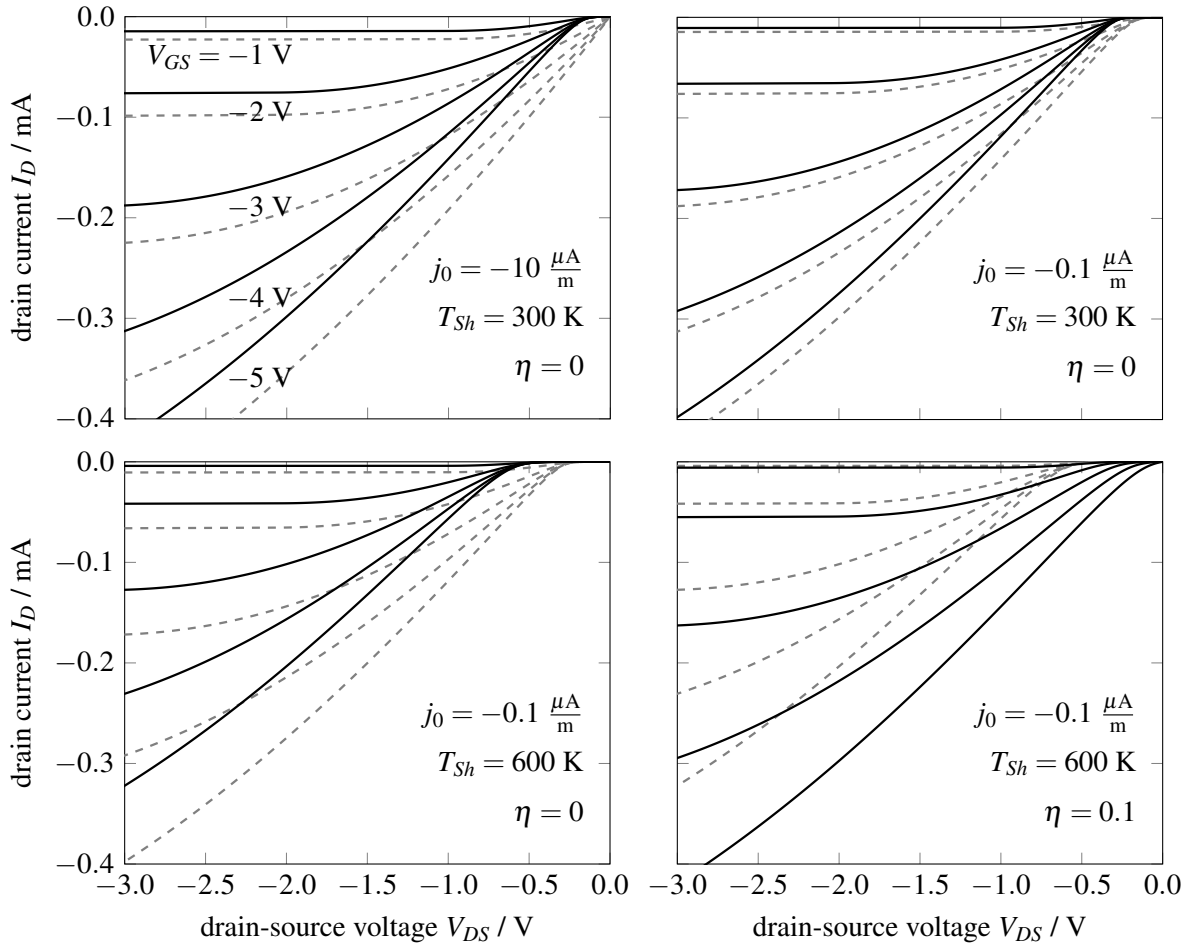

Figure 2.5: Influence of the parameters of the Schottky diode on the shape of the output characteristics of a p-type OTFT. The upper left panel shows a magnification of the lower right panel in Figure 2.4. For all remaining panels, one parameter is changed from panel to panel and the grey dashed line indicates the output characteristics prior to changing the parameter. From the upper left to the upper right panel, the Schottky current is changed from $j_0 = -10\ \frac{\mu A}{m}$ to $j_0 = -0.1\ \frac{\mu A}{m}$; upper right to lower left: Schottky temperature from $T_{Sh} = 300$ K to $T_{Sh} = 600$ K; lower left to lower right: gate-source voltage sensitivity to $\eta = 0.1$.

drain current $-I_D$ with the absolute gate-source voltage $-V_{GS}$. In contrast, including the channel-width-reduced ohmic drain resistance $r_{D,o} = 0.1$ kΩcm (middle left panel in Figure 2.4) purely effects the linear regime. Considering a charge-carrier-density-dependent mobility via the exponent of the sensitivity with respect to the charge-carrier density $\gamma = 0.2$ (middle right panel in Figure 2.4) increases the absolute drain current $-I_D$. The increase is more pronounced for larger absolute gate-source voltages $-V_{GS}$ leading to a similar output characteristics as the initial one in the upper left panel in Figure 2.4. The most important difference between the output characteristics in the upper left panel and the middle right panel in Figure 2.4 is, that the slope at $V_{DS} = 0$ V and $I_D = 0$ A is steeper in the upper left panel. This results in a more curved characteristic in the upper left panel in comparison to a more linear increase of the absolute drain current $-I_D$ with absolute drain-source voltage $-V_{DS}$ in the middle right panel.

Including the exponent of the field sensitivity $\kappa = 0.1$ (lower left panel in Figure 2.4) lifts the saturation, i.e., it provokes a linear increase of the absolute drain current $-I_D$ with respect to the absolute drain-source voltage $-V_{DS}$ in the saturation regime. In the lower right panel in Figure 2.4, the Schot-

tky diode is included by setting the Schottky temperature to $T_{Sh} = 300$ K and the Schottky current to $j_0 = -10\ \frac{\mu\mathrm{A}}{\mathrm{m}}$. The characteristic feature of the Schottky diode manifests at $V_{DS} = 0$ V and $I_D = 0$ A. There, the onset of the output characteristics is shifted towards higher absolute drain-source voltages $-V_{DS}$. To explore this region of the characteristic feature of the Schottky diode in more detail, the upper left panel in Figure 2.5 shows a magnification of the region at low absolute drain-source voltages.

The upper left panel in Figure 2.5 and the lower right panel in Figure 2.4 show exactly the same data with only the scale being changed. The shift of the onset of the output characteristics towards higher absolute drain-source voltages $-V_{DS}$ becomes more evident from the magnification in the upper left panel in Figure 2.5. In the upper panels in Figure 2.5, from the left to the right, the absolute Schottky current is reduced from $-j_0 = 10\ \frac{\mu\mathrm{A}}{\mathrm{m}}$ to $-j_0 = 0.1\ \frac{\mu\mathrm{A}}{\mathrm{m}}$ leading to a further shift of the onset towards even higher absolute drain-source voltages. Besides a further shift, changing the Schottky temperature from $T_{Sh} = 300$ K to $T_{Sh} = 600$ K (lower left panel in Figure 2.5) creates a more smooth onset with a tail at absolute drain-source voltages below the onset at $-V_{DS} \approx 0.6$ V is decreasing more slowly. Including a gate-source voltage sensitivity of $\eta = 0.1$ in the lower right panel in Figure 2.5 creates an individual onset of the output characteristics for the different gate-source voltages V_{GS}.

2.2 Fitting Procedure

Besides different transistor models, there is a huge variety of suggested procedures to extract material parameters from measured characteristics found in literature. A selection of the most common extraction procedures can be found in a review by Natali and Caironi [30], but there are many more suggested extraction procedures [39–43]. We have chosen a different approach because most extraction procedures focus only on a small share of the measured data. Such extraction procedures are not particularly suited to test transistor models because the transistor model is supposed to describe the transistor as a whole. Hence, the extracted parameters have to be chosen to get the best possible agreement of measurements and transistor model. This might not be guaranteed by an extraction method that extracts the parameters of the transistor model from a part of the measurements. As already stated by Fischer *et al.* [44], it is important to look at all the measured data.

We extract the parameters by fitting all measured data points of the transistor to the chosen transistor model via a Gauss-Newton algorithm with a variation suggested by Marquardt [45]. The algorithm is modified to be able to handle minimum and maximum values of parameters. A vector $\vec{a} = (a_1, a_2, \ldots, a_n)^\top$ collects the n parameters a_1 to a_n, that are to be determined by fitting. In its standard form, the algorithm calculates the difference $\Delta\vec{a} = \vec{a} - \vec{a}^0$ between the current parameters $\vec{a}^0$ and the suggested new parameters $\vec{a}$ by solving the system of linear equations

$$(A + \lambda D)\Delta\vec{a} = \vec{b} \tag{2.16}$$

with matrices A and D, the convergence factor λ introduced by Marquardt and a vector $\vec{b}$. The matrix A is given by

$$(A)_{ij} = \sum_{k=1}^{N} \frac{1}{\sigma_k^2} \frac{\partial f(\vec{x}_k;\vec{a}^0)}{\partial a_i} \frac{\partial f(\vec{x}_k;\vec{a}^0)}{\partial a_j} \tag{2.17}$$

containing the sum over all N measured values y_k, their standard deviation σ_k and the partial derivatives $\frac{\partial f(\vec{x}_k;\vec{a}^0)}{\partial a_{i/j}}$ of the model function f at the data value $\vec{x}_k$ and the current parameters $\vec{a}^0$ with respect to the

parameter a_i and a_j, respectively. The matrix D is a diagonal matrix built up by the diagonal elements of A

$$(D)_{ij} = \delta_{ij}(A)_{ij} \tag{2.18}$$

with δ_{ij} being the Kronecker delta returning 1 if $i = j$ and 0 if $i \neq j$. The vector $\vec{b}$ is given by

$$b_i = \sum_{k=1}^{N} \frac{y_k - f(\vec{x}_k;\vec{a}^0)}{\sigma_k^2} \frac{\partial f(\vec{x}_k;\vec{a}^0)}{\partial a_i} \tag{2.19}$$

involving the measured value y_k corresponding to the data value $\vec{x}_k$.

To consider minimum and maximum values of parameters, the matrices A and D, the vector $\vec{b}$ and the convergence factor λ are evaluated as usual and the system of linear equations, Equation (2.16), is solved to receive $\Delta\vec{a}$. Before going on with this calculated value for $\Delta\vec{a}$, it is checked if any of the suggested parameters $\vec{a} = \vec{a}^0 + \Delta\vec{a}$ is out of bounds. If this is the case, the corresponding value for Δa_j of the entry j that is possible to stay within the boundaries is calculated. If, e.g., the upper boundary is exceeded, we calculate $\Delta a_j = a_j^{max} - a_j^0$. This value for Δa_j is plugged into the system of linear equations, Equation (2.16), by discarding equation j and transferring $(A)_{ij}\Delta a_j$ to the right-hand side $b_i \rightarrow b_i - (A)_{ij}\Delta a_j$. The new system of linear equations is solved again and the check, whether all parameters are in bounds, is performed again. Only if all parameters are within bounds, $\Delta\vec{a}$ is accepted and the Gauss-Newton algorithm is continued.

In our case, the measured quantity is the drain current $y = I_D$ and the data values are the drain-source and gate-source voltage $\vec{x} = (V_{DS}, V_{GS})$. The parameters are $\vec{a} = (V_T, \mu_0, r_{S,o}, r_{D,o}, \gamma, \kappa, V_0, T_{Sh}, j_0, \eta)$ but not all of them necessarily need to be optimised. As discussed in Chapter 2.1.3, the parameters $\alpha_D = 0$ kΩcm and $\alpha_S = 0$ kΩcm are omitted due to their non-physical influence on certain operation regions of the OTFT (cf. Figure 2.3). The resulting implicit system of equations, Equation (2.15), determining the transistor model is rewritten for clarity:

$$V_{Sh} = \begin{cases} -\frac{|q|k_B T_{Sh}}{qe} \ln\left[1 + \frac{I_D}{Wj_0} \exp\left(\eta \frac{qeV_{GS}}{|q|k_B T_{Sh}}\right)\right] & \text{if } T_{Sh} > 0 \text{ K} \\ \begin{cases} V_0 & \text{if } qI_D < 0 \ \frac{\text{A}}{\text{V}} \\ 0 & \text{if } qI_D = 0 \ \frac{\text{A}}{\text{V}} \end{cases} & \text{if } T_{Sh} = 0 \text{ K} \end{cases} \tag{2.20}$$

$$\upsilon_{S'G'} = q\left(V_T - V_{GS} + V_{Sh} + I_D \frac{r_{S,o}}{W}\right) \tag{2.21}$$

$$\upsilon_{D'G'} = q\left(V_T - V_{GS} + V_{DS} - I_D \frac{r_{D,o}}{W}\right) \tag{2.22}$$

$$\upsilon_{S'D'} = \upsilon_{S'G'} - \upsilon_{D'G'} \tag{2.23}$$

$$I_D = -\frac{W\mu_0 C_G}{q|q|L(\gamma+2)} \exp\left(\kappa\sqrt{\frac{L_0}{L}\upsilon_{S'D'}}\right) \Theta(\upsilon_{S'D'}) \left(\upsilon_{S'G'}^{\gamma+2}\Theta(\upsilon_{S'G'}) - \upsilon_{D'G'}^{\gamma+2}\Theta(\upsilon_{D'G'})\right). \tag{2.24}$$

For the Gauss-Newton-Marquardt fitting algorithm, derivatives of the model function, Equations (2.20) to (2.24), with respect to the parameters are required. Due to the implicit nature of the system of equations, all explicit and implicit derivatives of the drain current with respect to the parameters have to be collected. Delta peaks from the derivative of the Heaviside-step-functions $\Theta(x)$ are neglected. The procedure to get the derivative of the drain current I_D with respect to a parameter is always the same. This

procedure is demonstrated by deriving I_D with respect to a_i.

$$\frac{\partial I_D}{\partial a_i} = \frac{\eth f(I_D)}{\eth a_i} - \frac{W\tilde{\mu}_0 C_G}{q|q|L}\left[\frac{\partial \upsilon_{S'G'}}{\partial a_i}T_{SG} - \frac{\partial \upsilon_{D'G'}}{\partial a_i}T_{DG}\right]\Theta(\upsilon_{S'D'}) \tag{2.25}$$

The partial derivative ∂ here denotes the derivative when the parameters $\vec{a}$ and the drain-source and gate-source voltage $\vec{x} = (V_{DS}, V_{GS})$ are independent variables. In contrast, the partial derivative $\eth$ denotes the derivative when the drain current I_D and the reduced voltages $\upsilon_{S'G'}$ and $\upsilon_{D'G'}$ are additionally considered as independent variables. This means that $\frac{\eth f(I_D)}{\eth a_i}$ considers only derivatives with respect to the parameter a_i of explicit appearance of a_i in the right-hand side of Equation (2.24). The mobility prefactor μ_0 and the Poole-Frenkel field dependence of the mobility are combined to a mobility prefactor $\tilde{\mu}_0$

$$\tilde{\mu}_0 = \mu_0 \exp\left(\kappa\sqrt{\frac{L_0}{L}\upsilon_{S'D'}}\right) \tag{2.26}$$

and the terms T_{SG} and T_{DG} are given by

$$T_{SG} = \upsilon_{S'G'}^{\gamma+1}\Theta(\upsilon_{S'G'}) + T_0 \tag{2.27}$$

and

$$T_{DG} = \upsilon_{D'G'}^{\gamma+1}\Theta(\upsilon_{D'G'}) + T_0 \tag{2.28}$$

with a term T_0 stemming from the Poole-Frenkel field dependence

$$T_0 = \kappa\sqrt{\frac{L_0}{L}}\frac{\upsilon_{S'G'}^{\gamma+2}\Theta(\upsilon_{S'G'}) - \upsilon_{D'G'}^{\gamma+2}\Theta(\upsilon_{D'G'})}{2(\gamma+2)\sqrt{\upsilon_{S'G'} - \upsilon_{D'G'}}}. \tag{2.29}$$

Derivatives of $\upsilon_{S'G'}$ and $\upsilon_{D'G'}$ are given by

$$\frac{\partial \upsilon_{S'G'}}{\partial a_i} = \frac{\eth f(\upsilon_{S'G'})}{\eth a_i} + \left(q\frac{r_{S,o}}{W} - \frac{|q|k_B T_{Sh}}{e(I_D + I_0)}\right)\frac{\partial I_D}{\partial a_i} \tag{2.30}$$

$$\frac{\partial \upsilon_{D'G'}}{\partial a_i} = \frac{\eth f(\upsilon_{D'G'})}{\eth a_i} - q\frac{r_{D,o}}{W}\frac{\partial I_D}{\partial a_i} \tag{2.31}$$

introducing the reference Schottky current I_0, given by

$$I_0 = Wj_0 \exp\left(-\eta\frac{qeV_{GS}}{|q|k_B T_{Sh}}\right). \tag{2.32}$$

The derivative $\frac{\eth f(\upsilon_{S'G'})}{\eth a_i}$ denotes the derivative of the right-hand side of Equation (2.21), in combination with Equation (2.20), with respect to an explicitly appearing parameter a_i. Accordingly, the derivative $\frac{\eth f(\upsilon_{D'G'})}{\eth a_i}$ denotes the derivative of the right-hand side of Equation (2.22) that accounts only for explicit appearances of the parameter a_i.

Inserting Equations (2.30) and (2.31) into Equation (2.25) and collecting all terms containing $\frac{\partial I_D}{\partial a_i}$ suggests the definition of

$$D_{I_D} = 1 + \frac{W\tilde{\mu}_0 C_G}{|q|L}\left[T_{SG}\left(\frac{r_{S,o}}{W} - \frac{|q|k_B T_{Sh}}{qe(I_D + I_0)}\right) + T_{DG}\frac{r_{D,o}}{W}\right]\Theta(\upsilon_{S'D'}). \tag{2.33}$$

With this definition, the desired solution for $\frac{\partial I_D}{\partial a_i}$ is received.

$$\frac{\partial I_D}{\partial a_i} = \frac{1}{D_{I_D}} \frac{\eth f(I_D)}{\eth a_i} - \frac{W\tilde{\mu}_0 C_G}{q|q|LD_{I_D}} \left(T_{SG} \frac{\eth f(\upsilon_{S'G'})}{\eth a_i} - T_{DG} \frac{\eth f(\upsilon_{D'G'})}{\eth a_i} \right) \Theta(\upsilon_{S'D'}) \tag{2.34}$$

All derivatives of the model function, Equations (2.20) to (2.24), with respect to the parameters are derived via Equation (2.34). The results of those derivations are given in Equations (2.35) to (2.44).

$$\frac{\partial I_D}{\partial V_T} = -\frac{W\tilde{\mu}_0 C_G}{|q|LD_{I_D}} \left(T_{SG} - T_{DG}\right) \Theta(\upsilon_{S'D'}) \tag{2.35}$$

$$\frac{\partial I_D}{\partial \mu_0} = \frac{I_D}{\mu_0 D_{I_D}} \tag{2.36}$$

$$\frac{\partial I_D}{\partial r_{S,o}} = -\frac{\tilde{\mu}_0 C_G}{|q|LD_{I_D}} T_{SG} I_D \Theta(\upsilon_{S'D'}) \tag{2.37}$$

$$\frac{\partial I_D}{\partial r_{D,o}} = -\frac{\tilde{\mu}_0 C_G}{|q|LD_{I_D}} T_{DG} I_D \Theta(\upsilon_{S'D'}) \tag{2.38}$$

$$\frac{\partial I_D}{\partial \gamma} = -\frac{I_D + \frac{W\tilde{\mu}_0 C_G}{q|q|L} \left(\ln(\upsilon_{S'G'}) \upsilon_{S'G'}^{\gamma+2} \Theta(\upsilon_{S'G'}) - \ln(\upsilon_{D'G'}) \upsilon_{D'G'}^{\gamma+2} \Theta(\upsilon_{D'G'}) \right) \Theta(\upsilon_{S'D'})}{D_{I_D}(\gamma+2)} \tag{2.39}$$

$$\frac{\partial I_D}{\partial \kappa} = \frac{I_D}{D_{I_D}} \sqrt{\frac{L_0}{L} \upsilon_{S'D'}} \tag{2.40}$$

$$\frac{\partial I_D}{\partial V_0} = \begin{cases} -\frac{W\tilde{\mu}_0 C_G}{|q|LD_{I_D}} T_{SG} \Theta(\upsilon_{S'D'}) & \text{if } T_{Sh} = 0\,\text{K} \\ 0 & \text{if } T_{Sh} > 0\,\text{K} \end{cases} \tag{2.41}$$

$$\frac{\partial I_D}{\partial T_{Sh}} = \begin{cases} 0 & \text{if } T_{Sh} = 0\,\text{K} \\ \frac{W\tilde{\mu}_0 C_G}{|q|LD_{I_D}} T_{SG} \left[\frac{|q|k_B}{qe} \ln\left(1 + \frac{I_D}{I_0}\right) - \frac{\eta V_{GS} I_D}{(I_D+I_0)T_{Sh}} \right] \Theta(\upsilon_{S'D'}) & \text{if } T_{Sh} > 0\,\text{K} \end{cases} \tag{2.42}$$

$$\frac{\partial I_D}{\partial j_0} = \begin{cases} 0 & \text{if } T_{Sh} = 0\,\text{K} \\ -\frac{W\tilde{\mu}_0 C_G}{LD_{I_D}} T_{SG} \frac{k_B T_{Sh} I_D}{q e j_0 (I_D+I_0)} \Theta(\upsilon_{S'D'}) & \text{if } T_{Sh} > 0\,\text{K} \end{cases} \tag{2.43}$$

$$\frac{\partial I_D}{\partial \eta} = \begin{cases} 0 & \text{if } T_{Sh} = 0\,\text{K} \\ \frac{W\tilde{\mu}_0 C_G}{q|q|LD_{I_D}} T_{SG} \frac{I_D V_{GS}}{I_D+I_0} \Theta(\upsilon_{S'D'}) & \text{if } T_{Sh} > 0\,\text{K} \end{cases} \tag{2.44}$$

Our variation of the Gauss-Newton-Marquardt fitting algorithm is able to consider minimum and maximum values of parameters, which is crucial to avoid non-physical parameters like negative resistances. The parameters μ_0, κ, $r_{S,o}$, $r_{D,o}$ and T_{Sh} have to be zero or positive. The exponent of the field sensitivity κ is additionally recommended to be not to high $\kappa \lesssim 20$. The exponent of the sensitivity with respect to the charge-carrier density γ has to be greater than $\gamma > -1$ and not too high $\gamma \lesssim 20$. The channel-width-reduced Schottky current j_0 has to be chosen in a way that $qj_0 \leq 0\ \frac{\mu\text{A}}{m}$. For the remaining parameters V_T, V_0 and η, no restrictions are necessary.

Due to the large amount of up to nine parameters that are required to determine the transistor model, fitting all of them at once to reproduce the measured characteristics will not lead to a proper result. To enable a convergence of the Gauss-Newton-Marquardt algorithm towards the optimum parameters, carefully chosen starting parameters are essential. Our approach to receive proper starting parameters is to, step by step, evolve the parameters by fitting only a part of the parameters and continuously improve the agreement with the measured data. In a final fit of all parameters, the Gauss-Newton-Marquardt

algorithm then converges and provides the desired parameters representing the measured data.

In the following, we demonstrate the fitting procedure on the example of a pentacene bottom-gate bottom-contact OTFT with the contacts being covered by a self-assembled monolayer (SAM) of biphenyl-4-thiol (for details see [1]). The work function of the contacts do not match well with the HOMO energy of pentacene, requiring the inclusion of the Schottky diode in the transistor model to capture the marked S-shape at the onset of the output characteristics for low absolute drain-source voltages (see Figure 2.6 and Figure 2.7). Each step of the fitting procedure is visualised in Figure 2.6 and Figure 2.7. The evolution of the parameters during the fitting procedure is given in Table 2.1. In total, 8 steps are required for this particular example.

The first step of each fitting procedure starts with the ideal transistor model, which contains only the mobility prefactor μ_0 and the threshold voltage V_T. All remaining parameters are zero. In this case, the drain current in the saturation regime ($\upsilon_{D'G'} < 0$ V) is given by

$$I_{D,sat} = -\frac{qW\mu_0 C_G}{2|q|L}\left(V_{GS} - V_T\right)^2 \Theta\left(qV_T - qV_{GS}\right). \tag{2.45}$$

The saturation drain current $I_{D,sat}$ for different gate-source voltages V_{GS} can be found in the output characteristics where the curves are flat. With those few data points for $I_{D,sat}$ and V_{GS}, a linear fit of $\sqrt{-qI_{D,sat}}$ as a function of V_{GS} provides V_T and μ_0. The outcome of this first step is shown in the upper left panel in Figure 2.6 with the measured data plotted as grey crosses and the calculated output characteristics as black lines. Although the agreement between measured data and calculations is very poor, it provides a value for the mobility prefactor μ_0 that is in the right order of magnitude. Those values for V_T and μ_0 enable the first fit which, in our example, is optimising V_T, μ_0 and V_0. The calculated output characteristics of this fit, shown in the upper right panel in Figure 2.6, is still far from a good agreement with the experimental curves, but much better compared to the starting guess in the upper left panel in Figure 2.6. Another fit, additionally optimising $r_{S,o}$ and $r_{D,o}$, shown in the lower left panel of Figure 2.6, slightly improves the agreement between measurement and calculation.

The next step of the fitting procedure is to convert the oversimplified form of the Schottky-diode related to the Schottky voltage V_0 to the actual Schottky diode. This is done by setting the Schottky temperature to $T_{Sh} = 300$ K, and calculating an estimate of the Schottky current j_0 for $\eta = 0$. This estimate of j_0 is calculated by assuming, that at an intermediate drain current of $I_{D,Sh} = -2$ μA (approximately where the curvature of the output characteristics with the highest absolute drain current is zero), the voltage V_0 drops at the Schottky diode. With Equation (2.20), we get the estimate for j_0:

$$j_0 = \frac{\frac{I_{D,Sh}}{W}}{\exp\left(-\frac{qeV_0}{|q|k_B T_{Sh}}\right) - 1}. \tag{2.46}$$

This conversion from V_0 to T_{Sh} and j_0 is shown in the lower right panel of Figure 2.6. The most important change appears at the onset of the output characteristics at about $V_{DS} \approx -0.5$ V. At this point, the sharp kink in the lower left panel in Figure 2.6 is getting rounded in the lower right panel of Figure 2.6. With this conversion being finished, the fitting procedure is continued in Figure 2.7.

With the estimated initial Schottky-diode parameters, the next step is to optimise those parameters T_{Sh} and j_0. In this example, the optimisation requires to include also the parameters V_T, μ_0 and $r_{D,o}$. The according agreement between measurement and calculation in the upper left panel in Figure 2.7 slightly

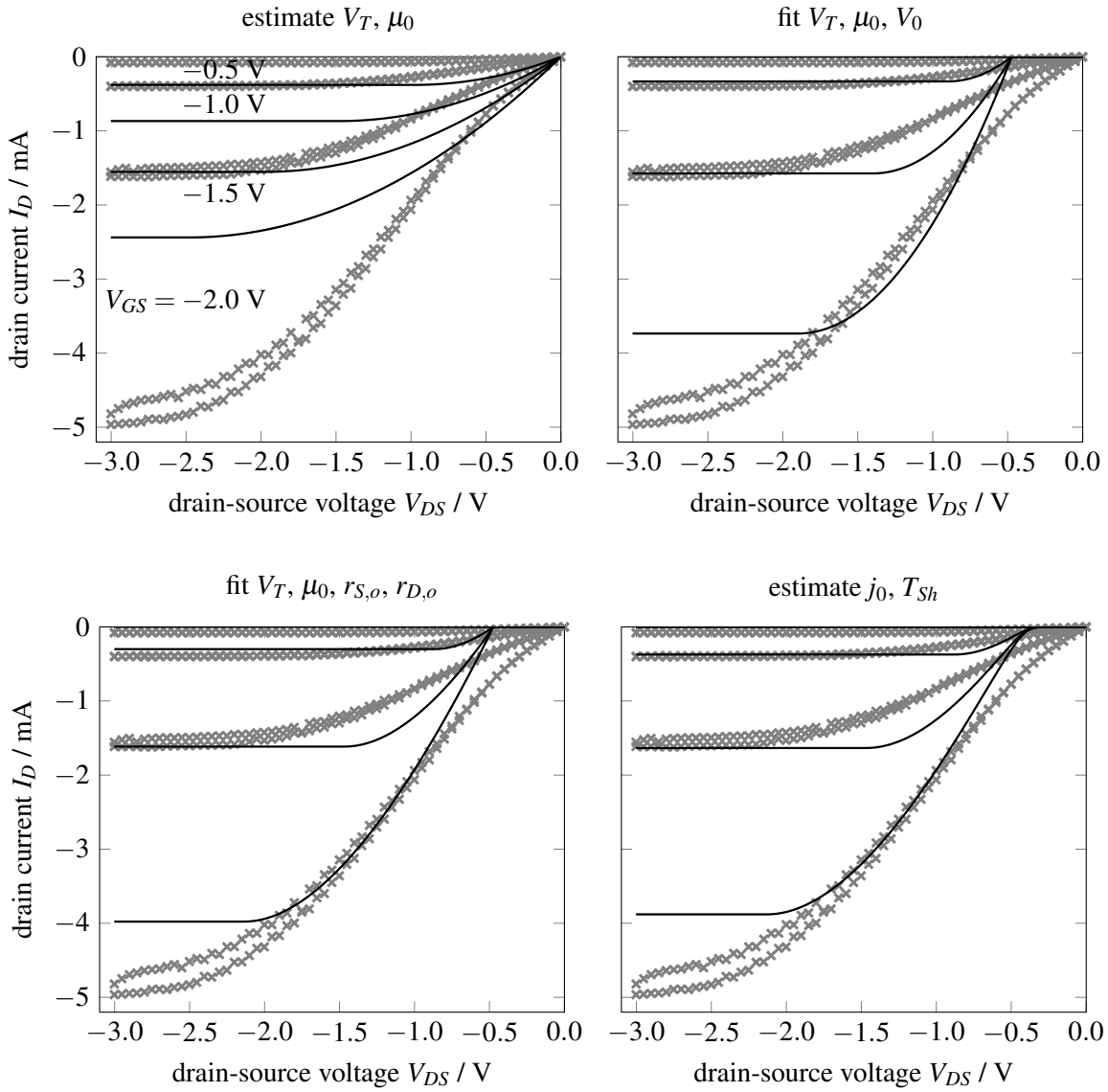

Figure 2.6: Fitting procedure to extract the optimum parameters for the transistor model that represent the measured data best. The measured output characteristics (drain current I_D as a function of drain-source voltage V_{DS} for different gate-source voltages V_{GS}) are marked with grey crosses and the output characteristics calculated with the corresponding parameters are shown as black lines. The upper left panel shows the first step assuming an ideal OTFT with only μ_0 and V_T being non-zero. Those two parameters are extracted by a linear fit of the saturation drain current $\sqrt{-qI_{D,sat}}$ as a function of the gate-source voltage V_{GS}. The first fit in the upper right panel includes μ_0, V_T and V_0 resulting in a much better agreement between measurement and calculation. Additionally including $r_{S,o}$ and $r_{D,o}$ in the next fit (lower left panel) slightly improves the agreement. The conversion from the Schottky voltage V_0 to a full Schottky-diode, visualised in the lower right panel, leads to a rounding of the curves at the onset of the output characteristics around $V_{DS} \approx -0.5$ V. The fitting procedure is continued in Figure 2.7.

improves in comparison to the lower right panel in Figure 2.6. The next fit optimising V_T, μ_0 and γ again slightly improves the agreement (upper right panel in Figure 2.7). The penultimate fit optimises 6 parameters: V_T, μ_0, $r_{D,o}$, γ, j_0 and T_{Sh}. The agreement of measurement and calculation from this fit is already quite good (lower left panel in Figure 2.7). Even more important, this fit provides proper starting values for the last fit over all parameters of the utilised transistor model. This last fit, including the nine

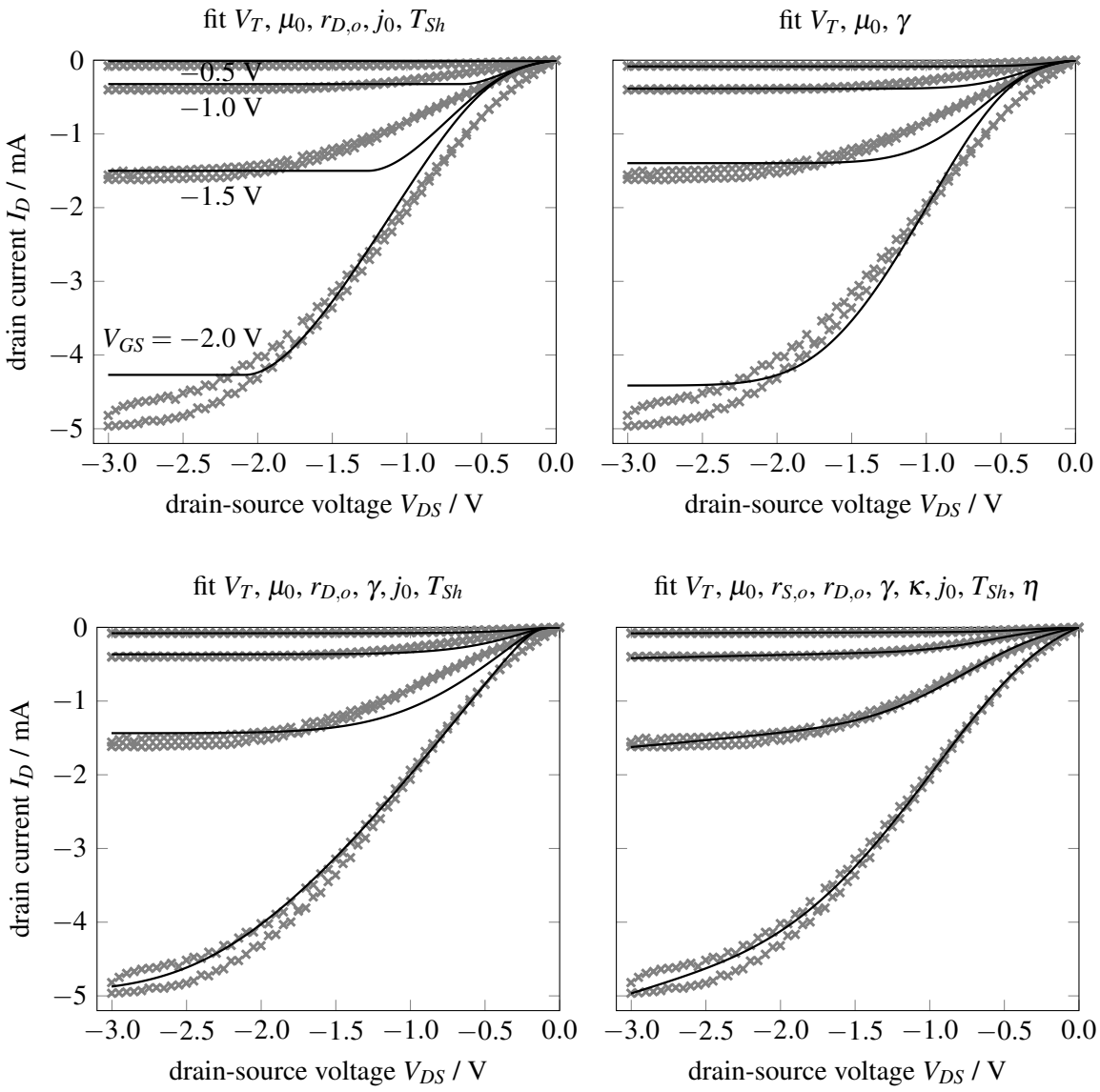

Figure 2.7: Continuation of the fitting procedure aiming to find the optimum parameters started in Figure 2.6. The measured output characteristics (drain current I_D as a function of drain-source voltage V_{DS} for different gate-source voltages V_{GS}) are marked with grey crosses and the output characteristics calculated with the corresponding parameters are shown as black lines. The fit in the upper left panel tries to optimise the Schottky-diode parameters T_{Sh} and j_0, additionally including V_T, μ_0 and $r_{D,o}$ as parameters. Compared to the lower right panel in Figure 2.6, the agreement between the measurement and the calculation slightly improves. Including the exponent of the sensitivity with respect to the charge-carrier density γ in the subsequent fit again improves the agreement (upper right panel). The optimisation of V_T, μ_0, $r_{D,o}$, γ, j_0 and T_{Sh} leads to a significant improvement of the agreement (lower left panel) and delivers the final starting parameters for the last fit. In the last fit, all parameters are optimised resulting in a decent agreement between measurement and calculation (lower right panel).

parameters V_T, μ_0, $r_{S,o}$, $r_{D,o}$, γ, κ, j_0, T_{Sh} and η, produces output characteristics that nicely agree with the measured data (lower right panel in Figure 2.7).

In Table 2.1 the evolution of the parameters during the fitting procedure can be found. A dash in the table indicates, that the parameter is not considered in the corresponding step of the fitting procedure. Not considering the parameter implies that, (i), the value of the parameter is set to zero, (ii), the parameter is

Table 2.1: Evolution of the parameters of the transistor model during the fitting procedure. A dash indicates, that the parameter is not considered in the transistor model (set to zero) in the corresponding step of the fitting procedure. From step to step, more parameters are considered until we end up with the optimum parameters after 8 steps.

V_T / V	μ_0 / $\frac{\mathrm{Vs}}{\mathrm{cm}^2}$	$r_{S,o}$ / kΩcm	$r_{D,o}$ / kΩcm	γ	κ	V_0 / V	j_0 / $\frac{\mu\mathrm{A}}{\mathrm{m}}$	T_{Sh} / K	η
0.478	0.01381	-	-	-	-	-	-	-	-
-0.101	0.06397	-	-	-	-	-0.473	-	-	-
-0.148	0.07281	0.0	7.003	-	-	-0.473	-	-	-
-0.148	0.07281	0.0	7.003	-	-	-	$-2.3\cdot10^{-5}$	300	-
-0.414	0.23765	0.0	11.468	-	-	-	-44.796	2012	-
1.021	0.00118	0.0	11.468	5.81	-	-	-44.796	2012	-
2.952	$1.1\cdot10^{-8}$	0.0	27.527	9.93	-	-	-0.688	375	-
0.665	0.01401	0.464	7.201	2.25	1.75	-	-7.063	3497	0.56

not optimised and, (iii), the parameter is not included in the transistor model. The purpose of the starting parameters in the first line of Table 2.1 is only to get an approximate value for the mobility which is close to the actual value, within some orders of magnitude. The first fit in the second line of Table 2.1 with only three optimised parameters converges reliably with minor dependence on the exact values of the starting guess. Including more and more parameters requires better starting parameters and the final fit over all considered parameters only converges due to the fact that the measured and the calculated output characteristics already match quite well for the starting parameters of this final fit (cf. lower left and lower right panel in Figure 2.7). From the third to the fourth line in Table 2.1, the conversion from the oversimplified Schottky-diode behaviour, determined by the Schottky-diode voltage loss V_0, to the actual Schottky-diode behaviour, described by the Schottky temperature T_{Sh} and the channel-width-reduced Schottky current j_0, is performed with the help of Equation (2.46).

This example for a successful sequence of the fitting procedure cannot be applied to all transistors. One has to decide, step by step, which parameters are important to be included next and check after each fitting step, if the agreement between measurement and calculation has improved as expected. To decide which parameters are most relevant for the next fitting step, the knowledge of the influence of parameters on the output characteristics is of particular importance (cf. Chapter 2.1.4). Usually, when fitting a huge amount of similar transistors (e.g. using the same materials and only changing the channel length) the sequence of the fitting procedure is always the same and can be automated.

Another important aspect is the stability of the optimised parameters. To roughly check if the optimised parameters are stable, meaning that they represent the best possible parameters, we suggest to slightly change the sequence, in which steps which parameter is optimised. This can lead to a distinctly different evolution of the parameters for intermediate steps of the fitting procedure. Nevertheless, the final set of optimised parameters must be the same, within numerical accuracy. Only if the optimised parameters always converge to the same final solution, given that they do converge to a reasonable solution, they can be assumed to be the best possible parameters.

Throughout the whole Chapter 2, we exclusively inspect output characteristics. In those output characteristics, the influence of parameters on the shape of the curves is often more pronounced and can be discriminated from the influence of other parameters more clearly than in transfer characteristics. Transfer characteristics, which are not shown in this chapter, demonstrate the dependence of the drain current I_D on the gate-source voltage V_{GS} for different values of the drain-source voltage V_{DS}. Note that for all fabricated transistors, output and transfer characteristics were measured and all measured values

of both characteristics were included in the fitting procedure. Transfer characteristics are not shown here because no additional information can be gained from them in our case. This does not necessarily apply for other transistors and other transistor models, for which an inspection of the transfer characteristics might be even more relevant than an inspection of the output characteristics.

2.3 Model Testing

In the following, we suggest an approach to test transistor models. The approach is inspired by the widely used transmission line model (TLM) [46, 47], which investigates a set of nominally equivalent OTFTs with only the channel length being changed. Our approach is based on the assumption, that all parameters of the OTFT like contact resistances and the mobility are not affected by a change in channel length. This means, if we possess the right transistor model that contains the correct channel-length dependence, parameters extracted from measurements of OTFTs with different channel lengths have to be the same.

The requirement, that the extracted parameters have to be the same for OTFTs with different channel lengths, constitutes our two-step-fitting approach (TSFA). In the first step of this TSFA, we suggest to extracts the parameters of the tested transistor model for each transistor individually from the measured output and transfer characteristics. The second step of the TSFA inspects the channel-length dependence of the extracted parameters. If the parameters exhibit a pronounced dependence on the channel length beyond unavoidable variations from device to device, the transistor model does not pass the test and has to be improved.

For the first step, in principle any reliable single transistor parameter extraction method can be utilised. A desired property of this extraction method is, that it considers all measured data of output and transfer characteristics to be able to test the transistor model over the full range of its operation modes. The fitting procedure, established in Chapter 2.2, is such a single transistor parameter extraction method.

Our suggested two-step-fitting approach (TSFA) initially fits the tested transistor model to the measured data of all output and transfer characteristics for each transistor individually. This results in, (i), calculated characteristics corresponding to the measured characteristics and, (ii), parameters of the transistor model for each transistor representing different channel lengths. With the calculated characteristics, we can perform a first test of the transistor model by inspecting the agreement of the measured characteristics and the calculated curves. If the calculated characteristics significantly deviate from the measured characteristics, the transistor model is not able to describe the full range of operation modes of the OTFT and has to be improved. A clear drawback of fitting algorithms is, that fitting can produce good results with wrong underlying model functions as long as the number of parameters is high enough. [48] So this first validity check is not sufficient to thoroughly test the transistor model. This drawback of fitting algorithms is obliterated by the second step of our TSFA, in which we inspect the extracted parameters of all transistors with different channel length. If the parameters show a pronounced dependence on the channel length, the transistor model does not pass this second test and has to be improved.

2.3.1 Constant Mobility Model

Our two-step-fitting approach (TSFA) is demonstrated by testing a transistor model with constant mobility. This transistor model contains only the mobility prefactor μ_0, the threshold voltage V_T,the

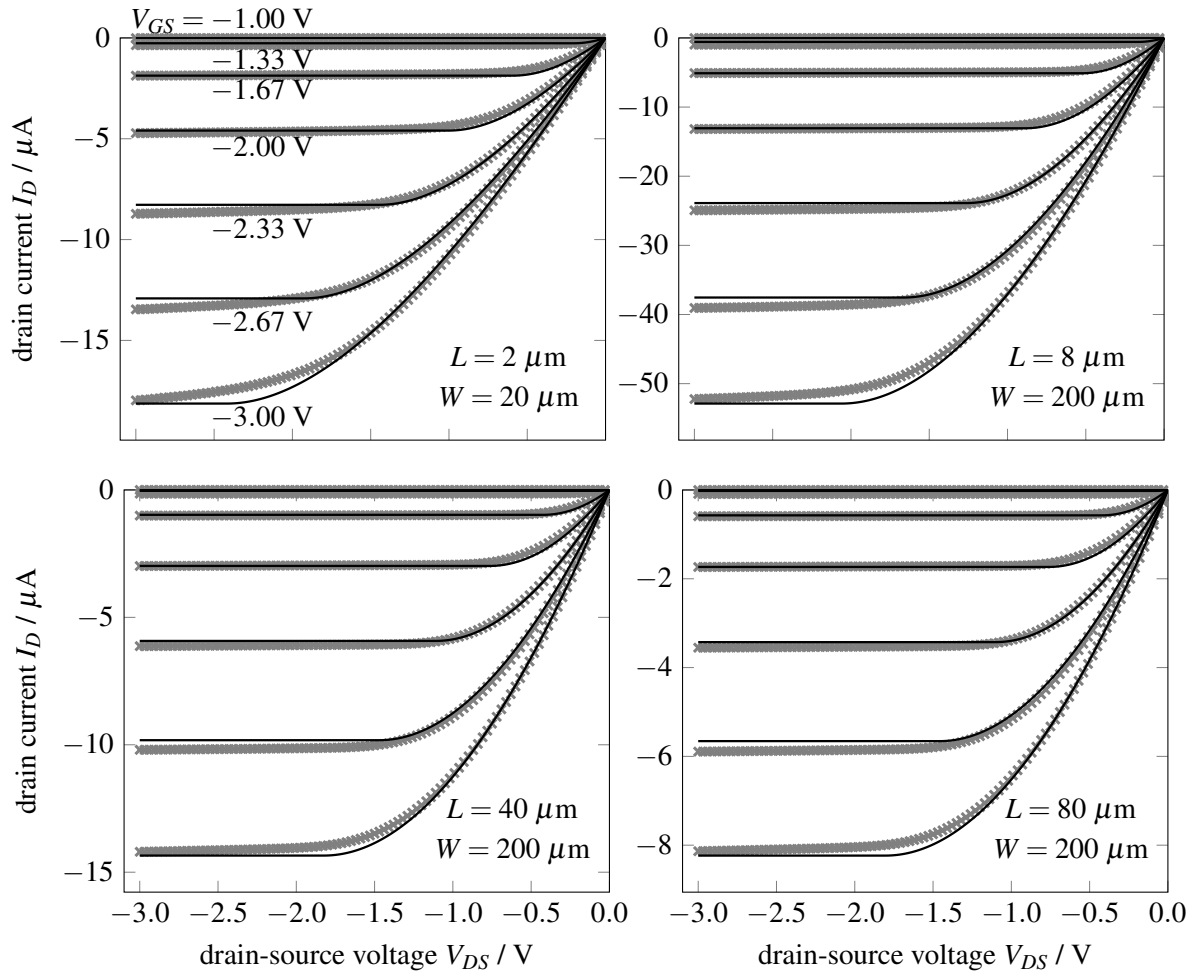

Figure 2.8: The grey crosses show measured output characteristics of bottom-gate bottom-contact OTFTs using dinaphtho[2,3-b:2',3'-f]thieno[3,2-b]thiophene (DNTT) as the organic semiconductor and gold (Au) contacts functionalised with pentafluorobenzenethiol (PFBT) for different channel lengths L and channel widths W. [24, 49, 50] The black lines correspond to the output characteristics calculated via the constant mobility model with the parameters extracted by the fitting procedure described in Chapter 2.2. The agreement between measured and calculated output characteristics is quite good, which makes the transistor model pass the first step of the two-step-fitting approach (TSFA). The minor deviations of measured and calculated output characteristics are most evident for the shortest channel length of $L = 2$ μm (upper left panel). Those deviations appear for the highest absolute gate-source voltage $-V_{GS} = 3.00$ V at the transition from linear to saturation regime $-V_{DS} \approx 2.2$ V and for lower absolute gate-source voltages $-V_{GS} < 3.00$ V in the saturation regime $-V_{DS} \approx 3.0$ V.

channel-width-reduced ohmic drain resistance $r_{D,o}$ and the channel-width-reduced ohmic source resistance $r_{S,o}$. To perform the test, James Borchert[5] provided us with measured characteristics of a set of bottom-gate bottom-contact OTFTs using dinaphtho[2,3-b:2',3'-f]thieno[3,2-b]thiophene (DNTT) as the OSC and gold (Au) contacts functionalised with pentafluorobenzenethiol (PFBT). Details about those transistors can be found in [24, 49, 50]. From the measured output characteristics, indicated with grey crosses in Figure 2.8, those OTFTs appear to be very close to the ideal thin-film transistor with very low contact resistances and a linear increase of the absolute drain current $-I_D$ for low absolute drain-source voltages $-V_{DS} \approx 0$ V, even for short channel lengths of $L = 2$ μm (upper left panel in Figure 2.8).

[5]Max Planck Institute for Solid State Research, Heisenbergstraße 1, 70569 Stuttgart, Germany; J.Borchert@fkf.mpg.de

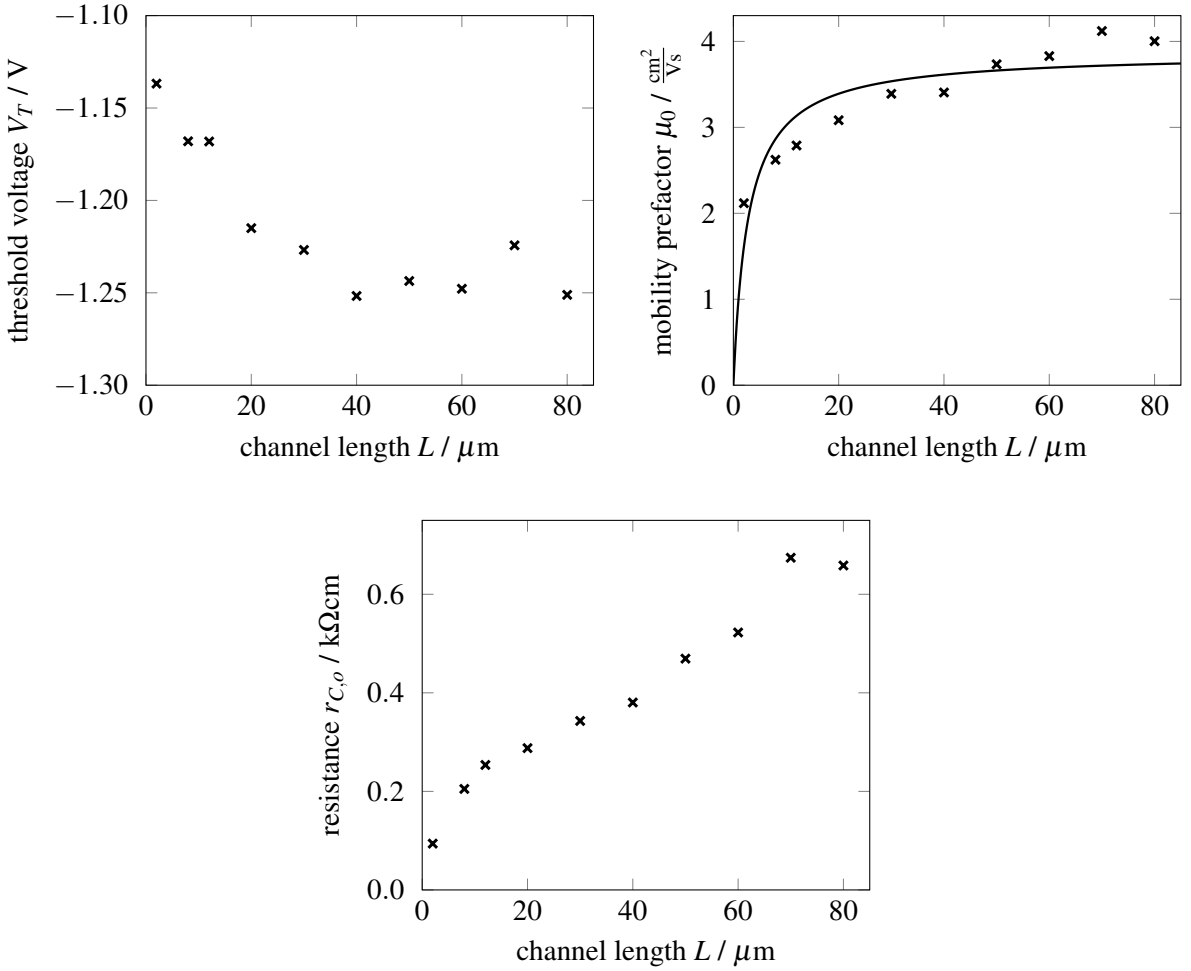

Figure 2.9: Parameters of the constant mobility model as a function of the channel length L of the transistors, for which the parameters were individually extracted via the fitting procedure described in Chapter 2.2. The threshold voltage V_T exhibits a minor channel-length dependence for low channel lengths $L \lesssim 20\ \mu$m (upper left panel). This dependence can be associated to the threshold-voltage roll-off, [51, 52] which is not considered in the tested transistor model. A more pronounced channel-length dependence is appearing for the mobility prefactor μ_0 in the upper right panel, which increases from about $\mu_0 \approx 2\ \frac{\text{Vs}}{\text{cm}^2}$ for $L = 2\ \mu$m to about $\mu_0 \approx 4\ \frac{\text{Vs}}{\text{cm}^2}$ for $L = 80\ \mu$m. This dependence cannot be explained by the black line representing the inclusion of a transfer length L_T in the transistor model (details see text). The total width reduced ohmic contact resistance $r_{C,o} = r_{D,o} + r_{S,o}$ shows a very pronounced dependence on the channel length in the lower panel. This dependence cannot be justified within the assumed transistor model. Both, the mobility and contact resistance dependence on the channel length provoke a failure of the transistor model.

The calculated output characteristics, shown as black lines in Figure 2.8, represent the constant mobility model with the parameters extracted for each transistor individually via the fitting procedure described in Chapter 2.2. The measured and calculated output characteristics match well enough to let the constant mobility model pass the first step of the TSFA. For the second step of the TSFA, we plot the parameters of the constant mobility model extracted for each transistor as a function of the channel length L of the corresponding transistor in Figure 2.9.

To pass the second step of the TSFA, the parameters of the transistor model, extracted in the first step for each transistor with a distinct channel length L, have to be independent of the channel length.

So, within unavoidable variations of the parameters, stemming from device-to-device-fluctuations, the parameters have to be the same for all transistors. Figure 2.9 shows the threshold voltage V_T (upper left panel in Figure 2.9), the mobility prefactor μ_0 (upper right panel in Figure 2.9) and the total channel-width-reduced ohmic contact resistance $r_{C,o} = r_{D,o} + r_{S,o}$ (lower panel in Figure 2.9). Note that the mobility prefactor μ_0 is equal to the total mobility μ given in Equation (2.1) in this case because we assume no charge-carrier-density dependence $\gamma = 0$ and no field dependence $\kappa = 0$.

The threshold voltage V_T shows only minor variations in the order of 0.1 V with respect to the channel length L (see upper left panel in Figure 2.9). The slight increase of the threshold voltage for low channel lengths $L \lesssim 20$ μm is commonly associated to the so-called threshold-voltage roll-off. [51, 52]

A much more pronounced dependence on the channel length L can be seen in the upper right panel in Figure 2.9 for the mobility prefactor μ_0 with an increase from a value of $\mu_0 \approx 2$ $\frac{\text{Vs}}{\text{cm}^2}$ for the shortest channel length $L = 2$ μm to $\mu_0 \approx 4$ $\frac{\text{Vs}}{\text{cm}^2}$ for $L = 80$ μm. We could try to explain this evident channel-length dependence of the mobility prefactor by introducing the so-called transfer length L_T. [47, 53–55] This transfer length accounts for an elongation of the channel $L \to L + L_T$. The reasons for this elongation can be multifaceted, e.g. due to etching processes or an additional distance that charge carriers have to travel in the OSC to reach the channel (in particular for bottom-gate top-contact OTFTs). Considering the transfer length L_T would result in a channel-length dependence of the mobility prefactor in the form of $\mu_0 = \mu_{0,T} \frac{L}{L+L_T}$ with a new mobility prefactor $\mu_{0,T}$. Performing a fit of the channel-length dependence of μ_0 involving the extracted parameters shown in the upper right panel in Figure 2.9 delivers a new mobility prefactor of $\mu_{0,T} = 3.87$ $\frac{\text{Vs}}{\text{cm}^2}$ and a transfer length of $L_T = 2.8$ μm. The associated curve is drawn as a black line in the upper right panel in Figure 2.9. This calculated curve does not represent the extracted parameters well, because it systematically underestimates the extracted values for high channel lengths $L > 50$ μm and overestimates them for intermediate channel lengths $L > 10$ μm and $L < 50$ μm.

Although the transistor model already failed due to the pronounced and inexplicable channel-length dependence of the mobility prefactor μ_0, an even more obvious failure of the transistor model can be seen in the lower panel in Figure 2.9, showing the total channel-width-reduced ohmic contact resistance $r_{C,o}$ as a function of the channel length L. This total contact resistance $r_{C,o}$ is the sum of the channel-width-reduced ohmic drain and source resistance $r_{C,o} = r_{D,o} + r_{S,o}$. The total contact resistance exhibits a nearly linear increase with respect to the channel length and increases from $r_{C,o} \approx 0.09$ kΩcm at $L = 2$ μm to $r_{C,o} \approx 0.66$ kΩcm at $L = 80$ μm.

Our two-step-fitting approach enables the analysis of the reason for the failure of the transistor model in the second step of the TSFA by looking at the deviations of the calculated output characteristics from the measured output characteristics shown in Figure 2.8. Those deviations deliver indications for necessary improvements of the transistor model. To interpret those indications, the knowledge of the influence of parameters on the shape of the output characteristics is required, which we developed in Chapter 2.1.4. Deviations between measured and calculated output characteristics can be found in two regions in Figure 2.8. The first region is in the saturation regime for high absolute drain-source voltages $-V_{DS} \approx 3.0$ V. In this region, the measured characteristics show a non-vanishing slope, whereas the calculated characteristics are flat. This deviation can be extenuated by including the exponent of the field sensitivity of the mobility κ (cf. lower left panel in Figure 2.4). The second region is at the transition between the linear and the saturation regime, particularly pronounced for the highest absolute gate-source voltage $-V_{GS} = 3.00$ V at about $-V_{DS} \approx 2.2$ V for $L = 2$ μm to $-V_{DS} \approx 1.7$ V for $L = 80$ μm. The shape of the output characteristics in this region is significantly influenced by the exponent of the sensitivity

with respect to the charge-carrier density of the mobility γ. So, the deviations in the two regions suggest, that we can try to improve the transistor model by including a field and charge-carrier-density dependence of the mobility.

2.3.2 Field and Charge-Carrier-Density Dependent Mobility Model

The results of the first step of the TSFA for the transistor model including the exponents of the sensitivity with respect to the field and charge-carrier density of the mobility κ and γ, respectively, are shown in Figure 2.10. As desired, the deviations in the saturation regime and at the transition between linear regime and saturation regime have significantly reduced, compared to the fits for the constant mobility model shown in Figure 2.8. The agreement between measured and calculated output characteristics is excellent and the first step of our TSFA is passed.

In the second step of the TSFA, the transistor model with field and charge-carrier-density dependent mobility fails even more evidently than the constant mobility model above. In the left panel in Fig-

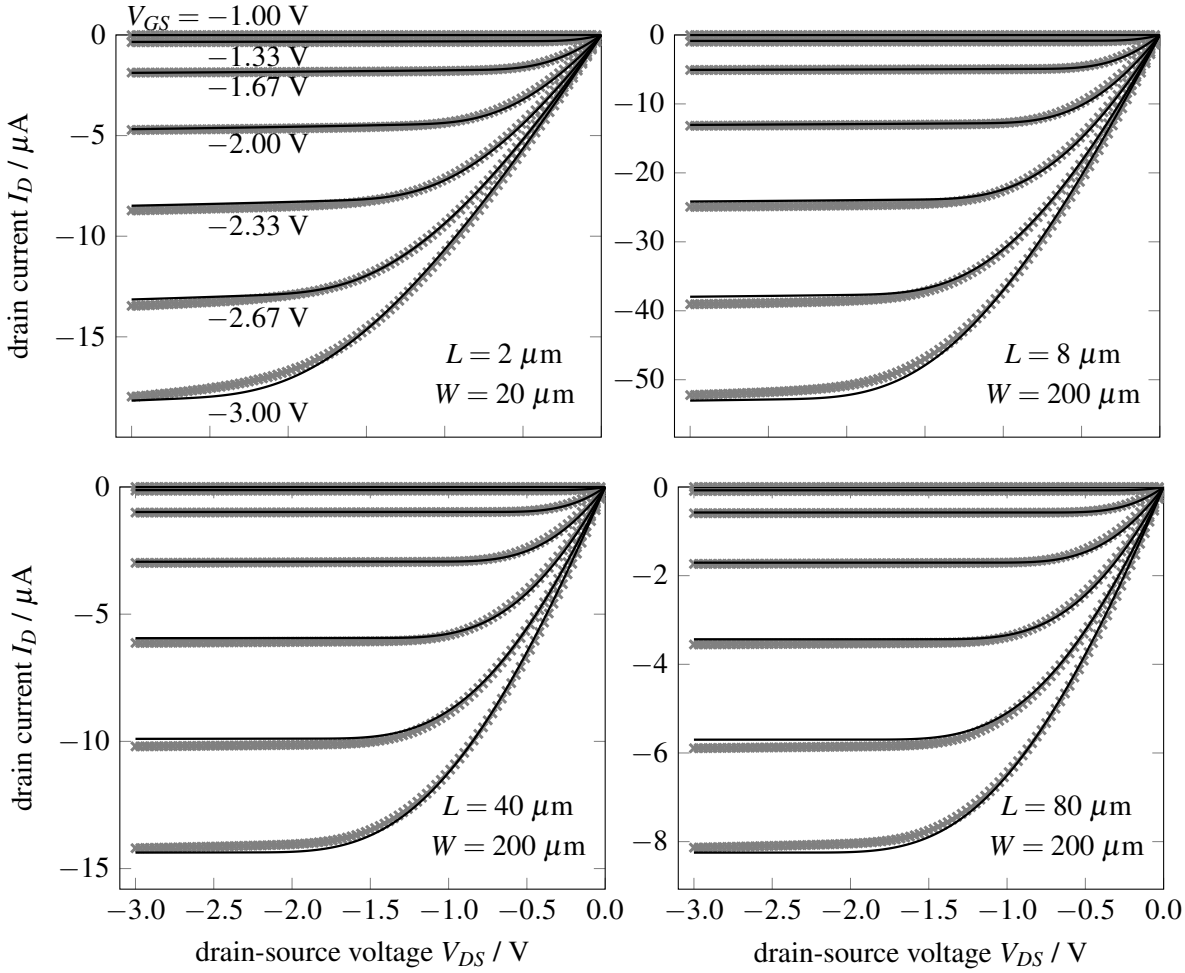

Figure 2.10: Measured (grey crosses) and calculated (black lines) output characteristics of the OTFTs underlying the data shown in Figure 2.8. In contrast to Figure 2.8, the calculated curves here represent fits of a transistor model incorporating a field and charge-carrier-density dependent mobility. The agreement between measured and calculated output characteristics significantly improves compared to the fits of the constant mobility model shown in Figure 2.8. As a consequence, the first step of our TSFA is well passed.

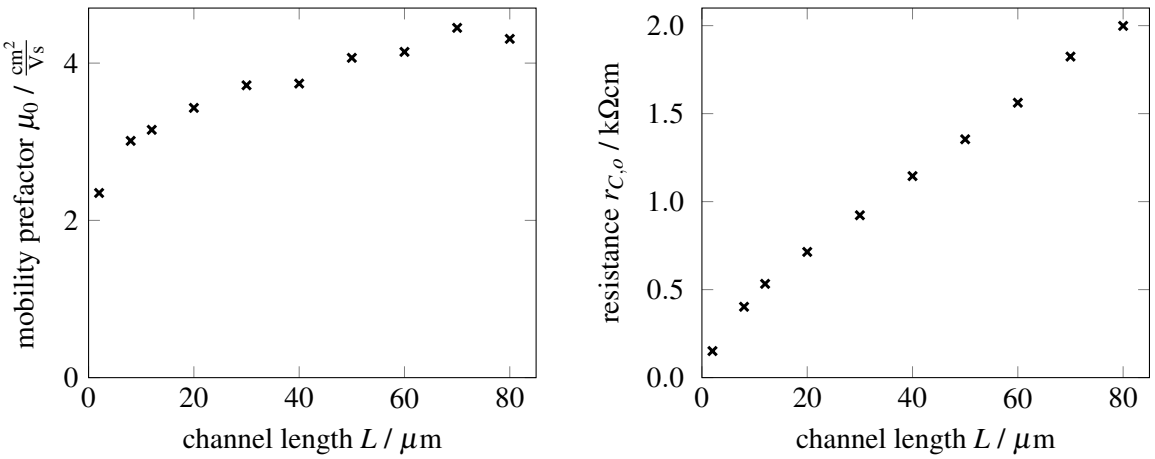

Figure 2.11: Selected parameters of the transistor model with field- and charge-carrier-density-dependent mobility extracted in the first step of the two-step-fitting approach as a function of the channel length L. The left panel shows an apparent channel-length dependence of the mobility prefactor μ_0, which, by its own, would already cause a failure of the transistor model. The right panel, showing the approximately linear channel-length dependence of the total channel-width-reduced ohmic contact resistance $r_{C,o} = r_{D,o} + r_{S,o}$, makes the failure of the transistor model even more evident with values increasing by more than one order of magnitude.

ure 2.11, the mobility prefactor μ_0 exhibits an apparent channel length L dependence with values in the range of $\mu_0 \approx 2.3$ $\frac{Vs}{cm^2}$ for $L = 2$ μm to $\mu_0 \approx 4.3$ $\frac{Vs}{cm^2}$ for $L = 80$ μm. This apparent channel-length dependence of the mobility prefactor μ_0 is surpassed by the obvious channel-length dependence of the total channel-width-reduced ohmic contact resistance $r_{C,o} = r_{D,o} + r_{S,o}$, illustrated in the right panel in Figure 2.11. The nearly perfect linear increase by more than one order of magnitude from $r_{C,o} \approx 0.15$ kΩcm for $L = 2$ μm to $r_{C,o} \approx 2.00$ kΩcm for $L = 80$ μm causes an obvious failure of the transistor model.

This failure of the transistor model is not just a peculiarity of the bottom-gate bottom-contact DNTT OTFTs investigated above. We tested several sets of OTFTs with different geometries, different OSCs, and different contact treatment fabricated and measured by two different groups. Measured and calculated output characteristics of a representative OTFT out of each set are shown in Figure 2.12 and the extracted total channel-width-reduced ohmic contact resistance $r_{C,o}$ as a function of the channel length L for each set of OTFTs is plotted in Figure 2.13. In short, all sets of OTFTs provoke a failure of the transistor model. In detail, the four additionally tested sets of OTFTs are discussed in the following.

The set of OTFTs represented by the output characteristics, shown in the upper left panel in Figure 2.12, uses the same OSC, DNTT, as the set of OTFTs investigated above with a different geometry. [56] Instead of bottom-contact architecture, the Au contacts are deposited as top-contacts. Regardless of the change in geometry, the calculated output characteristics for the set of bottom-gate top-contact DNTT OTFTs, determined by the parameters of the transistor model with field and charge-carrier density dependent mobility extracted in the first step of our TSFA, match well with the measured output characteristics (see upper left panel in Figure 2.12).

The remaining sets of OTFTs shown in Figure 2.12 are all bottom-gate bottom-contact OTFTs using pentacene (upper right panel in Figure 2.12) and C_{60} (lower panels in Figure 2.12) as OSC. For the OTFTs belonging to the upper right and the lower left panel in Figure 2.12, the Au contacts were coated with a self-assembled monolayer (SAM) of 2-phenylpyrimidine-5-thiol (BP0-down) and 4-(2-mercaptophenyl)pyrimidine (BP0-up), respectively, to avoid injection barriers. The contacts of the set of

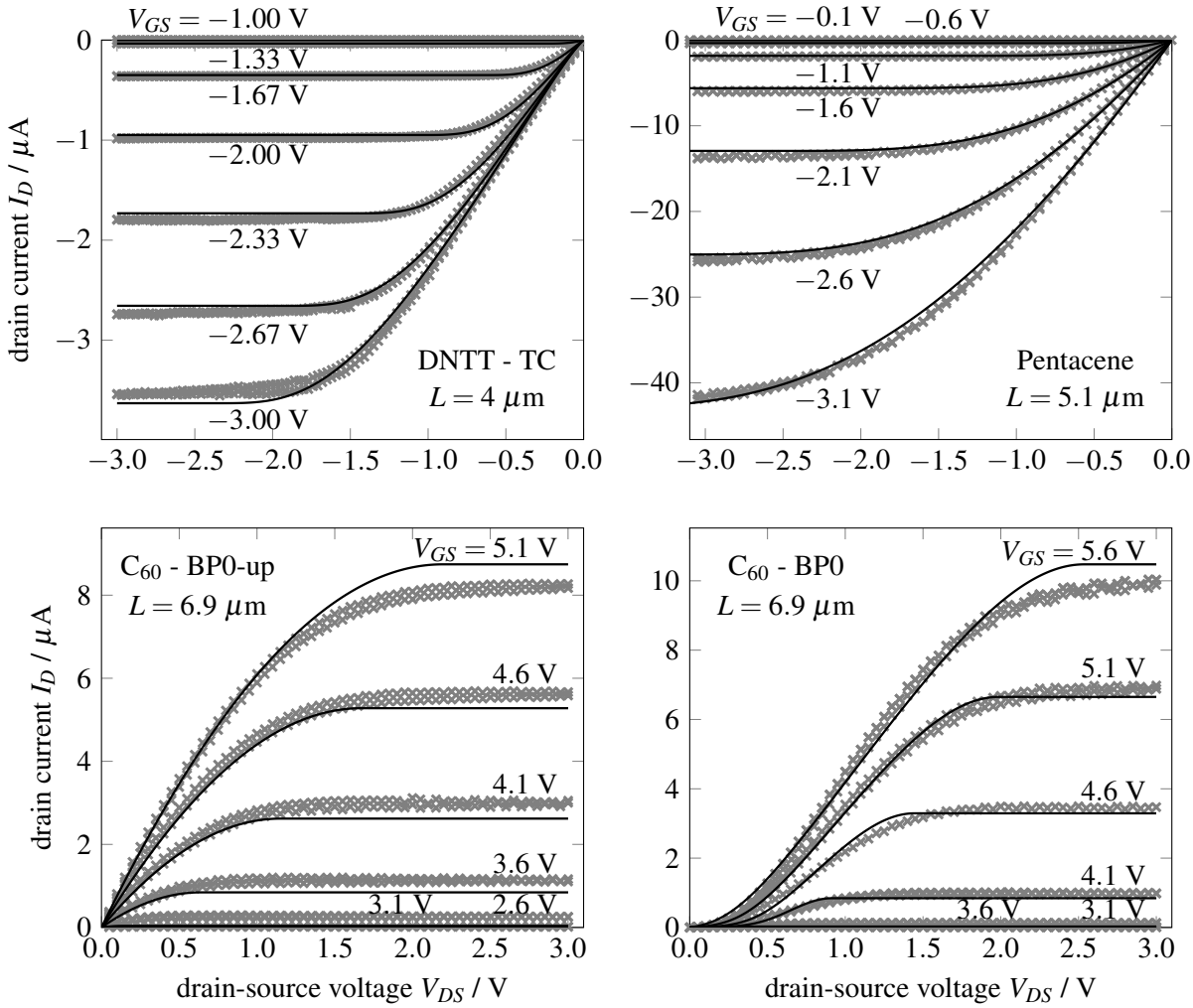

Figure 2.12: Representative measured output characteristics (grey crosses) of the tested additional sets of OTFTs and calculated output characteristics (black lines) for the fit of the corresponding transistor model performed within the first step of the two-step-fitting approach. In the upper left panel, the output characteristics for a bottom-gate top-contact (TC) OTFT using dinaphtho[2,3-b:2',3'-f]thieno[3,2-b]thiophene (DNTT) as OSC and gold (Au) contacts is shown. [56] The upper right panel is associated to a bottom-gate bottom-contact OTFT using pentacene as OSC and Au contacts coated with a self-assembled monolayer (SAM) of 2-phenylpyrimidine-5-thiol (BP0-down). The lower left and lower right panel shows output characteristics of bottom-gate bottom-contact OTFT using C_{60} as OSC and Au contacts coated with SAMs of 4-(2-mercaptophenyl)pyrimidine (BP0-up) and biphenyl-4-thiol (BP0), respectively. [1, 57] For the set of OTFTs represented by the lower right panel (C_{60} - BP0), a Schottky diode was considered to capture the non-linear behaviour in the linear regime (S-shape of the output characteristics for low absolute drain-source voltages $V_{DS} \approx 0$). The agreement between measured and calculated output characteristics is acceptable in all cases.

C_{60} OTFTs, referring to the lower right panel of Figure 2.12, are covered with a SAM of biphenyl-4-thiol (BP0). [1, 57] This contact treatment introduces a significant injection barrier and leads to an S-shape in the linear regime of the output characteristics below $V_{DS} \lesssim 0.5$ V (non-linear increase of the absolute drain current I_D with respect to the absolute drain-source voltage V_{DS} in the lower right panel in Figure 2.12). The agreement between measured and calculated output characteristics shown in Figure 2.12 is acceptable for all sets of OTFTs. So the first step of our TSFA is passed.

For the second step of the TSFA, the total channel-width-reduced ohmic contact resistance $r_{C,o} =$

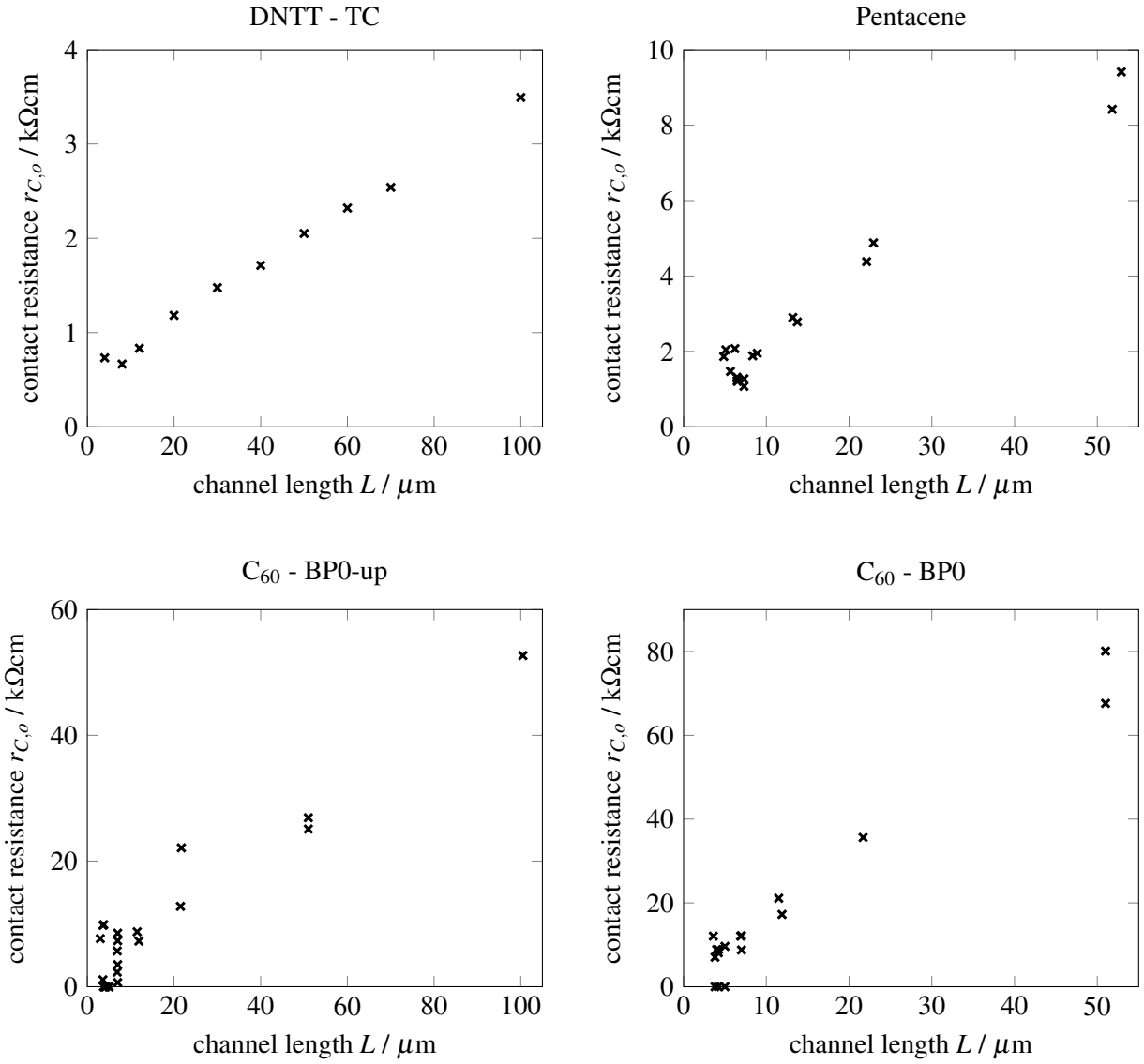

Figure 2.13: Total channel-width-reduced ohmic contact resistance $r_{C,o} = r_{D,o} + r_{S,o}$ as a function of the channel length L for different sets of OTFTs. Upper left panel: A set of bottom-gate top-contact OTFTs using dinaphtho[2,3-b:2',3'-f]thieno[3,2-b]thiophene (DNTT) as organic semiconductor (OSC) and gold (Au) contacts. Upper right panel: A set of bottom-gate bottom-contact OTFTs using pentacene as OSC and a self-assembled monolayer of 2-phenylpyrimidine-5-thiol (BP0-down) to cover the Au contacts. Lower left and lower right panel: A set of bottom-gate bottom-contact OTFTs using C_{60} as OSC and a self-assembled monolayer of 4-(2-mercaptophenyl)pyrimidine (BP0-up) and biphenyl-4-thiol (BP0), respectively, to cover the Au contacts. For all sets of OTFTs, the total channel-width-reduced ohmic contact resistance $r_{C,o}$ shows a pronounced dependence on the channel length. As a consequence, the transistor model is wrong, according to our two-step-fitting approach, for a representative variety of different geometries, OSC and contact treatments. The variation of $r_{C,o}$ for low channel lengths $L \lesssim 20$ μm in the upper right panel and the lower panels represents device-to-device fluctuations.

$r_{D,o} + r_{S,o}$ is depicted as a function of the channel length L in Figure 2.13 for the four different sets of OTFTs introduced in Figure 2.12. For all sets of OTFTs, a pronounced channel-length dependence of the total channel-width-reduced ohmic contact resistance $r_{C,o}$ is observed. This channel-length dependence provokes a failure of the tested transistor model in the second step of our TSFA. The representative sample of different sets of OTFTs including different geometries, different OSCs, and different contact

treatments implies that the state-of-the-art transistor model widely used in literature, which we tested, has to be reconsidered.

2.4 Model Evaluation

As already mentioned in Chapter 2.3, when evolving from the constant mobility model to the field- and charge-carrier-density-dependent mobility model, our two-step-fitting approach is not only a proper method to test transistor models, it also provides insight, why a transistor model fails. This insight can be gained from two different sources. On the one hand, by looking at the deviations between measured and calculated characteristics and, on the other hand, by looking at the channel-length dependence of the extracted parameters.

Starting with the first source to gain insight, we inspect the deviations of the calculated output characteristics from the measured output characteristics shown in Figure 2.10 and Figure 2.12. A close look reveals, that the calculated curve for the highest absolute gate-source voltage $|V_{GS}|$ systematically overestimates the measured curve in the saturation regime and the calculated curve for the second highest absolute gate-source voltage $|V_{GS}|$ systematically underestimates the measured curve in the saturation regime. This behaviour is present for all output characteristics of all sets of OTFTs shown in Figure 2.10 and Figure 2.12.

The spacing in the saturation regime of output-characteristics curves for different gate-source voltages V_{GS} is predominantly determined by the interplay of the contact resistance and the mobility. We already noticed in Chapter 2.1.4, that the shape of the output characteristics of an ideal OTFT (upper left panel in Figure 2.4) is comparable to the shape of the output characteristics of a device with ohmic contact resistances and a charge-carrier-density dependent mobility (middle right panel in Figure 2.4). To further illustrate the interplay of contact resistance and mobility, Figure 2.14 shows calculated output characteristics of two devices only differing in the channel-width-reduced ohmic source resistance $r_{S,o}$ and the mobility prefactor μ_0.

The black curves in Figure 2.14 show the calculated output characteristics for an OTFT with channel length $L = 43.4\ \mu$m, channel width $W = 200\ \mu$m, gate capacitance $C_G = 700\ \frac{\text{nF}}{\text{cm}^2}$, channel-width-reduced ohmic drain and source resistance $r_{D,o} = r_{S,o} = 0.07$ kΩcm, threshold voltage $V_T = -1.25$ V and mobility prefactor $\mu_0 = 3.2\ \frac{\text{cm}^2}{\text{Vs}}$. Due to the rather low contact resistances, the spacing of the curves in the saturation regime for high absolute drain-source voltages $-V_{DS} \gtrsim 2.0$ V is increasing nearly linear (nearly quadratic increase of the absolute saturation drain current with increasing absolute gate-source voltage). In comparison, the grey dashed curves in Figure 2.14 show the output characteristics of an OTFT with a 10 times larger channel-width-reduced ohmic source resistance $r_{S,o} = 0.7$ kΩcm and a mobility prefactor raised to $\mu_0 = 6.1\ \frac{\text{cm}^2}{\text{Vs}}$. Although the curves for the highest absolute gate-source voltage $-V_{GS} = 3.0$ V are approximately equal, the curves for lower absolute gate-source voltage $-V_{GS} < 3.0$ V differ considerably. The spacing between the dashed grey curves in Figure 2.14 in the saturation regime for high absolute drain-source voltages $-V_{DS} \gtrsim 2.0$ V are nearly equidistant (nearly linear increase of the absolute saturation drain current with increasing absolute gate-source voltage).

The comparison shown in Figure 2.14 demonstrates, that the spacing of the curves in the saturation regime of the output characteristics is significantly influenced by the interplay of the mobility and the contact resistance. If the field and/or charge-carrier-density dependence of the mobility is captured wrong in our transistor model, it can be compensated by a wrong contact resistance. As the contact resistance

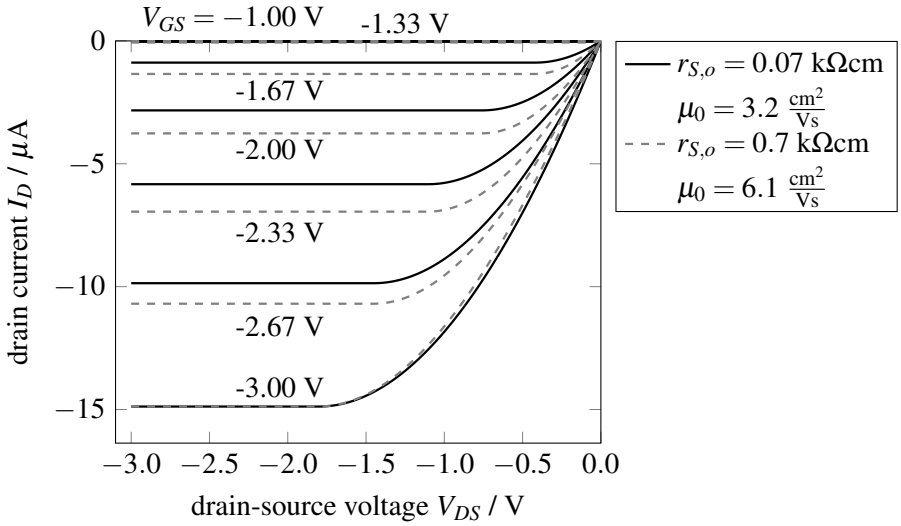

Figure 2.14: Calculated output characteristics of two OTFTs with channel length $L = 43.4$ μm, channel width $W = 200$ μm, gate capacitance $C_G = 700$ $\frac{nF}{cm^2}$, channel-width-reduced ohmic drain resistance $r_{D,o} = 0.07$ kΩcm and threshold voltage $V_T = -1.25$ V. The black lines represent an OTFT with mobility prefactor $\mu_0 = 3.2$ $\frac{cm^2}{Vs}$ and channel-width-reduced ohmic source resistance $r_{S,o} = 0.07$ kΩcm and the grey dashed lines show the output characteristics of an OTFT with $\mu_0 = 6.1$ $\frac{cm^2}{Vs}$ and $r_{S,o} = 0.7$ kΩcm. The solid black and dashed grey curves for the highest absolute gate-source voltage $-V_{GS} = 3.0$ V are approximately equal. For lower absolute gate-source voltage $-V_{GS} \leq 2.67$ V, the solid black and dashed grey curves are distinctly different, in particular in the saturation regime.

is a property of the contact and the mobility is a property of the channel, the wrong contact resistance has to increase with increasing channel length to compensate the wrong description of the channel. So, a wrong field and/or charge-carrier-density dependence of the mobility is able to explain the outcomes of our two-step-fitting approach performed in Chapter 2.3.

The second source to gain insight in the course of our two-step-fitting approach is to look at the channel-length dependence of the extracted parameters. The total channel-width-reduced ohmic contact resistance $r_{C,o} = r_{D,o} + r_{S,o}$ shows a nearly perfect linear increase with respect to the channel length. The channel length could indeed have a significant influence on the contact region due to the long-ranging nature of Coulomb interactions. Charge accumulations distributed over a large region in combination with a metal contact and the image charges associated with the metal contact can create dipoles. Those dipoles are able to seriously influence the contact region and especially the injection behaviour at the source contact. The longer the channel, the more pronounced the influence on the contact region, delivering a plausible explanation for the increase of the contact resistance with increasing channel length.

In summary, we identified two possible problems causing the failure of the transistor model within our two-step-fitting approach. First, the field and/or charge-carrier-density dependence of the mobility within the OSC might be wrong. This problem serves as a motivation to develop a new simulation technique for hopping transport in Chapter 3, which additionally provides insight into charge transport mechanisms investigated in Chapter 4. Second, the description of contacts might require the consideration of long-ranging Coulomb interactions from charge distributed over the entire device. This problem serves as a motivation for Chapter 5, which investigates the influence of the charge-carrier density within a device on the region close to the contact.

3 Correction Energy Concept

From a theoretical point of view, organic semiconductor (OSC) devices represent a challenging topic due to the huge range in length-scales that have to be covered. Starting from small molecules or segments of a polymer chain with diameters in the order of one nanometre, effects on all length scales up to the device size have to be considered for a proper theoretical description of the device. The size of such devices can range up to some decimetres for large area lighting [58, 59] or solar cells [60, 61]. Even organic transistors reach sizes of some millimetres. [1] Not all dimensions of an OSC device are large. As an example, Park *et al.* fabricated organic light-emitting diodes (OLEDs) with a thickness of the active layer of 113 nm and lateral sizes of 15 cm by 15 cm. [62] Although this is an extreme example, the lateral size in OSC devices is typically 4 to 5 orders of magnitude larger than the thickness. This huge range of appearing sizes requires multiscale approaches [63–66] to link insights gained on a molecular level to their influence on the device performance. On the microscopic level of molecules and segments of polymer chains, density functional theory (DFT) based approaches, e.g. [68], are widely used, often in combination with molecular dynamics, e.g. [67]. On the macroscopic device level, drift-diffusion simulations, e.g. [31], or analytical approximations, e.g. [26, 27], describing the device performance are common. [69] Those macroscopic considerations rely on a proper parametrisation of the material that incorporates the effects arising from the microscopic level. To link the microscopic and the macroscopic level, a so-called mesoscopic level can be introduced. [69] This mesoscopic level, which acts on the order of up to some hundred nanometres, is captured by a theoretical concept called hopping transport. [8, 70] Besides hopping transport, band transport and dynamic disorder models are the most important alternative approaches to describe charge transport in OSCs on a mesoscopic scale. [71–77] In this thesis, we will only focus on hopping transport.

In hopping transport, charge carriers are occupying spatially localised sites with certain energy levels. The charge carriers are allowed to hop between the spatially localised sites. This motion is regulated by hopping rates, which are determined by the energy levels of the localised sites, the distance between them, the temperature, and other input parameters. Those input parameters can be obtained from or at least justified by considerations on a microscopic level. As an outcome, hopping transport can provide a parametrisation for drift-diffusion simulations [31] or analytical device models (cf. Chapter 2). Hopping transport was even used to successfully simulate entire small devices [63, 78].

To extract observables such as mobilities from the theoretical concept of hopping transport, certain techniques are required. We can differentiate between two categories of those techniques: (i), analytical derivations and, (ii), simulations.

Analytical derivations, e.g., variable-range hopping (VRH) in combination with percolation theory [34] or multiple trapping and release (MTR) [35], provide an analytic expression for observables, e.g., the mobility depending on input parameters such as the density of states (DOS) of the energy levels of the localised sites, the temperature, the applied electric field, the charge-carrier density or the distance between the sites. Those analytical derivations are able to describe the system well in a certain parameter region. Due to the assumptions and approximations within their derivations, they unfortunately cannot provide a description of the system as a whole. In Chapter 2.4, we already found that the mobility model suggested by VRH or MTR does not provide a sufficient estimate for the range of electric fields and charge-carrier densities observed in an OTFT.

Simulations provide numbers for observables referring to a certain set of numbers for the input pa-

rameters with numerical or stochastical precision. The two most important simulation techniques for hopping transport are currently, (i), kinetic Monte Carlo (KMC) [3, 8, 79–85] and, (ii), the master equation (ME) approach [11, 86–91]. In KMC simulations, a stochastic process is applied to calculate the requested observables. In principle, all input parameters, effects, and interactions can be directly considered, provided that one can afford it computationally. In contrast, the ME approach can only account for interactions in a mean-field formalism. Going beyond mean-field in a ME approach is difficult and computationally expensive. [92]

Probably the most important reason to run simulations is to gain insight into the interplay of influences of different input parameters on the requested observables. For example, one could ask for the influence of the electric field on the bulk mobility in an OSC over a wide range of electric fields (cf. Chapter 4). With a such gained insight from simulations, an analytical expression for the desired observable can be proposed that covers a wide range of input parameters properly. This was, e.g., done by Pasveer *et al.* [11]. As the best conceivable case, it is desirable that this proposed analytical expression can be justified by an analytical derivation that utilises the gained insight to perform the right approximations for the right parameter ranges. Altogether, a clever combination of simulations and analytical considerations is likely preferable to advance the theoretical understanding.

In the following, we present a new simulation technique that is situated between KMC and ME. This new simulation technique, that we call correction energy concept (CEC), also enables new analytical derivations, especially regarding the electric field dependence of observables. Hence, the CEC can act on both sides, simulations (discussed in this chapter) and analytical considerations (discussed in Chapter 4). Regarding simulations, the benefits and drawbacks of KMC and ME are mostly contrary. KMC simulations can provide very precise results, but often with the drawback of high computational cost. In contrast, ME simulations are usually computationally much less expensive, but interactions and correlations are barely included sometimes resulting in untrustworthy outcomes. Our CEC combines the benefits of both simulation techniques by providing computationally cheap and trustworthy outcomes.

The CEC consists of two major parts. In the first part, the hopping rates are translated to so-called correction energies, which correctly account for the applied electric field. This translation is described by the example of charge transport in the bulk of an OSC in detail in Chapter 3.1. The nature and consequences of those correction energies are discussed in Chapter 4.1. The second part of the CEC regards the correct occupation statistics that is required to include the correction energies. Only if the correction energies are properly incorporated in the occupation statistics, an accurate extraction of observables is possible. This second part is found in Chapter 3.2. With the theoretical basics of the CEC being discussed in Chapter 3.1 and Chapter 3.2, the subsequent Chapter 3.3 describes the way we implemented the CEC with some intricacies that should be considered to enable a proper numerical evaluation. Finally, in Chapter 3.4 the results of our CEC are benchmarked against very accurate and computationally expensive KMC simulation results.

3.1 From Rates To Energies

For the derivation of the CEC, we focus on the example of charge transport in the bulk of an OSC with only one type of charge carrier present. In principle, the CEC can be applied to any system that can be simulated with hopping transport including contacts, electron-hole creation/annihilation, et cetera. To show the basic idea and to perform a first benchmark of the method, however, the most simple system in

hopping transport is suited best. This most simple system is the chosen example, considering only one type of charge carrier that hops around in the bulk of an OSC.

3.1.1 The Bulk System

A detailed description of such a bulk system, including a recipe to perform KMC simulations on it, can be found in [3, 93]. The key ingredients that we have to consider here are summarised briefly. Spatially localised sites i can be occupied by, at maximum, one charge carrier. The position of a site i is given by a vector $\vec{r}_i$. The boundary conditions are chosen such that when a charge carrier hops out towards a certain direction, it jumps back in on the opposite side of the simulation volume. This is reminiscent of periodic boundary conditions, but with the restriction, that this boundary condition does not conserve energy in the direction of the applied electric field, as will be discussed in detail in Chapter 3.1.2. We assign an energy level ε_i to each site i at the beginning of the simulation. This assignment can be made, e.g., by drawing random numbers from a Gaussian distribution determined by a probability density $p(\varepsilon)$

$$p(\varepsilon) = \frac{1}{\sqrt{2\pi}\sigma} \exp\left(-\frac{\varepsilon^2}{2\sigma^2}\right) \tag{3.1}$$

with a certain width called energetic disorder σ.

To make the charge carriers move, hopping rates $R_{ij}(\xi)$ have to be introduced for a hop of a charge carrier from site i to site j depending on the initial configuration ξ. A configuration $\xi = \{i_1, i_2, \ldots, i_{N_{cc}}\}$ is one possibility to place the fixed number of charge carriers N_{cc} on the N_s sites in the system volume with i_n being the site that charge carrier n occupies. All charge carriers are indistinguishable, so the order in ξ is irrelevant. The number of possible configurations N_{cnfg} is given by

$$N_{cnfg} = \binom{N_s}{N_{cc}} = \frac{N_s!}{N_{cc}!(N_s - N_{cc})!} \tag{3.2}$$

with the binomial coefficient being expressed by factorials. Only one charge carrier can hop at once. The hopping rate $R_{ij}(\xi)$ depends on the initial configuration ξ due to the interactions with the charge carriers that do not move during the hop from site i to site j. Additionally, site exclusion requires that at maximum one charge carrier can occupy a site, which implies that site i has to be occupied in state ξ and site j has to be unoccupied.

The two most common rate equations are the Miller-Abrahams rate equation [94]

$$R_{ij}^{MA}(\xi) = \nu_0 \exp\left(-2\alpha\Delta r_{ij}\right) \begin{cases} \exp\left(-\frac{E_j(\xi') - E_i(\xi)}{k_B T}\right) & \text{for } E_j(\xi') > E_i(\xi) \\ 1 & \text{else} \end{cases} \tag{3.3}$$

and the Marcus rate equation [95]

$$R_{ij}^{M}(\xi) = \nu_0 \exp\left(-2\alpha\Delta r_{ij}\right) \exp\left(-\frac{\left(E_j(\xi') - E_i(\xi) + E_r\right)^2}{4E_r k_B T}\right) \tag{3.4}$$

with a hopping prefactor ν_0, the charge delocalisation constant α, the distance $\Delta r_{ij} = |\Delta\vec{r}_{ij}|$ that is covered during the hop respecting the boundary conditions, the Boltzmann constant k_B, the temperature T, the reorganisation energy E_r, the energy $E_i(\xi)$ of a charge carrier at site i in the initial configuration ξ and

the energy $E_j(\xi')$ of a charge carrier at site j in the final configuration ξ':

$$E_i(\xi) = \varepsilon_i + e\vec{r}_i\vec{F} + \sum_{k\in\xi}^{k\neq i} E_{ik}^{int} \quad \text{and} \quad E_j(\xi') = \varepsilon_j + e\vec{r}_j\vec{F} + \sum_{k\in\xi'}^{k\neq j} E_{jk}^{int}. \tag{3.5}$$

The energy E_i^{ξ} of site i in configuration ξ contains the site energy ε_i, a contribution $e\vec{r}_i\vec{F}$ from the electric field $\vec{F}$ including the elemental charge e and the position $\vec{r}_i$ of site i, and a sum over the interactions E_{ik}^{int} with all other charge carriers in configuration ξ occupying sites k. Initial and final configuration ξ and ξ' have to be the same except that in ξ site i is occupied and site j is unoccupied and in ξ' site i is unoccupied and site j is occupied.

With respecting the boundary conditions for the evaluation of Δr_{ij}, we mean that hopping to a site j in the vicinity of the initial site i across a boundary covers only a short distance and not the total system size in the direction of the boundary as suggested by $|\vec{r}_j - \vec{r}_i|$, cf. Figure 3.1. Mathematically, this can be captured by introducing a distance

$$\vec{L}_{bd} = (l_{bd}^1 L_{sys}^1, l_{bd}^2 L_{sys}^2, l_{bd}^3 L_{sys}^3)^{\top} \tag{3.6}$$

with the size of the actually simulated system L_{sys}^i in spatial direction i and integer values l_{bd}^i indicating where the boundary was crossed. The symbol $^{\top}$ means that the vector is transposed. Without crossing any boundary, all $l_{bd}^i = 0$ are zero. If the charge carrier crosses the boundary, e.g., in positive direction of the second dimension, we would get $l_{bd}^1 = 0$, $l_{bd}^2 = 1$, and $l_{bd}^3 = 0$. Crossing the boundary in negative direction of the third dimension would give $l_{bd}^1 = 0$, $l_{bd}^2 = 0$, and $l_{bd}^3 = -1$ and so on. With this variable $\vec{L}_{bd}$, we can formulate the actually covered distance by a hop from site i to site j respecting the boundary conditions:

$$\Delta\vec{r}_{ij} = \vec{r}_j + \vec{L_{bd}} - \vec{r}_i \tag{3.7}$$

3.1.2 Violation of Energy Conservation

For our CEC, the boundary conditions are an essential ingredient being, in fact, the reason for the need to introduce correction energies. In the following, we will have a close look at the boundary conditions and the associated violation of energy conservation. Due to the boundary conditions, the simulation volume is periodically repeated in all three spatial dimensions. This repetition is not only happening for the sites and their energies, but also in terms of the charge carriers. So each charge carrier has an infinite number of periodic replicas. In Figure 3.1, the actually simulated system of an exemplary one-dimensional cartoon system is indicated as a black box with system size L_{sys}. The horizontal lines indicate the energy levels of the sites uniformly distributed in space. Due to an externally applied electric field, the energy levels of the sites linearly decrease with position. Black horizontal lines are in the actual system, while grey horizontal lines indicate sites within the periodic replicas. The black ball is the actual charge carrier that is considered in our simulation and the grey ball is a periodic replica of the black ball.

Looking at Figure 3.1, due to the externally applied electric field, the energy levels are always going down when the charge carrier hops right, even if it crosses the boundaries. In the left panel in Figure 3.1, the actual charge carrier at the right side of the simulation volume attempts to hop downwards in energy due to the electric field. After crossing the boundary, it converts from an actual charge carrier, indicated

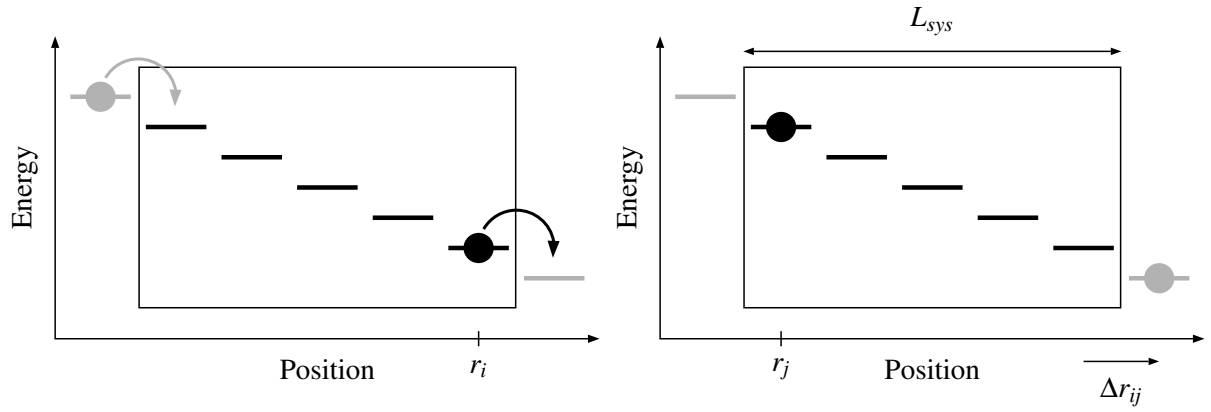

Figure 3.1: Charge carrier hopping over the boundary towards decreasing energy levels due to an externally applied electric field. The box shows the limits of the actual simulation volume. The black ball symbolises the actual charge carrier and the grey ball is a periodic replica of the actual charge carrier. The horizontal lines indicate the energy level of the site at the according position. The grey energy levels and the grey charge carrier shows a part of the periodic replicas of the system. The system size in field direction is labelled L_{sys}. When the actual charge carrier hops towards lower energies to the right (left panel), the energy of the considered system artificially increases due to the conversion of the actual charge carrier to a periodic replica and vice versa (right panel). The distance $\Delta r_{ij} = r_j + 1 \cdot L_{sys} - r_i$ related to the hop, respecting the boundary conditions, is determined by the initial position r_i, the final position r_j, the system size L_{sys} and the variable $l_{bd} = 1$ indicating that the boundary was crossed in positive direction, cf. Equations (3.6) and (3.7).

as a black ball, to a periodic replica, indicated as a grey ball (see right panel in Figure 3.1). Exactly at this conversion, energy conservation is violated. During the hop, the charge carrier at the right boundary of the system decreases its energy. We account for this decrease in energy in the hopping rate. This means, the hopping rate suggests that the energy of the charge carrier, and, hence, the total system, decreases. But due to the conversion, the energy of our actual system increases because it seems as if the charge carrier would have hopped upwards in energy.

Nevertheless, this choice of the boundary conditions describes charge transport in the bulk of an OSC appropriately, because if we cut a cube out of an OSC, charge carriers would also, on average, enter the cube on one side and leave it on the opposite side due to the electric field. Within the cube, energy from the electric field is converted into heat. The energy that is put into the system by the electric field corresponds to the energy gained during the conversion from an actual charge carrier to a periodic replica and vice versa. The dissipated heat is considered in the hopping rates, which prefer hops downwards in energy.

While we simulate the correct behaviour, the hopping rates and the total energy of the system do not observe the same change in energy when a charge carrier is crossing the boundaries of the actual system marked by the black box in Figure 3.1. This discrepancy between the energy change accounted for by the hopping rate and energy change in the total energy of the actual system is the reason why we will introduce correction energies in Chapter 3.1.4. Prior to that, a short introduction to the global balance equation and the steady-state-probability distribution is given in Chapter 3.1.3.

3.1.3 Global Balance Equation

A detailed introduction to continuous-time Markov chains, which is the mathematical foundation for hopping transport, can be found in [96]. An excerpt of the essential remarks that might be of avail in the following is given in [93]. Here, we will briefly discuss the mathematical basics required to understand the derivation leading to the correction energies.

To understand the global balance equation, we need to introduce two quantities: (i), the Q-matrix and, (ii), the steady-state-probability distribution $\vec{\pi}$. The Q-matrix $Q = (q_{\xi\xi'})$ contains the hopping rates $R_{ij}(\xi)$ linking the initial configuration ξ and the final configuration ξ'.

$$q_{\xi\xi'} = \begin{cases} R_{ij}(\xi) & \text{if } \forall ij \; \exists R_{ij}(\xi) \neq 0 \text{ linking } \xi \text{ and } \xi' \\ -\sum_{\xi'' \in \Xi \setminus \{\xi\}} q_{\xi\xi''} & \text{if } \xi = \xi' \\ 0 & \text{else} \end{cases} \tag{3.8}$$

This means that the off-diagonal elements of the Q-matrix are the rates $R_{ij}(\xi)$ for a hop from site i to site j and corresponding initial configuration ξ and final configuration ξ' only differing in the occupation of site i and site j. The diagonal elements of the Q-matrix are the negative sum over all configurations ξ'' in the configuration space Ξ except configuration ξ. This means we sum up all rates associated to hops with the initial configuration ξ. Due to the constraint that only one charge carrier can hop at once, most of the off-diagonal elements of the Q-matrix are zero because most pairs of configurations ξ and ξ' cannot be converted into one another by moving only one charge carrier. The configuration space Ξ is the set of all N_{cnfg} configurations and $\Xi \setminus \{\xi\}$ denotes the set of all configurations except configuration ξ.

The steady-state-probability distribution $\vec{\pi} = (\pi_\xi)$ contains the probability π_ξ that a configuration ξ is visited in steady state. As soon as the steady-state-probability distribution $\vec{\pi}$ is known, we can, in principle, calculate each steady-state observable.

The equation determining the steady-state-probability distribution $\vec{\pi}$ is the so-called global balance equation:

$$\sum_{\xi' \in \Xi \setminus \{\xi\}} \pi_\xi q_{\xi\xi'} = \sum_{\xi' \in \Xi \setminus \{\xi\}} \pi_{\xi'} q_{\xi'\xi}. \tag{3.9}$$

The term $\pi_\xi q_{\xi\xi'}$ is the probability flux from configuration ξ to configuration ξ', because the rate $q_{\xi\xi'}$ holds the outflow of probability from configuration ξ to configuration ξ' and this outflow weighted by the probability π_ξ for configuration ξ results in a probability flux. This means, the global balance equation, Equation (3.9), balances the probability flux out of configuration ξ to all other configurations ξ' in the configuration space Ξ (left-hand side) and the probability flux into configuration ξ from all other configurations ξ' in the configuration space Ξ (right-hand side). As the sum on the left-hand side of Equation (3.9) can be written as $-\pi_\xi q_{\xi\xi}$ due to Equation (3.8), a compact representation of the global balance equation can be given in matrix notation $(\vec{\pi})^\top Q = (\vec{0})^\top$, with $(\vec{0})^\top$ being a vector containing N_{cnfg} zeros.

When no external electric field is applied, an analytic solution for the steady-state-probability distribution $\vec{\pi}$ can be found, which we will sketch in the following. The two rate equations we have introduced above both locally conserve energy. With energy conservation, we denote that for Miller-Abrahams rates,

$R_{ij}^{MA}(\xi)$, Equation (3.3), as well as for Marcus rates, $R_{ij}^{M}(\xi)$, Equation (3.4), the relation

$$\exp\left(-\frac{E_i(\xi)}{k_B T}\right) R_{ij}(\xi) = \exp\left(-\frac{E_j(\xi')}{k_B T}\right) R_{ji}(\xi') \tag{3.10}$$

is valid. For a proof of this claim, see [3, 93]. This Equation (3.10) already suggests the solution for the steady-state-probability distribution $\vec{\pi}$:

$$\pi_\xi = \frac{1}{Z}\exp\left(-\frac{E^{noF}(\xi)}{k_B T}\right) \quad \text{with} \quad Z = \sum_{\xi\in\Xi}\exp\left(-\frac{E^{noF}(\xi)}{k_B T}\right) \tag{3.11}$$

with the partition function Z. The total energy $E^{noF}(\xi)$ of configuration ξ without applied electric field is given by

$$E^{noF}(\xi) = \sum_{i\in\xi}\left(\varepsilon_i + \frac{1}{2}\sum_{j\in\xi}^{j\neq i} E_{ij}^{int}\right). \tag{3.12}$$

In contrast to Equation (3.5), which denotes the energy required to remove the charge carrier occupying site i, a factor $\frac{1}{2}$ appears in front of the interaction term to avoid double counting. With Equations (3.8), (3.10), (3.11) and (3.12), we receive the relation

$$\pi_\xi q_{\xi\xi'} = \pi_{\xi'} q_{\xi'\xi}, \tag{3.13}$$

which is the so-called local balance equation. Summing this relation over all configurations ξ', we end up with the global balance equation, Equation (3.9). This shows that the steady-state-probability distribution $\vec{\pi}$, when no electric field is applied, is given by Equations (3.11) and (3.12).

When we apply an external electric field $\vec{F}$, the solution is no longer valid. The problem arises during the conversion from an actual charge carrier to a periodic replica upon a hop of a charge carrier across a boundary. At this moment, the change in field energy between the configurations ξ and ξ' and the change in field energy proposed by the rates does not match so that Equation (3.10) is violated. This is where correction energies come into play.

3.1.4 Correction Energies

Below, we will convert the global balance equation, Equation (3.9), into a system of equations that enables us to approximately calculate the steady-state-probability distribution $\vec{\pi}$ for arbitrary electric field strengths $\vec{F}$. In principle, this derivation can be adopted to any system simulated with hopping transport. As the only crucial prerequisite, rates that conserve energy are required. This means, Equation (3.10) has to be fulfilled for the chosen rate equation for all hops that are not influenced by boundaries.

The finite-dimensional and irreducible configuration space Ξ guarantees the existence of a unique steady-state-probability distribution $\vec{\pi}$ that can be found by the global balance equation $(\vec{\pi})^\top Q = (\vec{0})^\top$, Equation (3.9) (see [93, 96] for details). In order to find the solution, we enlarge our configuration space to an infinite-dimensional space and, thereby, prevent the violation of energy conservation. This prevention is achieved via advancing the configuration space by the variable $\vec{l}_{bd} = (l_{bd}^i)$ introduced in Equation (3.6). Here, l_{bd}^i is not just used for one hop, but it counts how many times the boundary in spatial dimension i was crossed in positive $l_{bd}^i \to l_{bd}^i + 1$ or negative $l_{bd}^i \to l_{bd}^i - 1$ direction for all hops

and all spatial dimensions i. With this variable, the configuration space is enlarged to $\xi \rightarrow (\xi, \vec{l}_{bd})$. In the illustrative one-dimensional example shown in Figure 3.1, the charge carrier performs a transition from ξ to ξ' in the old configuration space. In the enlarged configuration space, it performs a transition from (ξ, l_{bd}) to $(\xi', l_{bd}+1)$. Coming back to the three-dimensional system, the total energy of a configuration in the old configuration space is given by

$$E^{tot}(\xi) = \sum_{i \in \xi} \left(\varepsilon_i + e\vec{r}_i \vec{F} + \frac{1}{2} \sum_{j \in \xi}^{j \neq i} E_{ij}^{int} \right), \tag{3.14}$$

whereas in the new configuration space, the total energy of the system is

$$E^{tot}(\xi, \vec{l}_{bd}) = e\vec{L}_{bd}\vec{F} + \sum_{i \in \xi} \left(\varepsilon_i + e\vec{r}_i \vec{F} + \frac{1}{2} \sum_{j \in \xi}^{j \neq i} E_{ij}^{int} \right) = E^{tot}(\xi) + e\vec{L}_{bd}\vec{F} \tag{3.15}$$

with total distance travelled across boundaries $\vec{L}_{bd} = (l_{bd}^i L_{sys}^i)$, cf. Equation (3.6). The configuration ξ is still only accounting for the charge carriers in the actual system. Nevertheless, due to this new variable $\vec{l}_{bd}$, energy conservation is re-established when crossing the boundaries. Due to energy conservation, the local balance equation, Equation (3.13), is valid in this new configuration space in the form

$$\exp\left(-\beta E^{tot}(\xi, \vec{l}_{bd})\right) q_{(\xi, \vec{l}_{bd})(\xi', \vec{l}'_{bd})} = \exp\left(-\beta E^{tot}(\xi', \vec{l}'_{bd})\right) q_{(\xi', \vec{l}'_{bd})(\xi, \vec{l}_{bd})} \tag{3.16}$$

with the inverse temperature $\beta = \frac{1}{k_B T}$. This form of the local balance equation, Equation (3.16), is correct even for hops across the boundaries and we assume a steady-state-probability distribution of the form

$$\pi_{(\xi, \vec{l}_{bd})} = \frac{1}{Z} \exp\left(-\beta E^{tot}(\xi, \vec{l}_{bd})\right) \pi^0_{(\xi, \vec{l}_{bd})} \quad \text{with} \quad Z = \sum_{(\xi, \vec{l}_{bd})} \exp\left(-\beta E^{tot}(\xi, \vec{l}_{bd})\right) \pi^0_{(\xi, \vec{l}_{bd})} \tag{3.17}$$

with a remaining steady-state-probability distribution $\pi^0_{(\xi, \vec{l}_{bd})}$ required to satisfy the boundary conditions. The infinite number of periodic replicas of the charge carriers enforces, that the steady-state-probability distribution $\pi_{(\xi, \vec{l}_{bd})}$ does not depend on the number of boundary crossings $\vec{l}_{bd}$.

$$\pi_{(\xi, \vec{l}_{bd})} = \pi_{(\xi, \vec{l}'_{bd})} = \pi_\xi \quad \forall \vec{l}_{bd}, \vec{l}'_{bd} \in \mathbb{Z}^3 \tag{3.18}$$

with the steady-state-probability distribution π_ξ that we are looking for. This boundary condition, Equation (3.18), for the infinite-dimensional configuration space introduces a restriction for the remaining steady-state-probability distribution $\pi^0_{(\xi, \vec{l}_{bd})}$:

$$\begin{aligned} \pi_{(\xi, \vec{l}_{bd})} = \frac{1}{Z} \exp\left(-\beta \left(E^{tot}(\xi) + e\vec{L}_{bd}\vec{F}\right)\right) \pi^0_{(\xi, \vec{l}_{bd})} = \frac{1}{Z} \exp\left(-\beta \left(E^{tot}(\xi) + e\vec{L}'_{bd}\vec{F}\right)\right) \pi^0_{(\xi, \vec{l}'_{bd})} = \pi_{(\xi, \vec{l}'_{bd})} \\ \Rightarrow \quad \pi^0_{(\xi, \vec{l}_{bd})} = \pi^0_{(\xi, \vec{l}'_{bd})} \exp\left(\beta e(\vec{L}_{bd} - \vec{L}'_{bd})\vec{F}\right) = \pi^0_\xi \exp\left(\beta e\vec{L}_{bd}\vec{F}\right). \end{aligned} \tag{3.19}$$

A further assumption containing the remaining steady-state-probability distribution π^0_ξ of

$$\pi^0_\xi = \exp\left(\beta \sum_{i \in \xi} e\vec{r}_i \vec{F}\right) \pi^c_\xi \quad \text{with} \quad \pi^c_\xi = \exp\left(\beta E^c_\xi\right) \tag{3.20}$$

finally introduces the configuration-dependent correction energy E^c_ξ and its corresponding term π^c_ξ contributing to the probability π_ξ. With all those assumptions, we come back to the global balance equation, Equation (3.9), and plug in Equation (3.17).

$$\sum_{(\xi',\vec{l}'_{bd})\neq(\xi,\vec{l}_{bd})} \frac{1}{Z}\pi^0_{(\xi,\vec{l}_{bd})} \exp\left(-\beta E^{tot}(\xi,\vec{l}_{bd})\right) q_{(\xi,\vec{l}_{bd})(\xi',\vec{l}'_{bd})} = \\ = \sum_{(\xi',\vec{l}'_{bd})\neq(\xi,\vec{l}_{bd})} \frac{1}{Z}\pi^0_{(\xi',\vec{l}'_{bd})} \exp\left(-\beta E^{tot}(\xi',\vec{l}'_{bd})\right) q_{(\xi',\vec{l}'_{bd})(\xi,\vec{l}_{bd})} \quad (3.21)$$

Now we make use of the local balance equation in the infinite configuration space, Equation (3.16), and the relation $\pi^0_{(\xi,\vec{l}_{bd})} = \pi^0_\xi \exp\left(\beta e\vec{L}_{bd}\vec{F}\right)$ from Equation (3.19).

$$\sum_{(\xi',\vec{l}'_{bd})\neq(\xi,\vec{l}_{bd})} \frac{1}{Z}\pi^0_\xi \exp\left(\beta e\vec{L}_{bd}\vec{F}\right) \exp\left(-\beta E^{tot}(\xi,\vec{l}_{bd})\right) q_{(\xi,\vec{l}_{bd})(\xi',\vec{l}'_{bd})} = \\ = \sum_{(\xi',\vec{l}'_{bd})\neq(\xi,\vec{l}_{bd})} \frac{1}{Z}\pi^0_{\xi'} \exp\left(\beta e\vec{L}'_{bd}\vec{F}\right) \exp\left(-\beta E^{tot}(\xi,\vec{l}_{bd})\right) q_{(\xi,\vec{l}_{bd})(\xi',\vec{l}'_{bd})} \quad (3.22)$$

With some rearrangements within this equation, relation $q_{(\xi,\vec{l}_{bd})(\xi,\vec{l}_{bd})} = -\sum_{(\xi',\vec{l}'_{bd})\neq(\xi,\vec{l}_{bd})} q_{(\xi,\vec{l}_{bd})(\xi',\vec{l}'_{bd})}$ from Equation (3.8), and inserting the assumption for π^0_ξ from Equation (3.20), we receive

$$-\pi^c_\xi \exp\left(\beta \sum_{k\in\xi} e\vec{r}_k\vec{F}\right) q_{(\xi,\vec{l}_{bd})(\xi,\vec{l}_{bd})} = \\ = \sum_{(\xi',\vec{l}'_{bd})\neq(\xi,\vec{l}_{bd})} \pi^c_{\xi'} \exp\left(\beta \sum_{k'\in\xi'} e\vec{r}_{k'}\vec{F}\right) \exp\left(\beta e(\vec{L}'_{bd}-\vec{L}_{bd})\vec{F}\right) q_{(\xi,\vec{l}_{bd})(\xi',\vec{l}'_{bd})}. \quad (3.23)$$

Collecting all field dependent terms and some further rearrangements give

$$0 = \sum_{(\xi',\vec{l}'_{bd})\neq(\xi,\vec{l}_{bd})} \pi^c_{\xi'} \exp\left(\beta e\left(\sum_{k'\in\xi'} \vec{r}_{k'} + \vec{L}'_{bd} - \sum_{k\in\xi} \vec{r}_k - \vec{L}_{bd}\right)\vec{F}\right) q_{(\xi,\vec{l}_{bd})(\xi',\vec{l}'_{bd})} + \pi^c_\xi q_{(\xi,\vec{l}_{bd})(\xi,\vec{l}_{bd})}. \quad (3.24)$$

The term in the inner brackets is exactly the distance

$$\Delta\vec{r}_{ij} = \sum_{k'\in\xi'} \vec{r}_{k'} + \vec{L}'_{bd} - \sum_{k\in\xi} \vec{r}_k - \vec{L}_{bd} = \vec{r}_j - \vec{r}_i + \vec{L}'_{bd} - \vec{L}_{bd} \quad (3.25)$$

associated with the hop from site i to site j, respecting the boundary conditions, which is performed during the transition from configuration ξ to configuration ξ', cf. Equation (3.7). All terms $k \neq i$ and $k' \neq j$ of charge carriers that do not move during the hop cancel out and the difference $\vec{L}'_{bd} - \vec{L}_{bd}$ provides the required correction of the distance when a boundary is crossed during the hop.

Entries in the Q-matrix for different values of $\vec{l}_{bd}$ and $\vec{l}'_{bd}$ are all the same $q_{(\xi,\vec{l}_{bd})(\xi',\vec{l}'_{bd})} = q_{\xi\xi'}$ and the infinite-dimensional system of equations, Equation (3.24), provides always the same equations for different values of $\vec{l}_{bd}$. So we can reduce the configuration space back to our initial finite size

$$0 = \sum_{\xi'\neq\xi} \pi^c_{\xi'} \exp\left(\beta e\Delta\vec{r}_{ij}\vec{F}\right) q_{\xi\xi'} + \pi^c_\xi q_{\xi\xi} \quad (3.26)$$

and introduce a modified Q-matrix $\tilde{Q} = (\tilde{q}_{\xi\xi'})$ given by

$$\tilde{q}_{\xi\xi'} = \begin{cases} \exp\left(\beta e \Delta\vec{r}_{ij}\vec{F}\right) R_{ij}(\xi) & \text{if } \forall ij\ \exists R_{ij}(\xi) \neq 0 \text{ linking } \xi \text{ and } \xi' \\ q_{\xi\xi} & \text{if } \xi = \xi' \\ 0 & \text{else} \end{cases} \tag{3.27}$$

with the off-diagonal elements containing an additional factor $\exp\left(\beta e \Delta\vec{r}_{ij}\vec{F}\right)$ due to the electric field $\vec{F}$ and the main diagonal not being modified $\tilde{q}_{\xi\xi} = q_{\xi\xi}$. Finally, this results in an alternative form of the global balance equation

$$\tilde{Q}\vec{\pi}^c = 0 \quad \text{with} \quad \vec{\pi}^c = (\pi^c_\xi) \quad \text{and} \quad \pi^c_\xi = \exp\left(\beta E^c_\xi\right) \tag{3.28}$$

which has to be solved to receive the correction energies E^c_ξ

3.1.5 Example for the Modification of the Rates

As an illustrative example for the modification of the Q-matrix by the electric field, the modified Q-matrix for a single charge carrier simulation of the one-dimensional system shown in Figure 3.1 is derived. This system has five different configurations, illustrated in Figure 3.2. As we have only one charge carrier in the simulation, the specification of the configuration ξ is given by the site number i that is occupied $\xi = i \in \{1,2,3,4,5\}$.

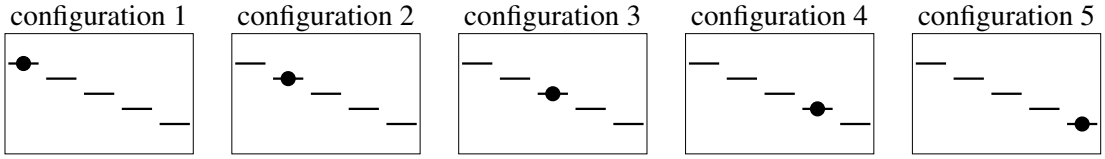

Figure 3.2: Possible configurations for the system introduced in Figure 3.1 with only a single charge carrier $N_{cc} = 1$ in the system.

If we allow only nearest neighbour hopping, the initial Q-matrix contains only rates R_{ij} of neighbouring sites, respecting the boundaries.

$$Q = \begin{pmatrix} -R_{12}-R_{15} & R_{12} & 0 & 0 & R_{15} \\ R_{21} & -R_{21}-R_{23} & R_{23} & 0 & 0 \\ 0 & R_{32} & -R_{32}-R_{34} & R_{34} & 0 \\ 0 & 0 & R_{43} & -R_{43}-R_{45} & R_{45} \\ R_{51} & 0 & 0 & R_{54} & -R_{54}-R_{51} \end{pmatrix} \tag{3.29}$$

To get the modified Q-matrix, defined in Equation (3.27), off-diagonal terms of the initial Q-matrix have to be multiplied by the term $\exp\left(\beta e \Delta\vec{r}_{ij}\vec{F}\right)$. This term is $\exp(-\beta eaF)$ for hops to the right towards lower energies and $\exp(\beta eaF)$ for hops to the left towards higher energies with the distance between

two neighbouring sites a and the absolute value of the electric field strength F.

$$\tilde{Q} = \begin{pmatrix} -R_{12}-R_{15} & \exp(-\beta eaF)R_{12} & 0 & 0 & \exp(\beta eaF)R_{15} \\ \exp(\beta eaF)R_{21} & -R_{21}-R_{23} & \exp(-\beta eaF)R_{23} & 0 & 0 \\ 0 & \exp(\beta eaF)R_{32} & -R_{32}-R_{34} & \exp(-\beta eaF)R_{34} & 0 \\ 0 & 0 & \exp(\beta eaF)R_{43} & -R_{43}-R_{45} & \exp(-\beta eaF)R_{45} \\ \exp(-\beta eaF)R_{51} & 0 & 0 & \exp(\beta eaF)R_{54} & -R_{54}-R_{51} \end{pmatrix} \tag{3.30}$$

3.1.6 Site- and Correlation-Correction Energies

With Equations (3.8), (3.27) and (3.28), we are theoretically able to calculate configuration-correction energies E^c_ξ for each configuration ξ and get the corresponding steady-state-probability distribution π_ξ. Combining Equations (3.15), (3.17), (3.18), (3.19) and (3.20), the steady-state-probability distribution π_ξ is given by

$$\pi_\xi = \frac{1}{Z}\exp\left[-\beta\left(\sum_{i\in\xi}\varepsilon_i + \frac{1}{2}\sum_{i\in\xi}\sum_{j\in\xi}^{j\neq i} E^{int}_{ij} - E^c_\xi\right)\right] \quad \text{with} \quad Z = \sum_{\xi\in\Xi}\pi_\xi. \tag{3.31}$$

The number of configurations rapidly explodes already for very low numbers of charge carriers N_{cc}. For a very small system of $10\times10\times10$ sites and $N_{cc}=3$ charge carriers, the number of configurations is $N_{cnfg}\approx 1.7\cdot10^8$ and for $N_{cc}=4$ charge carriers $N_{cnfg}\approx 4.1\cdot10^{10}$. The exponential increase in the number of configurations and the corresponding order of the system of linear equations that has to be solve impedes the applicability of directly calculating E^c_ξ already for very low numbers of charge carriers.

To make use of correction energies E^c_ξ, we need to introduce approximations. As an approximation for low numbers of charge carriers, we write the configuration-correction energies E^c_ξ as a series

$$E^c_\xi \approx \sum_{i\in\xi} E^c_i + \frac{1}{2}\sum_{i\in\xi}\sum_{j\in\xi}^{j\neq i} E^c_{ij} + \dots \tag{3.32}$$

with the site-correction energies E^c_i of site i and the correlation-correction energies E^c_{ij} considering correlations of the correction energies between site i and site j.

The site-correction energies E^c_i are calculated by placing only one charge carrier in the simulated system $N_{cc}=1$. In this case, the configuration ξ is given by the site index $\xi=i$ and the Q-matrix has the dimension of the number of sites N_s. The associated global balance equation is small enough to be numerically solvable. In many cases, calculating E^c_i is already an appropriate approximation for the configuration-correction energies E^c_ξ, especially for low charge-carrier densities and/or low electric fields (cf. Chapter 3.4).

If approximating the configuration-correction energies E^c_ξ by a sum over the corresponding site-correction energies E^c_i is not accurate enough, correlation-correction energies E^c_{ij} can be calculated for rather small systems. In this case, the number of configurations and, hence, the order of the linear system of equation that has to be solved is $\frac{1}{2}N_s(N_s-1)$. Going beyond correlation-correction energies is, commonly, neither necessary regarding accuracy of the results, nor computationally reasonable.

3.2 Occupation Statistics and Mobility

In Chapter 3.1, we derived an equation to calculate site-correction energies E_i^c and correlation-correction energies E_{ij}^c via a modification of the so-called global balance equation, Equation (3.28), to approximate the configuration-correction energy E_ξ^c via Equation (3.32). With this correction energy and Equation (3.31), the steady-state-probability distribution π_ξ can be approximated by

$$\pi_\xi = \frac{1}{Z}\exp\left[-\beta\sum_{i\in\xi}\left(\varepsilon_i - E_i^c + \frac{1}{2}\sum_{j\in\xi}^{j\neq i}\left(E_{ij}^{int} - E_{ij}^c\right)\right)\right] = \frac{1}{Z}\exp\left[-\beta\sum_{i\in\xi}\left(E_i^{tot} + \frac{1}{2}\sum_{j\in\xi}^{j\neq i}E_{ij}^{tot}\right)\right]$$
$$\text{with} \quad Z = \sum_{\xi\in\Xi}\pi_\xi \tag{3.33}$$

introducing the total site energy $E_i^{tot} = \varepsilon_i - E_i^c$ and the total interaction energy $E_{ij}^{tot} = E_{ij}^{int} - E_{ij}^c$.

In the following, we will derive an expression for the mobility considering different occupation statistics. In Chapter 3.2.1, Boltzmann statistics is used to calculate the mobility for a system with only one charge carrier. When two charge carriers are present in the simulation, the configuration space is low-dimensional enough to enable an evaluation of all configurations to calculate the mobility, which is demonstrated in Chapter 3.2.2. For high charge-carrier densities, Fermi-Dirac statistics is an adequate approximation for receiving the mobility in Chapter 3.2.3. To enable the inclusion of correlations and interactions in future, a new occupation statistics was derived and investigated in Chapter 3.2.4.

3.2.1 Boltzmann Statistics

With only one charge carrier in the simulation, the steady-state-probability distribution π_ξ holds the probability π_i that site $i = \xi$ is occupied, which is also the charge-carrier density $\langle n_i\rangle = \pi_i$ of site i in charge carriers per site (ccps). So the charge-carrier density $\langle n_i\rangle$ of site i is given by the Boltzmann statistics

$$\langle n_i\rangle = \sum_{\xi\in\Xi}\pi_\xi n_i^\xi = \frac{1}{Z}\exp\left(-\beta E_i^{tot}\right) \quad \text{with} \quad Z = \sum_{i=1}^{N_s}\exp\left(-\beta E_i^{tot}\right) \tag{3.34}$$

with the occupation $n_i^\xi \in \{0,1\}$ of site i in configuration ξ being occupied $n_i^\xi = 1$ ccps or unoccupied $n_i^\xi = 0$ ccps. In general, the mobility can be calculated from the steady-state-probability π_ξ

$$\mu = \sum_{\xi\in\Xi}\pi_\xi\sum_{i=1}^{N_s}\sum_{\substack{j=1\\ j\neq i}}^{N_s}R_{ij}(\xi)\frac{q\Delta\vec{r}_{ij}\vec{F}}{F^2} \tag{3.35}$$

with $q \in \{-1,1\}$ specifying the sign of the charge carrier (electron or hole). The rate $R_{ij}(\xi)$ can only be non-zero if site i is occupied $n_i^\xi = 1$ ccps in state ξ and site j is unoccupied $1 - n_j^\xi = 1$ ccps, so that:

$$\mu = \sum_{i=1}^{N_s}\sum_{\substack{j=1\\ j\neq i}}^{N_s}\frac{q\Delta\vec{r}_{ij}\vec{F}}{F^2}\sum_{\xi\in\Xi}\pi_\xi n_i^\xi\left(1 - n_j^\xi\right)R_{ij}(\xi). \tag{3.36}$$

If only one charge carrier is in the system or the total interaction energy $E_{ij}^{tot} = 0$ eV is vanishing, the rate $R_{ij}(\xi)$ does not depend on the initial state ξ. As a consequence, R_{ij} can be moved in front of the sum

over ξ in Equation (3.36) and with the relations

$$\langle n_i \rangle = \sum_{\xi \in \Xi} \pi_\xi n_i^\xi \quad \text{and} \quad \langle n_i n_j \rangle = \sum_{\xi \in \Xi} \pi_\xi n_i^\xi n_j^\xi, \tag{3.37}$$

the mobility can be calculated by

$$\mu = \sum_{i=1}^{N_s} \sum_{\substack{j=1 \\ j \neq i}}^{N_s} \frac{q \Delta \vec{r}_{ij} \vec{F}}{F^2} R_{ij} \left(\langle n_i \rangle - \langle n_i n_j \rangle \right). \tag{3.38}$$

For only one charge carrier in the simulation, the two-site occupation $\langle n_i n_j \rangle = 0$ ccps is zero, because one charge carrier cannot occupy two sites i and j at the same time. Overall, the mobility for a single-charge-carrier simulation is calculated by

$$\mu = \sum_{i=1}^{N_s} \sum_{\substack{j=1 \\ j \neq i}}^{N_s} \frac{q \Delta \vec{r}_{ij} \vec{F}}{F^2} R_{ij} \langle n_i \rangle \quad \text{with} \quad \langle n_i \rangle = \frac{1}{Z} \exp\left(-\beta E_i^{tot}\right) \quad \text{and} \quad Z = \sum_{i=1}^{N_s} \exp\left(-\beta E_i^{tot}\right). \tag{3.39}$$

When the total site energy $E_i^{tot} = \varepsilon_i - E_i^c$ contains the accurate site-correction energies E_i^c, the mobility given by Equation (3.39) is exactly the correct solution.

3.2.2 Considering Configurations for Two Charge Carriers

The configuration space of a system with two charge carriers is still manageable from a computational point of view. It is a perfect system to test the effect of, (i), interactions $E_{ij}^{int} \neq 0$ eV and, (ii), correlation-correction energies E_{ij}^c because it is possible to calculate the numerically correct solution of the mobility for this system.

A configuration in this system is given by $\xi = (i_1, i_2)$ with i_1 and i_2 being the occupied sites. The steady-state-probability density π_ξ is given by

$$\pi_\xi = \pi_{(i_1,i_2)} = \frac{1}{Z} \exp\left[-\beta \left(E_{i_1}^{tot} + E_{i_2}^{tot} + E_{i_1 i_2}^{tot}\right)\right]$$
$$\text{with} \quad Z = \sum_{i_1=1}^{N_s-1} \sum_{i_2=i_1+1}^{N_s} \exp\left[-\beta \left(E_{i_1}^{tot} + E_{i_2}^{tot} + E_{i_1 i_2}^{tot}\right)\right] \tag{3.40}$$

The mobility can be calculated from Equation (3.36) when considering $n_i^{(i_1,i_2)} = \delta_{ii_1} + \delta_{ii_2}$ with the Kronecker delta $\delta_{ij} = 1$ if $i = j$ and $\delta_{ij} = 0$ else.

$$\begin{aligned}
\mu &= \sum_{i=1}^{N_s} \sum_{\substack{j=1 \\ j \neq i}}^{N_s} \sum_{i_1=1}^{N_s-1} \sum_{i_2=i_1+1}^{N_s} \frac{q \Delta \vec{r}_{ij} \vec{F}}{F^2} \pi_{(i_1,i_2)} \left(\delta_{ii_1} + \delta_{ii_2}\right) \left(1 - \delta_{ji_1} - \delta_{ji_2}\right) R_{ij}(i_1, i_2) \\
&= \sum_{i_1=1}^{N_s-1} \sum_{i_2=i_1+1}^{N_s} \sum_{\substack{j=1 \\ j \neq i_1 \\ j \neq i_2}}^{N_s} \frac{q \Delta \vec{r}_{i_1 j} \vec{F}}{F^2} \pi_{(i_1,i_2)} R_{i_1 j}(i_1, i_2) + \frac{q \Delta \vec{r}_{i_2 j} \vec{F}}{F^2} \pi_{(i_1,i_2)} R_{i_2 j}(i_1, i_2) \\
&= \frac{q}{F^2} \sum_{i_1=1}^{N_s-1} \sum_{i_2=i_1+1}^{N_s} \pi_{(i_1,i_2)} \sum_{\substack{j=1 \\ j \neq i_1 \\ j \neq i_2}}^{N_s} \left[\left(\Delta \vec{r}_{i_1 j} \vec{F}\right) R_{i_1 j}(i_1, i_2) + \left(\Delta \vec{r}_{i_2 j} \vec{F}\right) R_{i_2 j}(i_1, i_2) \right]
\end{aligned} \tag{3.41}$$

3.2.3 Fermi-Dirac Statistics

When more than two charge carriers are in the simulated system, considering all configurations immediately becomes computationally far too expensive. An affordable alternative is to utilise Fermi-Dirac statistics. We will derive Fermi-Dirac statistics in the following as a reminder for the interested reader and to introduce the nomenclature that will be extensively used in Chapter 3.2.4.

The partition function for a system with N_s sites collected in the set $\mathcal{N}_s = \{1,2,\ldots,N_s\}$ and N_{cc} charge carriers is denominated as

$$Z_{\mathcal{N}_s}^{N_{cc}} = \sum_{\xi \in \Xi_{\mathcal{N}_s}^{N_{cc}}} \exp\left(-\beta \sum_{k \in \mathcal{N}_s} n_k^{\xi} E_k^{tot}\right) \tag{3.42}$$

with the configuration space $\Xi_{\mathcal{N}_s}^{N_{cc}}$ for a system with a set of $\mathcal{N}_s = \{1,2,\ldots,N_s\}$ sites and N_{cc} charge carriers.

In Fermi-Dirac statistics, the total interaction energies E_{ij}^{tot} have to be omitted. Considering the novel occupation statistics derived in Chapter 3.2.4, an approximate but direct inclusion of interactions is, in principle, possible. Nevertheless, within this thesis, we neglect the total interaction energies E_{ij}^{tot} also for the novel occupation statistics. Interactions in both cases can be approximately included via a mean-field (MF) approach (cf. Chapter 3.3.1).

Looking at the sum over all configurations ξ in Equation (3.42), we can select one arbitrary site i and explicitly sum over the possible configurations of this site, which are $n_i = 0$ ccps if it is unoccupied and $n_i = 1$ ccps if it is occupied. The remaining configuration space does not contain site i any longer and has one charge carrier less, if site i is occupied.

$$Z_{\mathcal{N}_s}^{N_{cc}} = \sum_{n_i=0}^{1} \exp\left(-\beta n_i E_i^{tot}\right) \underbrace{\sum_{\xi \in \Xi_{\mathcal{N}_s \setminus \{i\}}^{N_{cc}-n_i}} \exp\left(-\beta \sum_{k \in \mathcal{N}_s \setminus \{i\}} n_k^{\xi} E_k^{tot}\right)}_{=Z_{\mathcal{N}_s \setminus \{i\}}^{N_{cc}-n_i}} \tag{3.43}$$

The inner sum corresponds to the partition function $Z_{\mathcal{N}_s \setminus \{i\}}^{N_{cc}-n_i}$ of the reduced system that does not contain site i and has n_i charge carriers less than the full system. Performing the outer sum over n_i results in

$$Z_{\mathcal{N}_s}^{N_{cc}} = Z_{\mathcal{N}_s \setminus \{i\}}^{N_{cc}} + \exp\left(-\beta E_i^{tot}\right) Z_{\mathcal{N}_s \setminus \{i\}}^{N_{cc}-1}. \tag{3.44}$$

To get the site occupation $\langle n_i \rangle_{\mathcal{N}_s}^{N_{cc}}$ of the system with a set of $\mathcal{N}_s$ sites and N_{cc} charge carriers, the steady-state-probability distribution π_{ξ}, cf. Equation (3.33), is required.

$$\langle n_i \rangle_{\mathcal{N}_s}^{N_{cc}} = \frac{1}{Z_{\mathcal{N}_s}^{N_{cc}}} \sum_{\xi \in \Xi_{\mathcal{N}_s}^{N_{cc}}} n_i^{\xi} \exp\left(-\beta \sum_{k \in \mathcal{N}_s} n_k^{\xi} E_k^{tot}\right) \tag{3.45}$$

The same splitting of the sum as in Equations (3.43) and (3.44) provides

$$\langle n_i \rangle_{\mathcal{N}_s}^{N_{cc}} = \frac{1}{Z_{\mathcal{N}_s}^{N_{cc}}} \exp\left(-\beta E_i^{tot}\right) Z_{\mathcal{N}_s \setminus \{i\}}^{N_{cc}-1} \tag{3.46}$$

and replacing $Z_{\mathcal{N}_s}^{N_{cc}}$ by Equation (3.44) leads to

$$\langle n_i \rangle_{\mathcal{N}_s}^{N_{cc}} = \frac{1}{1 + \frac{Z_{\mathcal{N}_s \setminus \{i\}}^{N_{cc}}}{Z_{\mathcal{N}_s \setminus \{i\}}^{N_{cc}-1}} \exp\left(\beta E_i^{tot}\right)} \tag{3.47}$$

At this point, the approximation made within Fermi-Dirac statistics comes into play. The ratio

$$\frac{Z_{\mathcal{N}_s \setminus \{i\}}^{N_{cc}}}{Z_{\mathcal{N}_s \setminus \{i\}}^{N_{cc}-1}} \approx \exp\left(-\beta E_{F,0}^{N_{cc}}\right) \approx \frac{Z_{\mathcal{N}_s}^{N_{cc}}}{Z_{\mathcal{N}_s}^{N_{cc}-1}} \tag{3.48}$$

is approximated by a so-called Fermi level $E_{F,0}^{N_{cc}}$ for a system of N_{cc} charge carriers including all sites $\mathcal{N}_s$. We indicate the omittance of the dependence on the site i of the Fermi level $E_{F,0}^{N_{cc}}$ by the zero in the subscript. The key of the approximation is, that the ratio does not depend on the site i that is taken out of the system. This approximation is feasible for large systems with many charge carriers and densely lying energies at the Fermi level. Applying the approximation, we end up with the familiar form of the Fermi-Dirac statistics:

$$\langle n_i \rangle_{\mathcal{N}_s}^{N_{cc}} = \frac{1}{1 + \exp\left[\beta\left(E_i^{tot} - E_{F,0}^{N_{cc}}\right)\right]}. \tag{3.49}$$

Within this approximation, the Fermi level $E_{F,0}^{N_{cc}}$ can be determined by the implicit equation

$$N_{cc} = \sum_{i \in \mathcal{N}_s} \langle n_i \rangle_{\mathcal{N}_s}^{N_{cc}} \tag{3.50}$$

guaranteeing the correct number of charge carriers N_{cc} in the system.

To get the mobility μ, Equation (3.38) can be applied, because the rates R_{ij} do not change when no interactions are present. The remaining unknown in this Equation (3.38) for the mobility μ is the two-site occupation $\langle n_i n_j \rangle_{\mathcal{N}_s}^{N_{cc}}$:

$$\langle n_i n_j \rangle_{\mathcal{N}_s}^{N_{cc}} = \frac{1}{Z_{\mathcal{N}_s}^{N_{cc}}} \sum_{\xi \in \Xi_{\mathcal{N}_s}^{N_{cc}}} n_i^{\xi} n_j^{\xi} \exp\left(-\beta \sum_{k \in \mathcal{N}_s} n_k^{\xi} E_k^{tot}\right) = \frac{\exp\left[-\beta\left(E_i^{tot} + E_j^{tot}\right)\right] Z_{\mathcal{N}_s \setminus \{i,j\}}^{N_{cc}-2}}{Z_{\mathcal{N}_s}^{N_{cc}}}. \tag{3.51}$$

The second equality in the above relation is achieved by splitting the sum over the configurations for n_i, n_j and the remaining configuration space $\Xi_{\mathcal{N}_s \setminus \{i,j\}}^{N_{cc}-n_i-n_j}$ exactly in the same way as above for $Z_{\mathcal{N}_s}^{N_{cc}}$ in Equation (3.43). The partition function $Z_{\mathcal{N}_s \setminus \{i,j\}}^{N_{cc}-2}$ can be rewritten with the help of a variation of Equation (3.44)

$$\frac{\begin{array}{r} Z_{\mathcal{N}_s \setminus \{i\}}^{N_{cc}-1} = Z_{\mathcal{N}_s \setminus \{i,j\}}^{N_{cc}-1} + Z_{\mathcal{N}_s \setminus \{i,j\}}^{N_{cc}-2} \exp\left(-\beta E_j^{tot}\right) \\ Z_{\mathcal{N}_s \setminus \{j\}}^{N_{cc}-1} = Z_{\mathcal{N}_s \setminus \{i,j\}}^{N_{cc}-1} + Z_{\mathcal{N}_s \setminus \{i,j\}}^{N_{cc}-2} \exp\left(-\beta E_i^{tot}\right) \end{array} \Big] \ominus}{Z_{\mathcal{N}_s \setminus \{i\}}^{N_{cc}-1} - Z_{\mathcal{N}_s \setminus \{j\}}^{N_{cc}-1} = Z_{\mathcal{N}_s \setminus \{i,j\}}^{N_{cc}-2}\left(\exp(-\beta E_j^{tot}) - \exp(-\beta E_i^{tot})\right)} \tag{3.52}$$

yielding

$$Z^{N_{cc}-2}_{\mathcal{N}_s\setminus\{i,j\}} = \frac{Z^{N_{cc}-1}_{\mathcal{N}_s\setminus\{i\}} - Z^{N_{cc}-1}_{\mathcal{N}_s\setminus\{j\}}}{\exp(-\beta E^{tot}_j) - \exp(-\beta E^{tot}_i)}. \tag{3.53}$$

Combining Equations (3.51) and (3.53) leads to

$$\langle n_i n_j \rangle^{N_{cc}}_{\mathcal{N}_s} = \frac{\frac{Z^{N_{cc}-1}_{\mathcal{N}_s\setminus\{i\}}}{Z^{N_{cc}}_{\mathcal{N}_s}} - \frac{Z^{N_{cc}-1}_{\mathcal{N}_s\setminus\{j\}}}{Z^{N_{cc}}_{\mathcal{N}_s}}}{\exp(\beta E^{tot}_i) - \exp(\beta E^{tot}_j)}. \tag{3.54}$$

The ratios of the partition functions can be identified as site occupations in the spirit of Equation (3.46) and we finally receive

$$\langle n_i n_j \rangle^{N_{cc}}_{\mathcal{N}_s} = \frac{\langle n_i \rangle^{N_{cc}}_{\mathcal{N}_s} \exp(\beta E^{tot}_i) - \langle n_j \rangle^{N_{cc}}_{\mathcal{N}_s} \exp(\beta E^{tot}_j)}{\exp(\beta E^{tot}_i) - \exp(\beta E^{tot}_j)}. \tag{3.55}$$

This derivation for $\langle n_i n_j \rangle^{N_{cc}}_{\mathcal{N}_s}$ does not contain any approximations, it provides exactly the correct two-site occupation $\langle n_i n_j \rangle^{N_{cc}}_{\mathcal{N}_s}$ for a non-interacting system $E^{tot}_{ij} = 0$ eV if the correct site occupations $\langle n_i \rangle^{N_{cc}}_{\mathcal{N}_s}$ are known. As a side note, for the site occupation $\langle n_i \rangle^{1}_{\mathcal{N}_s}$ determined by the Boltzmann statistics, Equation (3.34), we get $\langle n_i n_j \rangle^{1}_{\mathcal{N}_s} = 0$ ccps from Equation (3.55), i.e., the correct result.

Inserting the site occupation $\langle n_i \rangle^{N_{cc}}_{\mathcal{N}_s}$ received from the approximation made within the framework of Fermi-Dirac statistics, given by Equation (3.49), into Equation (3.55) provides

$$\begin{aligned}
\langle n_i n_j \rangle^{N_{cc}}_{\mathcal{N}_s} &= \frac{\frac{\exp(\beta E^{tot}_i)}{1+\exp\left[\beta\left(E^{tot}_i - E^{N_{cc}}_{F,0}\right)\right]} - \frac{\exp(\beta E^{tot}_j)}{1+\exp\left[\beta\left(E^{tot}_j - E^{N_{cc}}_{F,0}\right)\right]}}{\exp(\beta E^{tot}_i) - \exp(\beta E^{tot}_j)} = \\
&= \frac{\exp(\beta E^{tot}_i) + \exp\left[\beta\left(E^{tot}_i + E^{tot}_j - E^{N_{cc}}_{F,0}\right)\right] - \exp(\beta E^{tot}_j) - \exp\left[\beta\left(E^{tot}_i + E^{tot}_j - E^{N_{cc}}_{F,0}\right)\right]}{\left(1+\exp\left[\beta\left(E^{tot}_i - E^{N_{cc}}_{F,0}\right)\right]\right)\left(1+\exp\left[\beta\left(E^{tot}_j - E^{N_{cc}}_{F,0}\right)\right]\right)\left(\exp(\beta E^{tot}_i) - \exp(\beta E^{tot}_j)\right)} = \\
&= \frac{1}{\left(1+\exp\left[\beta\left(E^{tot}_i - E^{N_{cc}}_{F,0}\right)\right]\right)\left(1+\exp\left[\beta\left(E^{tot}_j - E^{N_{cc}}_{F,0}\right)\right]\right)} = \langle n_i \rangle^{N_{cc}}_{\mathcal{N}_s} \langle n_j \rangle^{N_{cc}}_{\mathcal{N}_s}.
\end{aligned} \tag{3.56}$$

This relation $\langle n_i n_j \rangle = \langle n_i \rangle \langle n_j \rangle$, which is only valid for Fermi-Dirac statistics, demonstrates the fact that Fermi-Dirac statistics assumes an entirely uncorrelated system. So, the approximations within Fermi-Dirac statistics neglect all correlations. Although we do not include interactions E^{tot}_{ij}, site exclusion (allowing for at maximum one charge carrier per site) introduces correlations that cannot be accounted for within the framework of Fermi-Dirac statistics.

3.2.4 Going Beyond Fermi-Dirac Statistics

Fermi-Dirac statistics, by construction, does not include any correlations. Hence, refining Fermi-Dirac statistics is not advisable to include interactions. To be able to include interactions and associated correlations in future, we have derived a relation for the exact occupation statistics of a non-interacting system. This relation enables to numerically calculate the correct site occupation $\langle n_i \rangle^{N_{cc}}_{\mathcal{N}_s}$, given that $E^{tot}_{ij} = 0$ eV. With $\langle n_i \rangle^{N_{cc}}_{\mathcal{N}_s}$, also $\langle n_i n_j \rangle^{N_{cc}}_{\mathcal{N}_s}$ can be correctly calculated via Equation (3.55) and with this, the numerically correct value for the mobility μ can be received from Equation (3.38).

Starting point is Equation (3.47). But instead of applying the approximation leading to Equation (3.48), we introduce a site dependent Fermi level $E_{F,i}^{N_{cc}}$ defined by

$$\exp\left(-\beta E_{F,i}^{N_{cc}}\right) = \frac{Z_{\mathcal{N}_s\setminus\{i\}}^{N_{cc}}}{Z_{\mathcal{N}_s\setminus\{i\}}^{N_{cc}-1}}. \tag{3.57}$$

With this definition, we get the correct site occupation

$$\langle n_i\rangle_{\mathcal{N}_s}^{N_{cc}} = \frac{1}{1+\exp\left[\beta\left(E_i^{tot}-E_{F,i}^{N_{cc}}\right)\right]} \tag{3.58}$$

as long as we determine the correct *local* Fermi level $E_{F,i}^{N_{cc}}$. Besides the *local* Fermi level, we define a *global* Fermi level $E_{F,0}^{N_{cc}}$ closely related to the Fermi level introduced by the Fermi-Dirac formalism:

$$\exp\left(-\beta E_{F,0}^{N_{cc}}\right) = \frac{Z_{\mathcal{N}_s}^{N_{cc}}}{Z_{\mathcal{N}_s}^{N_{cc}-1}}. \tag{3.59}$$

Another definition

$$\Delta E_{F,i}^{N_{cc}} = E_{F,i}^{N_{cc}} - E_{F,0}^{N_{cc}} \tag{3.60}$$

introduces the *local* change in Fermi level or Fermi-level shift $\Delta E_{F,i}^{N_{cc}}$ of site i with respect to the *global* Fermi level $E_{F,0}^{N_{cc}}$.

This new occupation statistics is designed to cover the full range of possible numbers of charge carriers from $N_{cc}=1$ up to very high numbers of charge carriers. So it has to include Boltzmann statistics exactly for $N_{cc}=1$ and approach Fermi-Dirac statistics for increasing N_{cc}. With the definition

$$Z_{\mathcal{N}_s}^{0} = Z_{\mathcal{N}_s\setminus\{i\}}^{0} = 1 \tag{3.61}$$

and Equation (3.59), we can calculate $E_{F,0}^{1}$:

$$\exp\left(-\beta E_{F,0}^{1}\right) = Z_{\mathcal{N}_s}^{1} = \sum_{i\in\mathcal{N}_s}\exp\left(-\beta E_i^{tot}\right) \quad\Rightarrow\quad E_{F,0}^{1} = -k_B T\ln\left(\sum_{i\in\mathcal{N}_s}\exp\left(-\beta E_i^{tot}\right)\right). \tag{3.62}$$

The local Fermi level $E_{F,i}^{1}$ is received from combining Equations (3.34) and (3.58).

$$\langle n_i\rangle_{\mathcal{N}_s}^{1} = \frac{1}{1+\exp\left[\beta\left(E_i^{tot}-E_{F,i}^{1}\right)\right]} = \frac{\exp\left(-\beta E_i^{tot}\right)}{\sum_{i\in\mathcal{N}_s}\exp\left(-\beta E_i^{tot}\right)}$$

$$\Rightarrow\quad E_{F,i}^{1} = -k_B T\ln\left(\sum_{i\in\mathcal{N}_s\setminus\{i\}}\exp\left(-\beta E_i^{tot}\right)\right) \tag{3.63}$$

To get the Fermi-level shift $\Delta E_{F,i}^{1}$, Equations (3.60), (3.62) and (3.63) are required.

$$\Delta E_{F,i}^{1} = -k_B T \ln\left(1 - \frac{\exp\left(-\beta E_i^{tot}\right)}{Z_{\mathcal{N}_s}^{1}}\right) = -k_B T \ln\left\{1 - \exp\left[-\beta\left(E_i^{tot} - E_{F,0}^{1}\right)\right]\right\} = \\ = -k_B T \ln\left(1 - \langle n_i\rangle_{\mathcal{N}_s}^{1}\right) \quad (3.64)$$

From this known solution for $N_{cc} = 1$, we can derive an equation to iteratively calculate the solution for $N_{cc} > 1$. The Fermi-level shift can be written in terms of partition functions with Equations (3.57) and (3.59)

$$\exp\left(-\beta \Delta E_{F,i}^{N_{cc}}\right) = \frac{Z_{\mathcal{N}_s\setminus\{i\}}^{N_{cc}}}{Z_{\mathcal{N}_s}^{N_{cc}}} \frac{Z_{\mathcal{N}_s}^{N_{cc}-1}}{Z_{\mathcal{N}_s\setminus\{i\}}^{N_{cc}-1}} \quad (3.65)$$

The ratios in Equation (3.65) can be recast with the help of Equations (3.44), (3.46), (3.58) and (3.60) to arrive at

$$\exp\left(-\beta \Delta E_{F,i}^{N_{cc}}\right) = \frac{1 - \langle n_i\rangle_{\mathcal{N}_s}^{N_{cc}}}{1 - \langle n_i\rangle_{\mathcal{N}_s}^{N_{cc}-1}} = \frac{1 + \exp\left[-\beta\left(E_i^{tot} - \Delta E_{F,i}^{N_{cc}-1} - E_{F,0}^{N_{cc}-1}\right)\right]}{1 + \exp\left[-\beta\left(E_i^{tot} - \Delta E_{F,i}^{N_{cc}} - E_{F,0}^{N_{cc}}\right)\right]}. \quad (3.66)$$

Rearranging Equation (3.66) to get an explicit equation for $\Delta E_{F,i}^{N_{cc}}$ leads to

$$\Delta E_{F,i}^{N_{cc}} = -k_B T \ln\left(1 + \exp\left[-\beta\left(E_i^{tot} - \Delta E_{F,i}^{N_{cc}-1} - E_{F,0}^{N_{cc}-1}\right)\right] - \exp\left[-\beta\left(E_i^{tot} - E_{F,0}^{N_{cc}}\right)\right]\right). \quad (3.67)$$

In combination with the implicit definition of $E_{F,0}^{N_{cc}}$ via Equation (3.50), we are able to simultaneously extract $\Delta E_{F,i}^{N_{cc}}$ and $E_{F,0}^{N_{cc}}$ from the known values of $\Delta E_{F,i}^{N_{cc}-1}$ and $E_{F,0}^{N_{cc}-1}$. A more detailed description of this procedure can be found in Chapter 3.3.3.

This iterative evaluation of $\Delta E_{F,i}^{N_{cc}}$ and $E_{F,0}^{N_{cc}}$ is a very efficient method for very low amounts of charge carriers. Nevertheless, a significant drawbacks hinders the evaluation of $\Delta E_{F,i}^{N_{cc}}$ and $E_{F,0}^{N_{cc}}$ by Equations (3.50) and (3.67) for large amounts of charge carriers. The iteration becomes numerically instable already for very low numbers of charge carriers $N_{cc} \lesssim 10$. The relations for a stable alternative for large amounts of charge carriers are described below.

In this alternative, we start from Fermi-Dirac statistics as a first approximation for the requested system with N_{cc} charge carriers. This means we initially set $\Delta E_{F,i}^{N_{cc}} = 0$ eV and calculate $E_{F,0}^{N_{cc}}$ via Equation (3.50). The first iteration step begins with Fermi-Dirac statistics as well and approximates the system with $N_{cc} - 1$ charge carriers by setting $\Delta E_{F,i}^{N_{cc}-1} = 0$ eV and calculate $E_{F,0}^{N_{cc}-1}$ via Equation (3.50). With those two approximations for the system with $N_{cc} - 1$ and N_{cc} charge carriers, Equation (3.66) provides an improved estimate for the aspired system with N_{cc} charge carriers. In principle, we could now continue this upwards iteration including progressively smaller amounts of charge carriers. With upwards iteration, we indicate that $\Delta E_{F,i}^{N_{cc}}$ and $E_{F,0}^{N_{cc}}$ is calculated from approximations for systems with $N_{cc} - 1$ and N_{cc} charge carriers. However, it turned out that the iteration becomes much more stable and converges much faster if we combine it with a downwards iteration. Downwards iteration means, that we calculate $\Delta E_{F,i}^{N_{cc}}$ and $E_{F,0}^{N_{cc}}$ from approximations for systems with $N_{cc} + 1$ and N_{cc} charge carriers. To provide a relation that calculates $\Delta E_{F,i}^{N_{cc}}$ from approximations for systems with $N_{cc} + 1$ and N_{cc} charge carriers, we

have to revisit Equation (3.65) and incorporate Equation (3.59).

$$\exp\left(-\beta\Delta E_{F,i}^{N_{cc}}\right) = \frac{Z_{\mathcal{N}_s\setminus\{i\}}^{N_{cc}}}{\exp\left(\beta E_{F,0}^{N_{cc}+1}\right) Z_{\mathcal{N}_s}^{N_{cc}+1}} \frac{\exp\left(\beta E_{F,0}^{N_{cc}}\right) Z_{\mathcal{N}_s}^{N_{cc}}}{Z_{\mathcal{N}_s\setminus\{i\}}^{N_{cc}-1}} \tag{3.68}$$

Expanding the fraction with $\exp(-\beta E_i^{tot})$ in combination with Equations (3.46), (3.58) and (3.60) leads to

$$\begin{aligned}\exp\left(-\beta\Delta E_{F,i}^{N_{cc}}\right) &= \exp\left[\beta\left(E_{F,0}^{N_{cc}} - E_{F,0}^{N_{cc}+1}\right)\right] \frac{\langle n_i\rangle_{\mathcal{N}_s}^{N_{cc}+1}}{\langle n_i\rangle_{\mathcal{N}_s}^{N_{cc}}} = \\ &= \exp\left[\beta\left(E_{F,0}^{N_{cc}} - E_{F,0}^{N_{cc}+1}\right)\right] \frac{1+\exp\left[\beta\left(E_i^{tot} - \Delta E_{F,i}^{N_{cc}} - E_{F,0}^{N_{cc}}\right)\right]}{1+\exp\left[\beta\left(E_i^{tot} - \Delta E_{F,i}^{N_{cc}+1} - E_{F,0}^{N_{cc}+1}\right)\right]}.\end{aligned} \tag{3.69}$$

The iteration process itself is discussed in detail in Chapter 3.3.3. The consequences of this new occupation statistics are discussed in the following for the example of a system with $N_S = 1000$ sites. The total site energies E_i^{tot} were randomly drawn from a Gaussian distribution, Equation (3.1), with energetic disorder $\sigma = 100$ meV.

Figure 3.3 shows the Fermi-level shift $\Delta E_{F,i}^{N_{cc}}$ of site i as a function of the total site energy E_i^{tot} of this site. The different curves with different colours show different amounts of charge carriers N_{cc} in the simulation. Each site is represented by a filled circle and the straight lines between the filled circles serve as a guide for the eye. For low energies, there are only a few energy levels, each represented by a filled circle. Towards the peak of the Gaussian distribution at $E^{tot} = 0$ eV, the energy levels are lying more and more densely resulting in an apparently thick line consisting of filled circles. The global Fermi levels $E_{F,0}^{N_{cc}}$ for different amounts of charge carriers N_{cc} are indicated as dotted vertical lines colour coded in the same way as the Fermi-level shift.

Looking at the magenta line for $N_{cc} = 1$ in Figure 3.3, the logarithmic plot indicates an exponential decrease of the Fermi-level shift $\Delta E_{F,i}^{N_{cc}}$. To clarify this exponential decrease, Equation (3.64) has to be consulted. For $E_i^{tot} \gg E_{F,0}^1$, the term $\exp\left[-\beta\left(E_i^{tot} - E_{F,0}^1\right)\right] \ll 1$ becomes very small. Considering the relation $\ln(1+u) \approx u$ for low values of $u \ll 1$, the Fermi-level shift can be approximated by

$$\Delta E_{F,i}^1 \approx k_B T \exp\left[-\beta\left(E_i^{tot} - E_{F,0}^1\right)\right] \quad \text{for} \quad E_i^{tot} \gg E_{F,0}^1. \tag{3.70}$$

So, the exponential decrease of $\Delta E_{F,i}^{N_{cc}}$ for $E_i^{tot} \gg E_{F,0}^{N_{cc}}$ appearing in all curves in Figure 3.3, associated with the number of charge carriers N_{cc}, is a clear indication for a Boltzmann-like behaviour of the occupation statistics in this region $E_i^{tot} \gg E_{F,0}^{N_{cc}}$.

In contrast, Fermi-Dirac statistics assumes the same Fermi level across the entire system resulting in a constant value for the Fermi-level shift $\Delta E_{F,i}^{N_{cc}}$. When looking at the curves for high values of $N_{cc} \geq 32$ in Figure 3.3, regions of constant Fermi-level shift $\Delta E_{F,i}^{N_{cc}}$ appear for low total site energies $E_i^{tot} \ll E_{F,0}^{N_{cc}}$. This means that the correct occupation statistics behaves Fermi-Dirac-like for low total site energies $E_i^{tot} \ll E_{F,0}^{N_{cc}}$ and Boltzmann-like for high total site energies $E_i^{tot} \gg E_{F,0}^{N_{cc}}$.

To understand the consequences of the approximation within the Fermi-Dirac statistics, we take a closer look at the two-site occupation $\langle n_i n_j\rangle$. As already mentioned in Chapter 3.2.3, Fermi-Dirac statistics neglects all correlations, because the two-site occupation factorises $\langle n_i n_j\rangle = \langle n_i\rangle \langle n_j\rangle$. This

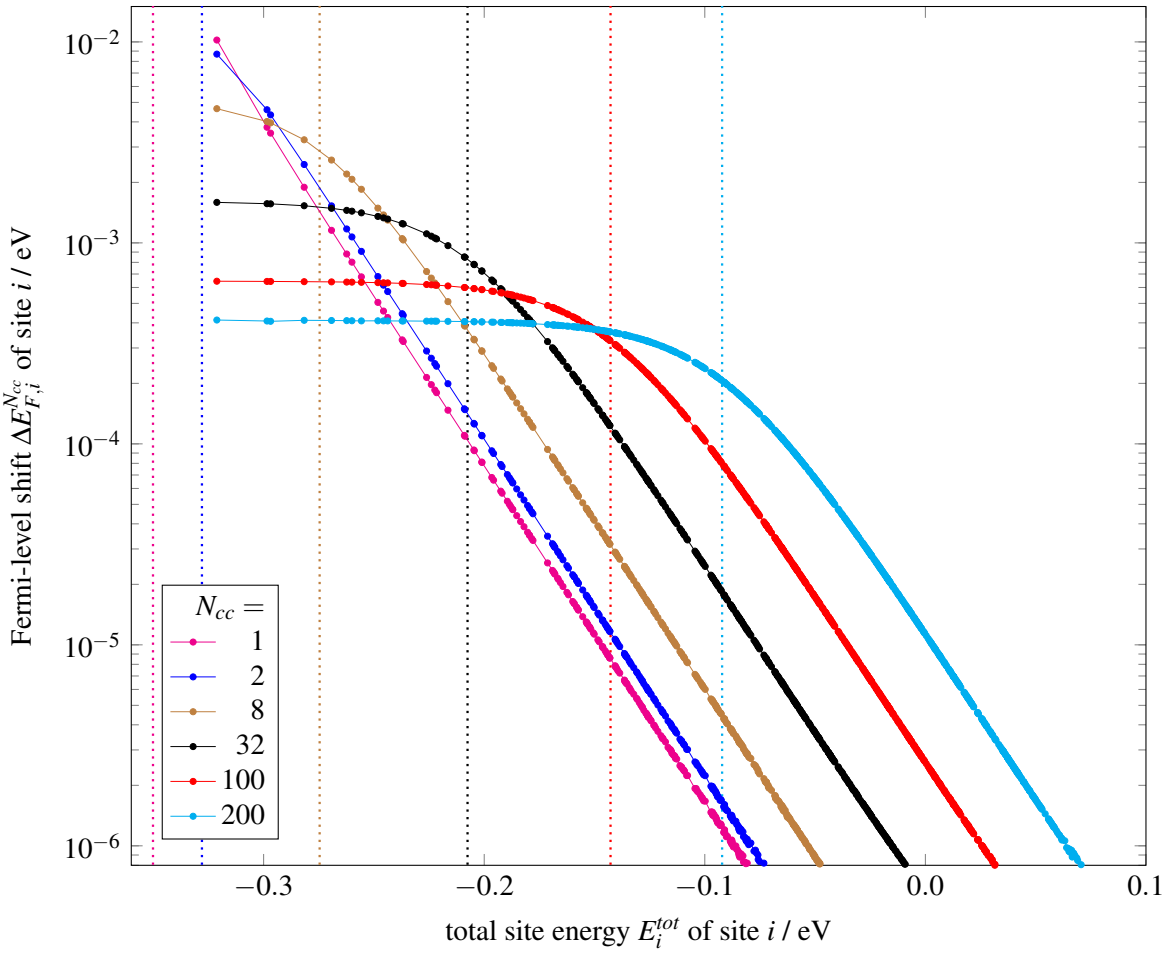

Figure 3.3: Fermi-level shift $\Delta E_{F,i}^{N_{cc}}$ of site i as a function of the total site energy E_i^{tot} of this site for different amounts of charge carriers N_{cc}. The total site energies E_i^{tot} of the system with 1000 sites are drawn from a Gaussian distribution with width $\sigma = 100$ meV centred at 0 eV. Each site is represented by a filled circle. As a guide for the eye, the filled circles are connected by straight lines. The dotted vertical lines mark the global Fermi level $E_{F,0}^{N_{cc}}$ of the corresponding number of charge carriers N_{cc}. Especially for large numbers of charge carriers $N_{cc} \geq 32$, the transition from a Fermi-Dirac-like behaviour (flat $\Delta E_{F,i}^{N_{cc}}$) for total site energies below $E_{F,0}^{N_{cc}}$ to a Boltzmann-like behaviour (exponentially decreasing $\Delta E_{F,i}^{N_{cc}}$) for total site energies above $E_{F,0}^{N_{cc}}$ can be observed.

means that the occupation $\langle n_i \rangle$ of a site i does not depend on the occupation $\langle n_j \rangle$ of any other site j. When comparing this to the Fermi-Dirac-like regime of low total site energies $E_i^{tot} \ll E_{F,0}^{N_{cc}}$ of the correct occupation statistics (cf. Figure 3.3), the relation $\langle n_i n_j \rangle = \langle n_i \rangle \langle n_j \rangle$ is still valid. So the nearly totally occupied sites are still not correlated. But the two-site occupation changes quite significantly when looking at the Boltzmann-like regime of high total site energies $E_i^{tot} \gg E_{F,0}^{N_{cc}}$. In Chapter 3.2.3, we found out that a Boltzmann-like regime results in $\langle n_i n_j \rangle = 0$ ccps. This means that the occupation of sites with high total site energies $E_i^{tot} \gg E_{F,0}^{N_{cc}}$ is strongly correlated, because if we occupy one of those sites i, no other high total site energy E_j^{tot} site j can be occupied. This correlation purely arises from the premise that we allow at maximum one charge carrier per site and has nothing to do with explicit interactions E_{ij}^{tot}. A consequence of this correlation is, that the correct occupation statistics populates sites with low total site energies $E_i^{tot} \ll E_{F,0}^{N_{cc}}$ more and sites with high total site energies $E_i^{tot} \gg E_{F,0}^{N_{cc}}$ less, compared to Fermi-Dirac statistics.

3.3 Implementation

After establishing the mathematical foundation of our new correction energy concept in Chapter 3.1 and Chapter 3.2, this chapter is focusing on the intricacies associated with the numerical implementation of the CEC. The consideration of interactions via a mean-field approach is discussed in Chapter 3.3.1. In Chapter 3.3.2, the evaluation of the correction energies is described. Extracting site occupations $\langle n_i \rangle_{\mathcal{N}_s}^{N_{cc}}$ with our improved occupation statistics is demonstrated in Chapter 3.3.3. Finally, Chapter 3.3.4 debates the calculation of the mobility and the associated convergence check for interacting simulations.

3.3.1 Mean-Field Approach

In the current state of the development of the CEC, interactions can be only considered by a mean field approach, except for simulations with two charge carriers. In future, it is conceivable that a direct consideration of the most important interactions and associated correlations is possible within the formalism of the CEC. Nevertheless, even if some interactions are considered explicitly, the majority of interactions would still be included via a mean-field approach.

The mean-field approach we use is an iterative process. In each iteration, correction energies are calculated and the occupation statistics is evaluated to provide site occupations $\langle n_i \rangle_{\mathcal{N}_s}^{N_{cc}}$ for a system with a set of $\mathcal{N}_s$ sites and N_{cc} charge carriers. Providing site occupations $\langle n_i \rangle_{\mathcal{N}_s}^{N_{cc}}$ enables us to calculate average interaction energies E_i^{int} of a site i

$$E_i^{int} = \sum_{j \in \mathcal{N}_s \setminus \{i\}} E_{ij}^{int} \langle n_j \rangle_{\mathcal{N}_s \setminus \{i\}}^{N_{cc}-1} \tag{3.71}$$

by summing over the interaction energies E_{ij}^{int} with all remaining sites j weighted by the site occupation $\langle n_j \rangle_{\mathcal{N}_s \setminus \{i\}}^{N_{cc}-1}$. This particular site occupation $\langle n_j \rangle_{\mathcal{N}_s \setminus \{i\}}^{N_{cc}-1}$ has to be chosen, because we want to know the average interaction energy that acts on a charge carrier sitting on site i from a site j. So site i has to be occupied, which results in the reduced system with $\mathcal{N}_s \setminus \{i\}$ sites and $N_{cc} - 1$ charge carriers.

The site occupation $\langle n_j \rangle_{\mathcal{N}_s \setminus \{i\}}^{N_{cc}-1}$ can be expressed with the help of Equations (3.46) and (3.51)

$$\langle n_j \rangle_{\mathcal{N}_s \setminus \{i\}}^{N_{cc}-1} = \frac{Z_{\mathcal{N}_s \setminus \{i,j\}}^{N_{cc}-2} \exp\left(-\beta E_j^{tot}\right)}{Z_{\mathcal{N}_s \setminus \{i\}}^{N_{cc}-1}} \frac{Z_{\mathcal{N}_s}^{N_{cc}} \exp\left(-\beta E_i^{tot}\right)}{Z_{\mathcal{N}_s}^{N_{cc}} \exp\left(-\beta E_i^{tot}\right)} = \frac{\langle n_i n_j \rangle_{\mathcal{N}_s}^{N_{cc}}}{\langle n_i \rangle_{\mathcal{N}_s}^{N_{cc}}} \tag{3.72}$$

by occupations $\langle n_i \rangle_{\mathcal{N}_s}^{N_{cc}}$ and $\langle n_i n_j \rangle_{\mathcal{N}_s}^{N_{cc}}$. For Fermi-Dirac statistics, this further simplifies to $\langle n_j \rangle_{\mathcal{N}_s \setminus \{i\}}^{N_{cc}-1} = \langle n_j \rangle_{\mathcal{N}_s}^{N_{cc}}$. For the correct occupation statistics, the occupation $\langle n_i n_j \rangle_{\mathcal{N}_s}^{N_{cc}}$ is determined by Equation (3.55).

At the end of every interaction iteration, the new average interaction energies $E_i^{int,new}$ are calculated for each site i. To improve the stability and speed of the convergence, the new average interaction energy is mixed with the old one $E_i^{int} = cE_i^{int,new} + (1-c)E_i^{int,old}$ with a mixing parameter $c \approx 0.6$. This mixed average interaction energy modifies the site energies $\varepsilon_i \rightarrow \varepsilon_i^{tot} = \varepsilon_i + E_i^{int}$ and the next iteration is started. Note that it is of particular importance that the site energies ε_i^{tot} for calculating the correction energies and the occupation statistics are the same. Otherwise, the calculated values for the mobility become totally random producing sometimes even negative numbers.

3.3.2 Correction Energies

Enabling the calculation of correction energies for large systems with millions of sites is a numerically challenging task involving the solution of a large system of linear equations. In the following, we will discuss which numerical algorithms we utilised to receive the correction energies. Most of those algorithms are taken from the book 'Iterative Methods for Sparse Linear Systems' by Yousef Saad. [97] Algorithms from other sources are explicitly cited. We will discuss the procedure to calculate the site-correction energies E_i^c in detail and, afterwards, outline the changes required to calculate the correlation-correction energies E_{ij}^c with the same procedure.

Site-Correction Energies E_i^c

The first step to calculate site-correction energies E_i^c is to construct the modified Q-matrix (cf. Chapter 3.1.4) for a single charge carrier in the system. The Q-matrix contains the hopping rates $R_{ij}(\Delta E_{ij})$ depending on the energy

$$\Delta E_{ij} = \varepsilon_j^{tot} - \varepsilon_i^{tot} + e\Delta\vec{r}_{ij}\vec{F}, \tag{3.73}$$

that is required to remove a charge carrier from site i and place it at a site j. The site energy might contain mean-field interactions $\varepsilon_i^{tot} = \varepsilon_i + E_i^{int}$ if desired or might omit them $\varepsilon_i^{tot} = \varepsilon_i$. The hopping distance $\Delta\vec{r}_{ij}$ is the distance covered during the hop from site i to site j respecting the boundary conditions (cf. Chapter 3.1.1). With this energy difference ΔE_{ij}, the rate $R_{ij}(\Delta E_{ij})$ is calculated via the chosen rate equation (Equation (3.3) for the Miller-Abrahams rate or Equation (3.4) for the Marcus rate) and the modified Q-matrix is given by

$$\tilde{q}_{ij} = \begin{cases} \exp\left(\beta e\Delta\vec{r}_{ij}\vec{F}\right) R_{ij}(\Delta E_{ij}) & \text{if } i \neq j \\ \sum_{k\in\mathcal{N}_s\setminus\{j\}} R_{ik}(\Delta E_{ik}) & \text{if } i = j. \end{cases} \tag{3.74}$$

The consideration of a maximum allowed hopping distance r_{hop} results in a sparse matrix $\tilde{Q} = (\tilde{q}_{ij})$ as rates $R_{ij} = 0$ Hz for hops $\Delta r_{ij} > r_{hop}$. With this modified Q-matrix, $\tilde{Q}$, the homogeneous system of linear equations $\tilde{Q}\vec{\pi}^c = \vec{0}$ has to be solved. The existence of a non-zero solution of this equation is guaranteed due to the properties of our simulated system (cf. Chapter 3.1.4 and [93, 96]). The solution of a homogeneous system contains ambiguity such that a non-zero solution $\vec{\pi}^c \neq \vec{0}$ of the system can be multiplied by any value to provide a different solution. This multiplicative ambiguity translates to an additive ambiguity regarding the correction energies $\pi_i^c = \exp(\beta E_i^c)$, which means that an energy shift $E_i^c \to E_i^c + E_0$ by any energy E_0 provides a proper solution. This ambiguity is not surprising as a constant shift E_0 of all energies does not change any observable in a closed system. Note that $\vec{\pi}^c$ is not a probability density, so it must not be normalised. The norm of the final steady-state-probability distribution $\vec{\pi}$ is ensured by the partition function Z.

In a first instance, the energy shift E_0 can be chosen arbitrarily. We fix one particular solution with a certain E_0 by setting one entry in $\pi_k^c = 1$ entailing $E_k^c = 0$ eV. Equation k is discarded from the system of equations and the entries containing k in the remaining system of equations is moved to the right-hand

side. This leads to a system of equations

$$\tilde{Q}^k \vec{\pi}^{c,k} = \vec{q}^{c,k} \quad \text{with} \quad (\tilde{Q}^k)_{ij} = \tilde{q}^k_{ij} = \begin{Bmatrix} \tilde{q}_{ij} & \text{if } i < k \\ \tilde{q}_{(i+1)j} & \text{if } i \geq k \end{Bmatrix},$$

$$\pi^{c,k}_i = \begin{Bmatrix} \pi^c_i & \text{if } i < k \\ \pi^c_{i+1} & \text{if } i \geq k \end{Bmatrix} \text{ and } \quad q^{c,k}_i = \begin{Bmatrix} -\tilde{q}_{ik} & \text{if } i < k \\ -\tilde{q}_{(i+1)k} & \text{if } i \geq k \end{Bmatrix}. \quad (3.75)$$

The choice of the discarded equation k has an influence on the condition number of the remaining system of equations. The condition number is a rough measure for the expected numerical uncertainty of the solution. We decided to take a very simple approach to improve the condition number by discarding the equation k with the lowest squared sum of its coefficients $\min_{k \in \mathcal{N}_s} \left(\sum_{j \in \mathcal{N}_s} (\tilde{q}_{kj})^2 \right)$. The choice of the discarded equation k is one of the finesses holding significant optimisation potential.

The system of linear equations, Equation (3.75), has a unique solution. To find this solution efficiently and swiftly even for large systems, we apply several algorithms:

- Divide each equation i by the norm of its coefficients $\sum_{j=1}^{N_s-1} (\tilde{q}^k_{ij})^2$.
- Perform a reverse Cuthill-McKee reordering algorithm to optimise the ordering of the system of equations. As a starting node for the algorithm, we took a site i which is a hopping neighbour of the site k whose equation was discarded from the system of equations.
- Calculate a preconditioner. The preconditioner of choice for us was suggested by Wu and Ma. [98] We tested other ILUT (Incomplete factorisation to a unit Lower triangular and Upper triangular matrix with Threshold) preconditioners showing comparable but slightly worse performance. As a threshold below which elements are dropped, we use $\tau = 10^{-4}$, the maximum average added elements per row is $p = 25$ and we calculated $b = 5$ rows exact before dropping elements.
- Perform a left preconditioned GMRES (Generalised Minimal RESidual) method. Convergence is checked after 5 iterations. After 200 iterations, the GMRES method is restarted. The accuracy of the solution vector was set to 10^{-8} and the residual accuracy to 10^{-4}.
- Reorder the solution vector with respect to the reverse Cuthill-McKee reordering algorithm.

An important variation of the GMRES algorithm customised for our system of equations is, that the solution vector cannot be zero or negative. This would imply diverging or complex correction energies. Hence, the convergence check of our GMRES algorithm includes, besides the desired accuracy of the residual and the solution vector, a check if all entries of the solution vector are strictly positive.

As a result of the application of those numerical algorithms, the solution vector $\vec{\pi}^{c,k}$ is received. From this solution vector, the shifted correction energies $E^{c,s}_i$ are calculated:

$$E^{c,s}_i = k_B T \begin{cases} \ln\left(\pi^{c,k}_i\right) & \text{if } i < k \\ 0 & \text{if } i = k \\ \ln\left(\pi^{c,k}_{i-1}\right) & \text{if } i > k \end{cases}. \quad (3.76)$$

To eliminate the ambiguity of the choice of the discarded equation k and get comparable correction

energies for similar systems, the correction energies are shifted such that the average value of all site-correction energies is zero:

$$E_i^c = E_i^{c,s} - \left\langle E^{c,1} \right\rangle \quad \text{with} \quad \left\langle E^{c,1} \right\rangle = \frac{1}{N_s} \sum_{j \in \mathcal{N}_s} E_j^{c,s}. \tag{3.77}$$

Correlation-Correction Energies E_{ij}^c

The procedure to calculate correlation-correction energies E_{ij}^c is, in principle, the same as for site-correction energies E_i^c except that we have to include two charge carriers in the system instead of one. As a consequence, configurations with two occupied sites $(i_1 i_2)$ instead of only one site i are taken into account. The energy difference $\Delta E_{i_1 j}(i_2)$ for a hop from site i_1 to site j while the second charge carrier resides on site i_2 is given by

$$\Delta E_{i_1 j}(i_2) = \varepsilon_j^{tot} - \varepsilon_{i_1}^{tot} + e\Delta\vec{r}_{i_1 j}\vec{F} + E_{j i_2}^{int} - E_{i_1 i_2}^{int}. \tag{3.78}$$

Interactions can be considered explicitly and/or in terms of a mean-field approximation. Within this thesis, no mean-field considerations were performed for calculating correlation-correction energies. The energy difference $\Delta E_{i_1 j}(i_2)$ is used to calculate the corresponding rate $R_{i_1 j}[\Delta E_{i_1 j}(i_2)]$ and the modified Q-matrix is given by

$$\tilde{q}_{(i_1 i_2)(j i_2)} = \begin{cases} \exp\left(\beta e \Delta\vec{r}_{i_1 j}\vec{F}\right) R_{i_1 j}[\Delta E_{i_1 j}(i_2)] & \text{if } i_1 \neq j \text{ and } i_2 \neq j \\ 0 & \text{if } i_2 = j \\ \sum_{k \in \mathcal{N}_s \setminus \{i_1, i_2\}} R_{i_1 k}[\Delta E_{i_1 k}(i_2)] & \text{if } i_1 = j. \end{cases} \tag{3.79}$$

The same procedure as described for site-correction energies E_i^c provides the shifted correlation-correction energies $E_{ij}^{c,s}$. Again, the correlation-correction energies E_{ij}^c are fixed by the requirement that the average is zero. Furthermore, the contribution from the site-correction energy is removed from the shifted correlation-correction energy.

$$E_{ij}^c = E_{ij}^{c,s} - E_i^c - E_j^c - \left\langle E^{c,2} \right\rangle \quad \text{with} \quad \left\langle E^{c,2} \right\rangle = \frac{2}{N_s(N_s-1)} \sum_{k_1=1}^{N_s-1} \sum_{k_2=k_1+1}^{N_s} E_{k_1 k_2}^{c,s} \tag{3.80}$$

The site-correction energies E_i^c and E_j^c must not be considered in the sum to evaluate $\left\langle E^{c,2} \right\rangle$, because their sum is zero.

3.3.3 Occupation Statistics

For Boltzmann statistics and the two-charge-carrier-configuration considerations, performing simple sums given in Chapter 3.2.1 and Chapter 3.2.2 provides the occupations $\langle n_i \rangle_{\mathcal{N}_s}^1$, $\langle n_i n_j \rangle_{\mathcal{N}_s}^1$, $\langle n_i \rangle_{\mathcal{N}_s}^2$ and $\langle n_i n_j \rangle_{\mathcal{N}_s}^2$. As this evaluation is very simple, we will only discuss the evaluation of $\langle n_i \rangle_{\mathcal{N}_s}^{N_{cc}}$ and $\langle n_i n_j \rangle_{\mathcal{N}_s}^{N_{cc}}$ for systems with $N_{cc} > 2$ with Fermi-Dirac statistics compared to our new occupation statistics.

For both, no direct consideration of interactions is implemented yet. So, the total site energies $E_i^{tot} = \varepsilon_i^{tot} - E_i^c$ are the only energies entering the occupation statistics. The site energies ε_i^{tot} can include mean-

field interactions if desired. For Fermi-Dirac statistics, the occupations are given by

$$\langle n_i \rangle_{\mathcal{N}_s}^{N_{cc}} = \frac{1}{1+\exp\left[\beta\left(E_i^{tot} - E_{F,0}^{N_{cc}}\right)\right]}, \quad \langle n_i n_j \rangle_{\mathcal{N}_s}^{N_{cc}} = \langle n_i \rangle_{\mathcal{N}_s}^{N_{cc}} \langle n_j \rangle_{\mathcal{N}_s}^{N_{cc}} \quad \text{and} \quad N_{cc} = \sum_{i \in \mathcal{N}_s} \langle n_i \rangle_{\mathcal{N}_s}^{N_{cc}}. \tag{3.81}$$

This implicit system of equations for $E_{F,0}^{N_{cc}}$ is solved by a simple bisection method.

For the new occupation statistics, two different approaches are used. The first approach, for very low numbers of charge carriers $N_{cc} \leq 5$, is to start with Boltzmann statistics and use Equation (3.67) to iteratively increase N_{cc}. The second approach is a two-sided iteration from higher and lower N_{cc} incorporating Fermi-Dirac statistics including Equations (3.66) and (3.69).

Boltzmann Iteration

Starting from the known solution for the local Fermi level $E_{F,i}^1 = \Delta E_{F,i}^1 + E_{F,0}^1$ with the local Fermi-level shift $\Delta E_{F,i}^1$ and the global Fermi level $E_{F,0}^1$

$$\Delta E_{F,i}^1 = -k_B T \ln\left\{1 - \exp\left[-\beta\left(E_i^{tot} - E_{F,0}^1\right)\right]\right\}$$
$$\text{and} \quad E_{F,0}^1 = -k_B T \ln\left(\sum_{i \in \mathcal{N}_s} \exp\left(-\beta E_i^{tot}\right)\right), \tag{3.82}$$

the step from $N_{cc}-1$ charge carriers to N_{cc} charge carriers is performed with the help of Equation (3.67).

$$\Delta E_{F,i}^{N_{cc}} = -k_B T \ln\left(1 + \exp\left[-\beta\left(E_i^{tot} - \Delta E_{F,i}^{N_{cc}-1} - E_{F,0}^{N_{cc}-1}\right)\right] - \exp\left[-\beta\left(E_i^{tot} - E_{F,0}^{N_{cc}}\right)\right]\right)$$
$$\text{and} \quad N_{cc} = \sum_{i \in \mathcal{N}_s} \frac{1}{1+\exp\left[\beta\left(E_i^{tot} - \Delta E_{F,i}^{N_{cc}} - E_{F,0}^{N_{cc}}\right)\right]} \tag{3.83}$$

With the known values for $\Delta E_{F,i}^{N_{cc}-1}$ and $E_{F,0}^{N_{cc}-1}$ and a guess value for $E_{F,0}^{N_{cc}}$, we can calculate guess values for $\Delta E_{F,i}^{N_{cc}}$ and evaluate the sum. So, we can solve the implicit system of equations, Equation (3.83), again with a simple bisection method with respect to $E_{F,0}^{N_{cc}}$.

Two-Sided Iteration

Compared to the Boltzmann-iteration scheme, this two-sided-iteration scheme is much more effort to be implemented. This effort is necessary as soon as more than $N_{cc} \gtrsim 5$ charge carriers are considered. This approach is very stable and, especially for high numbers of charge carriers, it converges within a few iterations. The principle of the iteration scheme is visualised in Figure 3.4.

The iteration calculates local Fermi-level shifts $\Delta E_{F,i}^{N_{cc},(k)}$ and global Fermi levels $E_{F,0}^{N_{cc},(k)}$ with a variable k specifying the level of approximation. For $k = 0$, Fermi-Dirac statistics is utilised as a first approximation of the occupation statistics and with increasing values of k, the approximation is improved. The variable k can take half-integer values, referring to the two half-cycles of each iteration consisting of an upwards and downwards iteration. But before going in detail, we start with the zero-order iteration. Fermi-Dirac statistics ($k = 0$) means that for the requested value of N_{cc}, we set $\Delta E_{F,i}^{N_{cc},(0)} = 0$ eV and

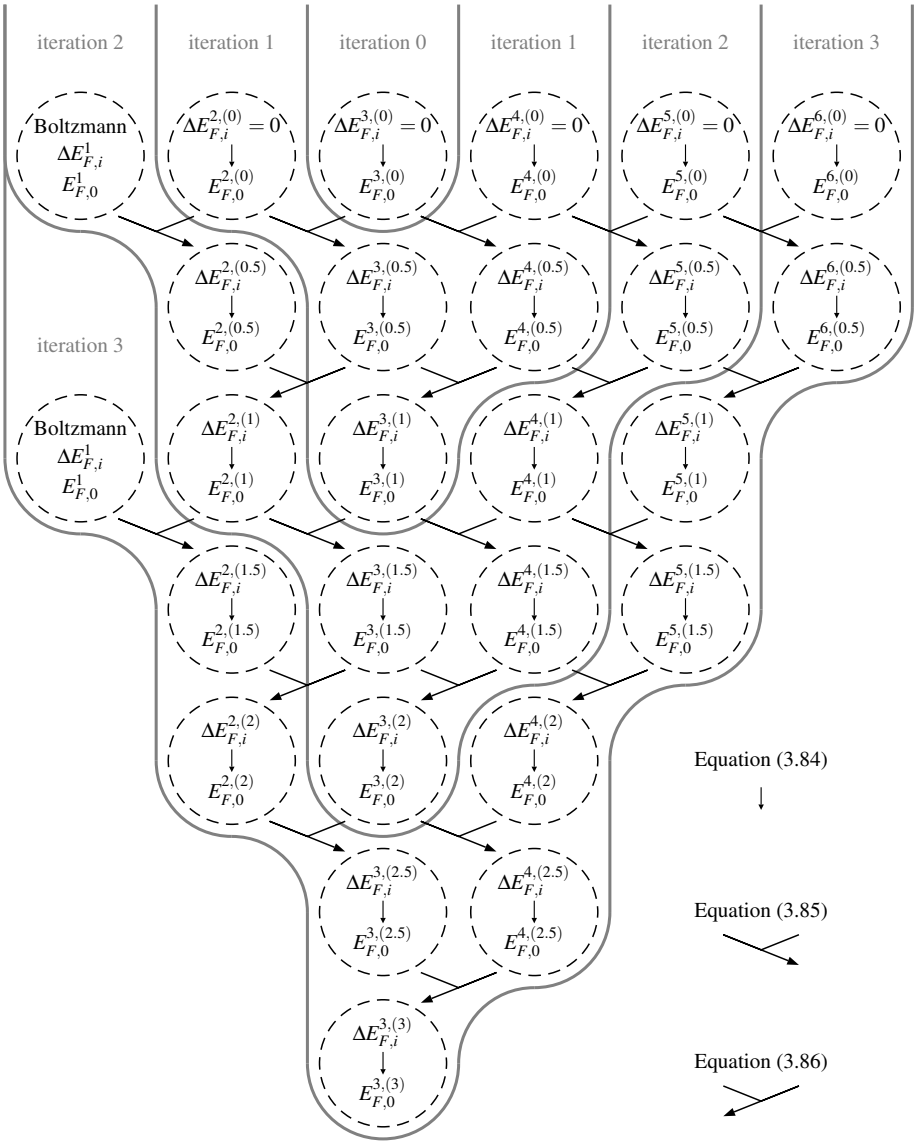

Figure 3.4: Illustrative example of the iteration scheme for the two-sided iteration required to calculate the local Fermi-level shift $\Delta E^{N_{cc}}_{F,i}$ of a site i and the global Fermi level $E^{N_{cc}}_{F,0}$ for large numbers of charge carriers $N_{cc} \gtrsim 5$. Three iterations are demonstrated and the number of charge carriers that is evaluated is $N_{cc} = 3$. Grey lines separate the required variables for the corresponding iteration.

calculate $E^{N_{cc},(0)}_{F,0}$ from the implicit equation for $k = 0$

$$N_{cc} = \sum_{i \in \mathcal{N}_s} \frac{1}{1 + \exp\left[\beta \left(E^{tot}_i - \Delta E^{N_{cc},(k)}_{F,i} - E^{N_{cc},(k)}_{F,0}\right)\right]} \tag{3.84}$$

solved by a simple bisection method. With this, the initial iteration 0 is finished.

To initiate iteration 1, we set $\Delta E^{N_{cc}-1,(0)}_{F,i} = 0$ eV and $\Delta E^{N_{cc}+1,(0)}_{F,i} = 0$ eV and calculate $E^{N_{cc}-1,(0)}_{F,0}$ and $E^{N_{cc}+1,(0)}_{F,0}$ via Equation (3.84). The first half-cycle of iteration 1 performs an upwards iteration to

calculate $\Delta E_{F,i}^{N_{cc},(0.5)}$ and $\Delta E_{F,i}^{N_{cc}+1,(0.5)}$ via

$$\Delta E_{F,i}^{N_{cc},(k+0.5)} = k_B T \ln\left(\frac{1+\exp\left[-\beta\left(E_i^{tot}-\Delta E_{F,i}^{N_{cc},(k)}-E_{F,0}^{N_{cc},(k)}\right)\right]}{1+\exp\left[-\beta\left(E_i^{tot}-\Delta E_{F,i}^{N_{cc}-1,(k)}-E_{F,0}^{N_{cc}-1,(k)}\right)\right]}\right) \tag{3.85}$$

for $k = 0$. With upwards iteration we mean that the new values of $\Delta E_{F,i}^{N_{cc},(k+0.5)}$ are calculated from systems with $N_{cc}-1$ and N_{cc} charge carriers for the level of approximation k being 0.5 lower. With Equation (3.84), we get $E_{F,0}^{N_{cc},(0.5)}$ and $E_{F,0}^{N_{cc}+1,(0.5)}$, ending the first half-cycle of iteration 1.

The second half-cycle of iteration 1 is a downwards iteration.

$$\Delta E_{F,i}^{N_{cc},(k+0.5)} = E_{F,0}^{N_{cc}+1,(k)} - E_{F,0}^{N_{cc},(k)} + k_B T \ln\left(\frac{1+\exp\left[\beta\left(E_i^{tot}-\Delta E_{F,i}^{N_{cc}+1,(k)}-E_{F,0}^{N_{cc}+1,(k)}\right)\right]}{1+\exp\left[\beta\left(E_i^{tot}-\Delta E_{F,i}^{N_{cc},(k)}-E_{F,0}^{N_{cc},(k)}\right)\right]}\right) \tag{3.86}$$

This means we calculate $\Delta E_{F,i}^{N_{cc},(k+0.5)}$ from systems with N_{cc} and $N_{cc}+1$ charge carriers for the level of approximation k being 0.5 lower. By setting $k = 0.5$, Equation (3.86) delivers $\Delta E_{F,i}^{N_{cc},(1)}$ and Equation (3.84) determines $E_{F,0}^{N_{cc},(1)}$ ending iteration 1.

This is continued by including two more systems in each iteration. The first additional system has one less charge carrier than the system with the previously lowest number of charge carriers and the second additional system has one charge carrier more than the system with the previously highest number of charge carriers. The principle of the iteration scheme is shown in Figure 3.4.

If we reach the lowest number for the possible amount of charge carriers $N_{cc} - i = 1$ in iteration i, we always use the exact solution, Equation (3.83), for upwards iterations including the system with only one charge carrier. For this system of one charge carrier, no downwards iteration is required as the Boltzmann statistics already provides the correct solution.

Convergence is reached, when the change in each local Fermi-level shift $\Delta E_{F,i}^{N_{cc},(k)}$ of the requested number of charge carriers N_{cc} after a full iteration i with $i \in \mathbb{N}$ is below a certain tolerance with respect to both, the approximation related to $k-0.5$ and $k-1$. We usually use a relative tolerance of 10^{-6} and an absolute tolerance of $k_B T \cdot 10^{-10}$ with at least one of them being fulfilled for convergence.

3.3.4 Mobility and Convergence

The requested observable calculated for a bulk simulation is the mobility μ. Without a direct consideration of interactions, the rates are the same for all configurations, enabling the application of Equation (3.38).

$$\mu = \sum_{i=1}^{N_s}\sum_{\substack{j=1\\ j\neq i}}^{N_s} \frac{q\Delta\vec{r}_{ij}\vec{F}}{F^2} R_{ij}\left(\langle n_i\rangle_{\mathcal{N}_s}^{N_{cc}} - \langle n_i n_j\rangle_{\mathcal{N}_s}^{N_{cc}}\right) \tag{3.87}$$

With $\langle n_i\rangle_{\mathcal{N}_s}^{N_{cc}}$ and $\langle n_i n_j\rangle_{\mathcal{N}_s}^{N_{cc}}$ determined in Chapter 3.3.3. For one and two charge carriers in the simulation, the mobility is given by Equations (3.39) and (3.41), respectively.

Without applying a mean-field approach to include interactions, the calculation of the mobility is the last step after calculating the correction energies and the occupation. When including interactions via a mean-field approach, an iterative approach to determine the correct average interaction energies E_i^{int}

is required. In this case, the mobility is used as a measure for convergence. If the relative change in mobility compared to the last iteration is less than a certain tolerance, it is assumed to be converged and the iteration is stopped. Else, new average interaction energies E_i^{int} are calculated as described in Chapter 3.3.1, new correction energies E_i^c are calculated as described in Chapter 3.3.2 and new occupations $\langle n_i \rangle_{\mathcal{N}_s}^{N_{cc}}$ and $\langle n_i n_j \rangle_{\mathcal{N}_s}^{N_{cc}}$ are calculated as described in Chapter 3.3.3. This delivers a new mobility μ via Equation (3.87) which is checked for convergence. This process is repeated until convergence for the mobility μ is reached. Commonly, we chose a relative tolerance of 10^{-6}.

3.4 Verification

To test the validity of our new simulation technique, we extracted the mobility μ with this new simulation technique and the mobility μ_{KMC} with kinetic Monte Carlo simulations, as a reference, for exactly the same system. With those two mobilities, the relative error $\Delta\mu_{rel}$ of our new simulation technique is estimated by

$$\Delta\mu_{rel} = \left| \frac{\mu_{KMC} - \mu}{\min(\mu_{KMC}, \mu)} \right|. \tag{3.88}$$

The minimum of μ_{KMC} and μ is taken in the denominator to receive an interpretable quantity for large errors. If the error is 1, the two values are off by a factor of 2 and if it is 10, they are off by approximately one order of magnitude.

The system to test the correction energy concept is described in Chapter 3.4.1. In Chapter 3.4.2, the validity of the site-correction energies is tested by simulations with only one charge carrier. Chapter 3.4.3 provides a test of the validity of the correlation-correction energies via a system with two charge carriers in the simulation. Finally, Chapter 3.4.4 performs tests for systems containing increasing amounts of charge carriers. This test examines the approximations within the CEC considering only site-correction energies. Furthermore, Chapter 3.4.4 compares the performance of our new occupation statistics in comparison to Fermi-Dirac statistics.

3.4.1 The Test System

The system used to test our new simulation technique is a rather small system with $10 \times 10 \times 10$ sites arranged on a simple cubic lattice with lattice constant of $a = 1$ nm. This small system is chosen to enable a low uncertainty well below 1% of the KMC results with an acceptable amount of computational effort. The maximum hopping distance is set to $r_{hop} = 2$ nm and the charge delocalisation constant to $\alpha = 5$ nm^{-1}. The site energies ε_i are randomly drawn from a Gaussian distribution with energetic disorder $\sigma = 100$ meV. The energy landscape, consisting of all site energies ε_i, is always the same for all simulations. The temperature is set to $T = 300$ K and the hopping prefactor is chosen to get a mobility of $\mu = 10^{-4}$ $\frac{\text{Vs}}{\text{cm}^2}$ for the isoenergetic case, which results in $\nu_0 = 22.497$ THz.

When interactions are considered, Coulomb interactions with all charge carriers and all periodic replicas of all charge carriers of the periodic system are taken into account with a relative permittivity of $\varepsilon_r = 4.0$. For details about the consideration of the Coulomb interactions, see [3, 93].

For the kinetic Monte Carlo simulations, 10^6 to $2 \cdot 10^9$ hops are required to achieve an error well below 1%. The error of the KMC simulations is determined by Jackknife. [3, 93, 99].

3.4.2 Single Charge Carrier Simulations

A first test of the applicability of the correction energy concept itself is to simulate a system with only one charge carrier. In this simplest case, no interactions are present and the occupation statistics is exactly given by the Boltzmann statistics. Furthermore, the site-correction energies E_i^c describe the system exactly correct, so we purely test the validity of our site-correction energies.

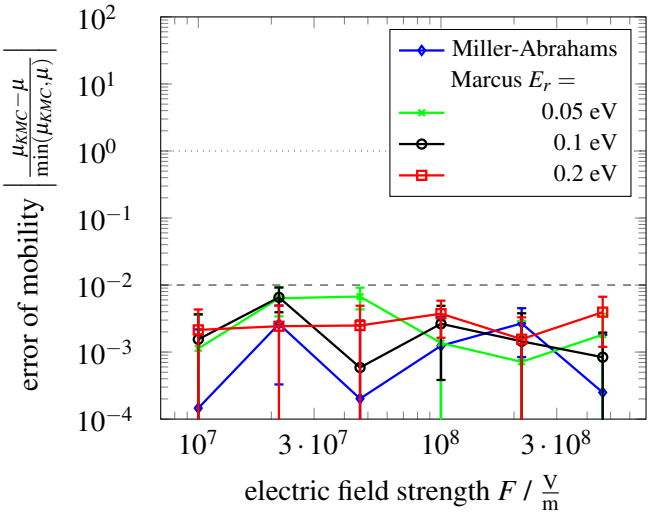

Figure 3.5: Error of the mobility evaluated with the correction energy concept with respect to precise results from kinetic Monte Carlo simulations as a function of the externally applied electric field strength F. The different curves refer to different hopping rates with the Miller-Abrahams rate, Equation (3.3), and Marcus rate for different reorganisation energies $E_r = 0.05$ eV, $E_r = 0.1$ eV and $E_r = 0.2$ eV, Equation (3.4), being considered. The dashed line marks an error of $10^{-2} = 1\%$ and the dotted line an error of 1. With only one charge carrier in the simulation, Boltzmann statistics can be applied and we solely test the validity of the site-correction energies E_i^c. This test is successfull, as the difference between the two methods is below the uncertainty of the kinetic Monte Carlo results, indicated by the errorbars, which is in the order of 1%.

Figure 3.5 shows the error of the CEC with respect to KMC simulation results for different electric field strengths F and different hopping rates with the Miller-Abrahams rate, Equation (3.3), and Marcus rate for different reorganisation energies $E_r = 0.05$ eV, $E_r = 0.1$ eV and $E_r = 0.2$ eV, Equation (3.4). With only one charge carrier in the simulation, the CEC and KMC have to result in exactly the same mobility. This equivalence of the results from the CEC and KMC can be nicely seen in Figure 3.5, because all errors of the mobility for all electric fields and all rates lie well below the dashed line, which indicates an error of $10^{-2} = 1\%$. So, the difference between CEC and KMC results is within the uncertainty of KMC.

3.4.3 Simulations With Two Charge Carriers

For two charge carriers, we are able to consider the correct occupation statistics, as described in Chapter 3.2.2. So we can test the effect of including correlation-correction energies E_{ij}^c for simulations without interactions and simulations including interactions. Considering the correct occupation statistics implies that CEC simulations including the correlation-correction energies E_{ij}^c provide the correct results. When only site-correction energies E_i^c are considered, the observed error arises from omitting

correlation-correction energies E_{ij}^c and, if interactions are present, additionally from the approximate consideration of those interactions via a mean-field approach.

In Figure 3.6, the error of the mobility is shown as a function of the electric field strength F for Miller-Abrahams rate equation, Equation (3.3), and Marcus rate equation with different reorganisation energies E_r, Equation (3.4). The two upper panels in Figure 3.6 are non-interacting simulations and the two lower panels are interacting ones. The two left panels in Figure 3.6 consider only site-correction energies E_i^c,

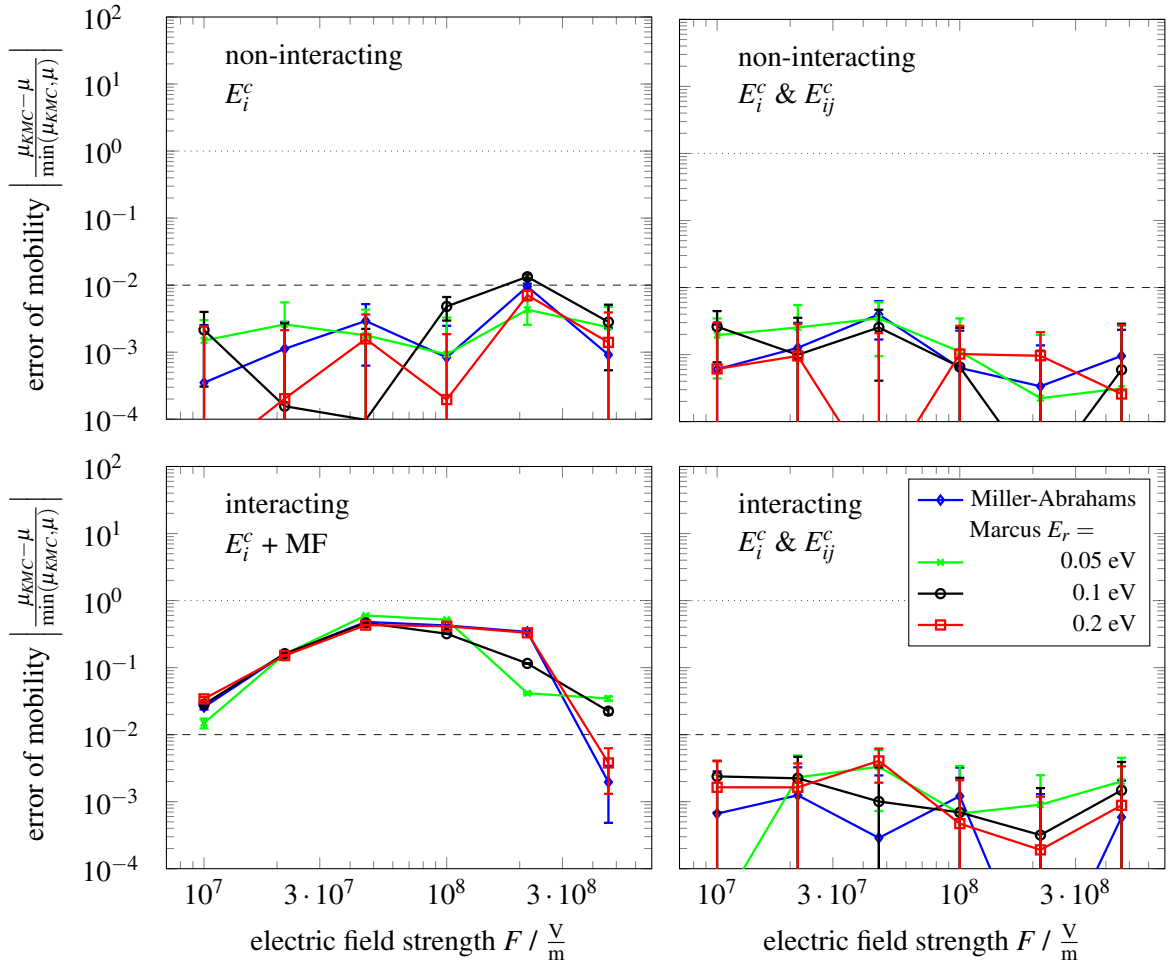

Figure 3.6: Error of the mobility evaluated with the correction energy concept with respect to the results from kinetic Monte Carlo simulations as a function of the applied external electric field strength F. Different curves refer to different hopping rates with the Miller-Abrahams rate equation, Equation (3.3), and Marcus rate equation for different reorganisations energies E_r, Equation (3.4). All simulations contain two charge carriers. The two upper panels omit interactions and the two lower panels include interactions. The correlation-correction energies E_{ij}^c are included in the two right panels, while in the two left panels, only site-correction energies E_i^c are considered. As the correct occupation statistics is evaluated for those simulations with only two charge carriers, the simulations containing the correlation-correction energies in the two right panels provide exactly the correct mobility with an error well below the dashed 1%-error line indicating the uncertainty of the KMC results. The individual uncertainties of the KMC results are indicated by errorbars. In the upper left panel, only a slightly increased error at $F = 2\cdot10^8\ \frac{\mathrm{V}}{\mathrm{m}}$ can be seen. For interacting simulations, the error of the mobility rises well above the 1% line, as seen in the lower left panel. But it still is below the dotted line at an error of 1, which means that the two determined mobilities for the CEC and KMC are within the same order of magnitude. Looking at the results for different hopping rates, the error is not affected significantly.

while the two right panels include also correlation-correction energies E_{ij}^c. As expected, the consideration of correlation-correction energies provides exactly the correct mobilities, for non-interacting simulations (upper right panel in Figure 3.6) as well as for interacting simulations (lower right panel in Figure 3.6), because all errors are well below the dashed line at $10^{-2} = 1\%$ indicating the KMC related uncertainty.

The non-interacting simulations, that neglect correlation-correction energies E_{ij}^c, in the upper left panel in Figure 3.6 show a slightly increased error for an electric field strength of $F = 2 \cdot 10^8 \ \frac{\mathrm{V}}{\mathrm{m}}$. Overall, this approximation still provides proper results. For interacting simulations, the error shown in the lower left panel in Figure 3.6 exhibits values well above the KMC uncertainties. Nevertheless, the error is still below the dotted line indicating an error of 1. So the results are still in the right order of magnitude, which might be precise enough for many applications.

None of the results, neither in Figure 3.5, nor in Figure 3.6, show a substantial dependence on the used rate equation (Miller-Abrahams or Marcus) or the chosen reorganisation energy E_r for Marcus rate. Hence, we will only focus on Miller-Abrahams rate equation in the following.

3.4.4 Multi-Charge Carrier Simulations

The last test of our new simulation technique examines the novel occupation statistics, considering Fermi-level shifts $\Delta E_{F,i}^{N_{cc}}$, by including multiple charge carriers $N_{cc} > 2$. The results, considering only site-correction energies E_i^c, are compared to Fermi-Dirac statistics. Figure 3.7 shows the error of the mobility of our CEC with respect to KMC results as a function of the electric field strength F for different amounts of charge carriers in the simulation going from $N_{cc} = 5$ corresponding to an average charge-carrier density of $\langle n \rangle = 5 \cdot 10^{-3}$ ccps (charge carriers per site) up to $N_{cc} = 100$ equivalent to a very high charge-carrier density of $\langle n \rangle = 10^{-1}$ ccps. All simulations were performed with the Miller-Abrahams rate equation, Equation (3.3).

Comparing the results for Fermi-Dirac statistics (two left panels in Figure 3.7) and the new occupation statistics (two right panels in Figure 3.7), we see that the error of the new occupation statistics always lies below the error of Fermi-Dirac statistics. For the non-interacting simulations (two upper panels in Figure 3.7), the new occupation statistics is much better for rather low charge-carrier densities $\langle n \rangle = 5 \cdot 10^{-3}$. For higher charge-carrier densities $\langle n \rangle > 2 \cdot 10^{-2}$, the two different occupation statistics become increasingly comparable. This behaviour is reasonable, because the approximation within Fermi-Dirac statistics is improving for increasing charge-carrier density. This also lines out that the occupation correlations discussed at the end of Chapter 3.2.4 are most important for low numbers of charge carriers in the simulation.

In contrast to the non-interacting simulations, for which the error is still acceptably low, the error of the interacting simulations is much higher (see lower panels in Figure 3.7). It goes beyond one order of magnitude difference between the mobility values suggested by KMC and our new occupation statistics (lower right panel in Figure 3.7) for the highest charge-carrier densities $\langle n \rangle \geq 5 \cdot 10^{-2}$. For Fermi-Dirac statistics (lower left panel in Figure 3.7), it exceeds even two orders of magnitude. The only values which might be acceptable for rough estimations of the mobility for interacting simulations are the simulations with the new occupation statistics for charge-carrier densities below $\langle n \rangle \leq 2 \cdot 10^{-2}$, for which the CEC-mobility is at least in the right order of magnitude.

In summary, our new correction energy concept provides reliable mobility values for non-interacting simulations up to high charge-carrier densities beyond $\langle n \rangle > 10^{-1}$ ccps and acceptable mobility values for interacting simulations with not too high charge-carrier densities below $\langle n \rangle \lesssim 10^{-2}$ ccps. The results

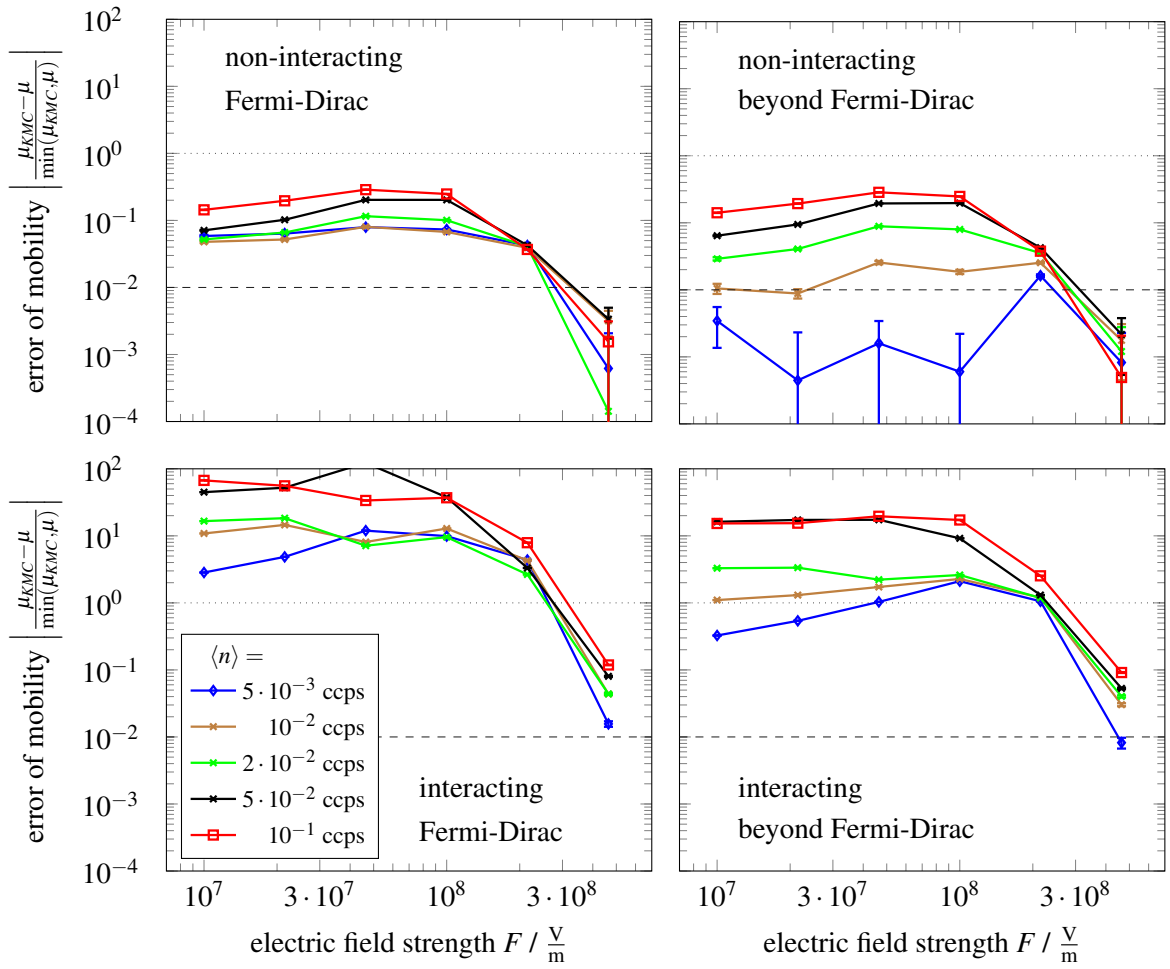

Figure 3.7: Error of the mobility of the correction energy concept with respect to accurate kinetic Monte Carlo simulation results as a function of the applied electric field strength F for different charge-carrier densities $\langle n\rangle$. The lowest charge-carrier density of $\langle n\rangle = 5\cdot10^{-3}$ ccps (charge carriers per site) corresponds to $N_{cc} = 5$ charge carriers in the simulation and $\langle n\rangle = 10^{-1}$ ccps to $N_{cc} = 100$. The two upper panels represent non-interacting simulations and the two lower panels interacting ones. For all simulations, only site-correction energies E_i^c are considered with the Miller-Abrahams rate equation, Equation (3.3), being applied. If interactions are considered, they are included by a mean-field approach. The two left panels show results received by assuming Fermi-Dirac occupation statistics and the two right panels by considering our new occupation statistics. For all simulations, the new occupation statistics shows a perceptible lower error compared to Fermi-Dirac statistics. Nearly all errors are above the uncertainty of the KMC results at about 1% (dashed line). Nevertheless, for the non-interacting simulations (upper two panels), the order of magnitude is still the right one with an error well below 1. For interacting simulations, the error is exceeding the dotted line at an error of 1 resulting in mobilities being wrong by approximately one order of magnitude for the highest charge-carrier densities for the new occupation statistics and two orders of magnitude for Fermi-Dirac statistics.

received with our correction energy concept require, from a computational point of view, much less effort compared to kinetic Monte Carlo simulations. Especially for low electric field strengths $F \lesssim 10^7\ \frac{\mathrm{V}}{\mathrm{m}}$, KMC has to perform an enormous amount of hops to converge whereas the CEC delivers results increasingly efficient with decreasing electric field. With further development, the correction energy concept is ought to be able to provide reliable mobility values even for interacting simulations with high charge-carrier densities beyond $\langle n\rangle > 10^{-2}$ ccps. The key to those reliable mobility values is the proper inclusion of

interactions and correlations. As the correction energy concept provides a method within which we can take a precise look at the effect of certain interactions and correlations on the mobility, it is possible to identify the most important interactions and correlations efficiently. The important interactions and correlations can then be directly included and the remaining interactions and correlations are treated with a mean-field-like approach. So it should be possible, within the framework of the correction energy concept, to, (i), identify and, (ii), include the most relevant interactions and correlations to get reliable mobility values even for high charge-carrier densities by only slightly increasing the computational effort.

4 Charge Transport in Bulk

Probably the most basic question regarding charge transport in organic semiconductor (OSC) devices is the question of charge transport in the bulk of the OSC. Regardless of the device, being it an organic light-emitting diode (OLED), an organic solar cells, or an organic thin-film transistor (OTFT), charge transport in the bulk of the material always plays an important role and often is one of the bottlenecks of the device performances.

There has already been a lot of research associated with charge transport in the bulk of amorphous materials like OSCs, on the experimental side as well as on the theoretical side. [8–17] By now, it is known that the bulk mobility shows a pronounced dependence on the applied electric field F as well as on the charge-carrier density $\langle n \rangle$. The field dependence is often described with a Poole-Frenkel like behaviour [32,33] and the charge-carrier density was suggested to show an exponential dependence $\langle n \rangle^{\gamma}$ with an exponent γ as discussed in Chapter 2. This exponential behaviour was suggested by variable-range hopping (VRH) in combination with percolation theory [34] as well as by multiple trapping and release (MTR) [35]. In Chapter 2, we discussed that this simplification of the charge-carrier-density dependence of the mobility does not apply to the full range of charge-carrier densities observed in an OTFT. Other charge transport models provide more reasonable estimates for the electric field and charge-carrier-density dependence of the mobility. [11]

From the perspective of the correction energy concept, introduced in Chapter 3, we are able to interpret the electric field and charge-carrier-density dependence of the mobility in a completely new way. The development of this new perspective will start by exploring the nature of the correction energies in Chapter 4.1. The knowledge gained from this exploration is utilised to develop a way of thinking about charge transport reminiscent to water running through basins in Chapter 4.2. This new way of thinking is not in contradiction with the common way of thinking in deepest traps and most significant barriers. Both pictures can benefit from one another. We demonstrate an example for the usefulness of the basin picture by identifying charge transport regimes seen in the charge mobility in Chapter 4.3.

4.1 The Nature of Correction Energies

In Chapter 3, we already noticed that the correction energies E_i^c are closely related to the applied electric field F. To get an idea of the relation between correction energies and electric field, we will discuss a one-dimensional toy system with only one charge carrier and an intermediate applied electric field of $F = 10^7 \ \frac{\mathrm{V}}{\mathrm{m}}$. In Figure 4.1, all energies appearing in a system are visualised.

The illustrative toy system shown in Figure 4.1 is one-dimensional and periodic with 51 sites and $a = 1$ nm spacing between the sites. The site energies ε_i are randomly drawn from a Gaussian distribution with disorder $\sigma = 100$ meV. The black horizontal lines with grey shading underneath shown in Figure 4.1 represent the sum of the site energy and the electric field energy $\varepsilon_i - eFx_i$. The underlying trend of the electric field energy is indicated as a red line in Figure 4.1. The blue line with dots shows the site-correction energy and the electric field energy $E_i^c - eFx_i$ and the difference between the blue line and the red line is the site-correction energy E_i^c. To get the site-correction energies E_i^c, we restricted the maximum hopping distance to nearest neighbours only and applied Miller-Abrahams rate equation, Equation (3.3), with a charge delocalisation constant $\alpha = 5 \ \mathrm{nm}^{-1}$, a hopping prefactor $\nu_0 = 22.497$ THz, and a temperature $T = 300$ K.

The correction energies E_i^c are predominantly determined by the electric field strength F. When no

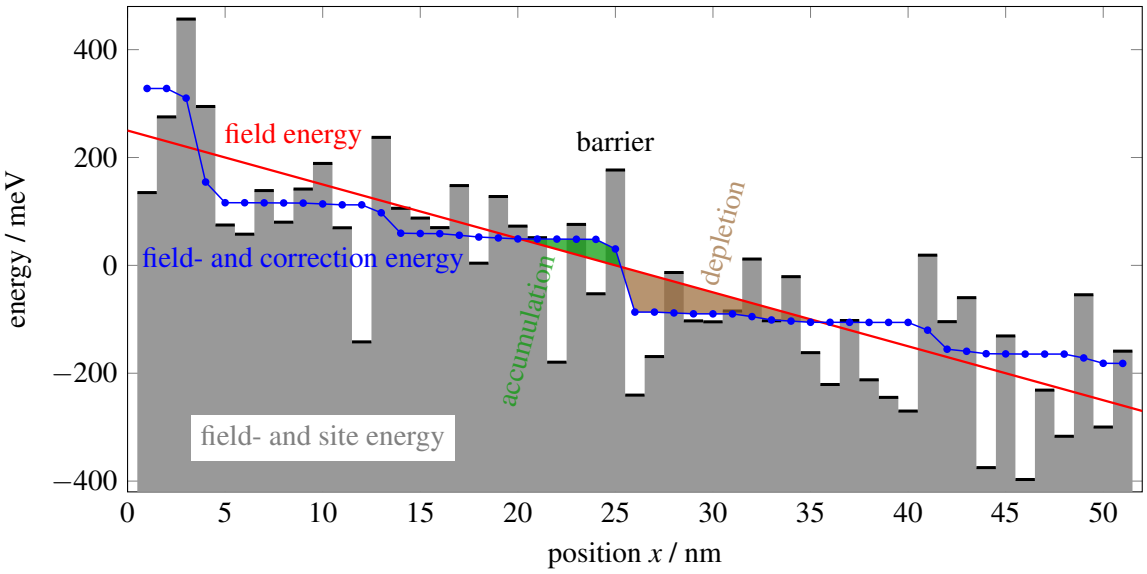

Figure 4.1: Field-induced charge rearrangement captured by correction energies for a one-dimensional, periodic system with 51 sites at positions $x = 1$ nm to $x = 51$ nm. Black horizontal lines with grey shading underneath indicate the sum of the randomly chosen site energy and the field energy $\varepsilon_i - eFx_i$ of site i at position x_i. The site plus field energies follow the trend of the electric field energy $-eFx$ shown as a red line. In blue, the sum of the site-correction energy and the field energy $E_i^c - eFx$ is drawn. The difference between the red and the blue line represents the site-correction energy E_i^c. A positive site-correction energy E_i^c indicates charge accumulation compared to the case without an electric field $F = 0 \frac{\mathrm{V}}{\mathrm{m}} \rightarrow E_i^c = 0$ eV and a negative E_i^c indicates charge depletion. In front of the barrier at position $x = 25$ nm, charge carriers get stuck and we observe a charge accumulation (green shaded area) suggested by the site-correction energies. Right behind the barrier, we see charge depletion (brown shaded area). In front of and behind the barrier refers to the transport direction, which is following decreasing energies from left to right.

electric field is applied, the correction energies are zero $E_i^c = 0$ eV. As soon as we apply an electric field, the correction energies become non-zero and change the occupation of the sites, because the correction energies E_i^c enter the exponent in the occupation statistics $\beta(\varepsilon_i - E_i^c)$, cf. Chapter 3.2. A negative correction energy $E_i^c < 0$ eV indicates that the site is less occupied than without an electric field. A positive correction energy $E_i^c > 0$ eV implies an increase of the charge-carrier density of the site i due to the electric field. Looking at Figure 4.1, this means that when the blue line is above the red line (positive $E_i^c > 0$ eV), the electric field creates a charge accumulation at the affected site i. When the blue line is below the red line (negative $E_i^c < 0$ eV), the field induces a charge depletion. An example for charge accumulation and depletion is shaded green and brown, respectively. Marked accumulation and depletion occur, for example, around barriers like site 25 at $x = 25$ nm, which is the highest energy that has to be overcome in this region. As the transport direction is from left to right in Figure 4.1, the charge carriers get stuck on the left side of the barrier before overcoming it, creating a region of charge accumulation on the left side of the barrier. After overcoming the barrier, charge carriers can move away from it more easy due to the electric field and get stuck in front of the next barrier resulting in this pattern of depletion and accumulation regions around barriers.

When looking even closer at the blue line in Figure 4.1, we see that this blue line is nearly flat in extended regions and those flat regions are separated by steep steps. This behaviour is reminiscent of a water level with water running through basins and waterfalls between the basins. The steps of the blue

line exclusively appear at local barriers of the energy landscape. So we can think of our energy landscape as basins that are separated by barriers.

This picture of basins and barriers reveals the nature of the correction energies. When no electric field is applied $F = 0\ \frac{\mathrm{V}}{\mathrm{m}}$, all sites are in balance, locally and globally (cf. Chapter 3.1). Balance relies on steady-state conditions, which means that a charge carrier must have a lot of time to explore the energy landscape to reach balance. A consequence of this local and global balance is, that all correction energies are zero $E_i^c = 0$ eV for a vanishing field. Hence, the flat correction energies indicate balance.

Applying an electric field adds a tilt to the energy landscape which makes the charge carriers, on average, move in a preferential direction. Balance in this case means that the correction energies in combination with this tilt in energy due to the electric field would be flat. The field- and correction energy cannot be flat everywhere due to the violation of energy conservation at the boundaries, which would create artificial steps in the field- and correction energy at the boundary. Nevertheless, the field- and correction energy is flat within the basins, which means that a charge carrier spends a lot of time in the basin establishing nearly steady state. Crossing the barrier between basins is done within one hop. This quick transition is the position at which balance is broken, which creates the steps at the barriers between the flat region of the blue line in Figure 4.1. In summary, the nature of correction energies lies in establishing balance within basins in the energy landscape and breaking the balance at the barriers separating those basins. This basically refers to the structure of ramps and cliffs observed by Cottaar *et al.* in [100].

4.2 Barriers, Basins and Clusters

The one-dimensional toy system in Figure 4.1 taught us to think in terms of basins, in which charge carrier reside for a certain time, and barriers separating those basins, at which charge carriers have to work hard to overcome them. When overcoming a barrier, the next basin is entered and a charge carrier hops around for some time in this next basin. This strongly simplified picture of the energy landscape with basins and barriers is shown as a cartoon in Figure 4.2.

In the left panel in Figure 4.2, the basin and barrier structure is visualised without an electric field. The black line illustrates a cartoon of the energy landscape with lower site energies in the basin and a barrier energy E_B separating the basins. The barrier energy E_B is indicated by the grey dotted line. The red line marks the most likely energy of the charge carriers E_{ML} within the system. This energy E_{ML} is the energy at which the occupied density of states (ODOS) reaches its maximum. The ODOS can be approximated by multiplying the density of states (DOS) with the Fermi-Dirac statistics:

$$\mathrm{ODOS}(E) = \frac{\mathrm{DOS}(E)}{1+\exp\left(\frac{E-E_{F,0}^{N_{cc}}}{k_B T}\right)}, \qquad \mathrm{ODOS}(E_{ML}) = \max_E \mathrm{ODOS}(E). \tag{4.1}$$

The Fermi-Dirac statistics contains the temperature T and the Boltzmann constant k_B. The Fermi level $E_{F,0}^{N_{cc}}$ is determined by the number of charge carriers N_{cc} in the simulation and the DOS. In our case, the DOS is given by a Gaussian distribution. In total, the most likely energy of the charge carriers E_{ML} is fixed by the DOS, the number of charge carriers N_{cc}, and the temperature T. Increasing the number of charge carriers N_{cc}, equivalent to increasing the charge-carrier density $\langle n \rangle = \frac{N_{cc}}{N_s}$ (N_S is the number of sites), raises the most likely energy of the charge carriers E_{ML}.

The right panel in Figure 4.2 shows the same energy landscape as the left panel when an electric field

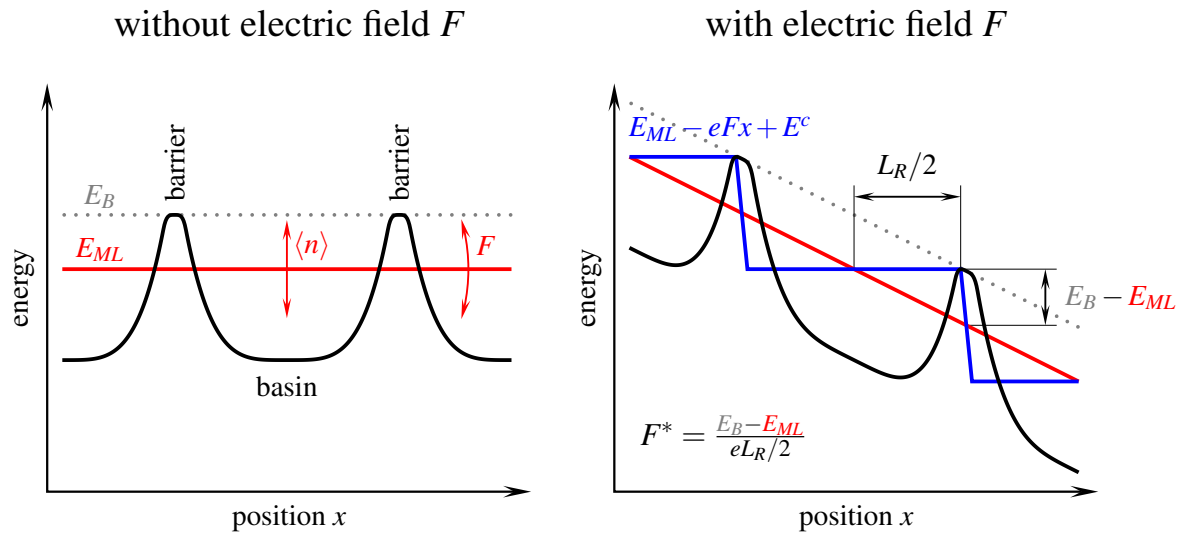

Figure 4.2: Cartoon of a one-dimensional energy landscape in the form of basins and barriers (black line). The energy level of the barriers E_B is indicated as a grey dotted line and the most likely energy of the charge carriers E_{ML} as red line. The blue line represents the field- and correction energy $E^c - eFx$ relative to the most likely energy of the charge carriers E_{ML}. In the left panel, no electric field is applied and in the right panel, the tilt in the energy landscape reflects the applied electric field F. The most likely energy of the charge carriers E_{ML} is shifted up or down if the charge-carrier density $\langle n \rangle$ is increased or decreased, respectively. Due to balance, the blue line in the right panel represents a local version of the most likely energy of the charge carriers. If the blue line reaches the barrier, charge carriers can easily overcome the barrier and charge transport gets more efficient at that condition. This means that a transition field F^* can be estimated, around which a transition between charge transport regimes happens. This transition field F^* is determined by the barrier energy E_B, the most likely energy of the charge carriers E_{ML} and the size of the basin as the transport-relevant region L_R.

F is applied. This tilts the whole energy landscape and requires the consideration of correction energies E^c. The blue line in the right panel in Figure 4.2 indicates the field- and correction energy $E^c - eFx$ relative to the red line. This red line indicates the most likely energy of the charge carriers E_{ML} from the left panel tilted by the field energy. As discussed in Chapter 4.1, the field- and correction energy represents a local variation of the occupation comparable to a local Fermi level. This means that the blue line in the right panel in Figure 4.2 indicates a local version of the most likely energy of the charge carriers. When the blue line reaches the energy of the barrier, it becomes very likely, that the barrier site is occupied. As a consequence, overcoming the barrier becomes also very likely and charge transport will get very efficient. In our analogy of water running through basins, this would mean that the water flows efficiently as soon as the water level is high enough so that all basins are filled. From the cartoon in Figure 4.2, we can make an estimate for a transition field F^* between charge transport regimes from the barrier energy E_B, the most likely energy of the charge carriers E_{ML} and half the size of the basin as the transport-relevant region $\frac{L_R}{2}$

$$F^* = 2\frac{E_B - E_{ML}}{eL_R} \tag{4.2}$$

with the elemental charge e. At this transition field F^*, we expect a significant increase of the mobility μ.

As we are interested in three-dimensional systems with randomly chosen site energies, we have to transfer the estimate for the transition field F^*, Equation (4.2), to such a system. The most relevant barrier E_B of such a system is the highest barrier energy of the lowest energy pathway in field direction. This is the highest barrier energy that has to be overcome by a charge carrier when travelling through the entire system in field direction along the easiest possible pathway. This easiest or lowest energy pathway possesses a maximum energy (the highest barrier energy), which is the lowest maximum energy of all pathways. This highest energy of the lowest energy pathway is associated with the barrier energy E_B in Equation (4.2). Implementing a search algorithm for the highest energy of the lowest energy pathway can be done by sorting all site energies ε_i. The lowest of all site energies creates the first path. When including the site with the lowest energy of the remaining sites one after the other, we can distinguish three possibilities. First, if no nearest neighbour belongs to a path, the site creates a new path. Second, if one or more nearest neighbours belong to the same path, the site is assigned to this path. Third, if nearest neighbours belong to different paths, the paths are linked and merged to one bigger path. At a certain energy, a closed path across the boundary of the system in field direction is established. The energy where this happens is exactly the highest barrier energy of the lowest energy pathway E_B.

The next ingredient for the estimate for a transition field F^* is the most likely energy of the charge carriers E_{ML}. This energy E_{ML} is estimated via Equation (4.1), e.g., by calculating the derivative of the ODOS and using a simple bisection method to find the energy at which the derivative is zero.

To get the estimate for a transition field F^*, the size of the transport-relevant regions L_R is the last remaining ingredient. The evaluation of this size L_R for a three-dimensional system requires some more effort. We start our search for the size of the transport-relevant regions L_R by defining a basin as a region with only one local energy minimum in the randomly chosen site energies ε_i. The basins are separated from each other by barrier sites, which are defined as sites that can be related to at least two local energy minima. This means when continuously going down in energy from a barrier site in different directions, one can end up in at least two different local energy minima. An implementation to get this basin structure could start by sorting all site energies ε_i. The lowest of all energies creates the first basin. Afterwards, all sites are included in the basin structure one after the other. This inclusion is done stepwise by selecting the lowest energy of the remaining sites and looking at the nearest neighbours of this site. If, (i), none of the nearest neighbours is included in the basin structure, neither as a site belonging to a basin, nor as a barrier site, the new site is a local minimum and creates a new basin. If, (ii), at least one of the nearest neighbours is a barrier site, the new site is associated to at least two basins and is a barrier site as well. If, (iii), the nearest neighbour sites that are already included in the basin structure contain only one basin, the new site is added to this basin. If, (iv), the nearest neighbour sites contain sites associated to more than one basin, the new site is a barrier site.

This definition of basins creates a basin structure, in which more than half of the basins contain only one site for an uncorrelated Gaussian disorder in three dimensions. As a consequence, the basin size in field direction of most basins is only one site $a = 1$ nm (see black dashed line in the right panel in Figure 4.3). Basins with a size of one site are not really affected by the field-induced charge rearrangements described by correction energies. So they are definitely not the transport-relevant regions that we are searching for to get L_R. The one-dimensional system in Figure 4.1 also suggests, that we have to consider larger regions containing more than one local energy minimum. To find the size of the transport-relevant regions L_R, we form clusters out of the basins. When creating the basin structure, we registered the barrier energies between basins and stored the lowest barrier energies between basins in

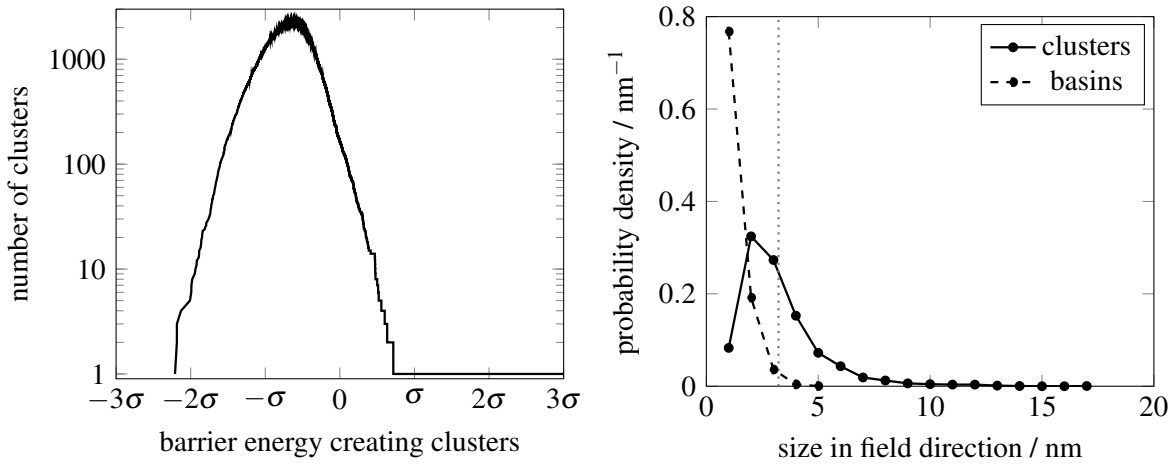

Figure 4.3: The left panel shows the evolution of the number of clusters which are created by merging basins linked by barriers up to a certain barrier energy as a function of this barrier energy. At a certain energy, the first cluster is created by the barrier between basins with the lowest energy followed by a rapid increase of the number of clusters. For a high barrier energy, clusters are merged resulting in a decrease in the number of clusters until only one big cluster is left. The right panel shows the probability distribution of the size of clusters in field direction at the maximum number of clusters (solid black line) and the probability distribution of the size of basins in field direction (black dashed line). The average cluster size $L_R = 3.22$ nm refers to the size of the transport-relevant regions and is marked with a vertical grey dotted line. The investigated system includes an uncorrelated Gaussian DOS and $51 \times 51 \times 51$ sites on a simple cubic lattice.

a list. To build clusters, we take the lowest barrier energy in this list and merge the basins linked by it into a cluster. Continuing to create clusters by including barrier energies with increasing energy, merging more and more basins, raises the number of clusters for low barrier energies, illustrated in the left panel in Figure 4.3. At a certain barrier energy, the increase of the number of clusters saturates and reaches a maximum before it goes down because clusters are merged to larger clusters by barriers until only one huge clusters is left.

Looking at this evolution of the number of clusters as a function of the barrier energy up to which basins and clusters are merged together (left panel in Figure 4.3), the question is: Which cluster size is correct for our transport-relevant regions? On the one hand, the transport-relevant regions should be extended regions to be able to profit from the field-induced charge rearrangement suggested by the correction energies. On the other hand, the extended regions should not have the size of the total system, so the regions should still be separated by intermediate barriers. Our suggested compromise to get the transport-relevant cluster size is to take the cluster distribution corresponding to the barrier energy at which the evolution of the number of clusters reaches its maximum (cf. left panel in Figure 4.3). The probability distribution of the clusters size in field direction for this choice of the transport-relevant cluster size can be seen as a black solid line in the right panel in Figure 4.3. In comparison to the probability distribution of the basin size in field direction (black dashed line), the probability distribution of the transport-relevant cluster size in field direction shows significant values above one site $a = 1$ nm. The average cluster size in field direction $L_R = 3.22$ nm is indicated by a vertical grey dotted line in the right panel in Figure 4.3.

With those recipes to determine the barrier energy, E_B, the most likely energy of the charge carriers, E_{ML}, and the size of the transport-relevant regions, L_R, we collected all ingredients to calculate the tran-

sition field, F^*, Equation (4.2), around which we expect the mobility to change significantly. All those ingredients are very simple to extract from the energy landscape. The computationally most expensive step is sorting the site energies ε_i of all sites i and of all barrier energies, which is an $\mathcal{O}(N_s \log N_s)$ process. All remaining steps are only $\mathcal{O}(N_s)$. So the calculation of the transition field F^* is computationally very cheap.

4.3 Bulk Mobility and Transport Regimes

The transition field F^* estimated in Chapter 4.2, Equation (4.2), is supposed to indicate the electric field strength around which a transition between transport regimes happens. This transition is supposed to result in a significant increase of the bulk mobility. To investigate the bulk mobility in this chapter, simulations are performed. The corresponding parameters are specified In Chapter 4.3.1. A first example for the evolution of the bulk mobility with respect to the applied electric field and the charge-carrier density for an exemplary energy landscape is discussed in detail in Chapter 4.3.2. In Chapter 4.3.3, the influence of the energetic disorder on the mobility is investigated. The mobility shows a pronounced dependence on the randomly chosen energy landscape, which is illustrated in Chapter 4.3.4. This pronounced dependence on the energy landscape is analysed in Chapter 4.3.5, in which different charge transport regimes are discussed. Finally, the evolution of the mobility is explored for different hopping radii and different rate equations in Chapter 4.3.6.

4.3.1 The Model System

The system to check the appearance of the transition between mobility regimes in Chapter 4.3 is, in principle, always the same. If not specified explicitly in the corresponding chapter, the parameters of the system are stated in the following. We simulate a $51 \times 51 \times 51$ sites simple cubic lattice with lattice constant of $a = 1$ nm and hopping restricted to nearest neighbours only. The rates are calculated by the Miller-Abrahams rate equation, Equation (3.3), with a hopping prefactor of $\nu_0 = 22.497$ THz, a charge delocalisation constant of $\alpha = 5$ nm^{-1} and a temperature of $T = 300$ K. The site energies are randomly drawn from a Gaussian distribution with width $\sigma = 100$ meV. No interactions are considered. The bulk mobility μ was evaluated with our new correction energy concept (CEC) for a wide range of applied electric fields F and charge-carrier densities $\langle n \rangle = \frac{N_{cc}}{N_s}$. In the CEC, site-correction energies and our new occupation statistics was utilised.

4.3.2 Exemplary Energy Landscape

To perform a first test of the transition field F^* and discuss the evolution of the bulk mobility with respect to the electric field and the charge-carrier density, we selected one particular energy landscape out of 25 different energy landscapes that we simulated. This particular energy landscape reflects the average behaviour of the 25 simulated ones. With average behaviour, we mean that the evolution of the mobility of this particular energy landscape is close to the mobility evolution observed when we average over all 25 energy landscapes. Investigating this exemplary energy landscape has the advantages that, (i), less simulations are required when changing parameters and, (ii), the validity of the CEC results can be directly tested by accurate kinetic Monte Carlo (KMC) simulations of exactly the same system. The lines in Figure 4.4 represent the mobility μ as a function of the electric field F for different amounts of charge carriers N_{cc} evaluated with the CEC and the crosses indicate the validation via computationally

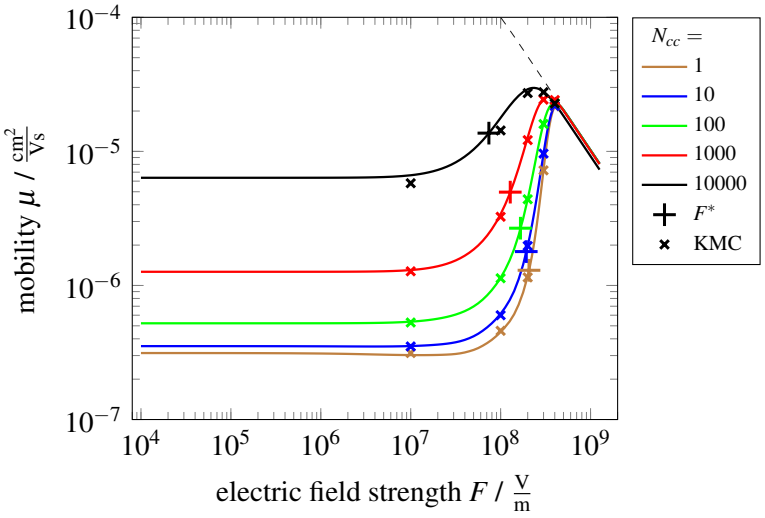

Figure 4.4: Bulk mobility μ as a function of the applied external electric field F for different amounts of charge carriers $N_{cc} = 1$ to $N_{cc} = 10000$ in the system with $51 \times 51 \times 51$ sites, a Gaussian DOS with disorder $\sigma = 100$ meV, nearest neighbour hopping only and Miller-Abrahams rate equation. The energy landscape is one representative example out of 25 tested energy landscapes. The lines are calculated with our CEC and the crosses are KMC results for validation. The dashed line indicates the isoenergetic mobility and the plus signs mark the transition field F^*. Around the transition field F^*, the predicted increase of the mobility appears.

expensive KMC simulations. The CEC and KMC results match very well, only the black line of the CEC for the highest charge-carrier density lies slightly above the black crosses of the KMC simulation results.

The values for the electric field are in a range of $F = 10^4 \ \frac{\text{V}}{\text{m}}$ to $F = 10^9 \ \frac{\text{V}}{\text{m}}$. The amounts of charge carriers N_{cc} in the range of $N_{cc} = 1$ to $N_{cc} = 10000$ refer to a charge-carrier density of $\langle n \rangle \approx 7.54 \cdot 10^{-6}$ charge carriers per site (ccps) to $\langle n \rangle \approx 7.54 \cdot 10^{-2}$ ccps, respectively. One site has a volume of $a^3 = 1 \text{ nm}^3$ in our system, so the charge-carrier density with respect to the volume is $\frac{\langle n \rangle}{a^3} \approx 7.54 \cdot 10^{-6} \text{ nm}^{-3}$ to $\frac{\langle n \rangle}{a^3} \approx 7.54 \cdot 10^{-2} \text{ nm}^{-3}$, respectively.

All curves illustrating the bulk mobilities μ for different amounts of charge carriers in the simulation shown in Figure 4.4, in principle, exhibit a similar dependence on the electric field F. For low electric fields $F \lesssim 10^7 \ \frac{\text{V}}{\text{m}}$, the mobility μ is constant. For high electric fields $F \gtrsim 5 \cdot 10^8 \ \frac{\text{V}}{\text{m}}$, the energy contribution due to the electric field dominates the energy landscape and the mobility converges to the isoenergetic mobility (dashed line in Figure 4.4). This isoenergetic mobility is the mobility of a system without energetic disorder ($\varepsilon_i = 0$ eV for all sites i) and it decreases due to the chosen rate equation. Hops downwards always happen with the same frequency for Miller-Abrahams rate equation, cf. Equation (3.3). This means that increasing the electric field does not make the charge carriers move faster, resulting in a saturation of the drift velocity for high electric fields. Hence, the isoenergetic mobility for Miller-Abrahams rate equation is proportional to $\mu \sim F^{-1}$ for high electric fields. For intermediate electric fields $F \gtrsim 10^7 \ \frac{\text{V}}{\text{m}}$ and $F \lesssim 5 \cdot 10^8 \ \frac{\text{V}}{\text{m}}$, the mobility significantly increases. The electric field around which this increase appears matches nicely with the estimate for the transition field F^*, which is indicated by a plus sign for each charge-carrier density in Figure 4.4.

With increasing charge-carrier density, the mobility at low electric fields $F \lesssim 10^7 \ \frac{\text{V}}{\text{m}}$ increases. This is in line with our picture of barriers and basins, because the most likely energy of the charge carriers E_{ML} increases with increasing charge-carrier density $\langle n \rangle$ and, hence, the remaining barrier energy $E_B - E_{ML}$

that has to be overcome by the charge carriers decreases, on average. In the isoenergetic limit, the charge-carrier density $\langle n \rangle$ plays a minor role and all curves of the mobility for different charge-carrier densities approximately converge to the same isoenergetic mobility for high fields $F \gtrsim 5 \cdot 10^8 \frac{\mathrm{V}}{\mathrm{m}}$. As a consequence, the raise in mobility at the transition field F^* varies from nearly two orders of magnitude for $N_{cc} = 1$ to approximately a factor of 5 for $N_{cc} = 10000$.

4.3.3 Influence of the Energetic Disorder

To explore the influence of the energetic disorder σ, Figure 4.5 shows mobilities for different values of σ as a function of the applied electric field F and the number of charge carriers $N_{cc} = 1$ to $N_{cc} = 10000$.

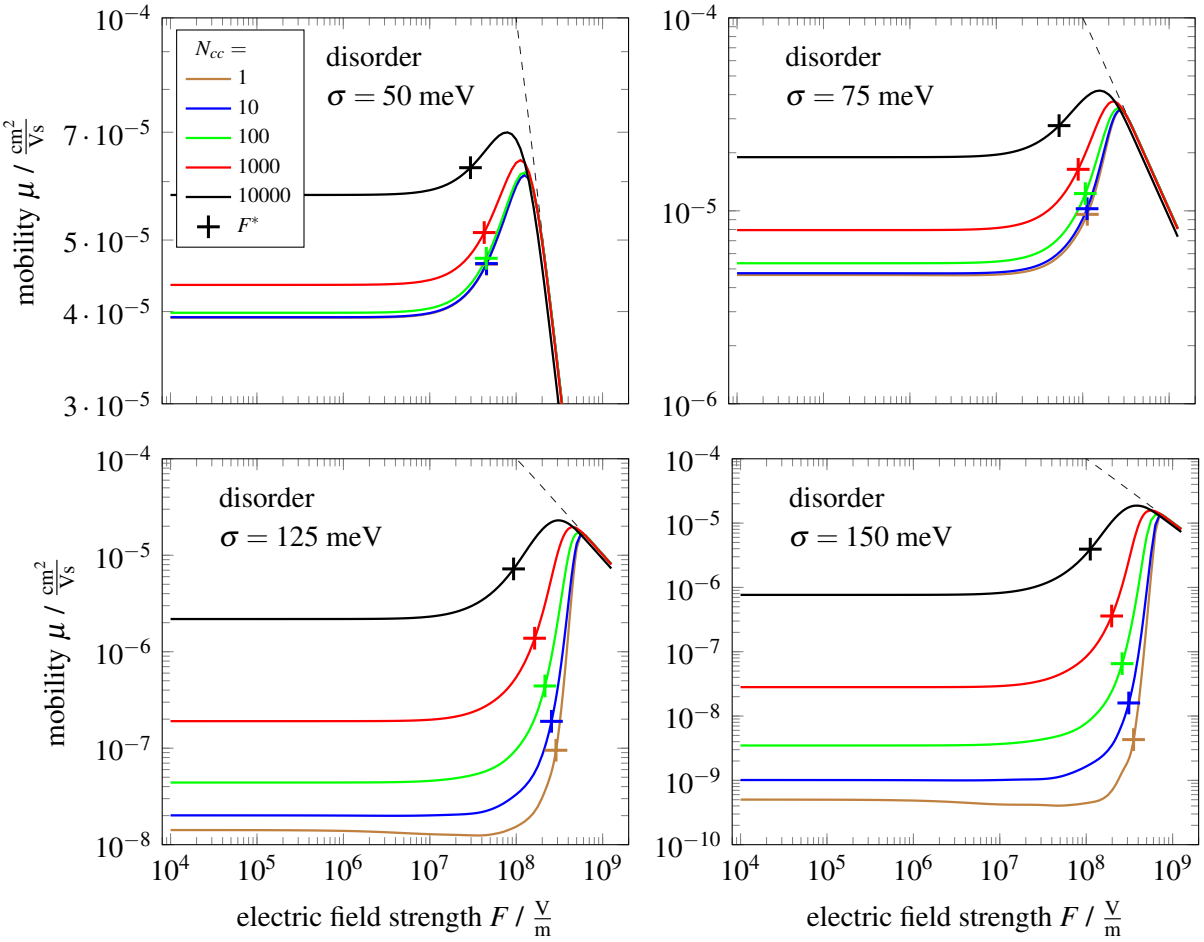

Figure 4.5: Bulk mobility μ as a function of the applied external electric field F for different amounts of charge carriers N_{cc}. The system is the same as simulated in Chapter 4.3.2 with the energy landscape being scaled to receive different energetic disorders σ. The energetic disorder is $\sigma = 50$ meV and $\sigma = 75$ meV for the upper left and upper right panel and $\sigma = 125$ meV and $\sigma = 150$ meV for the lower left and lower right panel, respectively. Note that the limits of the axis of the mobility change considerable for different energetic disorders σ. The general field dependence of the mobility is the same as in Figure 4.4. The estimate of the transition field F^* (marked with plus sign) matches the field around which the mobility increases. The higher the disorder σ and the less charge carriers N_{cc} in the system, the larger the ratio of maximum and low field minimum of the mobility, going from a factor of 1.2 for $\sigma = 50$ meV and $N_{cc} = 10000$ to a factor of 10^4 for $\sigma = 150$ meV and $N_{cc} = 1$. The isoenergetic mobility is indicated as dashed line in each panel.

The energy landscape is the same as the exemplary energy landscape selected in Chapter 4.3.2, but with a different disorder σ of the Gaussian DOS. This means the site energies ε_i are multiplied by $\frac{\sigma_{\text{new}}}{\sigma_{\text{old}}}$ with the old disorder $\sigma_{\text{old}} = 100$ meV and the new disorder $\sigma_{\text{new}} = \sigma$. The upper left panel in Figure 4.5 shows the mobility for a system with disorder $\sigma = 50$ meV, the upper right for $\sigma = 75$ meV, the lower left for $\sigma = 125$ meV, and the lower right for $\sigma = 150$ meV. The dashed line in Figure 4.5, indicating the isoenergetic limit of the mobility, is always the same in all panels, but appears different due to the different limits of the axis.

The general shape of all mobility curves with respect to the electric field dependence shown in Figure 4.5 is the same as discussed in Chapter 4.3.2. The estimate for the transition field F^*, discussed in Chapter 4.2, Equation (4.2), matches nicely with the electric field, around which the increase in mobility happens, for all energetic disorders σ and all numbers of charge carriers N_{cc} in the system. Note that this transition field F^* is significantly changing from $F^* \approx 3.0 \cdot 10^7 \ \frac{\text{V}}{\text{m}}$ for $\sigma = 50$ meV and $N_{cc} = 10000$ to $F^* \approx 3.5 \cdot 10^8 \ \frac{\text{V}}{\text{m}}$ for $\sigma = 150$ meV and $N_{cc} = 1$.

Comparing the mobilities for the different energetic disorders σ shown in the four panels of Figure 4.5, the most significant difference between them is the ratio of maximum to minimum mobility. In this context, the minimum mobility is the mobility for a low electric field and the lowest number of charge carriers $N_{cc} = 1$ and the maximum mobility appears in the curve for the largest amount of charge carriers $N_{cc} = 10000$. With a total range of the mobility between $\mu \approx 4 \cdot 10^{-5} \ \frac{\text{Vs}}{\text{cm}^2}$ and $\mu \approx 7 \cdot 10^{-5} \ \frac{\text{Vs}}{\text{cm}^2}$, the mobility for the lowest energetic disorder $\sigma = 50$ meV shows a very weak dependence on the electric field F and the charge-carrier density $\langle n \rangle$ (upper left panel in Figure 4.5). This dependence of the mobility on the electric field and the charge-carrier density increases with increasing disorder σ. For the highest energetic disorder $\sigma = 150$ meV, the mobility exhibits a very pronounced dependence, with a mobility in the range of $\mu \approx 4 \cdot 10^{-10} \ \frac{\text{Vs}}{\text{cm}^2}$ and $\mu \approx 2 \cdot 10^{-5} \ \frac{\text{Vs}}{\text{cm}^2}$ (lower right panel in Figure 4.5).

Our perspective of basins and barriers enables an interpretation of the significant increase of the field and charge-carrier-density dependence of the mobility with increasing energetic disorder σ. For low energetic disorders σ, the barrier energy $E_B - E_{ML}$, that has to be overcome by charge carriers for low electric fields, is much lower due to a much smaller spread of the site energies ε_i. Hence, the charge transport for low σ is already rather efficient and an increase of the electric field does not improve it significantly. Regarding the charge-carrier-density dependence of the mobility, the most likely energy of the charge carriers E_{ML} plays an important role. With increasing disorder σ, the sensitivity of E_{ML} with respect to the charge-carrier density significantly increases. This results in a larger range for the barrier energy $E_B - E_{ML}$ with respect to the charge-carrier density for larger disorder σ and a subsequent larger range for the mobility.

4.3.4 Outliers and Average

The mobility is not only depending on the disorder σ, it also depends notably on the random choice of the energy landscape. Different energy landscapes with the same disorder σ can result in distinctly different values for the mobility. In the upper panels of Figure 4.6, two further examples of the 25 different energy landscapes with a disorder of $\sigma = 100$ meV are shown. For those examples, additional features appear for the lowest charge-carrier density (brown lines) between $F = 10^7 \ \frac{\text{V}}{\text{m}}$ and $F = 10^8 \ \frac{\text{V}}{\text{m}}$. The example energy landscapes represent the maximum outliers out of the 25 simulated ones with a significantly increasing mobility at $F = 10^7 \ \frac{\text{V}}{\text{m}}$ in the upper left panel in Figure 4.6 and a significantly decreasing mobility at the same field in the upper right panel in Figure 4.6. For higher charge-carrier

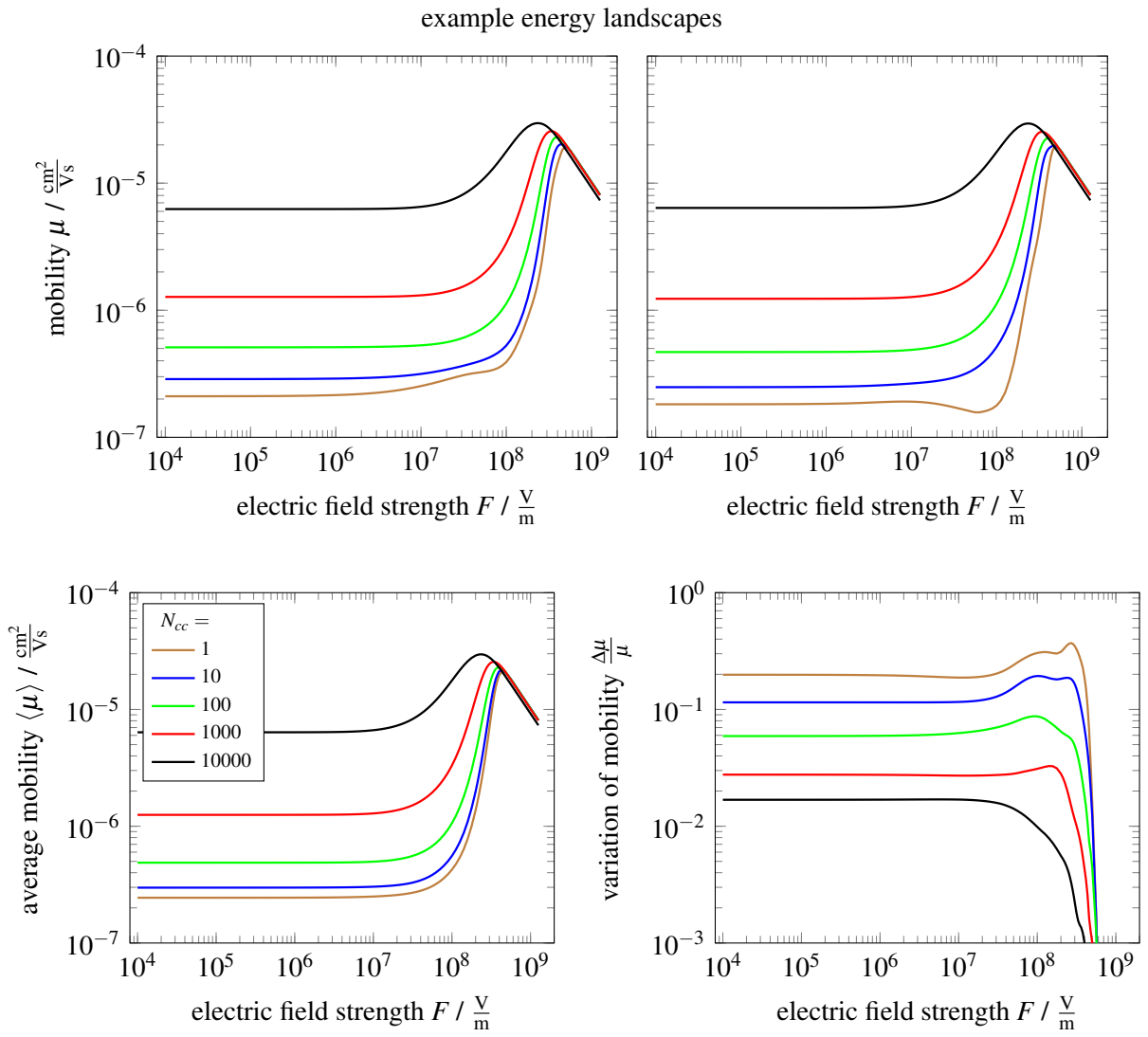

Figure 4.6: The upper panels show the bulk mobility μ as a function of the electric field F and the amount of charge carriers N_{cc} for two example energy landscapes selected from the 25 simulated ones. The lower left panel shows the mobility $\langle\mu\rangle$ averaged over the 25 different energy landscapes and the lower right panel shows the relative variation of the mobility $\frac{\Delta\mu}{\mu}$ of those 25 different energy landscapes. The system is the same as in Chapter 4.3.2 with an energetic disorder of $\sigma = 100$ meV. Additional features appear in the example energy landscapes (upper panels) between an electric field of $F = 10^7 \frac{V}{m}$ and $F = 10^8 \frac{V}{m}$ for the lowest amount of charge carriers $N_{cc} = 1$ (brown curves). In the mobility $\langle\mu\rangle$ averaged over all energy landscapes (lower left panel), those features disappear. The variation of the mobility (lower right panel) is highest for the lowest charge-carrier density with a slight increase in the region of the significant mobility raise for not too high charge-carrier densities $N_{cc} < 10000$.

densities, those features are smoothed and disappear. The lowest charge-carrier density with only one charge carrier in the system is most affected by the deepest trap, which varies from energy landscape to energy landscape. So it is quite likely that this deepest trap is responsible for the occurring features (further discussed in Chapter 4.3.5).

When averaging the mobility $\langle\mu\rangle$ over different energy landscapes, the features at electric fields $F = 10^7 \frac{V}{m}$ to $F = 10^8 \frac{V}{m}$ disappear (lower left panel in Figure 4.6). So the energy landscapes with increasing mobility and decreasing mobility around $F = 10^7 \frac{V}{m}$ seem to be equiprobable. In the lower

right panel in Figure 4.6, the relative variation of the mobility

$$\frac{\Delta\mu}{\mu} = \sqrt{\frac{\langle\mu^2\rangle}{\langle\mu\rangle^2} - 1} \tag{4.3}$$

is plotted as a function of the applied electric field F and the amount of charge carriers N_{cc}. The variation of the mobility significantly decreases with increasing charge-carrier density due to the reduction of the influence of the deepest trap with increasing N_{cc}. At the electric field around which the significant increase of the mobility appears, $F \approx 10^8 \frac{\mathrm{V}}{\mathrm{m}}$, the variation of the mobility is higher for amounts of charge carriers below $N_{cc} < 10000$. This peaks are caused by the fact, that the highest barrier energy of the lowest energy pathway slightly changes from energy landscape to energy landscape. This small change slightly shifts the transition field. Due to the steep slope of the mobility in this region, the variation of the mobility is notably increased around the transition field.

4.3.5 Transport Regimes

In the following, we will discuss a possible explanation for the features of the mobility at electric fields between $F = 10^7 \frac{\mathrm{V}}{\mathrm{m}}$ and $F = 10^8 \frac{\mathrm{V}}{\mathrm{m}}$ in the upper panels of Figure 4.6 incorporating the data presented in Figure 4.7. In conjunction with Figure 4.7, we revisit the one-dimensional system introduced in Chapter 4.1. The upper panel in Figure 4.7 illustrates the energy landscape with the highest barrier at position $x = 3$ nm and the deepest trap at position $x = 12$ nm. The magenta and the red line demonstrate the tilt of the energy landscape at an electric field of $F = 2 \cdot 10^6 \frac{\mathrm{V}}{\mathrm{m}}$ and $F = 10^7 \frac{\mathrm{V}}{\mathrm{m}}$. The lines are aligned to the highest barrier energy at $x = 3$ nm to get an idea which barriers are important at which electric field. The lower panel in Figure 4.7 shows the normalised field- and correction energy $\frac{E^c - eFx}{eFL_{sys}}$, with the characteristic flat regions separated by steps, already discussed in Chapter 4.1. To see all curves on the same scale, the energies are normalised by dividing them by the total field energy eFL_{sys} that a charge carrier gains when moving through the entire system once. The dashed dark green line in the lower panel in Figure 4.7 marks the normalised field energy $-\frac{eFx}{eFL_{sys}}$ and the difference between this line and the normalised field- and correction energies indicate the normalised correction energies $\frac{E^c}{eFL_{sys}}$.

When looking at the evolution of the correction energies with respect to the applied electric field F, seen in the lower panel in Figure 4.7, the three lines for the lowest electric field $F \leq 2 \cdot 10^6 \frac{\mathrm{V}}{\mathrm{m}}$ (brown, blue and magenta) have the by far highest step at the highest barrier at $x = 3$ nm. The much smaller steps at the intermediate barriers at $x = 13$ nm, $x = 25$ nm, $x = 41$ nm and $x = 49$ nm are nearly negligible. This means for a low electric field $F \leq 2 \cdot 10^6 \frac{\mathrm{V}}{\mathrm{m}}$, the charge carrier gets almost exclusively stuck in front of the highest barrier. For intermediate electric fields around $F \approx 10^7 \frac{\mathrm{V}}{\mathrm{m}}$ (red line in the lower panel in Figure 4.7), the intermediate barriers become more and more relevant and the size of the transport-relevant clusters is reduced from the total system size to the size determined by the intermediate barriers. When increasing the electric field F even more, the transport-relevant cluster size decreases more and more until the field energy dominates the energy landscape and no barriers are left. The field- and correction energies underline this trend by showing more and more steps (yellow, black and purple lines in the lower panel in Figure 4.7) until the field energy dominates the correction energy at very high electric fields (grey line in the lower panel in Figure 4.7).

The mobility for a single charge carrier $N_{cc} = 1$ in the system corresponding to this evolution of the field- and correction energies with respect to the applied electric field F, depicted in Figure 4.7, is

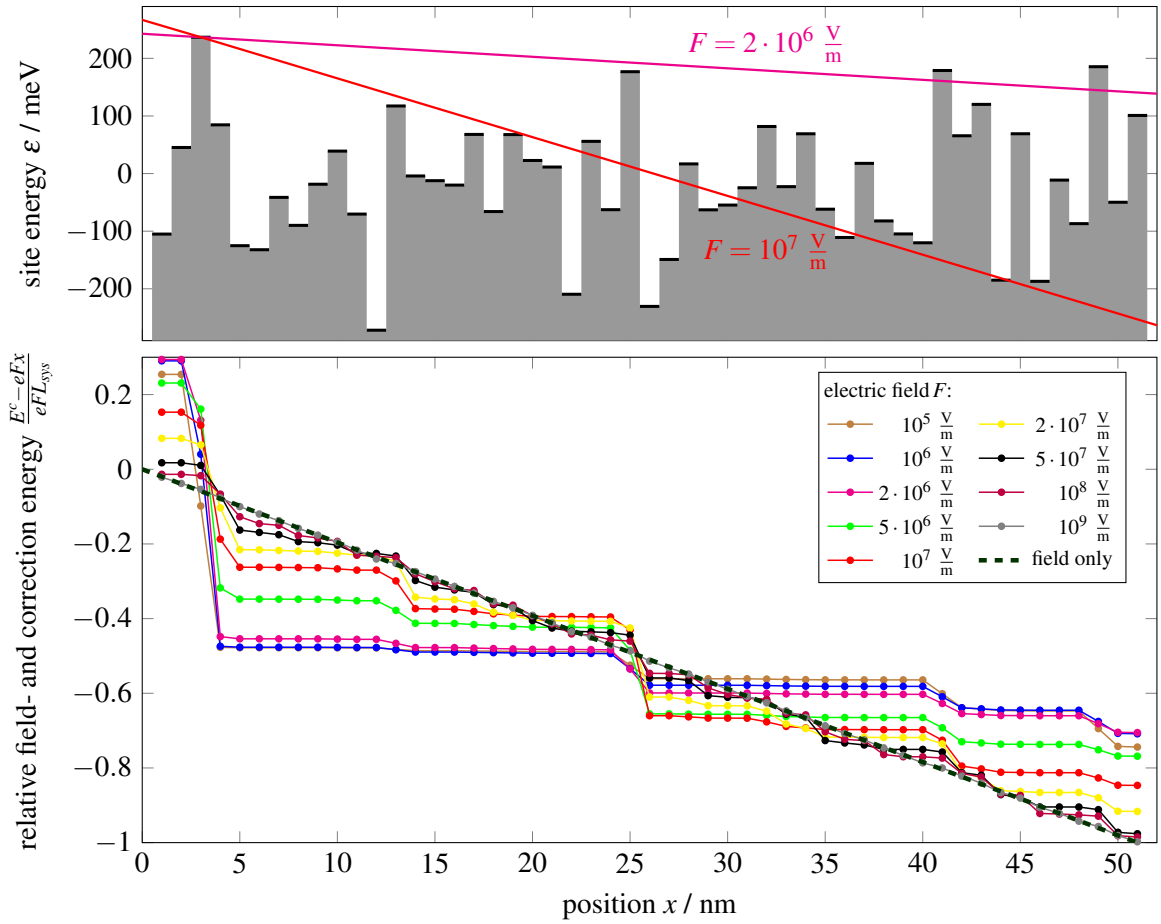

Figure 4.7: The upper panel shows the energy landscape of the one-dimensional system introduced in Chapter 4.1. The two lines represent the steepness of the tilt of the energy landscape by the labelled electric field. In the lower panel, the normalised field- and correction energy $\frac{E^c - eFx}{eFL_{sys}}$ as a function of the position x is plotted for a wide range of electric fields F demonstrating the different transport regimes (details see text). The dashed dark green line indicates the field energy without correction energies.

shown in the upper panel in Figure 4.8. The lower panel in Figure 4.8 presents the occupation $\langle n_{12} \rangle$ of the deepest trap at position $x = 12$ nm as a function of the applied electric field F. The blue lines in Figure 4.8 show the mobility and occupation in forward direction, meaning that the charge carrier moves from left to right. This corresponds to the direction assumed for the calculation of the field- and correction energies given in the lower panel in Figure 4.7. The red lines in Figure 4.8 correspond to the reverse direction, meaning that the charge carrier moves from right to left due to a reversed electric field. The filled circles on the blue line in Figure 4.8 mark the fields at which the field- and correction energies are drawn in Figure 4.7, with the same colour code applied.

With Figure 4.7 and Figure 4.8, we are able to deliver the promised possible explanation for the additional features appearing in the upper panels in Figure 4.6 for $N_{cc} = 1$ in the electric field range of $F = 10^7 \frac{\mathrm{V}}{\mathrm{m}}$ and $F = 10^8 \frac{\mathrm{V}}{\mathrm{m}}$. In the evolution of the field- and correction energies (lower panel in Figure 4.7), we can identify at least three different transport regimes. For very low electric fields $F \leq 2 \cdot 10^6 \frac{\mathrm{V}}{\mathrm{m}}$, the only significant step in the field- and correction energy, e.g. in the blue line in the lower panel in Figure 4.7, appears at the site with the highest barrier energy at $x = 3$ nm. This means, that the transport-relevant cluster size corresponds to the entire system size and the only barrier that is relevant is the one with the highest energy at $x = 3$ nm. For intermediate electric fields around $F \approx 10^7 \frac{\mathrm{V}}{\mathrm{m}}$ (red

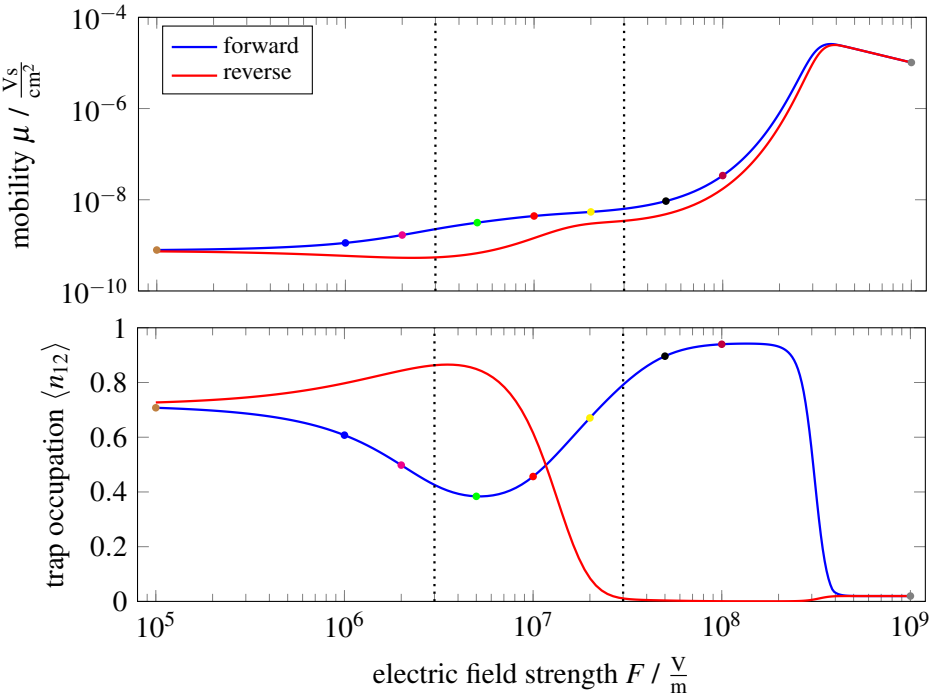

Figure 4.8: Mobility (upper panel) and occupation $\langle n_{12} \rangle$ of the deepest trap at $x = 12$ nm (lower panel) of the one-dimensional system shown in Figure 4.7 as a function of the applied electric field F for one charge carrier $N_{cc} = 1$ in the system. The blue lines represents the mobility and occupation when the charge carrier moves from left to right (forward), corresponding to the field- and correction energies given in the lower panel in Figure 4.7. The red line is the mobility and occupation for the charge carrier moving from right to left (reverse) due to a reversed electric field. The filled circles mark the fields at which the field- and correction energies are visualised in Figure 4.7 with the same colour code being used. The dotted lines approximately separate the three transport regimes discussed in the text.

line in the lower panel in Figure 4.7), more steps in the field- and correction energy in the lower panel in Figure 4.7 emerge at the intermediate barriers at $x = 13$ nm, $x = 25$ nm, $x = 41$ nm and $x = 49$ nm. Hence, the size of the transport-relevant clusters is significantly reduced. Increasing the electric field even more continuously breaks up the cluster structure until we reach the isoenergetic transport regime when the field energy is so high that no barriers are left. So we can distinguish three transport regimes with respect to the applied electric field. In the first transport regime for low electric fields, the entire system is one transport-relevant cluster. In the second transport regime for intermediate electric fields, the size of the transport-relevant clusters is reduced but we still see flat regions and steps in the field and correction energies. Finally, in the third transport regime the transport-relevant cluster size is further reduced until every site is its own cluster and no barriers between the clusters exist due to the high electric field.

Those three transport regimes, separated by dotted lines in Figure 4.8, can be seen in the mobility as well, plotted in the upper panel in Figure 4.8. For low fields $F \leq 10^6 \ \frac{\mathrm{V}}{\mathrm{m}}$, the mobility does not change much and is not depending on the transport direction. Up to an electric field of $F = 3 \cdot 10^6 \ \frac{\mathrm{V}}{\mathrm{m}}$ the mobility in forward direction increased and in reverse direction decreased. This is a consequence of the relative position of the deepest trap and the highest barrier. In forward direction, the deepest trap is in the region which is depleted by the highest barrier resulting in a decrease of the occupation of the deepest trap (lower panel in Figure 4.8). A reduced occupation of the deepest trap implies an increase of the mobility. In reverse direction, it is exactly the other way round. The deepest trap is in the accumulation zone of the

highest barrier resulting in a decrease of the mobility. Approximately at an electric field of $F \approx 3 \cdot 10^6 \frac{\mathrm{V}}{\mathrm{m}}$, the transition to the second mobility regime happens and the intermediate barriers take over. Now the deepest trap is next to the intermediate barrier at $x = 12$ nm. In forward direction, the deepest trap is in the accumulation zone of this barrier and in reverse direction, it is in the depletion zone. This results in a respective increase and decrease in occupation (see lower panel in Figure 4.8). As a consequence, the increase in mobility in forward direction above an electric field of $F \approx 3 \cdot 10^6 \frac{\mathrm{V}}{\mathrm{m}}$ is not as steep as the increase below this field, while the mobility in reverse direction notably increases above $F = 3 \cdot 10^6 \frac{\mathrm{V}}{\mathrm{m}}$ (see upper panel in Figure 4.8). The transition to the third transport regime starts approximately at an electric field of $F \approx 3 \cdot 10^7 \frac{\mathrm{V}}{\mathrm{m}}$, at which the transport-relevant clusters continuously reduce their size resulting in a significant increase of the mobility in forward and reverse direction until the isoenergetic limit is reached.

In summary, the properties of the first transport regime for low electric fields and very low charge-carrier densities are predominantly determined by the highest energy barrier and the deepest trap of the system. For the second transport regime, incorporating intermediate electric fields and/or intermediate charge-carrier densities, not just the highest barrier energy that has to be overcome is important but also intermediate barriers. When going to very high electric fields, the isoenergetic transport regime takes over and the initial energy landscape plays only a minor role.

4.3.6 Influence of Hopping Radius and Rates

Within the assumptions leading to the transition field F^*, hopping is restricted to nearest neighbours only with a hopping radius of $r_{hop} = 1$ nm. Revoking this constraint and allowing for hops up to $r_{hop} = 2$ nm is supposed to have an impact on the transition field F^* and the mobility. In Figure 4.9, simulation results for the system introduced in Chapter 4.3.2 with exactly the same energy landscape an energetic disorder $\sigma = 100$ meV are presented. The only difference is that the maximum allowed hopping distance r_{hop} is raised from 1 nm to 2 nm. The four panels in Figure 4.9 represent four different hopping rates with the Miller-Abrahams rate equation (upper left panel in Figure 4.9), Equation (3.3), and Marcus rate equation, Equation (3.4), for three different reorganisation energies $E_r = 0.05$ eV (upper right panel in Figure 4.9), $E_r = 0.1$ eV (lower left panel in Figure 4.9) and $E_r = 0.2$ eV (lower right panel in Figure 4.9). The CEC simulations were verified by KMC simulations visualised as crosses in Figure 4.9.

The mobility as a function of electric field F and number of charge carriers N_{cc} shown in Figure 4.4 and in the upper left panel in Figure 4.9 both consider Miller-Abrahams rate equation. The only difference is the hopping radius $r_{hop} = 1$ nm and $r_{hop} = 2$ nm, respectively. When looking at the mobility values in Figure 4.4 and the upper left panel in Figure 4.9, the increase of r_{hop} for charge delocalisation constant $\alpha = 5$ nm^{-1} results in a consistent increase of the mobility by a factor of up to 1.6 for $N_{cc} = 1$. The rapid increase in mobility for $r_{hop} = 1$ nm appears around an electric field of $F \approx 10^8 \frac{\mathrm{V}}{\mathrm{m}}$, whereas for $r_{hop} = 2$ nm, the increase happens at a lower electric field of $F \approx 5 \cdot 10^7 \frac{\mathrm{V}}{\mathrm{m}}$. As expected, the mobility slightly increases and the transition field slightly decreases for an increase of r_{hop} from 1 nm to 2 nm.

The mobilities for different rate equations in Figure 4.9 differ quite significantly in values and also in their actual shape. However, the transition field F^*, around which the rapid increase of the mobility occurs, is very similar for all rate equations. We can see the onset of the increase in all panels in Figure 4.9 at an electric field of approximately $F \approx 5 \cdot 10^7 \frac{\mathrm{V}}{\mathrm{m}}$. This result nicely agrees with our derivation of the transition field F^*, because the derivation suggest that the choice of the rate equation has only a minor influence on the transition field F^*.

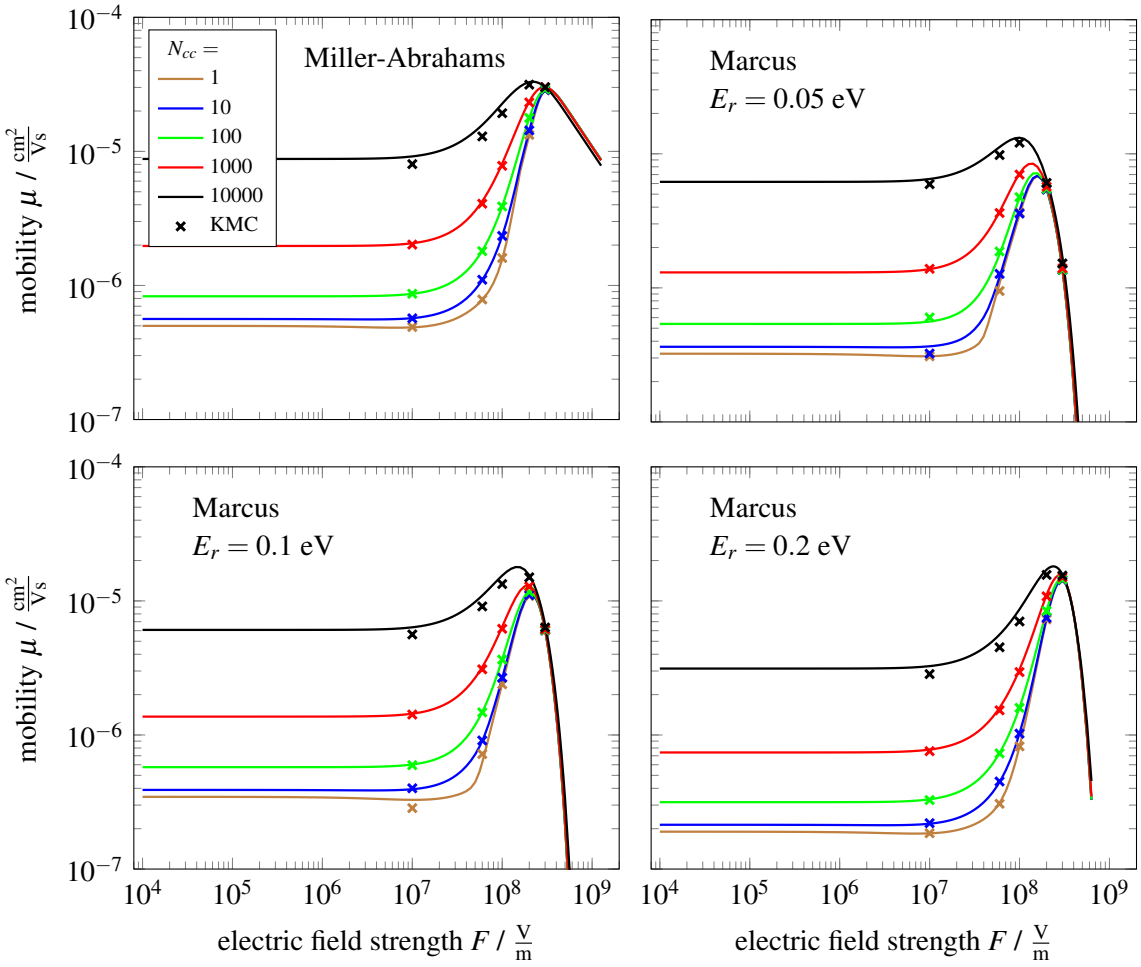

Figure 4.9: Bulk mobility μ as a function of the applied electric field F for different amounts of charge carriers $N_{cc} = 1$ to $N_{cc} = 10000$ in the system. The simulated system is exactly the same as the one in Chapter 4.3.2 with exactly the same energy landscape and energetic disorder $\sigma = 100$ meV. The only difference is that the maximum allowed hopping radius is increased to $r_{hop} = 2$ nm. The upper left panel used Miller-Abrahams rate equation and the remaining panels used Marcus rate equation with different reorganisation energies E_r. The crosses represent a verification by kinetic Monte Carlo (KMC) simulations of the lines, for which the mobility was extracted with our new correction energy concept (CEC). The agreement between CEC and KMC results is appropriate. The significant increase of the mobility at $F \approx 5 \cdot 10^7 \frac{V}{m}$ appears for lower fields compared to the $r_{hop} = 1$ nm results (cf. Figure 4.4) and always at the same transition field for all rate equations, as expected.

In this chapter we demonstrated the strength of the correction energy concept to provide insight into charge transport mechanisms. With this insight, we derived an easily accessible transition field F^* around which a significant increase of the mobility as a function of the electric field appears. As an outlook, our simple estimate of the transition field might be the foundation for a new mobility model or could be used to improve existing mobility models like the model suggested by Pasveer *et al.* [11].

5 Metal-Organic Semiconductor Interface

Interfaces are essential parts of every device. In organic electronic devices, like organic thin-film transistors (OTFTs) and organic light-emitting diodes (OLEDs), the interface between the organic semiconductor (OSC) and the metal contact is of particular importance to efficiently provide mobile charge carriers for a proper device operation. For OTFTs, the preparation of the contacts is gaining more and more attention as it is a crucial bottleneck of modern high mobility OSC materials based transistors. [6]

The direct vicinity of the metal-OSC interface has been extensively studied with DFT-based approaches resulting in a well-founded knowledge of the basic processes governing the interface energetics and corresponding level alignments. [101, 102] This fundamental improvement in understanding the interface enables a precise tuning of interface properties like the work function. [1, 103] Small changes of interface properties can cause severe changes in the injection behaviour and, subsequently, the device performance. The influence of interface properties on the injection current density has already been investigated for two decades. Several analytical expressions to describe the injection current density emerged from these investigations. [104–106] Furthermore, investigations on the current density through a metal-OSC-metal single layer unipolar diode revealed two distinct operation scenarios, i.e., space-charge-limited current (SCLC) and injection-limited current (ILC). [107–109]

To understand the influence of interface properties on device performance, it is insufficient to consider the vicinity of the interface. Rather, the interface needs to be considered as a region that is imbedded into a device. The injection can be influenced by charge accumulations within the device, even if these accumulations occur far away from the interface. Such a mutual influence across distant device locations is due to the long-ranging Coulomb interactions. The importance of looking at the entire device was already emphasised by Varo *et al.* [108]. These authors suggested a unified model for organic single layer unipolar diodes discriminating between SCLC and ILC.

In this chapter, we will revisit the model system, for which previously suggested analytical expressions for the current density through a metal-OSC interface were conceived, to identify the conditions that provoke a transition from SCLC to ILC. After advancing the model system by refining the description of the metal contact by distinguishing between the injection barrier and the Fermi level of the contact in Chapter 5.1, we perform kinetic Monte Carlo (KMC) simulations to explore the behaviour of this model system in the full range of SCLC to ILC in Chapter 5.2. From the insight gained by the simulation results, we derive an estimate for the injection barrier separating the SCLC regime and the ILC regime in Chapter 5.3. The interpretability of the suggested model system and its advantages and disadvantages are discussed in Chapter 5.4 before we compare our results to experimental data from Raoufi and co-workers [110] in Chapter 5.5.

5.1 Model System for the Interface

To calculate the current density through a metal-OSC interface, we performed kinetic Monte Carlo simulations of an interface model based on the idea of Wolf *et al.* [79] with modifications to include Coulomb interactions as described in the following. The idea of Wolf *et al.* [79] was to simulate only the region nearby the interface instead of simulating the whole device. This notion is appealing as it saves computational resources and allows to extract interface properties, that are independent of the full device. Yet, the disregard of the full device limits the extent to which the results can be interpreted (cf. Chapter 5.4).

5.1.1 Geometry

In our interface model, charge carriers can occupy spatially localised sites. In contrast to bulk simulations, we have to distinguish between active and passive sites. Active sites are sites that can be occupied or unoccupied, i.e., charge carriers hop on and off that sites. Bulk simulations exclusively consist of active sites. Passive sites are sites that are not contained in the actual simulation volume. Those passive sites can provide charge carriers for an active site and remove charge carriers from an active site, but they cannot host charge carriers. The ability to provide and remove charge carriers is related to an occupation probability (cf. Chapter 5.1.3). In interface simulations, e.g. the metal sites in the contact are described as passive sites.

In our simulation, sites are arranged on a simple cubic lattice with $a = 1$ nm lattice constant. The layers parallel to the metal contact contain $N_l \times N_l = 25 \times 25$ sites with periodic boundary conditions in both directions. The active OSC region contains $N_x = 50$ layers parallel to the metal contact. The hopping range is restricted to distances of at maximum $r_{hop} = 2$ nm. Reminiscent of Wolf *et al.*, [79] we added two layers of passive OSC to one facet of the active volume, which act as so-called extraction layers. Charge carriers can hop to sites in those extraction layers in the same manner as for all other empty sites. However, in the moment a charge carrier hops to a site in the extraction layers, it is taken out of the simulation. Hence, those passive extraction sites are assumed to be unoccupied. On the opposite side of the extraction layers, we add one layer of contact sites. The properties of the contact sites are discussed in detail in Chapter 5.1.3.

5.1.2 Energy Levels in the Organic Semiconductor

To make the charge carriers move, rates for hops of charge carriers from one site to another are required. Those rates depend on the difference in energy that the charge carrier possesses when occupying the initial site before the hop and the final site after the hop. This energy E_i of a charge carrier occupying site i consist of terms related to, (i), the randomly chosen site energy ε_i drawn from a Gaussian distribution with energetic disorder σ, (ii), the energy from the externally applied electric field $-eFx_i$ with the elemental charge e, the electric field F and the distance of the site to the metal contact x_i, (iii), the own image charge potential $-e^2(16\pi\varepsilon_0\varepsilon_r x_i)^{-1}$ with the vacuum permittivity ε_0 and the relative permittivity ε_r of the OSC, (iv), Coulomb interactions with other charge carriers $e\Phi(\vec{r}_i)$ with the potential Φ created by all other charge carriers and the spatial position of the site occupied by the charge carrier $\vec{r}_i$ and, (v), Coulomb interactions with other image charge carriers $-e\Phi^{img}(\vec{r}_i)$ with the potential Φ^{img} of the other image charge carriers.

$$E_i = \varepsilon_i - eFx_i - \frac{e^2}{16\pi\varepsilon_0\varepsilon_r x_i} + e\Phi(\vec{r}_i) - e\Phi^{img}(\vec{r}_i) \tag{5.1}$$

Due to the periodic boundary conditions, Coulomb interactions with all charge carriers and all periodic replica of all charge carriers have to be considered. The contributions of Φ and Φ^{img} can be conveniently obtained from the potential of a single charge carrier $\varphi(\Delta\vec{r})$. To get the potential $\varphi(\Delta\vec{r})$ created by one charge carrier under consideration of all its periodic replica, we developed a 2D Ewald summation method [93, 111–114]. The argument $\Delta\vec{r}$ is the distance between the charge carrier and the position at which the potential is requested. To get this potential, we proceeded in a similar way as for the 3D Ewald summation described in [3, 93] combined with the 2D summation method illustrated by

Lee and Cai. [113] In essence, Ewald summation splits the infinite sum over all periodic replicas into a fast converging real-space sum and a fast converging reciprocal-space sum. This split is characterised by a splitting parameter ζ. The problem, that the sum of a charged system is actually diverging, is overcome by cleverly introducing a counter charge that does not affect the shape of the potential, but only delivers a constant contribution. A detailed description can be found in [93]. The result of this derivation is

$$\begin{aligned}\varphi(\Delta\vec{r}) = \frac{e}{4\pi\varepsilon_0\varepsilon_r}\Bigg\{ & \frac{\operatorname{erfc}(\zeta\,|\Delta\vec{r}|)}{|\Delta\vec{r}|} + \frac{2\zeta}{\sqrt{\pi}} + \frac{2\sqrt{\pi}}{A\zeta}\left(1-\exp\left(-\zeta^2\,|\Delta x|^2\right)\right) - \frac{2\pi\,|\Delta x|}{A}\operatorname{erf}(\zeta\,|\Delta x|) \\ & + \sum_{\vec{T}\neq 0}\left(\frac{\operatorname{erfc}\left(\zeta\left|\Delta\vec{r}+\vec{T}\right|\right)}{\left|\Delta\vec{r}+\vec{T}\right|} - \frac{\operatorname{erfc}\left(\zeta\left|\vec{T}\right|\right)}{\left|\vec{T}\right|}\right) \\ & + \frac{\pi}{A}\sum_{\vec{G}\neq 0}\Bigg[\frac{\cos\left(\vec{G}\Delta\vec{r}\right)}{\left|\vec{G}\right|}\Bigg(\exp\left(\left|\vec{G}\right|\,|\Delta x|\right)\operatorname{erfc}\left(\frac{\left|\vec{G}\right|}{2\zeta}+\zeta\,|\Delta x|\right) \\ & \qquad + \exp\left(-\left|\vec{G}\right|\,|\Delta x|\right)\operatorname{erfc}\left(\frac{\left|\vec{G}\right|}{2\zeta}-\zeta\,|\Delta x|\right)\Bigg) - \frac{2\operatorname{erfc}\left(\frac{|\vec{G}|}{2\zeta}\right)}{\left|\vec{G}\right|}\Bigg]\Bigg\} \end{aligned} \tag{5.2}$$

with the error function $\operatorname{erf}(u)$ and the complementary error function $\operatorname{erfc}(u) = 1-\operatorname{erf}(u)$, the area of the periodically repeated unit $A = (N_l \cdot a)^2$, the distance Δx between the charge carrier and the position at which the potential is requested perpendicular to the metal contact plane, a sum over the 2D real space translation vector $\vec{T}$ and the 2D reciprocal space vector $\vec{G}$. The splitting parameter ζ determines the speed of convergence of the two sums. For a low value of ζ, the sum over $\vec{G}$ converges fast and the sum over $\vec{T}$ converges slow, and for a high value of ζ, it is the other way round. For our chosen intermediate value of $\zeta = \frac{\sqrt{\pi}}{N_l \cdot a}$, both sums converge fast.

This potential for a single charge carrier bears the essential benefit that we can calculate it prior to the simulation and store it. During the simulation, we simply need to figure out the index distance between the charge carrier and the site for which the potential is calculated and look up the corresponding potential in the stored array. So we only need to calculate the potential once for a given geometry resulting in no additional computational effort during the actual simulation.

From the potential of a single charge carrier $\varphi(\Delta\vec{r})$, the interaction potential $\Phi(\vec{r}_i)$ and the image charge interaction potential $\Phi^{img}(\vec{r}_i)$ can be calculated by summing over all charge carriers except the charge carrier for which the interaction potentials are calculated.

$$\Phi(\vec{r}_i) = \sum_{\substack{j=1 \\ k_j\neq i}}^{N_{cc}} \varphi\left(\vec{r}_i - \vec{r}_{k_j}\right) \quad \text{and} \quad \Phi^{img}(\vec{r}_i) = \sum_{\substack{j=1 \\ k_j\neq i}}^{N_{cc}} \varphi\left(\vec{r}_i - \vec{r}^{\,img}_{k_j}\right) \tag{5.3}$$

with the index of the site i that is occupied by the charge carrier for which the interaction potential is calculated, the number of the charge carrier j over which we sum, the index oft the site k_j of charge carrier j, the total number of charge carriers N_{cc}, the spatial position $\vec{r}_i$ of site i, the spatial position $\vec{r}_{k_j}$ of site k_j occupied by charge carrier j and the spatial position of the image charge carrier $\vec{r}^{\,img}_{k_j}$ mirrored at the metal contact corresponding to the charge carrier j occupying site k_j. The restriction $k_j \neq i$ takes into account that the charge carrier for which the potential is calculated is excluded from the sum.

The energy levels E_i are used to calculate rates for hops of charge carrier from their current position

i to a position j within a maximum hopping range of $r_{hop} = 2$ nm. We took the Miller-Abrahams rate equation [94] to calculate the rate R_{ij} for a hop from site i to site j

$$R_{ij} = \nu_0 \exp\left(-2\alpha\left|r_j - r_i\right|\right) \begin{cases} \exp\left(-\frac{E_j - E_i}{k_B T}\right) & \text{for } E_j - E_i > 0 \\ 1 & \text{for } E_j - E_i \leq 0 \end{cases} \tag{5.4}$$

with the hopping prefactor ν_0, the charge delocalisation constant α, the Boltzmann constant k_B and the temperature T.

5.1.3 Contact Treatment

The description of the metal contact by Wolf *et al.* [79] is proposed for a system with only a single charge carrier. This contact treatment is not directly applicable for our system with interacting charge carriers but lends the essential idea. At the facet of the active OSC, which is opposite to the extraction layers, we put one layer of metal sites with the same spacing as in the OSC. The connection of the metal contact with the OSC and vice versa is achieved by injection and extraction rates. In this context, we use injection to indicate a hop of a charge carrier from a metal site to a site in the OSC (create a new charge carrier in the simulation) and extraction to indicate a hop of a charge carrier from a site in the OSC to a metal site in the contact (remove one charge carrier from the simulation). Hence, an injection rate is a rate with which charge carriers are injected from a metal site in the contact to the OSC and an extraction rates is the rate with which charge carriers can hop from the OSC to a metal site in the contact. The rates are determined by certain properties of the metal contact. Wolf *et al.* [79] proposed, that we solely need to consider the energy levels E_i^m of the metal sites in the contact. This energy can be set to $E_i^m = -\Delta$ with the nominal injection barrier Δ. The energy of a metal site is not influenced by Coulomb interactions from charge carriers within the OSC, because it is assumed that the surface charge of the metal at the interface shields those interactions. Note that the derivation below is not restricted to $E_i^m = -\Delta$. In principle, E_i^m can take different values for different sites i.

To receive appropriate rate expressions for injection and extraction in our system with interacting charge carriers, we have to go beyond the single charge carrier considerations by Wolf *et al.* [79]. Besides the energy level of the metal sites E_i^m, we have to additionally choose a distinct Fermi-level of the metal E_F^m. The site energies E_i^m refer to a strongly simplified density of states with a sharp peak at $-\Delta$ and the Fermi-level E_F^m accounts for the occupation probability $\langle n_i^m \rangle$ of sites i in the metal contact via Fermi-Dirac statistics.

$$\langle n_i^m \rangle = \frac{1}{1 + \exp\left(\frac{E_i^m - E_F^m}{k_B T}\right)} \tag{5.5}$$

The metal sites are passive sites, which means that they are not occupied or unoccupied like active sites in the OSC, but are described by an occupation probability.

In the following, we will derive the injection and extraction rates that arise from this description of the metal sites via an energy level E_i^m and the Fermi-level E_F^m. For this purpose, we have to consider the perspective of configurations ξ as done in Chapter 3. A configuration ξ is one possibility to place charge carriers at the active sites. In contrast to bulk simulations with a fixed number of charge carriers in the system throughout the entire simulation, interface simulations are an open system with changing

numbers of charge carriers. As a consequence, the number of possible configurations for a system with a number of N_s active sites is with 2^{N_s} much higher for interface simulations than for bulk simulations with $\binom{N_s}{N_{cc}}$ possible configurations considering N_{cc} charge carriers. The nomenclature for configurations ξ is different to that in Chapter 3. In Chapter 3, we wrote $\xi = \{i_1, i_2, \ldots, i_{N_{cc}}\}$ for a configuration ξ with a number of charge carriers N_{cc} and sites i_j occupied by the charge carrier j. Here, we write whether a site i is occupied, $n_i = 1$ charge carriers per site (ccps), or not, $n_i = 0$ ccps, in the form $\xi = \{n_1, n_2, \ldots, n_{N_s}\}$ for the N_s active sites in the simulation. As the number of charge carriers N_{cc} changes during simulation, this is the more adequate notation in this case, although it holds the same content of information due to the indistinguishability of the charge carriers.

To receive the desired rates, we will artificially enlarging the system to enable a well defined inclusion of the Fermi level E_F^m with clearly defined assumptions. Enlarging means that the metal sites are transformed from passive sites to active sites. After including the Fermi level E_F^m, the system is reduced to the initial size with active sites only within the OSC. This reduction delivers the desired injection and extraction rates. The assumptions we propose to describe the metal contact and the injection and extraction process are, (i), each metal site is not correlated to the remaining system, (ii), the occupation probability of a metal site $\langle n_i^m \rangle$ is given by Equation (5.5).

To include the contact sites in the active region that can be occupied by charge carriers, the configuration space has to be enlarged. A configuration ξ of the total system is now a combination of the configuration $\xi_o = \{n_1^o, n_2^o, \ldots, n_{N_s}^o\}$ of the charge carriers in the OSC, with $n_i^o \in \{0,1\}$ being the number of charge carriers at site i in the OSC and N_s the number of active sites in the OSC, and the configuration $\xi_m = \{n_1^m, n_2^m, \ldots, n_{N_m}^m\}$ of the charge carriers in the metal contact, with $n_i^m \in \{0,1\}$ being the number of charge carriers at site i in the metal contact and N_m the number of metal sites. Furthermore, we define a configuration ξ_i that partially includes the metal sites

$$\xi_i = \{n_{N_m-i+1}^m, n_{N_m-i+2}^m, \ldots, n_{N_m}^m, n_1^o, n_2^o, \ldots, n_{N_s}^o\} = \{n_{N_m-i+1}^m, n_{N_m-i+2}^m, \ldots, n_{N_m}^m, \xi_o\} \tag{5.6}$$

and define $\xi_0 = \xi_o$ for $i = 0$. Note that those definitions for ξ_i imply $\xi_{N_m} = \xi = \{\xi_m, \xi_o\}$.

To obey the two assumptions of uncorrelated metal sites and occupation probabilities given by Equation (5.5), the contact sites are coupled to a charge reservoir. Each contact site i assigns an individual rate $R_{r,m\,i}$ for a hop from the reservoir to the metal site i and $R_{m\,i,r}$ for a hop from the metal site i to the reservoir. It is not necessary to know the exact values of the rates $R_{r,m\,i}$ and $R_{m\,i,r}$. Rather, the range of their values should justify the two required assumptions. The first assumption of uncorrelated metal sites is justified if the rates $R_{r,m\,i}$ and $R_{m\,i,r}$ are much higher than the rates involving OSC sites. The second assumption of the occupation probability $\langle n_i^m \rangle$ given by Equation (5.5) is justified if the ratio between $R_{r,m\,i}$ and $R_{m\,i,r}$ is appropriate. The first assumption is approximately justified for metal contacts, because processes in metals happen on a much faster timescale than in OSC. The second assumption relies on the concept of a Fermi level E_F^m in the metal contact. Both assumptions rely, in principle, on an efficient shielding of the surface charge at the metal surface in such a way that neither the site energy E_i^m, nor the Fermi level E_F^m is influenced by the charge carriers in the OSC.

With all the initial assumptions being made and justified, the next step is to reduce the system again and convert the active metal sites to passive sites. This conversion is performed via the global balance equation which links the probability π_ξ that a configuration ξ is visited in steady state and the rates $R_{\xi\xi'}$

for transitions from configuration ξ to configuration ξ'

$$\sum_{\xi' \neq \xi} \pi_{\xi} R_{\xi\xi'} = \sum_{\xi' \neq \xi} \pi_{\xi'} R_{\xi'\xi}. \tag{5.7}$$

The global balance equation balances the probability flux out of configuration ξ to all other configurations ξ' determined by the rates $R_{\xi\xi'}$ (left-hand side) with the probability flux into configuration ξ from all other configurations ξ' determined by the rates $R_{\xi'\xi}$ (right-hand side).

A configuration of the enlarged system ξ can be split into two subsystems $\xi = \{n_1^m, \xi_{N_m-1}\}$ comprising a metal site n_1^m and all other sites. Considering those two subsystems in the global balance Equation (5.7) leads to three terms in the sum over ξ':

$$\begin{aligned}\sum_{\xi' \neq \xi} \pi_{\xi} R_{\xi\xi'} \quad = \quad & \sum_{\xi'_{N_m-1} \neq \xi_{N_m-1}} \pi_1^m(n_1^m)\, \pi_{\xi_{N_m-1}} R_{\{n_1^m, \xi_{N_m-1}\}\{n_1^m, \xi'_{N_m-1}\}} \\ & + \pi_1^m(n_1^m)\, \pi_{\xi_{N_m-1}} R_{\{n_1^m, \xi_{N_m-1}\}\{1-n_1^m, \xi_{N_m-1}\}} \\ & + \sum_{\xi'_{N_m-1} \neq \xi_{N_m-1}} \pi_1^m(n_1^m)\, \pi_{\xi_{N_m-1}} R_{\{n_1^m, \xi_{N_m-1}\}\{1-n_1^m, \xi'_{N_m-1}\}}\end{aligned} \tag{5.8}$$

and

$$\begin{aligned}\sum_{\xi' \neq \xi} \pi_{\xi'} R_{\xi'\xi} \quad = \quad & \sum_{\xi'_{N_m-1} \neq \xi_{N_m-1}} \pi_1^m(n_1^m)\, \pi_{\xi'_{N_m-1}} R_{\{n_1^m, \xi'_{N_m-1}\}\{n_1^m, \xi_{N_m-1}\}} \\ & + \pi_1^m(1-n_1^m)\, \pi_{\xi_{N_m-1}} R_{\{1-n_1^m, \xi_{N_m-1}\}\{n_1^m, \xi_{N_m-1}\}} \\ & + \sum_{\xi'_{N_m-1} \neq \xi_{N_m-1}} \pi_1^m(1-n_1^m)\, \pi_{\xi'_{N_m-1}} R_{\{1-n_1^m, \xi'_{N_m-1}\}\{n_1^m, \xi_{N_m-1}\}}\end{aligned} \tag{5.9}$$

using the assumption of uncorrelated metal sites $\pi_{\{n_1^m, \xi_{N_m-1}\}} = \pi_1^m(n_1^m)\, \pi_{\xi_{N_m-1}}$ with the probability $\pi_i^m(n_i^m)$ that metal site i is in state $n_i^m \in \{0,1\}$ being unoccupied or occupied, respectively. The term in the first line of Equations (5.8) and (5.9) represents the hops restricted to the reduced subsystem with configurations ξ_{N_m-1} as the occupation of metal site 1 does not change. The rate in this term is not influenced by the occupation n_1^m of metal site 1, so the rate can be rewritten to $R_{\{n_1^m, \xi_{N_m-1}\}\{n_1^m, \xi'_{N_m-1}\}} = R_{\xi_{N_m-1}\xi'_{N_m-1}}$. The term in the second line of Equations (5.8) and (5.9) is the coupling of the metal site 1 with the charge reservoir, indicated by a change in n_1^m without changing ξ_{N_m-1}. So the rate can be identified as $R_{\{n_1^m, \xi_{N_m-1}\}\{1-n_1^m, \xi_{N_m-1}\}} = R_{r,m\,1}$ for $n_1^m = 0$ ccps and $R_{\{n_1^m, \xi_{N_m-1}\}\{1-n_1^m, \xi_{N_m-1}\}} = R_{m\,1,r}$ for $n_1^m = 1$ ccps. Finally, the term in the third line of Equations (5.8) and (5.9) links the metal site 1 to the remaining subsystem changing both, n_1^m and ξ_{N_m-1}, resulting in an injection or extraction process. As a consequence, the rate can be rewritten to

$$R_{\{n_1^m, \xi_{N_m-1}\}\{1-n_1^m, \xi'_{N_m-1}\}} = R^{ex,1}_{\xi_{N_m-1}\xi'_{N_m-1}} \quad \text{for} \quad n_1^m = 0 \text{ ccps} \tag{5.10}$$

with the rate $R^{ex,1}_{\xi_{N_m-1}\xi'_{N_m-1}}$ for charge extraction from the OSC to the metal site 1 and

$$R_{\{n_1^m, \xi_{N_m-1}\}\{1-n_1^m, \xi'_{N_m-1}\}} = R^{in,1}_{\xi_{N_m-1}\xi'_{N_m-1}} \quad \text{for} \quad n_1^m = 1 \text{ ccps} \tag{5.11}$$

with the rate $R^{in,1}_{\xi_{N_m-1}\xi'_{N_m-1}}$ for charge injection from the metal site 1 to the OSC. With the two possible states $n_1^m \in \{0,1\}$ for being unoccupied or occupied, we get two equations out of the global balance

Equation (5.7):

$$\sum_{\xi'_{N_m-1}\neq\xi_{N_m-1}} \pi_1^m(0)\pi_{\xi_{N_m-1}}R_{\xi_{N_m-1}\xi'_{N_m-1}} + \pi_1^m(0)\pi_{\xi_{N_m-1}}R_{r,m\,1} + \sum_{\xi'_{N_m-1}\neq\xi_{N_m-1}} \pi_1^m(0)\pi_{\xi_{N_m-1}}R^{ex,1}_{\xi_{N_m-1}\xi'_{N_m-1}} =$$
$$= \sum_{\xi'_{N_m-1}\neq\xi_{N_m-1}} \pi_1^m(0)\pi_{\xi'_{N_m-1}}R_{\xi'_{N_m-1}\xi_{N_m-1}} + \pi_1^m(1)\pi_{\xi_{N_m-1}}R_{m\,1,r} + \sum_{\xi'_{N_m-1}\neq\xi_{N_m-1}} \pi_1^m(1)\pi_{\xi'_{N_m-1}}R^{in,1}_{\xi'_{N_m-1}\xi_{N_m-1}} \tag{5.12}$$

for $n_1^m = 0$ ccps and

$$\sum_{\xi'_{N_m-1}\neq\xi_{N_m-1}} \pi_1^m(1)\pi_{\xi_{N_m-1}}R_{\xi_{N_m-1}\xi'_{N_m-1}} + \pi_1^m(1)\pi_{\xi_{N_m-1}}R_{m\,1,r} + \sum_{\xi'_{N_m-1}\neq\xi_{N_m-1}} \pi_1^m(1)\pi_{\xi_{N_m-1}}R^{in,1}_{\xi_{N_m-1}\xi'_{N_m-1}} =$$
$$= \sum_{\xi'_{N_m-1}\neq\xi_{N_m-1}} \pi_1^m(1)\pi_{\xi'_{N_m-1}}R_{\xi'_{N_m-1}\xi_{N_m-1}} + \pi_1^m(0)\pi_{\xi_{N_m-1}}R_{r,m\,1} + \sum_{\xi'_{N_m-1}\neq\xi_{N_m-1}} \pi_1^m(0)\pi_{\xi'_{N_m-1}}R^{ex,1}_{\xi'_{N_m-1}\xi_{N_m-1}} \tag{5.13}$$

for $n_1^m = 1$ ccps.

Upon adding Equations (5.12) and (5.13), the terms in the middle, containing the coupling to the reservoir, $\pi_1^m(1)\pi_{\xi_{N_m-1}}R_{m\,1,r}$ and $\pi_1^m(0)\pi_{\xi_{N_m-1}}R_{r,m\,1}$ cancel out. Due to $\pi_1^m(0)+\pi_1^m(1)=1$, which means that the metal site 1 has to be either unoccupied or occupied, we get the relation

$$\sum_{\xi'_{N_m-1}\neq\xi_{N_m-1}} \pi_{\xi_{N_m-1}}\left(R_{\xi_{N_m-1}\xi'_{N_m-1}} + \pi_1^m(0)R^{ex,1}_{\xi_{N_m-1}\xi'_{N_m-1}} + \pi_1^m(1)R^{in,1}_{\xi_{N_m-1}\xi'_{N_m-1}}\right) =$$
$$= \sum_{\xi'_{N_m-1}\neq\xi_{N_m-1}} \pi_{\xi'_{N_m-1}}\left(R_{\xi'_{N_m-1}\xi_{N_m-1}} + \pi_1^m(0)R^{ex,1}_{\xi'_{N_m-1}\xi_{N_m-1}} + \pi_1^m(1)R^{in,1}_{\xi'_{N_m-1}\xi_{N_m-1}}\right) \tag{5.14}$$

that contains only the reduced subsystem of configurations ξ_{N_m-1} with the coupling to metal site 1 for injection and extraction rates containing an extra factor of $\pi_1^m(n_i^m)$.

With this first metal site being removed from the active region, we can propose that removing N_r metal sites results in

$$\sum_{\xi'_{N_m-N_r}\neq\xi_{N_m-N_r}} \pi_{\xi_{N_m-N_r}}\left(R_{\xi_{N_m-N_r}\xi'_{N_m-N_r}} + \sum_{i=1}^{N_r}\pi_i^m(0)R^{ex,i}_{\xi_{N_m-N_r}\xi'_{N_m-N_r}} + \sum_{i=1}^{N_r}\pi_i^m(1)R^{in,i}_{\xi_{N_m-N_r}\xi'_{N_m-N_r}}\right) =$$
$$= \sum_{\xi'_{N_m-N_r}\neq\xi_{N_m-N_r}} \pi_{\xi'_{N_m-N_r}}\left(R_{\xi'_{N_m-N_r}\xi_{N_m-N_r}} + \sum_{i=1}^{N_r}\pi_i^m(0)R^{ex,i}_{\xi'_{N_m-N_r}\xi_{N_m-N_r}} + \sum_{i=1}^{N_r}\pi_i^m(1)R^{in,i}_{\xi'_{N_m-N_r}\xi_{N_m-N_r}}\right) \tag{5.15}$$

and prove this claim by induction with the basis already given by Equation (5.14) and the step from N_r to N_r+1 sketched below.

The approach is the same as for the removal of the first metal site 1. We divide the system with configurations $\xi_{N_m-N_r}$ into two subsystems $\xi_{N_m-N_r} = \{n^m_{N_r+1}, \xi_{N_m-N_r-1}\}$, rewrite the sum over $\xi'_{N_m-N_r}$ to get three terms as demonstrated in Equations (5.8) and (5.9), receive two equations for $n^m_{N_r+1}=0$ ccps and $n^m_{N_r+1}=1$ ccps and add them. For the rates $R^{ex,i}$ and $R^{in,i}$, the second and third term from rewriting the sum are both zero. There is no possible transition to change the occupation of metal site N_r+1 due to extraction from the OSC to the metal site i or injection from the metal site i to the OSC. Those forbidden

transition leads to a vanishing rate for the second and third term. The fact that the metal site N_r+1 has to be either unoccupied or occupied $\pi^m_{N_r+1}(0)+\pi^m_{N_r+1}(1)=1$ results in a change of $\pi_{\xi_{N_m-N_r}} R^{ex/in,i}_{\xi_{N_m-N_r}\xi'_{N_m-N_r}}$ to $\pi_{\xi_{N_m-N_r-1}} R^{ex/in,i}_{\xi_{N_m-N_r-1}\xi'_{N_m-N_r-1}}$ due to adding the two equations for $n^m_{N_r+1}=0$ ccps and $n^m_{N_r+1}=1$ ccps. The remaining part of Equation (5.15) changes in exactly the same way as for going from $N_r=0$ to $N_r=1$ creating the extra term in the sum over i in Equation (5.15) running from 1 to N_r+1 after adding up the equations for $n^m_{N_r+1}=0$ ccps and $n^m_{N_r+1}=1$ ccps. This finishes the sketch of the proof for the step from N_r to N_r+1 of the induction.

When removing all the metal sites $N_r=N_m$, we end up with the relation

$$\sum_{\xi'_o\neq\xi_o}\pi_{\xi_o}\left(R_{\xi_o\xi'_o}+\sum_{i=1}^{N_m}\pi^m_i(0)R^{ex,i}_{\xi_o\xi'_o}+\sum_{i=1}^{N_m}\pi^m_i(1)R^{in,i}_{\xi_o\xi'_o}\right)= \\ =\sum_{\xi'_o\neq\xi_o}\pi_{\xi'_o}\left(R_{\xi'_o\xi_o}+\sum_{i=1}^{N_m}\pi^m_i(0)R^{ex,i}_{\xi'_o\xi_o}+\sum_{i=1}^{N_m}\pi^m_i(1)R^{in,i}_{\xi'_o\xi_o}\right). \quad (5.16)$$

By close inspection, we can identify Equation (5.16) as a global balance equation. With this equation, the steady-state probabilities π_{ξ_o} are determined by the rates in the brackets consisting of, (i), rates for hops in the OSC $R_{\xi_o\xi'_o}$, (ii), extraction rates $\pi^m_i(0)R^{ex,i}_{\xi_o\xi'_o}$ and, (iii), injection rates $\pi^m_i(1)R^{in,i}_{\xi_o\xi'_o}$. The probability flux out of (left-hand side) and into (right-hand side) configuration ξ_o is, hence, not only determined by the rates of charge carriers hopping in the OSC $R_{\xi_o\xi'_o}$, but also by injection and extraction rates for charge carriers injected from and extracted to the metal contact. When implementing those rates in kinetic Monte Carlo simulations, the steady-state probabilities π_{ξ_o} can be determined.

The global balance equation in Equation (5.16) provides a simple and intuitive recipe to include the Fermi level E^m_F in the injection and extraction rates. As expected, the Fermi level of the metal contact does not influence the rates $R_{\xi_o\xi'_o}$ within the OSC. The injection rates for a hop of a charge carrier from a metal site i to an OSC site j contains, (i), the rate R_{ij} for this hop accounting for the dependence on the energy levels E^m_i and E_j and, (ii), the occupation probability of the injecting metal site $\pi^m_i=\langle n^m_i\rangle$. The rate R_{ij} is, e.g., received by the Miller-Abrahams Equation (5.4) and the occupation probability $\langle n^m_i\rangle$ is given by Equation (5.5) containing the Fermi level. In the same way, the extraction rate for a hop of a charge carrier from an OSC site j to a metal site i is given by, (i), the rate R_{ji} of this hop times, (ii), the probability that the metal site is unoccupied $\pi^m_i(0)=1-\langle n^m_i\rangle$.

In summary, we start from initial injection and extraction rates, that describe the hop of a charge carrier from an occupied metal site to an unoccupied OSC site and from an occupied OSC site to an unoccupied metal site, respectively. The actual injection and extraction rates are determined by multiplying those initial rates with the occupation probability of the metal site, unoccupied for extraction and occupied for injection. The only prerequisite is the assumption of uncorrelated metal sites that are shielded from the charge distribution in the OSC by a perfect surface charge at the metal-OSC interface.

5.1.4 Simulation Details

The parameters for calculating the energies and hopping rate were chosen in a range that is commonly used in literature. The relative permittivity was chosen to be $\varepsilon_r=4$, the temperature $T=300$ K, the charge delocalisation constant $\alpha=5$ nm^{-1} and the hopping prefactor $\nu_0=2.2497\cdot10^{13}$ Hz. The hopping prefactor ν_0 was chosen to get a mobility of $\mu=10^{-4}\,\frac{\mathrm{cm}^2}{\mathrm{Vs}}$ for an isoenergetic energy landscape

($\sigma = 0$ eV) and an electric field of $F = 10^8 \frac{\text{V}}{\text{m}}$ with nearest neighbour hopping only. The rather high delocalisation constant α results in a sufficient convergence of the measured quantities already for a rather low maximum hopping distance of $r_{hop} = 2$ nm. This maximum hopping distance of $r_{hop} = 2$ nm is taken for both, OSC sites and metal sites in the contact. I.e., a charge carrier is allowed to hop to an OSC site within a distance of $r_{hop} = 2$ nm and to a metal site within a distance of $r_{hop} = 2$ nm. A metal site can inject a charge carrier to sites in the OSC within a distance of $r_{hop} = 2$ nm.

To reduce the computational effort, we do not recalculate all rates after every single hop, injection, or extraction of a charge carrier, but only hopping rates for charge carriers and injection rates for the metal sites in the vicinity of the previously happened process. [3, 84, 93] All hopping rates for charge carriers within a distance of 8 nm to the previously hopped, injected or extracted charge carrier are recalculated and all injection rates for metal sites within a distance of 20 nm are updated. When the previous process was an extraction, the distance is measured from the position of the charge carrier prior to extraction. The distances are chosen to guarantee a negligible methodological error. The distance for metal-site updates has to be significantly higher compared to the update radius for charge carriers, because we are creating a virtual charge layer parallel to the metal contact at the update distance for simulations with very high injection barriers (in detail discussed in [93]). This virtual charge layer artificially increases the injection barrier for simulations with very high injection barriers and, hence, provokes wrong results. A larger update radius, (i), decreases the charge-carrier density in the virtual charge layer and, (ii), increases the distance of the virtual charge layer to the metal contact. This motivates the choice of the large update radius for metal sites.

For each simulation, we choose values for the nominal injection barrier Δ, the energetic disorder σ and the electric field F. The Fermi level in the metal contact is set to $E_F^m = -\Delta$, implying a half filled discrete energy level of the metal sites at $E^m = -\Delta$. Prior to the actual simulation, we thermalise the system to avoid any influence of the starting configuration on the measurements by performing an additional amount of 10% of the simulation steps of the main simulation. After thermalisation, we perform N_{KMC} steps and measure occupation probabilities and the current density within the OSC. One simulation step can be either a hop, an injection or an extraction. The number of steps are chosen in such a way that the current density in the OSC converges. A proper convergence required 10^6 steps for low energetic disorders $\sigma = 50$ meV and 10^7 steps for higher energetic disorers $\sigma = 100$ meV and $\sigma = 150$ meV. All measurements were averaged over 10 different randomly chosen energy landscapes.

5.2 Bulk- and Contact-Limited Regime

To answer the question why the current density through a metal-OSC interface is bulk-limited or contact-limited, we performed simulations that reproduce the transition between the bulk- and contact-limited regime by changing the nominal injection barrier Δ for our interface model with an energetic disorder of $\sigma = 100$ meV and an applied electric field of $F = 10^8 \frac{\text{V}}{\text{m}}$. The results of those simulations can be seen in Figure 5.1. For very high nominal injection barriers $\Delta > 0.6$ eV, we can see an exponential drop of the current density j_{if} with increasing nominal injection barrier Δ. The slope of this drop matches the temperature-activated behaviour of a thermal injection, that shows an exponential functional dependence with the exponent $-\frac{\Delta}{k_B T}$ with respect to the nominal injection barrier Δ. The temperature associated to this drop matches the temperature $T = 300$ K selected in the simulations. For very low nominal injection barriers, $\Delta < 0.4$ eV in Figure 5.1, the current density j_{if} is not influenced by the nominal injection

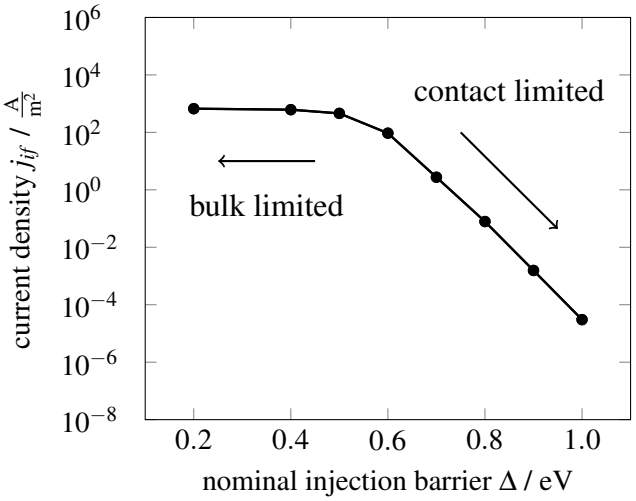

Figure 5.1: Current density j_{if} through a metal-OSC interface as a function of the nominal injection barrier Δ for an applied electric field of $F = 10^8 \frac{\mathrm{V}}{\mathrm{m}}$ and an energetic disorder of $\sigma = 100$ meV. For high injection barriers, the current density decreases exponentially representing the contact-limited regime. For low injection barriers, the current density saturates to a constant value indicating the bulk-limited regime.

barrier Δ. Upon approaching lower barriers from the contact-limited regime, the current density saturates towards a constant bulk-limited current density.

The current density j_B in the bulk of the OSC can be calculated by

$$j_B = e \langle n \rangle \mu F \tag{5.17}$$

multiplying the elemental charge e with the charge-carrier density at the requested position in the OSC $\langle n \rangle$, the mobility μ and the electric field F. The mobility μ in the OSC depends on the charge-carrier density $\langle n \rangle$ and the electric field F (cf. Chapter 4). The electric field itself is given by the externally applied electric field and the interactions from the charge carriers that depend on the charge-carrier density $\langle n \rangle$. Hence, the charge-carrier density plays an important role. We search for the reason behind the transition from the contact-limited to the bulk-limited regime in the charge-carrier density shown in Figure 5.2. This figure plots the average charge-carrier density in a layer parallel to the interface plane as a function of the distance to the interface plane for different nominal injection barriers Δ corresponding to the data shown in Figure 5.1 with an energetic disorder of $\sigma = 100$ meV and an applied electric field of $F = 10^8 \frac{\mathrm{V}}{\mathrm{m}}$.

Due to the energetic disorder of $\sigma = 100$ meV, a small system size of 25×25 sites in a plane parallel to the interface and the averaging over a rather small data set of 10 different energy landscapes, the data in Figure 5.2 is a bit noisy. Nevertheless, we can clearly distinguish the graphs for different nominal injection barriers Δ and, in combination with Figure 5.1, find a signature behaviour for the bulk-limited regime and the contact-limited regime.

For high nominal injection barriers $\Delta \geq 0.7$ eV (red, yellow, black and purple data in the lower part of Figure 5.2), the layer-averaged charge-carrier density is approximately the same for all layers regardless of the distance to the interface. This is the signature behaviour of the contact-limited regime for which the limiting step is to overcome the large injection barrier. When this limiting step is successfully achieved,

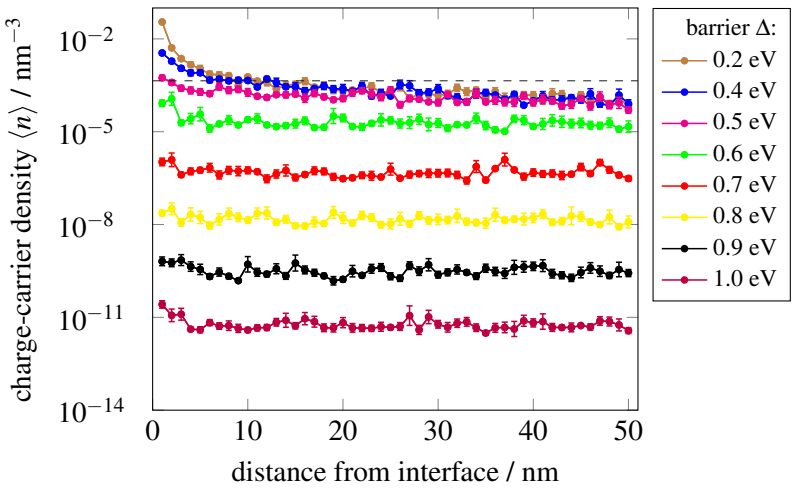

Figure 5.2: Layer-averaged charge-carrier density in layers parallel to the interface as a function of the distance of the layer to the interface plane with energetic disorder $\sigma = 100$ meV and applied electric field $F = 10^8 \frac{\text{V}}{\text{m}}$. Each line for different nominal injection barriers Δ corresponds to one data point for the current density shown in Figure 5.1. In the contact-limited regime at high nominal injection barriers $\Delta \geq 0.7$ eV, the charge-carrier density is approximately constant all over the organic semiconductor (OSC) with exponentially decreasing charge-carrier density for increasing nominal injection barrier Δ. This decrease in charge-carrier density results in the decrease of current density shown in Figure 5.1 due to the relation between charge-carrier density and current density in the OSC given by Equation (5.17). The bulk-limited regime at low nominal injection barriers $\Delta \leq 0.5$ eV shows the behaviour of a space-charge-limited regime with slightly decreasing charge-carrier density with increasing distance from the interface. The charge-carrier density beyond a distance of 10 nm is approximately the same for low nominal injection barriers $\Delta \leq 0.5$ eV, causing the current density to saturate (cf. bulk-limited regime in Figure 5.1). The influence of the nominal injection barrier Δ in the bulk-limited regime is restricted to the region close to the interface, at which the lowering of Δ results in more and more charge carriers being pushed from the contact towards the OSC. Nevertheless, the excess of charge carriers at the interface cannot be transported away, thus, causing no effect on the charge-carrier density farther away from the interface. The dashed line is the limiting charge-carrier density $\langle n_0 \rangle$ estimated in Chapter 5.3.

charge carriers can easily move through the OSC towards the extracting layers at the opposite side of the OSC. Due to the use of the Miller-Abrahams rate Equation (5.4) for injection, the injection is increasingly less likely with increasing injection barrier. This leads to an exponential decrease of the charge-carrier density in the OSC (cf. Figure 5.2) and, hence, to an exponential decrease of the current density (cf. Figure 5.1).

When looking at low nominal injection barriers $\Delta \leq 0.5$ eV (magenta, blue and brown data in the upper part of Figure 5.2), the layer-averaged charge-carrier density shows a significantly different behaviour compared to the contact-limited regime for high nominal injection barriers $\Delta \geq 0.7$ eV. In the region between 10 nm and 50 nm distance from the interface, all three curves approximately coincide. In this region, a space-charge-limited behaviour is encountered, i.e., the charge-carrier density is slightly increasing with decreasing distance to the contact. In contrast, the charge-carrier density within a distance to the interface below 10 nm is increasing with decreasing Δ. Although the interface pushes more charge carriers into the OSC for decreasing Δ, the OSC cannot transport them away from the contact. When the charge-carrier density and the electric field in the OSC are unchanged, the current density in the OSC, determined by Equation (5.17), will not change as well, resulting in a saturation of the current density.

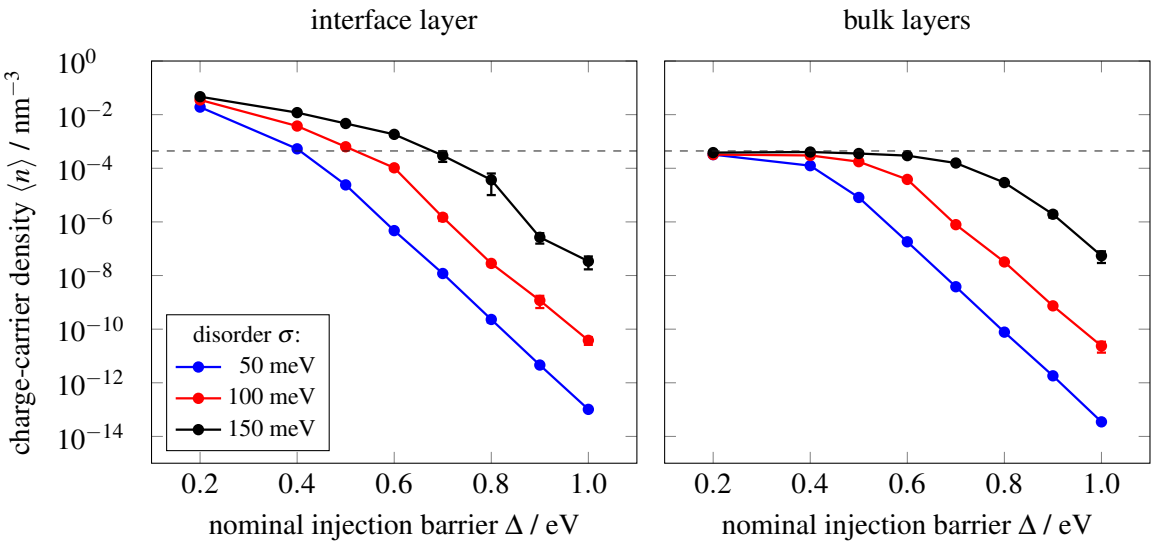

Figure 5.3: Average charge-carrier density $\langle n \rangle$ as a function of the nominal injection barrier Δ for energetic disorders of $\sigma = 50$ meV (blue), $\sigma = 100$ meV (red), and $\sigma = 150$ meV (black). In the left panel, the charge-carrier density is averaged over the first layer in the OSC directly adjacent to the metal contact. In the right panel, the charge-carrier density is averaged over all layers in a distance from the contact between 10 nm and 40 nm. The charge-carrier density at the interface (left panel) increases with decreasing nominal injection barrier Δ even for very low Δ. In contrast, the charge-carrier density in the bulk (right panel) saturates for low Δ to a certain value which we call limiting charge-carrier density. This limiting charge-carrier density is indicated by a dashed line and its value is calculated in Chapter 5.3. All curves for different energetic disorders saturate to the same limiting charge-carrier density. As already observed in Figure 5.2, lowering the nominal injection barrier Δ results in an increase in the charge-carrier density $\langle n \rangle$ allover the OSC in the contact-limited regime. When decreasing Δ more and entering the bulk-limited regime, the contact tries to push more charges into the OSC and increases the charge-carrier density at the interface. But the bulk cannot take more charge carriers so that the charge-carrier density in the bulk saturates with decreasing Δ.

Figure 5.3 compares the charge-carrier density $\langle n \rangle$ at the interface (left panel) and within the bulk layers (right panel) as a function of the nominal injection barrier Δ for different energetic disorders σ. Independent of the value of σ, the same quantitative behaviour at the interface and in the bulk is found. It is probably best seen for the bulk charge-carrier density (right panel) that the bulk-limited regime (constant charge-carrier density) gradually evolves into the contact-limited regime (exponential decrease) for increasing Δ. However, larger values for the energetic disorder σ sustain bulk-limited charge densities to markedly higher barriers.

The charge-carrier density in the bulk (left panel in Figure 5.3) saturates already at much higher nominal injection barriers Δ compared to the charge-carrier density at the interface (right panel in Figure 5.3). As discussed, decreasing the barrier in the bulk-limited regime increases the charge-carrier density at the interface but has no influence on the charge carrier density in the bulk. However, it is remarkable that, independent of the energetic disorder σ, the charge-carrier density in the bulk saturates to a certain value in the bulk-limited regime, indicated by dashed lines in Figures 5.2 and 5.3. In the next Chapter 5.3, we will derive an estimate for this charge-carrier density at which the transition between bulk-limited and contact-limited regime happens. This estimate will be used to get a rough estimate for the limiting behaviour of the current density for the bulk- and contact-limited regime.

5.3 Estimation of the Current Density

To get a rough, direct estimate for the current density suggested by our interface model, we take a look at the energy landscape close to the interface in the contact-limited regime. A schematic drawing of the different influences on the energy levels in the layers of the OSC close to the interface is shown in Figure 5.4.

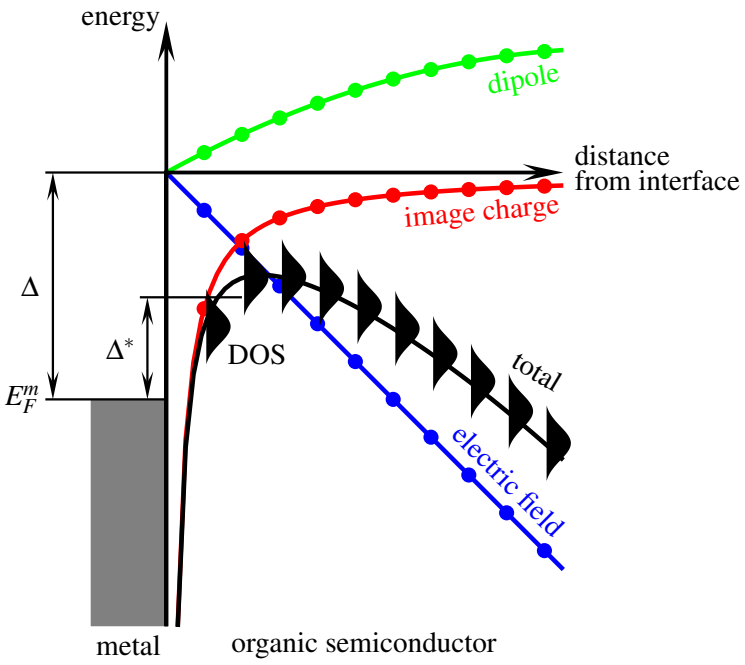

Figure 5.4: Influences on the energy levels of sites in layers parallel to the interface as a function of the distance to the interface. The metal contact is described by a nominal injection barrier Δ and a Fermi level $E_F^m = -\Delta$ resulting in one discrete half filled energy level for charge injection and extraction. In the OSC, the energy level of a site is determined by the DOS (black Gaussian curves), a contribution from the image charge due to the metal contact (red), the applied electric field (blue) and the dipole potential (green) created by the charge-carrier density in the OSC and the corresponding image charge in the metal contact. Summing up all terms (cf. Equation (5.18)), we receive the total energy level shown in black. The actual injection barrier that has to be overcome by charge carriers reduces from the nominal injection barrier Δ to the actual injection barrier Δ^* due to the modification of the energy landscape in the vicinity of the interface.

The energy of a site i in the OSC in a distance x_i from the interface is given by

$$E_i = \varepsilon_i - \frac{e^2}{16\pi\varepsilon_0\varepsilon_r x_i} - eFx_i + \frac{e^2\langle n\rangle}{\varepsilon_0\varepsilon_r} x_i \left(L - \frac{x_i}{2}\right) \tag{5.18}$$

with the four terms (from right to left) arising from: the energetic disorder, the own image charge, the applied electric field, and the dipole created by the charge-carrier density $\langle n\rangle$ in the OSC and the corresponding image charge in the metal contact. The first three terms were already introduced in Chapter 5.1.2, Equation (5.1). The fourth term in Equation (5.18) represents the approximate consideration of the potential created by the charge-carrier density in the OSC. This approximation is referring to the contact-limited regime, in which we can assume a constant charge-carrier density $\langle n\rangle$ throughout the OSC. This spatially extended charge-carrier density $\langle n\rangle$ creates a potential having a quadratic dependence on the distance to the interface, x_i^2. The length L is the size of the active region of the OSC

perpendicular to the interface plane, which is $L = 50$ nm for our model system.

Coming from the contact-limited regime with a very high nominal injection barrier Δ, the potential created by the very low constant charge-carrier density $\langle n \rangle$ in the OSC has practically no influence on the energy levels at the interface. However, when the charge-carrier density $\langle n \rangle$ increases, the force created by the charge-carrier density $\langle n \rangle$ directly at the interface increases, until it reaches the value corresponding to the applied electric field. At this condition, when the force created by the charge-carrier density $\langle n \rangle$ at the interface is equal to the force of the applied electric field, the transition to the bulk-limited regime happens. When this condition is met, the charge carriers can no longer be transported away from the interface, because they do not feel any force to move away (diffusion neglected). Evaluating this condition provides the limiting charge-carrier density $\langle n_0 \rangle$.

$$F = \frac{1}{e}\frac{\partial}{\partial x_i}\frac{e^2 \langle n_0 \rangle}{\varepsilon_0 \varepsilon_r} x_i \left(L - \frac{x_i}{2}\right)\Bigg|_{x_i=0} = \frac{e \langle n_0 \rangle L}{\varepsilon_0 \varepsilon_r} \quad \Rightarrow \quad \langle n_0 \rangle = \frac{\varepsilon_0 \varepsilon_r}{eL} F \tag{5.19}$$

This limiting charge-carrier density $\langle n_0 \rangle$ is plotted in Figures 5.2 and 5.3 as a dashed line providing a rough estimate for the charge-carrier density in the bulk-limited regime. Especially for the distances beyond 10 nm, which are more important for the influence on the region close to the interface, the space-charge limited charge-carrier density approaches the limiting charge-carrier density $\langle n_0 \rangle$ well.

From the limiting charge-carrier density $\langle n_0 \rangle$, we can calculate a corresponding Fermi level $E_F^o(\langle n_0 \rangle)$ of the Gaussian DOS with energetic disorder σ in the OSC with respect to the maximum of the DOS numerically by solving the implicit integral equation

$$\frac{\langle n_0 \rangle}{a^3} = \int_{-\infty}^{\infty} dE \frac{1}{1 + \exp\left(\frac{E - E_F^o(\langle n_0 \rangle)}{k_B T}\right)} \frac{1}{\sqrt{2\pi}\sigma} \exp\left(-\frac{E^2}{2\sigma^2}\right). \tag{5.20}$$

We propose that the transition between bulk- and contact-limited regime occurs when the Fermi level of the metal contact is equal to the Fermi level in the OSC at the maximum of the average total energy (maximum of the black curve in Figure 5.4). This proposition corresponds to the assumption that the actual injection barrier is zero $\Delta^* = 0$ eV (cf. Figure 5.4). To translate this proposition into formulas, we need the maximum of the average total energy E^{max}. To get E^{max}, we simplify the derivation of the transition injection barrier Δ_T even more by, (i), neglecting the energy contribution from the charge-carrier density in the OSC (dipole potential) and, (ii), neglecting the discrete nature of the system. The maximum energy of $E(x) = -e^2(16\pi\varepsilon_0\varepsilon_r x)^{-1} - eFx$ is given by $E^{max} = -e\sqrt{eF(4\pi\varepsilon_0\varepsilon_r)^{-1}}$. With this we get the transition injection barrier Δ_T from the proposed condition

$$E_F^m = E^{max} + E_F^o(\langle n_0 \rangle), \quad E_F^m = -\Delta_T \quad \Rightarrow \quad \Delta_T = e\sqrt{\frac{eF}{4\pi\varepsilon_0\varepsilon_r}} - E_F^o(\langle n_0 \rangle) \tag{5.21}$$

The Fermi level $E_F^o(\langle n_0 \rangle)$ with respect to the maximum of the DOS is determined by Equation (5.20). This transition injection barrier Δ_T approximately distinguishes nominal injection barriers Δ with respect to the bulk-limited regime, $\Delta < \Delta_T$, and the contact-limited regime, $\Delta > \Delta_T$.

With this very rough estimate of the transition injection barrier Δ_T, we can move on to derive a rough estimate of the current density j_{if}. In Chapter 5.2, we already found out that in the bulk-limited regime, the current density j_B is constant with respect to the nominal injection barrier Δ. In contrast, the current density j_C in the contact-limited regime exponentially decreases with increasing nominal injection barrier

Δ with a temperature-activated decrease. The assumption that the two currents are equal at the transition injection barrier Δ_T results in a contact-limited current of the form

$$j_C = j_B \exp\left(\frac{\Delta_T - \Delta}{k_B T}\right). \tag{5.22}$$

In total, the current density has to flow through both regions, the contact region and the bulk region further away from the interface. So we have to add up the two resistivities $\rho_{B/C} = F \cdot j_{B/C}^{-1}$ to get the total current density j_{if}:

$$j_{if} = \frac{F}{\rho_B + \rho_C} = \frac{F}{\frac{F}{j_B} + \frac{F}{j_C}} = \frac{j_B}{1 + \exp\left(\frac{\Delta - \Delta_T}{k_B T}\right)} \tag{5.23}$$

The current density in the bulk-limited regime j_B can be estimated with the help of Equation (5.17), assuming that the charge-carrier density is approximately given by the limiting charge-carrier density $\langle n_0 \rangle$ and the electric field corresponds approximately to the applied electric field F neglecting influences from the charge-carrier density. The only unknown quantity remaining is the bulk mobility $\mu_B(\langle n \rangle, F)$ which shows a pronounced dependence on the charge-carrier density $\langle n \rangle$ and the electric field F (cf. Chapter 4). The bulk mobility μ_B was extracted from KMC simulations of bulk systems (no contacts, periodic boundary conditions in all three dimensions) with the corresponding limiting charge-carrier densities $\langle n_0 \rangle$ and applied electric fields F. These values result in an estimate for the current density given by

$$j_{if} = \frac{e \langle n_0 \rangle \mu_B(\langle n_0 \rangle, F) F}{1 + \exp\left(\frac{\Delta - \Delta_T}{k_B T}\right)}. \tag{5.24}$$

For the KMC simulations, that evaluate the bulk mobility $\mu_B(\langle n_0 \rangle, F)$, the charge-carrier density was increased to match the next higher possible integer number of charge carriers in a finite system of $35 \times 35 \times 50$ sites. An averaging over 10 different energy landscapes was performed.

A comparison of the simulated and estimated current density j_{if} as a function of the nominal injection barrier Δ for different applied electric fields F and energetic disorders σ can be found in Figure 5.5. The red data points in both plots corresponds to the data shown in Figure 5.1. The data points connected by lines show the simulated current density, the continuous lines are the estimate predicted by Equation (5.24) and the crosses mark the transition injection barrier Δ_T.

Looking at the left panel in Figure 5.5, the current density j_{if} as a function of the nominal injection barrier Δ for three different energetic disorders $\sigma = 50$ meV, $\sigma = 100$ meV, and $\sigma = 150$ meV are plotted in blue, red, and black, respectively, for an applied electric field of $F = 10^8 \ \frac{\mathrm{V}}{\mathrm{m}}$. When focusing only on the simulated data, an interesting effect can be seen. In the bulk-limited regime (low nominal injection barriers $\Delta \leq 0.4$ eV), the current density is much higher for lower energetic disorders σ. This is due to the higher mobility μ for lower energetic disorder, because the charge carriers can move much more efficient when the energetic disorder is low. In contrast, the current density in the contact-limited regime (high nominal injection barrier $\Delta \geq 0.8$ eV) increases with increasing energetic disorder due to the fact that charge carriers can find lower energy pathways through the barrier for high energetic disorder. This reduction of the actual barrier is also reflected by a lower Fermi level in the bulk. Correspondingly also the transition injection barrier Δ_T increases, as indicated by the crosses in Figure 5.5. For all three

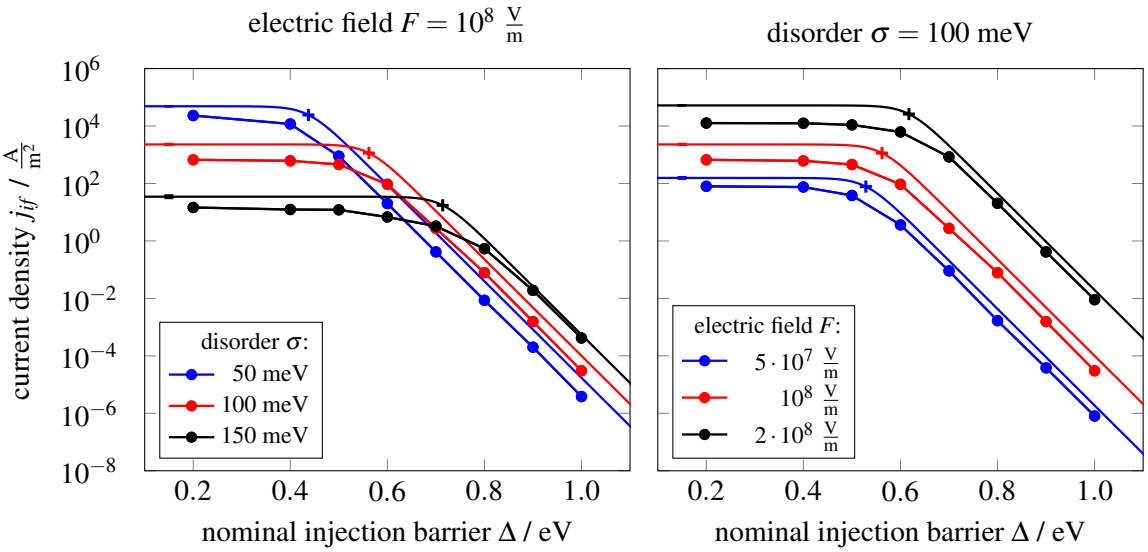

Figure 5.5: Current density j_{if} through a metal-OSC interface as a function of the nominal injection barrier Δ for different energetic disorders σ of the OSC and applied electric fields F. The dots linked by lines represent the data simulated by KMC, the continuous line shows the estimate of the current density predicted by our strongly simplifying derivation and the plus signs indicate the position of the estimated transition injection barrier Δ_T.

energetic disorders, the estimate of the transition injection barrier matches well the one suggested by the simulated data, which is in accord with well matching kinks that illustrate the transition between bulk- and contact- limited regime. The estimated current densities in the bulk-limited regime systematically overestimate the simulated current density due to the approximation of a constant charge-carrier density. The consideration of a non-constant distribution of the charge-carrier density including the variation of the bulk mobility with the charge-carrier density might reduce this discrepancy.

The right panel in Figure 5.5 shows the current density j_{if} as a function of the nominal injection barrier Δ for different applied electric fields $F = 5 \cdot 10^7$ $\frac{\text{V}}{\text{m}}$, $F = 10^8$ $\frac{\text{V}}{\text{m}}$, and $F = 2 \cdot 10^8$ $\frac{\text{V}}{\text{m}}$ plotted in blue, red, and black, respectively, for an energetic disorder of $\sigma = 100$ meV. The comparison between estimated and simulated current density reveals a reasonable semi-quantitative agreement, despite a marked deviation of the current density values in the bulk-limited regime. Also, those deviations arise from the assumption of a constant charge-carrier density in the OSC. The dependence of the transition injection barrier Δ_T on the applied electric field F is captured remarkably well. This is actually surprising due to the fact that neglecting the effect of the limiting charge-carrier density $\langle n_0 \rangle$ on the transition injection barrier Δ_T could be supposed to make the estimate much worse.

In both panels in Figure 5.5, the main deviations between estimated and simulated current density are found in the bulk-limited regime and, in particular, at the transition between the regimes. The former could be improved as discussed above. The latter deviation was expected, because the estimate was derived to only cover the limiting regions for very high and very low nominal injection barrier. In all instances, the estimate for the transition injection barrier Δ_T shows a remarkably good agreement with the transition between the regimes suggested by the simulated data.

5.4 Interpretability of the Model System

The choice of the model system for the interface simulations was clearly inspired by the work of Wolf *et al.* [79], especially the extracting layers on the facet of the OSC, which is opposite to the metal contact. The restrictions introduced by those extracting layers and the remaining geometric conditions, as well as their influence on the interpretability of the simulation results will be discussed in this chapter. We will transfer the knowledge from the model system for the interface simulations to an actual device.

The basic idea of our model system was to equalise the Fermi level of the contact and the Fermi level at a certain position in the device to detect a transition between charge transport regimes. This idea might also be transferred to other device structures like organic thin-film transistors or organic light-emitting diodes. Nevertheless, the only device that we can describe with our model system is a single layer unipolar diode with a layer thickness of the OSC which is twice the thickness of the simulated model system.

Even the single layer unipolar diode is just approximately represented due to the extracting layers. In those layers, a charge carrier practically does not feel a force from the other charge carriers. This is due to the fact, that a homogeneous charge-carrier density infinitely extended in two dimensions in combination with its image charge due to the metal contact results in a vanishing electric field outside the charged region (easily shown by applying Gauss's law). Transferring this required condition of a vanishing force to a device implies that the charge-carrier density has to be symmetric with respect to the extracting layers, because a symmetric charge-carrier density results in no force in the plane of symmetry. This implies that, (i), the single layer unipolar diode has twice the thickness of the simulated system and, (ii), the charge-carrier density has to be approximately constant allover the device. If the charge-carrier density is not constant, the model system is applicable only if the charge-carrier density is symmetric, which is very unlikely. In the contact-limited regime, the charge-carrier density is approximately constant, enabling the applicability of our model system. In the bulk-limited regime the charge-carrier density decreases from the contact towards the extracting layers (cf. Figure 5.2). Considering the single layer unipolar diode, it is not reasonable to assume that the charge-carrier density in the second half of the device increases towards the contact at which the charge carriers leave the diode. Hence, the applicability of our model system becomes less trustworthy in the bulk-limited regime. As the assumptions and the argumentation put forward in Chapter 5.3 are based on the contact-limited regime, our findings should be applicable to interpret experimental results, as we will attempt in the following Chapter 5.5.

5.5 Comparison with Experiment

The measurements performed by Raoufi *et al.* [110] provide a perfect data set to test the plausibility of our model system for the interface and the estimate of the current density. They built single layer unipolar diodes with Poly(3-hexylthiophen-2,5-diyl) (P3HT) as OSC and Zinc oxide (ZnO) as injecting contact material coated with a variety of different self-assembled monolayers (SAMs) to tune the work function of the ZnO. Additionally to tuning the work function with SAMs, they exposed the devices to UV radiation which changes the work function of ZnO. In total, they were able to provide current density-voltage (j-V) characteristics for 14 different work functions from 7 different contact treatments with and without UV soaking. The achieved range of work functions spans nearly 2 eV between 3.8 eV and 5.8 eV.

5.5.1 Extraction of the Transition Work Function

The basic assumptions within our model system of a perfect metal contact are not strictly fulfilled for the injecting ZnO contact, but are met reasonably well. Hörmann *et al.* successfully applied an image charge based model to describe the polarisability of a molecule in the vicinity of a ZnO surface. [115] So our model system is applicable to interpret the measurements performed on the devices fabricated by Raoufi and co-workers. [110] The hole-conductor P3HT, used as the OSC in the devices, has an onset of the highest occupied molecular orbital (HOMO) of approximately $E_{HOMO} \approx 4.9$ eV [116] and its deposited layer thickness is $2L = 200$ nm. To translate the transition injection barrier Δ_T for electron transport to a transition work function W_T^F for hole transport, we identify the onset of the HOMO E_{HOMO} as the onset of the Gaussian DOS, which is assumed to be 2σ below the maximum of the Gaussian DOS. With Equation (5.21), the transition work function W_T^F is given by

$$W_T^F = E_{HOMO} + 2\sigma - \Delta_T = E_{HOMO} + 2\sigma - e\sqrt{\frac{eF}{4\pi\varepsilon_0\varepsilon_r}} + E_F^o\left(\langle n_0\rangle\right). \tag{5.25}$$

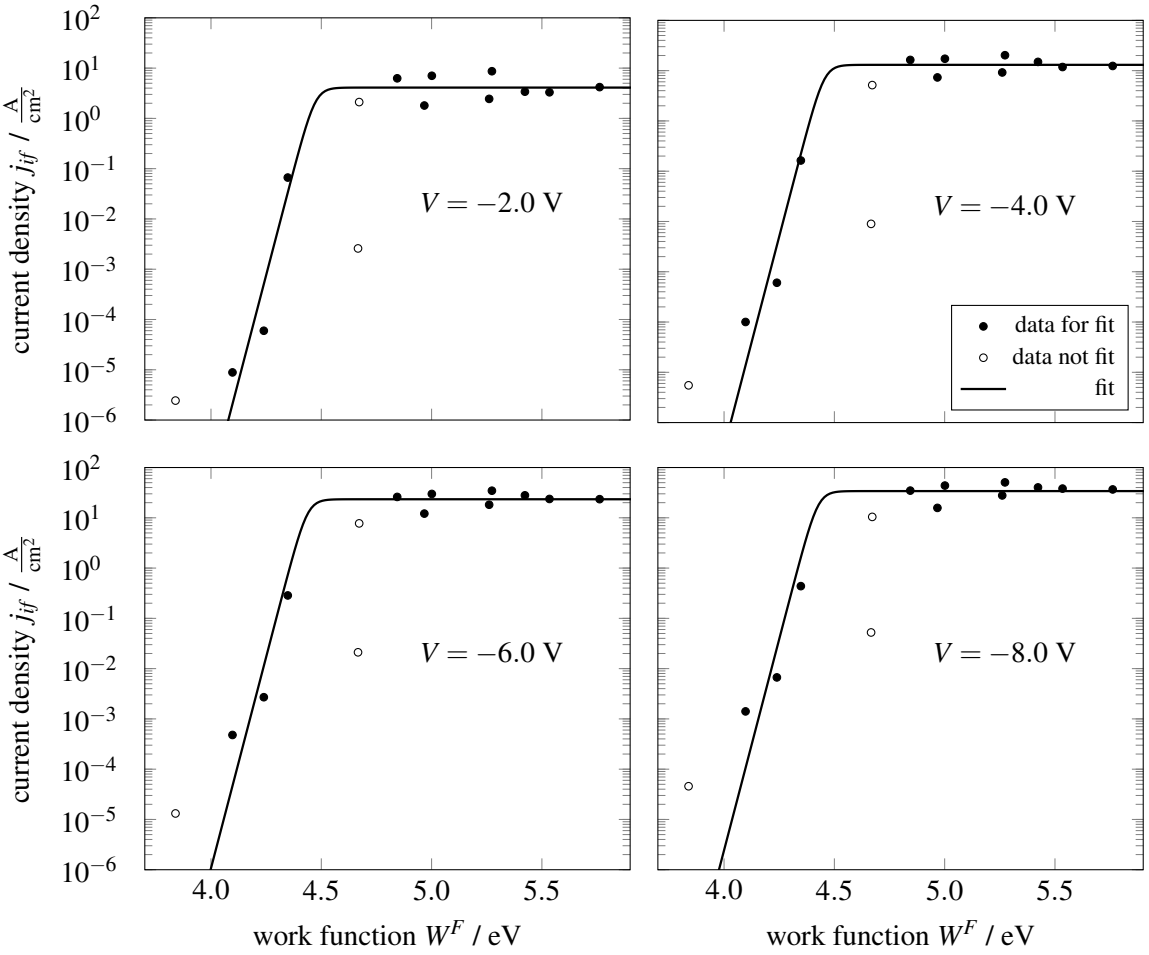

Figure 5.6: Measured current density j_{if} (symbols) as a function of the measured work function of the single layer unipolar diodes measured by Raoufi *et al.* [110] for different applied voltages V. The lines represent a fit with respect to the estimate of the current density derived in Chapter 5.3. The open symbols correspond to data points that are not considered for the extraction of the fit parameters (details see text).

The applied electric field $F = -\frac{V}{2L}$ is determined by the applied voltage V and the thickness $2L$ of the OSC.

To extract the transition work function W_T^F from the measured current density-voltage (j-V) characteristics of the set of devices, we performed a fit of the estimate of the current density in analogy to Equation (5.23) for the transition injection barrier Δ_T:

$$j_{if} = \frac{j_B}{1+\exp\left(\frac{W_T^F - W^F}{k_B T}\right)}. \tag{5.26}$$

For each applied voltage V, the measured current densities j_{if} of the devices with different measured work functions W^F are fit to this Equation (5.26), yielding the transition work function W_T^F and the current density j_B as a function of the applied voltage. The temperature is set to $T = 300$ K for all fits. Exemplary fits for voltages of $V = -2$ V, -4 V, -6 V, and -8 V are shown in Figure 5.6.

For the fits of the current density j_{if} as a function of the work function W^F shown in Figure 5.6, not all devices were used. The device with the lowest work function of about $W^F \approx 3.8$ eV was excluded, because the data is quite noisy and not overly trustworthy. Two further data points close to the transition barrier were excluded as well, because our simple estimate is supposed to only cover the limiting cases of very low and very high work functions well (cf. discussion at the end of Chapter 5.3). The devices excluded from the fit are marked with open symbols and the devices entering the fit are marked with filled symbols. For all voltages shown in Figure 5.6, the filled symbols are represented well by the fitted curve, in the contact-limited regime (work function between 4.0 eV$< W^F <$ 4.4 eV) as well as in the bulk-limited regime (work function between 4.8 eV$< W^F <$ 5.8 eV).

5.5.2 Interpretation of the Transition Work Function

Figure 5.7 shows the transition work function W_T^F as a function of the applied voltage V. The symbols in all four panels refer to the transition work function W_T^F extracted in Chapter 5.5.1. This transition work function W_T^F clearly decreases for increasing absolute values of the voltage above $|V| > 2$ V. This corresponds to a reduction of the injection barrier with increasing electric field strength, in line with the expectation that the electric field promotes injection. For low absolute values of the voltage below $|V| < 2$ V, the extracted data becomes rather noisy and less trustworthy. In this region $|V| < 2$ V, the transition work function W_T^F appears to decrease for decreasing absolute values of the voltage. This might be an artefact of the spread of the measurements for such low $|V|$ in combination with the extraction procedure. Hence, the behaviour in this low voltage region has to be interpreted with particular care.

To enable an interpretation of the transition work function W_T^F, we now attempt to reproduce the evolution of W_T^F with respect to the applied voltage V with different assumptions. In a first step, the extracted transition work functions are fit to Equation (5.25) under the assumption that the Fermi level E_F^o in the OSC is held constant for varying electric field F. The curve calculated from this fit is shown as a line in the upper left panel in Figure 5.7. The calculated curve agrees well with the extracted transition work functions W_T^F in the region of high absolute values of the applied voltage $|V| > 2$ V. For low absolute values of the voltage $|V| < 2$ V, the curve is not according with the data. This might be either due to a failure of the calculation or due to the inferior quality of the extracted data in this region. The fit reveals the relative permittivity $\varepsilon_r = 6.54$ and the zero-field transition work function $W_{F0}^F = 4.52$ eV. This zero-field transition work function W_{F0}^F is the transition work function at $V = 0$ V,

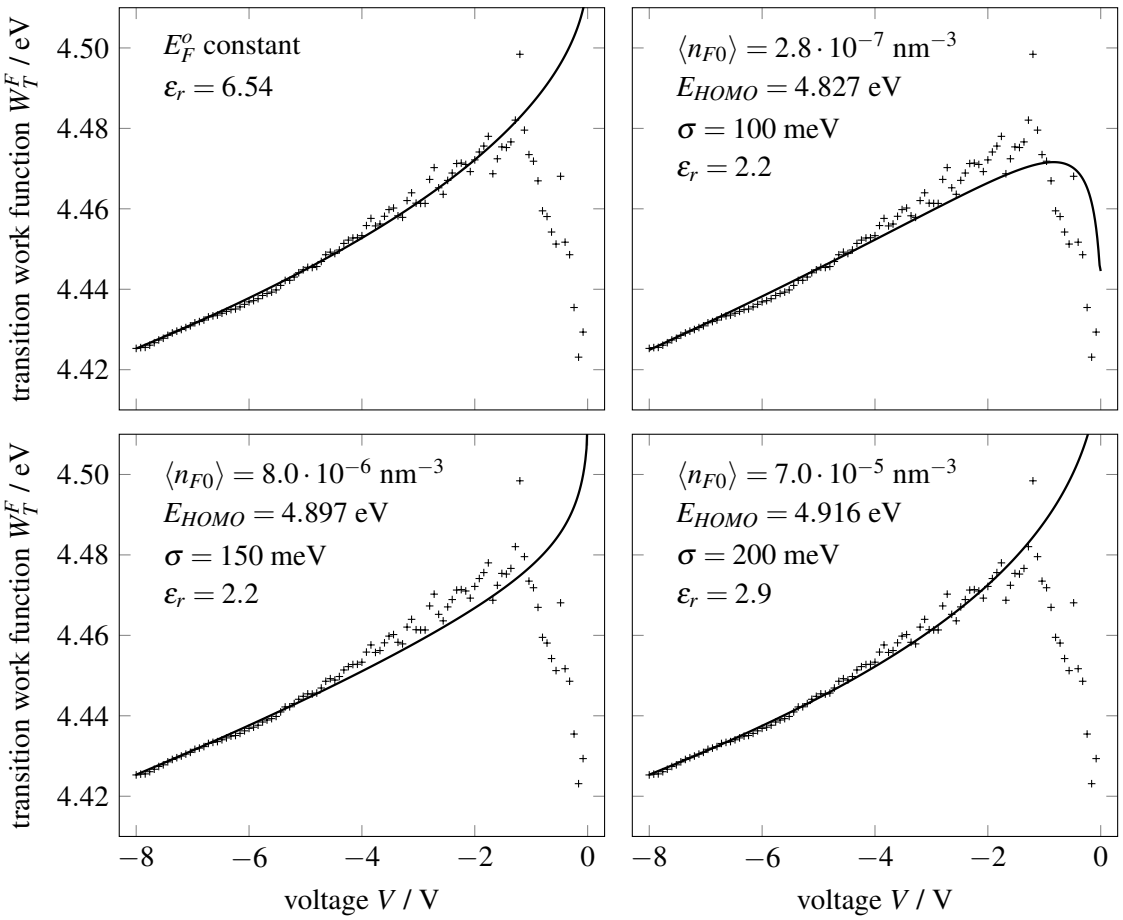

Figure 5.7: Transition work function W_T^F of the transition between bulk-limited and contact-limited regime as a function of the applied voltage V. The symbols show the values extracted in Chapter 5.5.1 from the measurements by Raoufi *et al.* [110]. The lines indicate calculations referring to Equation (5.25) for different assumptions of the parameters. In the upper left panel, we neglect the field dependence of the Fermi level E_F^o in the OSC and only fit the square root behaviour of the electric field-induced barrier lowering resulting in $\varepsilon_r = 6.54$. The remaining panels are considering the field dependence of the Fermi level $E_F^o(\langle n_0 \rangle)$ in the OSC with different values for the zero-field charge-carrier density $\langle n_{F0} \rangle$ (cf. Equation (5.27)), the onset of the HOMO E_{HOMO}, the energetic disorder σ and the relative permittivity ε_r. All curves show good agreement with the data extracted from the measurements for high absolute values of the applied voltage $V < -4$ V with significant deviations only in the noisy region of low absolute values of the applied voltage $V > -2$ V. The parameters are in a reasonable range for σ between 100 meV and 200 meV and for ε_r between 2.2 and 6.54. For a low zero-field charge-carrier density $\langle n_{F0} \rangle$ (upper right panel), a decrease of the transition work function W_T^F with decreasing absolute values of the applied voltage appears for the calculations. The decrease in electric field results in a decrease of the charge-carrier density and a subsequent decrease of the Fermi level provoking the decrease of W_T^F (details see text).

which is composed of $W_{F0}^F = E_{HOMO} + 2\sigma + E_F^o$, cf. Equation (5.25). Assuming an onset of the HOMO at $E_{HOMO} \approx 4.9$ eV, we can calculate Fermi levels $E_F^o = W_{F0}^F - E_{HOMO} - 2\sigma$ in the OSC that correspond to different energetic disorders σ. With the help of Equation (5.20), we can calculate the charge-carrier densities $\langle n_0 \rangle$ corresponding to each of the disorder-determined Fermi levels. For energetic disorders of $\sigma = 100$ meV, $\sigma = 150$ meV, and $\sigma = 200$ meV, the corresponding charge-carrier densities are $\langle n_0 \rangle = 2.97 \cdot 10^{-7}$ nm^{-3}, $\langle n_0 \rangle = 8.79 \cdot 10^{-6}$ nm^{-3}, and $\langle n_0 \rangle = 7.38 \cdot 10^{-5}$ nm^{-3}, respectively.

In a next step, we attempt to more accurately estimate the transition work function W_T^F by including

the charge-carrier-density $\langle n_0 \rangle$ dependence of the Fermi level $E_F^o(\langle n_0 \rangle)$ in the OSC. Each refinement is shown in a dedicated panel in Figure 5.7 along with an indication of the used parameters $\langle n_{F0} \rangle$, E_{HOMO}, σ, and ε_r. Considering those parameters, the charge-carrier density $\langle n_0 \rangle$ splits into two contributions. For a certain value of the applied electric field $F = \frac{V}{2L}$, the total charge-carrier density $\langle n_0 \rangle$ is given by

$$\langle n_0 \rangle = \langle n_{F0} \rangle + \frac{\varepsilon_0 \varepsilon_r F}{eL}. \tag{5.27}$$

The zero-field charge-carrier density $\langle n_{F0} \rangle$ is the charge-carrier density in the OSC when no electric field is applied and can be, e.g., associated to an unintentional doping-induced charge-carrier density. For each of the above-specified disorders σ, we choose values for the zero-field charge-carrier density $\langle n_{F0} \rangle$ that are slightly lower than the charge-carrier density values from the fits with constant Fermi level. To get the total charge carrier density $\langle n_0 \rangle$ from Equation (5.27), we also need to specify the relative permittivity ε_r. The last parameter that is required to get the transition work function W_T^F from Equation (5.25) is the onset of the HOMO E_{HOMO}. For each of the disorder values σ, we choose a value for $\langle n_{F0} \rangle$, ε_r and E_{HOMO} such that the transition work functions extracted from the experimental data (symbols in Figure 5.7) are recovered well.

In the upper right panel in Figure 5.7, the calculated curve for the lowest of the chosen energetic disorders, $\sigma = 100$ meV, and the lowest zero-field charge-carrier density, $\langle n_{F0} \rangle = 2.8 \cdot 10^{-7}$ nm^{-3}, is shown. The change in the evolution of $W_T^F(V)$ from the upper left to the upper right panel in Figure 5.7 is a combination of, (i), the voltage-dependence of the Fermi level E_F^o and, (ii), the lowering of the injection barrier due to the electric field F, cf. Equation (5.25). The voltage-dependence of E_F^o occurs due to the dependence of the charge-carrier density $\langle n_0 \rangle$ on the applied electric field F, cf. Equation (5.27). An important indicator to assess the evolution of E_F^o with respect to $\langle n_0 \rangle$ is the voltage V_{nF} at which the charge-carrier density induced by the electric field $\varepsilon_0 \varepsilon_r F/(eL)$ is equal to the zero-field charge-carrier density $\langle n_{F0} \rangle$:

$$V_{nF} = \frac{2eL^2 \langle n_{F0} \rangle}{\varepsilon_0 \varepsilon_r}. \tag{5.28}$$

We can distinguish two voltage regimes. For absolute values of the applied voltage below this voltage, $|V| < V_{nF}$, we get a nearly constant Fermi level E_F^o. For such voltages, the charge-carrier density $\langle n_0 \rangle$ approaches $\langle n_{F0} \rangle$. For voltages $|V|$ far below V_{nF}, a reduction of the voltage by a factor of two would have virtually no impact on the charge-carrier density $\langle n_0(V) \rangle \approx \langle n_0(V/2) \rangle \approx \langle n_{F0} \rangle$. For absolute values of the voltage above this voltage $|V| > V_{nF}$, the charge-carrier density $\langle n_0 \rangle$ significantly increases, $\langle n_0(2 \cdot V) \rangle \approx 2 \cdot \langle n_0(V) \rangle$, leading to an increase in the Fermi level E_F^o. Upon increasing the applied voltage $|V|$ above V_{nF}, the transition work function W_T^F is increased by the Fermi level E_F^o, but simultaneously reduced by the term $\sim \sqrt{F}$ responsible for the field-induced lowering of the injection barrier.

This observation is important for the choice of the parameter values, with which we intend to match the experimentally extracted $W_T^F(V)$ evolution. To reproduce the experimental data at least as well as in the case of assuming a constant Fermi level (upper left panel in Figure 5.7), we need to lower the relative permittivity ε_r in order to compensate the rise in Fermi level. The decrease of the relative permittivity ε_r is observed for all disorder values σ considered in Figure 5.7 (upper right, lower left and lower right panel). Based on the voltage V_{nF}, we can now rationalise the evolution of the transition work function W_T^F with the applied voltage V for different extents of disorder σ. In the upper right panel in Figure 5.7,

the voltage is $V_{nF} = 0.044$ V, which is not distinguishable from 0 V on the plotted scale. For low absolute values of the voltage below $|V| < 0.5$ V, the transition work function in the upper right panel in Figure 5.7 increases with increasing absolute values for the voltage, because the Fermi level E_F^o increases the transition work function faster than the field-induced-barrier lowering decreases it. The voltages V_{nF} for the higher values of disorder, i.e., for $\sigma = 150$ meV in the lower left panel in Figure 5.7 and for $\sigma = 200$ meV in the lower right panel in Figure 5.7, are $V_{nF} = 1.3$ V and $V_{nF} = 11.5$ V, respectively. As the Fermi level E_F^o does not change much below $|V| < V_{nF}$, no increase of the transition work function W_T^F with increasing absolute voltage $|V|$ is observed for the lower panels in Figure 5.7.

All calculated curves in Figure 5.7 match the data extracted from the measurements well in the region where the data is trustworthy $V < -4$ V. This implies that the data is consistent with a wide range of parameter values that, in turn, cannot be quantified precisely. On the other hand, our simple estimations are able to explain the behaviour of the single layer unipolar diodes for different work functions of the injecting contact. The range of parameter values used to calculate the curves in Figure 5.7 is reasonable and plausible for the materials used in the single layer unipolar diodes. Nevertheless, our estimate of the current density and the subsequently extracted transition work function is not accurate enough to deliver quantitative results.

6 Summary and Outlook

In this thesis, we were investigating charge transport in organic semiconductor (OSC) devices with the goal to improve the basic understanding of charge transport in the bulk of the OSC as well as charge transport through the interface between a metal and an OSC. The necessity of this improved understanding was motivated in Chapter 2, in which we developed a new method to verify or falsify theoretical transistor models describing the operation of organic thin-film transistors (OTFTs). The idea behind the new method is, that a correct transistor model has to contain the correct channel-length dependence. Based on this idea, experimentally measured output and transfer characteristics of a set of formally equivalent OTFTs with varying channel length are required. With those sets of measured OTFT data corresponding to a certain channel length, we suggested a two-step-fitting approach (TSFA) to test the transistor model. In the first step, the parameters of the tested transistor model are extracted by fitting all measured output and transfer characteristics of a single OTFT to the transistor model. This fitting approach ensures, that we extract the best possible parameters representing the assumptions of the tested transistor model from the measurements of each OTFT separately. The second step collects all extracted parameters of all formally equivalent OTFTs and inspects the channel-length dependence of the parameters. A pronounced channel-length dependence of a parameter implies that the transistor model does not distinguish correctly between contact and channel, i.e., it indicates the failure of the transistor model. With our TSFA, we tested a state-of-the-art OTFT model incorporating a field and charge-carrier-density dependence of the mobility. The test included several sets of OTFTs with different OSCs, different geometries, and different contact treatments, providing a representative sample of OTFT-technologies. All sets of OTFTs provoked a clear failure of the transistor model, indicated by a pronounced dependence of the ohmic contact resistance on the channel length. The reason for this failure can be analysed within our TSFA as well. This analysis identified two potential problems in the tested transistor model. First, our TSFA suggested that the assumed field and charge-carrier-density dependence of the charge-carrier mobility is wrong. Second, we supposed that the disregard of the influence of charge accumulations in the channel of the OTFT on the contact region close to the metal-OSC interface due to long-ranging Coulomb interactions might be unjustified. The first problem motivated Chapters 3 and 4, whereas the second problem motivated Chapter 5.

The necessity to improve the understanding of charge transport within the OSCs, discussed in Chapter 2, triggered the development of a novel simulation technique for hopping transport. We demonstrated the applicability of this novel simulation technique for the example of charge transport in the bulk of OSCs in Chapter 3. The novel simulation technique, which we named correction energy concept (CEC), is a formal link between the two established simulation techniques for hopping transport, which are kinetic Monte Carlo (KMC) and master equation (ME). In its most basic version, the CEC is comparable to ME, in which interactions can be included via a mean field approach. In ME, it is difficult to consider interactions beyond a mean field approach. In contrast, the CEC enables the direct inclusion of correlations and interactions. While correlations and interactions increase the computational cost, they reduce the methodological error, so that results evolve towards the accurate results received by computationally expensive KMC simulations. In Chapter 3, we discussed the mathematical foundation and the implementation of our new CEC in detail and performed simulations to verify our CEC by comparing the results to the outcome of accurate KMC simulations.

Our CEC does not only provide an efficient simulation technique, it also delivers a novel insight

into charge transport in OSCs. In Chapter 4, we were able to utilise the insight gained by the CEC to explain the field and charge-carrier-density dependence of the bulk mobility. The gained insight provided a rough estimate for a transition field, at which a significant increase of the mobility with respect to the applied electric field was proposed. Indeed, CEC simulations (validated by KMC simulations) showed this proposed increase of the mobility around the estimated transition field for a wide range of different charge-carrier densities and energetic disorders. With this explanation of the field and charge-carrier-density dependence of the mobility, an important step towards a revised mobility model was achieved.

The second problem revealed in Chapter 2 was investigated in Chapter 5. This problem is related to the interplay between charge accumulations within the OSC and the behaviour of charge carriers in the region close to the metal-OSC interface via long-ranging Coulomb interactions. With the help of KMC simulations, the contact region of a metal-OSC interface was investigated. For those simulations, we derived a refined description of the metal contact to enable the consideration of the occupation probability within the metal in addition to the energy level of the metal contact. The outcome of such a simulation is the current density through the interface, which can be either contact limited or bulk limited. Contact-limited transport means that the injection from the metal contact to the OSC is the bottleneck for charge transport. Bulk-limited transport refers to the situation in which the contact wants to push more and more charge carriers into the OSC while the bulk is not able to transport the charge carriers away from the contact region. We saw, that the transition from the contact-limited regime to the bulk-limited regime is determined by the dipole built up by, (i), the charge accumulation in the bulk of the OSC far away from the interface and, (ii), the image charge of this charge accumulation due to the metal contact. When a certain charge-carrier density is reached in the bulk of the OSC, the associated dipole compensates the externally applied electric field in the contact region, so that charge carriers cannot be transported away. A strongly simplifying model for the current density through the interface captured this behaviour semi-quantitatively well and was further used to describe experimentally measured current-voltage characteristics of a set of single layer unipolar diodes with injection barriers varying over more than 1.5 eV.

It is quite natural that, by answering questions, new questions arise. This is particularly true for the present thesis. The new methods and their outcomes discussed above provide numerous possibilities for further developments and applications. From Chapter 5, we learned that charge accumulations throughout the whole device can have a perceptible influence on the contact region due to long-ranging Coulomb interactions. This know-how can be applied to organic semiconducting devices, in particular to OTFTs enabling an improvement of the transistor model. With the insight gained in Chapter 4, it is possible to derive an improved description of the field and charge-carrier-density dependence of the mobility. Concerning the predominantly two-dimensional charge transport in OTFTs, the new insight into charge transport can even help to develop a mobility model particularly suited for OTFTs. With those two improvements of the transistor model with respect to the contact description and the mobility model, our TSFA can be utilised to test the improved transistor model. Also other transistor models, possibly including sophisticated mobility models, can be tested by our TSFA to continuously gain more and more experimental insight into charge transport mechanisms in OSCs.

To gain theoretical insight into charge transport mechanisms in OSCs, our correction energy concept (CEC) is suited very well. From the fundamental nature of the correction energies, we learned how to interpret the field and charge-carrier-density dependence of the bulk mobility in Chapter 4. Beyond its fundamental nature, the CEC can be viewed as a method to systematically include certain correlations

and/or interactions. By including particular correlations or particular interactions, it is possible to reveal, which correlations and interactions are relevant for the mobility and which correlations and interactions can be neglected. This insight might be used to, (i), speed up CEC simulations and simultaneously reduce the methodological error and, (ii), improve analytical models by including the impact of the relevant correlations and interactions. So the CEC holds the potential to decipher the effect of correlations and interactions in hopping transport. Before this potential is released, a further development of the CEC is required to efficiently include interactions and correlations in the occupation statistics.

We derived the CEC in Chapter 3 for charge transport in bulk. This derivation was just an example and can be generalised for any steady-state hopping transport simulation, e.g., including contacts, ambipolar charge transport, excitons, electron-hole recombination and many more. The only prerequisite is, that the rates for charge transport are energy conserving with respect to a closed system. This prerequisite is assured for the Miller-Abrahams as well as for the Marcus rate equation.

In summary, the CEC is a powerful method to investigate charge transport in OSC devices and opens up new possibilities for numerical as well as for analytical advances in describing charge transport. With the TSFA, theoretical insight gained via the CEC can be verified experimentally.

7 Abbreviations and Formula Symbols

Abbreviations

ccps	charge carrier per site
CEC	correction energy concept
DFT	density functional theory
DOS	density of states
HOMO	highest occupied molecular orbital
ILC	injection-limited current
KMC	kinetic Monte Carlo
LUMO	lowest unoccupied molecular orbital
ME	master equation
MF	mean field
MTR	multiple trapping and release
ODOS	occupied density of states
OLED	organic light-emitting diode
OSC	organic semiconductor
OTFT	organic thin-film transistor
SAM	self-assembled monolayer
SCLC	space-charge-limited current
TLM	transmission line model
TSFA	two-step-fitting approach
VRH	variable-range hopping

Formula Symbols

a	lattice constant, distance between nearest neighbours
α	charge delocalisation constant
α_D	weighting factor of the non-ohmic contribution to the drain resistance
α_S	weighting factor of the non-ohmic contribution to the source resistance
β	inverse temperature $\beta = \frac{1}{k_B T}$
C_G	gate capacitance per unit area
$\mathrm{DOS}(E)$	density of states for a given energy E
δ_{ij}	Kronecker delta $\delta_{ij} = 1$ for $i = j$ and $\delta_{ij} = 0$ else
Δ	nominal injection barrier
Δ^*	actual injection barrier
Δ_T	transition injection barrier determining the transition from the contact-limited to the bulk-limited regime
$\Delta E_{F,i}^{N_{cc}}$	local change in Fermi level of site i of a system with N_{cc} charge carriers
$\Delta\mu$	variance of the mobility with respect to different energy landscapes $\Delta\mu = \sqrt{\langle\mu^2\rangle - \langle\mu\rangle^2}$
$\Delta\mu_{rel}$	relative error of the mobility evaluated with the CEC with respect to KMC results

Formula Symbols (continued)

$\Delta\vec{r}_{ij}$	spatial distance between site i and site j
Δr_{ij}	absolute spatial distance between site i and site j
e	elemental charge
$E_i(\xi)$	energy of a charge carrier at site i in configuration ξ
E_B	barrier energy
E_i^c	site-correction energy of site i
E_{ij}^c	correlation-correction energy between site i and site j
E_F^m	Fermi level of the metal contact
$E_{F,0}^{N_{cc}}$	global Fermi level of a system with N_{cc} charge carriers
$E_{F,i}^{N_{cc}}$	local Fermi level of site i of a system with N_{cc} charge carriers
E_{HOMO}	energy of the onset of the highest occupied molecular orbital
E_i^{int}	average interaction energy at site i
E_{ij}^{int}	interaction energy between charge carriers occupying site i and site j
E_i^m	energy of a contact site i in the metal contact
E_{ML}	most likely energy of the charge carriers
E_r	reorganisation energy
$\mathrm{erf}(u)$	error function
$\mathrm{erfc}(u)$	complementary error function $\mathrm{erfc}(u) = 1 - \mathrm{erf}(u)$
$E^{tot}(\xi)$	total energy of the system in configuration ξ
E_i^{tot}	total energy of a site i containing the site energy and the site-correction energy $E_i^{tot} = \varepsilon_i - E_i^c$
E_{ij}^{tot}	total interaction energy between site i and site j containing the interaction energy and the correlation-correction energy $E_{ij}^{tot} = E_{ij}^{int} - E_{ij}^c$
ε_i	randomly chosen site energy of site i
ε_0	vacuum permittivity
ε_r	relative permittivity of the material
η	gate-source voltage sensitivity of the Schottky diode
F	absolute value of the electric field strength
$\vec{F}$	electric field
F^*	transition field determining the transition between charge transport regimes
γ	exponent of the sensitivity with respect to the charge-carrier density of the mobility
h	channel height of the OTFT
I_D	drain current of an OTFT
$I_{D,sat}$	saturation drain current
j_0	channel-width-reduced Schottky current
j_B	current density in the bulk-limited regime
j_C	current density in the contact-limited regime
j_{Ch}	current density in the channel of the OTFT
j_{if}	current density flowing through the metal-organic semiconductor interface
k_B	Boltzmann constant

Formula Symbols (continued)

κ	exponent of the field sensitivity of the mobility
L	channel length of the OTFT
L_0	constant length scale $L_0 = 1\ \mu$m
L_R	average size in field direction of the transport-relevant region
L^i_{sys}	system size in spatial direction i
L_T	transfer length
μ	mobility
μ_0	mobility prefactor
$\langle\mu\rangle$	mobility averaged over multiple energy landscapes
$\langle\mu^2\rangle$	square of the mobility averaged over multiple energy landscapes
n_i^ξ	occupation of site i in configuration ξ
n_i^m	occupation of site i in the metal contact
n_i^o	occupation of site i in the organic semiconductor
$\langle n\rangle$	total average charge-carrier density in the system
$\langle n_i\rangle$	average charge-carrier density of site i
$\langle n_i\rangle^{N_{cc}}_{\mathcal{N}_s}$	average charge-carrier density of site i for a system with a set of sites $\mathcal{N}_s$ and N_{cc} charge carriers
$\langle n_i^m\rangle$	average charge-carrier density of contact site i in the metal contact
$\langle n_i n_j\rangle$	average two-site occupation of site i and site j
$\langle n_i n_j\rangle^{N_{cc}}_{\mathcal{N}_s}$	average two-site occupation of site i and site j for a system with a set of sites $\mathcal{N}_s$ and N_{cc} charge carriers
$\langle n_0\rangle$	limiting charge-carrier density for the metal-organic semiconductor interface
$\langle n_{F0}\rangle$	zero-field charge-carrier density for the measured single layer unipolar diode
N_{cc}	number of charge carriers in the simulated system
N_{cnfg}	number of possible configuration of the simulated system
N_l	number of sites in one direction in a layer parallel to the contact
N_r	number of metal sites in the contact removed from the simulated system
N_s	number of sites in the simulated system
$\mathcal{N}_s$	set of sites
N_x	number of organic semiconductor layers parallel to the contact without contact and extraction layers
ν_0	hopping prefactor
$\mathrm{ODOS}(E)$	occupied density of states for a given energy E
$\mathcal{O}(n)$	big O / Bachmann-Landau / asymptotic notation indicating that the algorithm has order n time complexity
$\varphi(\Delta\vec{r})$	interaction potential of a charge carrier at a distance $\Delta\vec{r}$ including all its periodic replica
$\Phi(\vec{r})$	interaction potential at position $\vec{r}$ created by all charge carriers and their periodic replica, except the charge carrier at position $\vec{r}$
$\Phi^{img}(\vec{r})$	interaction potential at position $\vec{r}$ created by all image charge carriers and their periodic replica, except the image charge carrier associated to position $\vec{r}$

Formula Symbols (continued)

$\vec{\pi}$	steady-state-probability distribution
π_ξ	probability that configuration ξ is visited in steady state
$\pi_i^m(n)$	probability that metal site i is occupied $n=1$ or unoccupied $n=0$
q	charge sign
$q_{\xi\xi'}$	Q-matrix entry for a transition from configuration ξ to configuration ξ'
R_{ij}	rate for a hop from site i to site j
$R_{ij}(\xi)$	rate for a hop from site i to site j with initial configuration ξ
$\vec{r}_i$	spatial position of site i
$r_{C,o}$	total channel-width-reduced ohmic contact resistance $r_{C,o}=r_{D,o}+r_{S,o}$
$r_{D,o}$	channel-width-reduced ohmic drain resistance
R_D	drain resistance
R^{ex}	extraction rate for the extraction of charge carriers from the organic semiconductor
r_{hop}	maximum considered hopping distance
R^{in}	injection rate for the injection of charge carriers to the organic semiconductor
R^{MA}	Miller-Abrahams rate
R^M	Marcus rate
$r_{S,o}$	channel-width-reduced ohmic source resistance
R_S	source resistance
ρ_B	resistivity associated to the bulk-limited current density
ρ_C	resistivity associated to the contact-limited current density
$\rho_{Ch}(x)$	charge carriers per unit area at position x in the channel of an OTFT
σ	energetic disorder determining the width of the Gaussian distribution
T	temperature
T_{Sh}	temperature associated with the Schottky diode
$\Theta(\upsilon)$	Heaviside-step-function, $\Theta(\upsilon)=1$ for $\upsilon\geq 0$ and $\Theta(\upsilon)=0$ for $\upsilon<0$
$\upsilon=qV$	reduced voltage
V_0	simplified voltage loss at the Schottky diode
$V_{Ch}(x)$	channel potential at position x in the channel of an OTFT
V_{DS}	drain-source voltage of an OTFT
$V_{D'S'}$	drain-source voltage of the ideal OTFT
V_{GS}	gate-source voltage of an OTFT
$V_{G'S'}$	gate-source voltage of the ideal OTFT
V_{nF}	voltage applied to the single layer unipolar diode at which the charge-carrier density induced by the electric field is equal to the zero-field charge-carrier density
V_{Sh}	voltage loss at the Schottky diode
V_T	threshold voltage
W	channel width of the OTFT

Formula Symbols (continued)

W^F	measured work function of the injecting contact of the single layer unipolar diode
W^F_{F0}	zero-field transition work function of the measured single layer unipolar diode
W^F_T	transition work function determining the transition from the contact-limited to the bulk-limited regime
x	spatial position
ξ	configuration determining the occupied sites
ξ_m	configuration in the metal contact
ξ_o	configuration in the organic semiconductor
Ξ	configuration space containing all N_{cnfg} configurations ξ
$\Xi^{N_{cc}}_{\mathcal{N}_s}$	configuration space for a system with a set of sites $\mathcal{N}_s$ and N_{cc} charge carriers
Z	partition function
$Z^{N_{cc}}_{\mathcal{N}_s}$	partition function for a system with a set of sites $\mathcal{N}_s$ and N_{cc} charge carriers
ζ	splitting parameter of the Ewald summation

References

[1] A. Petritz, M. Krammer, E. Sauter, M. Gärtner, G. Nascimbeni, B. Schrode, A. Fian, H. Gold, A. Cojocaru, E. KarnerPetritz, R. Resel, A. Terfort, E. Zojer, M. Zharnikov, K. Zojer, and B. Stadlober, "Embedded Dipole Self-Assembled Monolayers for Contact Resistance Tuning in p-Type and n-Type Organic Thin Film Transistors and Flexible Electronic Circuits," *Advanced Functional Materials*, vol. 28, p. 1804462, Nov. 2018.

[2] M. Krammer, J. W. Borchert, A. Petritz, E. Karner-Petritz, G. Schider, B. Stadlober, H. Klauk, and K. Zojer, "Critical Evaluation of Organic Thin-Film Transistor Models," *Crystals*, vol. 9, p. 85, Feb. 2019.

[3] M. Krammer and K. Zojer, "Modelling Organic Devices - Foundation, Implementation, and Merit of the Kinetic Monte Carlo Method," in *World Scientific Reference of Hybrid Materials*, World Scientific Series in Nanoscience and Nanotechnology, pp. 135–185, World Scientific, Mar. 2019. ISBN: 9789813270534.

[4] M. L. Tietze, J. Benduhn, P. Pahner, B. Nell, M. Schwarze, H. Kleemann, M. Krammer, K. Zojer, K. Vandewal, and K. Leo, "Elementary steps in electrical doping of organic semiconductors," *Nature Communications*, vol. 9, p. 1182, Mar. 2018.

[5] R. Das, X. He, and K. Ghaffarzadeh, "Printed, organic and flexible electronics 2020-2030: Forecasts, technologies, markets." `https://www.idtechex.com/de/research-report/printed-organic-and-flexible-electronics-2020-2030-forecasts-technologies-markets/687`, Oct. 2019. Accessed: 2019-11-11.

[6] H. Klauk, "Will We See Gigahertz Organic Transistors?," *Advanced Electronic Materials*, vol. 4, no. 10, p. 1700474, 2018.

[7] S. Tiwari and N. C. Greenham, "Charge mobility measurement techniques in organic semiconductors," *Optical and Quantum Electronics*, vol. 41, pp. 69–89, Jan. 2009.

[8] H. Bässler, "Charge Transport in Disordered Organic Photoconductors a Monte Carlo Simulation Study," *physica status solidi (b)*, vol. 175, pp. 15–56, Jan. 1993.

[9] M. V. d. Auweraer, F. C. D. Schryver, P. M. Borsenberger, and H. Bässler, "Disorder in Charge Transport in doped polymers," *Advanced Materials*, vol. 6, no. 3, pp. 199–213, 1994.

[10] Y. Roichman, Y. Preezant, and N. Tessler, "Analysis and modeling of organic devices," *physica status solidi (a)*, vol. 201, no. 6, pp. 1246–1262, 2004.

[11] W. F. Pasveer, J. Cottaar, C. Tanase, R. Coehoorn, P. A. Bobbert, P. W. M. Blom, D. M. de Leeuw, and M. A. J. Michels, "Unified Description of Charge-Carrier Mobilities in Disordered Semiconducting Polymers," *Physical Review Letters*, vol. 94, May 2005.

[12] I. I. Fishchuk, V. I. Arkhipov, A. Kadashchuk, P. Heremans, and H. Bässler, "Analytic model of hopping mobility at large charge carrier concentrations in disordered organic semiconductors: Polarons versus bare charge carriers," *Physical Review B*, vol. 76, p. 045210, July 2007.

[13] J. Zhou, Y. C. Zhou, J. M. Zhao, C. Q. Wu, X. M. Ding, and X. Y. Hou, "Carrier density dependence of mobility in organic solids: A Monte Carlo simulation," *Physical Review B*, vol. 75, Apr. 2007.

[14] S. V. Novikov, "Hopping charge transport in organic materials," *Russian Journal of Electrochemistry*, vol. 48, pp. 388–400, Apr. 2012.

[15] I. I. Fishchuk, A. Kadashchuk, S. T. Hoffmann, S. Athanasopoulos, J. Genoe, H. Bässler, and A. Köhler, "Unified description for hopping transport in organic semiconductors including both energetic disorder and polaronic contributions," *Physical Review B*, vol. 88, p. 125202, Sept. 2013.

[16] N. J. van der Kaap, I. Katsouras, K. Asadi, P. W. M. Blom, L. J. A. Koster, and D. M. de Leeuw, "Charge transport in disordered semiconducting polymers driven by nuclear tunneling," *Physical Review B*, vol. 93, p. 140206, Apr. 2016.

[17] J. O. Oelerich, A. V. Nenashev, A. V. Dvurechenskii, F. Gebhard, and S. D. Baranovskii, "Field dependence of hopping mobility: Lattice models against spatial disorder," *Physical Review B*, vol. 96, p. 195208, Nov. 2017.

[18] H. H. Choi, K. Cho, C. D. Frisbie, H. Sirringhaus, and V. Podzorov, "Critical assessment of charge mobility extraction in FETs," *Nature Materials*, vol. 17, pp. 2–7, Dec. 2017.

[19] Y. Xu, H. Sun, A. Liu, H. Zhu, B. Li, T. Minari, F. Balestra, G. Ghibaudo, and Y.-Y. Noh, "Essential Effects on the Mobility Extraction Reliability for Organic Transistors," *Advanced Functional Materials*, vol. 28, no. 42, p. 1803907, 2018.

[20] A. F. Paterson, S. Singh, K. J. Fallon, T. Hodsden, Y. Han, B. C. Schroeder, H. Bronstein, M. Heeney, I. McCulloch, and T. D. Anthopoulos, "Recent Progress in High-Mobility Organic Transistors: A Reality Check," *Advanced Materials*, vol. 30, no. 36, p. 1801079, 2018.

[21] X. Guo, Y. Xu, S. Ogier, T. N. Ng, M. Caironi, A. Perinot, L. Li, J. Zhao, W. Tang, R. A. Sporea, A. Nejim, J. Carrabina, P. Cain, and F. Yan, "Current Status and Opportunities of Organic Thin-Film Transistor Technologies," *IEEE Transactions on Electron Devices*, vol. 64, pp. 1906–1921, May 2017.

[22] A. Yamamura, S. Watanabe, M. Uno, M. Mitani, C. Mitsui, J. Tsurumi, N. Isahaya, Y. Kanaoka, T. Okamoto, and J. Takeya, "Wafer-scale, layer-controlled organic single crystals for high-speed circuit operation," *Science Advances*, vol. 4, p. eaao5758, Feb. 2018.

[23] S. D. Ogier, H. Matsui, L. Feng, M. Simms, M. Mashayekhi, J. Carrabina, L. Terés, and S. Tokito, "Uniform, high performance, solution processed organic thin-film transistors integrated in 1 MHz frequency ring oscillators," *Organic Electronics*, vol. 54, pp. 40–47, Mar. 2018.

[24] J. W. Borchert, B. Peng, F. Letzkus, J. N. Burghartz, P. K. L. Chan, K. Zojer, S. Ludwigs, and H. Klauk, "Small contact resistance and high-frequency operation of flexible low-voltage inverted coplanar organic transistors," *Nature Communications*, vol. 10, pp. 1–11, Mar. 2019.

[25] J. Zaumseil and H. Sirringhaus, "Electron and Ambipolar Transport in Organic Field-Effect Transistors," *Chemical Reviews*, vol. 107, pp. 1296–1323, Apr. 2007.

[26] W. Shockley, "A Unipolar 'Field-Effect' Transistor," *Proceedings of the IRE*, vol. 40, pp. 1365–1376, Nov. 1952.

[27] O. Marinov, M. J. Deen, U. Zschieschang, and H. Klauk, "Organic Thin-Film Transistors: Part I-Compact DC Modeling," *IEEE Transactions on Electron Devices*, vol. 56, pp. 2952–2961, Dec. 2009.

[28] G. Horowitz, "Organic Field-Effect Transistors," *Advanced Materials*, vol. 10, no. 5, pp. 365–377, 1998.

[29] H. Sirringhaus, "Device Physics of Solution-Processed Organic Field-Effect Transistors," *Advanced Materials*, vol. 17, no. 20, pp. 2411–2425, 2005.

[30] D. Natali and M. Caironi, "Charge injection in solution-processed organic field-effect transistors: physics, models and characterization methods," *Advanced Materials*, vol. 24, pp. 1357–1387, Mar. 2012.

[31] S. K. Possanner, K. Zojer, P. Pacher, E. Zojer, and F. Schürrer, "Threshold Voltage Shifts in Organic Thin-Film Transistors Due to Self-Assembled Monolayers at the Dielectric Surface," *Advanced Functional Materials*, vol. 19, no. 6, pp. 958–967, 2009.

[32] R. B. Hall, "The Poole-Frenkel effect," *Thin Solid Films*, vol. 8, pp. 263–271, Oct. 1971.

[33] S. Locci, M. Morana, E. Orgiu, A. Bonfiglio, and P. Lugli, "Modeling of Short-Channel Effects in Organic Thin-Film Transistors," *IEEE Transactions on Electron Devices*, vol. 55, pp. 2561–2567, Oct. 2008.

[34] M. C. J. M. Vissenberg and M. Matters, "Theory of the field-effect mobility in amorphous organic transistors," *Physical Review B*, vol. 57, pp. 12964–12967, May 1998.

[35] G. Horowitz, M. E. Hajlaoui, and R. Hajlaoui, "Temperature and gate voltage dependence of hole mobility in polycrystalline oligothiophene thin film transistors," *Journal of Applied Physics*, vol. 87, pp. 4456–4463, Apr. 2000.

[36] D. Natali, L. Fumagalli, and M. Sampietro, "Modeling of organic thin film transistors: Effect of contact resistances," *Journal of Applied Physics*, vol. 101, p. 014501, Jan. 2007.

[37] Y. Xu, H. Sun, and Y. Noh, "Schottky Barrier in Organic Transistors," *IEEE Transactions on Electron Devices*, vol. 64, pp. 1932–1943, May 2017.

[38] J. Li, W. Ou-Yang, and M. Weis, "Electric-field enhanced thermionic emission model for carrier injection mechanism of organic field-effect transistors: understanding of contact resistance," *Journal of Physics D: Applied Physics*, vol. 50, no. 3, p. 035101, 2017.

[39] M. J. Deen, O. Marinov, U. Zschieschang, and H. Klauk, "Organic Thin-Film Transistors: Part II-Parameter Extraction," *IEEE Transactions on Electron Devices*, vol. 56, pp. 2962–2968, Dec. 2009.

[40] S. D. Wang, Y. Yan, and K. Tsukagoshi, "Transition-Voltage Method for Estimating Contact Resistance in Organic Thin-Film Transistors," *IEEE Electron Device Letters*, vol. 31, pp. 509–511, May 2010.

[41] S. Takagaki, H. Yamada, and K. Noda, "Extraction of contact resistance and channel parameters from the electrical characteristics of a single bottom-gate/top-contact organic transistor," *Japanese Journal of Applied Physics*, vol. 55, p. 03DC07, Feb. 2016.

[42] F. Torricelli, M. Ghittorelli, L. Colalongo, and Z.-M. Kovacs-Vajna, "Single-transistor method for the extraction of the contact and channel resistances in organic field-effect transistors," *Applied Physics Letters*, vol. 104, p. 093303, Mar. 2014.

[43] R. Di Pietro, D. Venkateshvaran, A. Klug, E. J. W. List-Kratochvil, A. Facchetti, H. Sirringhaus, and D. Neher, "Simultaneous extraction of charge density dependent mobility and variable contact resistance from thin film transistors," *Applied Physics Letters*, vol. 104, p. 193501, May 2014.

[44] A. Fischer, H. Zündorf, F. Kaschura, J. Widmer, K. Leo, U. Kraft, and H. Klauk, "Nonlinear Contact Effects in Staggered Thin-Film Transistors," *Physical Review Applied*, vol. 8, p. 054012, Nov. 2017.

[45] D. Marquardt, "An Algorithm for Least-Squares Estimation of Nonlinear Parameters," *Journal of the Society for Industrial and Applied Mathematics*, vol. 11, pp. 431–441, June 1963.

[46] J. Kanicki, F. R. Libsch, J. Griffith, and R. Polastre, "Performance of thin hydrogenated amorphous silicon thin-film transistors," *Journal of Applied Physics*, vol. 69, pp. 2339–2345, Feb. 1991.

[47] S. Luan and G. W. Neudeck, "An experimental study of the source/drain parasitic resistance effects in amorphous silicon thin film transistors," *Journal of Applied Physics*, vol. 72, pp. 766–772, July 1992.

[48] J. Mayer, K. Khairy, and J. Howard, "Drawing an elephant with four complex parameters," *American Journal of Physics*, vol. 78, pp. 648–649, May 2010.

[49] D. J. Gundlach, J. E. Royer, S. K. Park, S. Subramanian, O. D. Jurchescu, B. H. Hamadani, A. J. Moad, R. J. Kline, L. C. Teague, O. Kirillov, C. A. Richter, J. G. Kushmerick, L. J. Richter, S. R. Parkin, T. N. Jackson, and J. E. Anthony, "Contact-induced crystallinity for high-performance soluble acene-based transistors and circuits," *Nature Materials*, vol. 7, pp. 216–221, Mar. 2008.

[50] J.-P. Hong, A.-Y. Park, S. Lee, J. Kang, N. Shin, and D. Y. Yoon, "Tuning of Ag work functions by self-assembled monolayers of aromatic thiols for an efficient hole injection for solution processed triisopropylsilylethynyl pentacene organic thin film transistors," *Applied Physics Letters*, vol. 92, p. 143311, Apr. 2008.

[51] M. Shur, *Physics of semiconductor devices*. New Jersey: Prentice Hall, 1990. ISBN: 9780136664963.

[52] S. M. Sze and K. K. Ng, *Physics of semiconductor devices.* New York: John Wiley & Sons, 2007. ISBN: 9780471143239.

[53] P. Servati, D. Striakhilev, and A. Nathan, "Above-threshold parameter extraction and modeling for amorphous silicon thin-film transistors," *IEEE Transactions on Electron Devices*, vol. 50, pp. 2227–2235, Nov. 2003.

[54] D. J. Gundlach, L. Zhou, J. A. Nichols, T. N. Jackson, P. V. Necliudov, and M. S. Shur, "An experimental study of contact effects in organic thin film transistors," *Journal of Applied Physics*, vol. 100, p. 024509, July 2006.

[55] K. Jung, Y. C. Kim, B. Park, H. Shin, and J. D. Lee, "Modeling and Parameter Extraction for the Series Resistance in Thin-Film Transistors," *IEEE Transactions on Electron Devices*, vol. 56, pp. 431–440, Mar. 2009.

[56] U. Kraft, K. Takimiya, M. J. Kang, R. Rödel, F. Letzkus, J. N. Burghartz, E. Weber, and H. Klauk, "Detailed analysis and contact properties of low-voltage organic thin-film transistors based on dinaphtho[2,3-b:2',3'-f]thieno[3,2-b]thiophene (DNTT) and its didecyl and diphenyl derivatives," *Organic Electronics*, vol. 35, pp. 33–40, Aug. 2016.

[57] M. Gärtner, E. Sauter, G. Nascimbeni, A. Petritz, A. Wiesner, M. Kind, T. Abu-Husein, M. Bolte, B. Stadlober, E. Zojer, A. Terfort, and M. Zharnikov, "Understanding the Properties of Tailor-Made Self-Assembled Monolayers with Embedded Dipole Moments for Interface Engineering," *The Journal of Physical Chemistry C*, vol. 122, pp. 28757–28774, Dec. 2018.

[58] J. W. Park, D. C. Shin, and S. H. Park, "Large-area OLED lightings and their applications," *Semiconductor Science and Technology*, vol. 26, p. 034002, Feb. 2011.

[59] D. Ma, "White OLED Devices," in *Handbook of Advanced Lighting Technology* (R. Karlicek, C.-C. Sun, G. Zissis, and R. Ma, eds.), pp. 321–361, Cham: Springer International Publishing, 2017. ISBN: 9783319001760.

[60] J. Zhang, Y. Zhao, J. Fang, L. Yuan, B. Xia, G. Wang, Z. Wang, Y. Zhang, W. Ma, W. Yan, W. Su, and Z. Wei, "Enhancing Performance of Large-Area Organic Solar Cells with Thick Film via Ternary Strategy," *Small*, vol. 13, no. 21, p. 1700388, 2017.

[61] S. Dong, K. Zhang, B. Xie, J. Xiao, H.-L. Yip, H. Yan, F. Huang, and Y. Cao, "High-Performance Large-Area Organic Solar Cells Enabled by Sequential Bilayer Processing via Nonhalogenated Solvents," *Advanced Energy Materials*, vol. 9, no. 1, p. 1802832, 2019.

[62] J. Park, J. Lee, D. Shin, and S. Park, "Luminance Uniformity of Large-Area OLEDs With an Auxiliary Metal Electrode," *Journal of Display Technology*, vol. 5, pp. 306–311, Aug. 2009.

[63] M. Mesta, M. Carvelli, R. J. de Vries, H. van Eersel, J. J. M. van der Holst, M. Schober, M. Furno, B. Lüssem, K. Leo, P. Loebl, R. Coehoorn, and P. A. Bobbert, "Molecular-scale simulation of electroluminescence in a multilayer white organic light-emitting diode," *Nature Materials*, vol. 12, pp. 652–658, Apr. 2013.

[64] A. B. Walker, "Multiscale Modeling of Charge and Energy Transport in Organic Light-Emitting Diodes and Photovoltaics," *Proceedings of the IEEE*, vol. 97, pp. 1587–1596, Sept. 2009.

[65] J. Cottaar, R. Coehoorn, and P. A. Bobbert, "Modeling of charge transport across disordered organic heterojunctions," *Organic Electronics*, vol. 13, pp. 667–672, Apr. 2012.

[66] H. Li, Y. Qiu, and L. Duan, "Multi-scale calculation of the electric properties of organic-based devices from the molecular structure," *Organic Electronics*, vol. 33, pp. 164–171, June 2016.

[67] M. L. Jones, D. M. Huang, B. Chakrabarti, and C. Groves, "Relating Molecular Morphology to Charge Mobility in Semicrystalline Conjugated Polymers," *The Journal of Physical Chemistry C*, vol. 120, pp. 4240–4250, Mar. 2016.

[68] C. Winkler, F. Mayer, and E. Zojer, "Analyzing the Electronic Coupling in Molecular Crystals-The Instructive Case of α-Quinacridone," *Advanced Theory and Simulations*, vol. 2, no. 5, p. 1800204, 2019.

[69] C. Groves, "Simulating charge transport in organic semiconductors and devices: a review," *Reports on Progress in Physics*, vol. 80, p. 026502, Dec. 2016.

[70] S. D. Baranovskii, "Theoretical description of charge transport in disordered organic semiconductors," *physica status solidi (b)*, vol. 251, no. 3, pp. 487–525, 2014.

[71] V. Coropceanu, J. Cornil, D. A. da Silva Filho, Y. Olivier, R. Silbey, and J.-L. Brédas, "Charge Transport in Organic Semiconductors," *Chemical Reviews*, vol. 107, pp. 926–952, Apr. 2007.

[72] A. Troisi and G. Orlandi, "Charge-Transport Regime of Crystalline Organic Semiconductors: Diffusion Limited by Thermal Off-Diagonal Electronic Disorder," *Physical Review Letters*, vol. 96, p. 086601, Mar. 2006.

[73] Y.-C. Cheng and R. J. Silbey, "A unified theory for charge-carrier transport in organic crystals," *The Journal of Chemical Physics*, vol. 128, p. 114713, Mar. 2008.

[74] F. Ortmann, F. Bechstedt, and K. Hannewald, "Theory of charge transport in organic crystals: Beyond Holstein's small-polaron model," *Physical Review B*, vol. 79, p. 235206, June 2009.

[75] S. Fratini and S. Ciuchi, "Bandlike Motion and Mobility Saturation in Organic Molecular Semiconductors," *Physical Review Letters*, vol. 103, p. 266601, Dec. 2009.

[76] S. Ciuchi, S. Fratini, and D. Mayou, "Transient localization in crystalline organic semiconductors," *Physical Review B*, vol. 83, p. 081202, Feb. 2011.

[77] S. Fratini, S. Ciuchi, D. Mayou, G. T. de Laissardière, and A. Troisi, "A map of high-mobility molecular semiconductors," *Nature Materials*, vol. 16, pp. 998–1002, Oct. 2017.

[78] H. Li, Y. Li, H. Li, and J.-L. Brédas, "Organic Field-Effect Transistors: A 3D Kinetic Monte Carlo Simulation of the Current Characteristics in Micrometer-Sized Devices," *Advanced Functional Materials*, vol. 27, no. 9, p. 1605715, 2017.

[79] U. Wolf, V. I. Arkhipov, and H. Bässler, "Current injection from a metal to a disordered hopping system. I. Monte Carlo simulation," *Physical Review B*, vol. 59, pp. 7507–7513, Mar. 1999.

[80] R. A. Marsh, C. Groves, and N. C. Greenham, "A microscopic model for the behavior of nanostructured organic photovoltaic devices," *Journal of Applied Physics*, vol. 101, p. 083509, Apr. 2007.

[81] P. K. Watkins, A. B. Walker, and G. L. B. Verschoor, "Dynamical Monte Carlo Modelling of Organic Solar Cells: The Dependence of Internal Quantum Efficiency on Morphology," *Nano Letters*, vol. 5, pp. 1814–1818, Sept. 2005.

[82] J. J. M. van der Holst, F. W. A. van Oost, R. Coehoorn, and P. A. Bobbert, "Monte Carlo study of charge transport in organic sandwich-type single-carrier devices: Effects of Coulomb interactions," *Physical Review B*, vol. 83, p. 085206, Feb. 2011.

[83] N. J. van der Kaap and L. J. A. Koster, "Charge carrier thermalization in organic diodes," *Scientific Reports*, vol. 6, p. 19794, Jan. 2016.

[84] M. C. Heiber and A. Dhinojwala, "Dynamic Monte Carlo modeling of exciton dissociation in organic donor-acceptor solar cells," *The Journal of Chemical Physics*, vol. 137, p. 014903, July 2012.

[85] C. Groves, R. G. E. Kimber, and A. B. Walker, "Simulation of loss mechanisms in organic solar cells: A description of the mesoscopic Monte Carlo technique and an evaluation of the first reaction method," *The Journal of Chemical Physics*, vol. 133, p. 144110, Oct. 2010.

[86] L. J. A. Koster, "Charge carrier mobility in disordered organic blends for photovoltaics," *Physical Review B*, vol. 81, p. 205318, May 2010.

[87] Z. G. Yu, D. L. Smith, A. Saxena, R. L. Martin, and A. R. Bishop, "Molecular geometry fluctuations and field-dependent mobility in conjugated polymers," *Physical Review B*, vol. 63, p. 085202, Feb. 2001.

[88] W. F. Pasveer, P. A. Bobbert, H. P. Huinink, and M. A. J. Michels, "Scaling of current distributions in variable-range hopping transport on two- and three-dimensional lattices," *Physical Review B*, vol. 72, p. 174204, Nov. 2005.

[89] M. Casalegno, A. Bernardi, and G. Raos, "Numerical simulation of photocurrent generation in bilayer organic solar cells: Comparison of master equation and kinetic Monte Carlo approaches," *The Journal of Chemical Physics*, vol. 139, p. 024706, July 2013.

[90] R. Coehoorn and S. L. M. van Mensfoort, "Effects of disorder on the current density and recombination profile in organic light-emitting diodes," *Physical Review B*, vol. 80, p. 085302, Aug. 2009.

[91] A. Massé, R. Coehoorn, and P. Bobbert, "Universal Size-Dependent Conductance Fluctuations in Disordered Organic Semiconductors," *Physical Review Letters*, vol. 113, p. 116604, Sept. 2014.

[92] J. Cottaar and P. A. Bobbert, "Calculating charge-carrier mobilities in disordered semiconducting polymers: Mean field and beyond," *Physical Review B*, vol. 74, p. 115204, Sept. 2006.

[93] M. Krammer, "Coulomb Interactions in Kinetic Monte Carlo Simulations for Charge Transport in Organic Semiconductors," Master's thesis, Graz University of Technology, Graz, June 2016.

[94] A. Miller and E. Abrahams, "Impurity Conduction at Low Concentrations," *Physical Review*, vol. 120, pp. 745–755, Nov. 1960.

[95] R. A. Marcus, "Electron transfer reactions in chemistry. Theory and experiment," *Reviews of Modern Physics*, vol. 65, pp. 599–610, July 1993.

[96] W. J. Anderson, *Continuous-time Markov chains: an applications-oriented approach*. New York; Berlin: Springer-Vlg, 1991. ISBN: 9780387973692.

[97] Y. Saad, *Iterative methods for sparse linear systems*. Philadelphia, PA: SIAM, Society for Industrial and Applied Mathematics, 2007. ISBN: 9780898715347.

[98] J.-P. Wu and H. Ma, "MRILDU: An improvement to ILUT based on incomplete LDU factorization and dropping in multiple rows," *Journal of Applied Mathematics*, vol. 2014, pp. 1–9, Aug. 2014.

[99] R. G. Miller, "The Jackknife-A Review," *Biometrika*, vol. 61, no. 1, pp. 1–15, 1974.

[100] J. Cottaar, R. Coehoorn, and P. A. Bobbert, "Field-induced detrapping in disordered organic semiconducting host-guest systems," *Physical Review B*, vol. 82, p. 205203, Nov. 2010.

[101] H. Ishii, K. Sugiyama, E. Ito, and K. Seki, "Energy Level Alignment and Interfacial Electronic Structures at Organic/Metal and Organic/Organic Interfaces," *Advanced Materials*, vol. 11, no. 8, pp. 605–625, 1999.

[102] E. Zojer, T. C. Taucher, and O. T. Hofmann, "The Impact of Dipolar Layers on the Electronic Properties of Organic/Inorganic Hybrid Interfaces," *Advanced Materials Interfaces*, vol. 6, no. 14, p. 1900581, 2019.

[103] E. Sauter, C.-O. Gilbert, J.-F. Morin, A. Terfort, and M. Zharnikov, "Mixed Monomolecular Films with Embedded Dipolar Groups on Ag(111)," *The Journal of Physical Chemistry C*, vol. 122, pp. 19514–19523, Aug. 2018.

[104] J. C. Scott and G. G. Malliaras, "Charge injection and recombination at the metal-organic interface," *Chemical Physics Letters*, vol. 299, pp. 115–119, Jan. 1999.

[105] A. L. Burin and M. A. Ratner, "Charge injection into disordered molecular films," *Journal of Polymer Science Part B: Polymer Physics*, vol. 41, no. 21, pp. 2601–2621, 2003.

[106] F. Neumann, Y. A. Genenko, C. Melzer, S. V. Yampolskii, and H. von Seggern, "Self-consistent analytical solution of a problem of charge-carrier injection at a conductor/insulator interface," *Physical Review B*, vol. 75, p. 205322, May 2007.

[107] P. López Varo, J. A. Jiménez Tejada, J. A. López Villanueva, J. E. Carceller, and M. J. Deen, "Modeling the transition from ohmic to space charge limited current in organic semiconductors," *Organic Electronics*, vol. 13, pp. 1700–1709, Sept. 2012.

[108] P. López Varo, J. A. Jiménez Tejada, J. A. López Villanueva, and M. J. Deen, "Space-charge and injection limited current in organic diodes: A unified model," *Organic Electronics*, vol. 15, pp. 2526–2535, Oct. 2014.

[109] V. I. Arkhipov, H. von Seggern, and E. V. Emelianova, "Charge injection versus space-charge-limited current in organic light-emitting diodes," *Applied Physics Letters*, vol. 83, pp. 5074–5076, Dec. 2003.

[110] M. Raoufi, U. Hörmann, G. Ligorio, E. List-Kratochvil, S. Hecht, and D. Neher, "Simultaneous effect of UV-radiation and surface modification on energy level alignment and charge injection across hybrid metal oxide/organic interfaces.." in preparation.

[111] P. P. Ewald, "Die Berechnung optischer und elektrostatischer Gitterpotentiale," *Annalen der Physik*, vol. 369, no. 3, pp. 253–287, 1921.

[112] S. W. de Leeuw, J. W. Perram, and E. R. Smith, "Simulation of Electrostatic Systems in Periodic Boundary Conditions. I. Lattice Sums and Dielectric Constants," *Proceedings of the Royal Society A: Mathematical, Physical and Engineering Sciences*, vol. 373, pp. 27–56, Oct. 1980.

[113] H. B. Lee and W. G. Cai, "Ewald Summation for Coulomb Interactions in a Periodic Supercell." `http://micro.stanford.edu/mediawiki/images/4/46/Ewald_notes.pdf`, 2009. Accessed: 2019-06-28.

[114] M. Casalegno, G. Raos, and R. Po, "Methodological assessment of kinetic Monte Carlo simulations of organic photovoltaic devices: The treatment of electrostatic interactions," *The Journal of Chemical Physics*, vol. 132, p. 094705, Mar. 2010.

[115] U. Hörmann, S. Zeiske, F. Piersimoni, L. Hoffmann, R. Schlesinger, N. Koch, T. Riedl, D. Andrienko, and D. Neher, "Stark effect of hybrid charge transfer states at planar ZnO/organic interfaces," *Physical Review B*, vol. 98, p. 155312, Oct. 2018.

[116] I. Lange, S. Reiter, J. Kniepert, F. Piersimoni, M. Pätzel, J. Hildebrandt, T. Brenner, S. Hecht, and D. Neher, "Zinc oxide modified with benzylphosphonic acids as transparent electrodes in regular and inverted organic solar cell structures," *Applied Physics Letters*, vol. 106, p. 113302, Mar. 2015.